Determining Optimum Thickness for Long-Life Concrete Pavement in Ohio

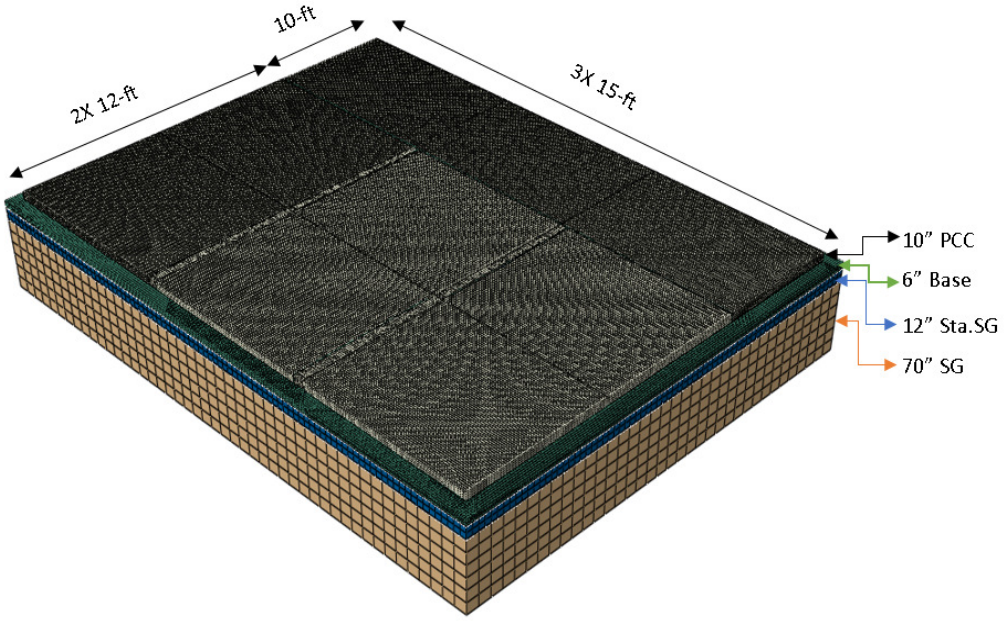

Prepared by Shad Sargand, Anwer Al-Jhayyish,
Issam Khoury, and Roger Green

Prepared for the Ohio Department of Transportation
Office of Statewide Planning and Research

State Job Number 135244

August 2018

Final Report

U.S. Department of Transportation
Federal Highway Administration

1 8 0 4

OHIO UNIVERSITY

Ohio Research Institute for Transportation and the Environment

1. Report No. FHWA/OH-2018-14	**2. Government Accession No.**	**3. Recipient's Catalog No.**
4. Title and Subtitle Determining Optimum Thickness for Long-Life Concrete Pavement in Ohio		**5. Report Date** August 2018 **6. Performing Organization Code**
7. Author(s) Shad Sargand (ORCID 0000-0002-1633-1045), Anwer Al-Jhayyish, Issam Khoury (0000-0003-4856-7535) and Roger Green (0000-0003-2497-825X)		**8. Performing Organization Report No.**
9. Performing Organization Name and Address Ohio Research Institute for Transportation and the Environment (ORITE) 233 Stocker Center Ohio University Athens, OH 45701-2979		**10. Work Unit No. (TRAIS)** **11. Contract or Grant No.** State Job No. 135244
12. Sponsoring Agency Name and Address Ohio Department of Transportation 1980 West Broad St. Columbus, OH 43223		**13. Type of Report and Period Covered** Final Report August 2015 – December 2017 **14. Sponsoring Agency Code**

15. Supplementary Notes
Prepared in cooperation with the Ohio Department of Transportation (ODOT) and the U.S. Department of Transportation, Federal Highway Administration

16. Abstract
The AASHTO 1993 design equation for rigid pavements implies an increasing thickness of concrete will be needed as traffic increases. However, fatigue testing of concrete beams has shown concrete can endure an unlimited number of loads if the stress ratio (SR) is less than a critical value. Any greater thickness results in an overdesigned slab and is not cost effective. Field and experimental data from Ohio concrete pavements were used to validate a 3D finite element (FE) model with which critical slab stresses were calculated for several slab geometries. Long term pavement performance analysis conducted with AASHTOWare Pavement ME Design software showed the 12 in (305 mm) thick by 13.5 ft (4.1 m) long slab exhibited superior performance in terms of IRI, faulting, cracking, and cost over a 50-year design life. A fatigue analysis using the PCA and zero maintenance models, verified this conclusion. Small variabilities were noticed in the AASHTOWare Pavement ME Design software predicted percent cracking that were caused by different freeze-thaw cycles recorded at different weather stations in Ohio. An increase in k-values was observed when stabilized subgrade was introduced to the pavement system. The AASHTO method of determining a composite k-value is still valid when using the modulus of stabilized subgrade.

17. Key Words Rigid pavement thickness design, finite element modeling, stabilized subgrade, MEPDG	**18. Distribution Statement** No Restrictions. This document is available to the public through the National Technical Information Service, Springfield, Virginia 22161

19. Security Classif. (of this report) Unclassified	**20. Security Classif. (of this page)** Unclassified	**21. No. of Pages** 178	**22. Price**

SI* (MODERN METRIC) CONVERSION FACTORS

APPROXIMATE CONVERSIONS TO SI UNITS

Symbol	When You Know	Multiply By	To Find	Symbol
LENGTH				
in	inches	25.4	millimeters	mm
ft	feet	0.305	meters	m
yd	yards	0.914	meters	m
mi	miles	1.61	kilometers	km
AREA				
in^2	square inches	645.2	square millimeters	mm^2
ft^2	square feet	0.093	square meters	m^2
yd^2	square yards	0.836	square meters	m^2
ac	acres	0.405	hectares	ha
mi^2	square miles	2.59	square kilometers	km^2
VOLUME				
fl oz	fluid ounces	29.57	milliliters	mL
gal	gallons	3.785	liters	L
ft^3	cubic feet	0.028	cubic meters	m^3
yd^3	cubic yards	0.765	cubic meters	m^3
NOTE: Volumes greater than 1000 L shall be shown in m^3.				
MASS				
oz	ounces	28.35	grams	g
lb	pounds	0.454	kilograms	kg
T	short tons (2000 lb)	0.907	megagrams (or "metric ton")	Mg (or "t")
TEMPERATURE (exact)				
°F	Fahrenheit temperature	5(°F-32)/9 or (°F-32)/1.8	Celsius temperature	°C
ILLUMINATION				
fc	foot-candles	10.76	lux	lx
fl	foot-Lamberts	3.426	candela/m^2	cd/m^2
FORCE and PRESSURE or STRESS				
lbf	poundforce	4.45	newtons	N
lbf/in^2 or psi	poundforce per square inch	6.89	kilopascals	kPa

APPROXIMATE CONVERSIONS FROM SI UNITS

Symbol	When You Know	Multiply By	To Find	Symbol
LENGTH				
mm	millimeters	0.039	inches	in
m	meters	3.28	feet	ft
m	meters	1.09	yards	yd
km	kilometers	0.621	miles	mi
AREA				
mm^2	square millimeters	0.0016	square inches	in^2
m^2	square meters	10.764	square feet	ft^2
m^2	square meters	1.195	square yards	yd^2
ha	hectares	2.47	acres	ac
km^2	square kilometers	0.386	square miles	mi^2
VOLUME				
mL	milliliters	0.034	fluid ounces	fl oz
L	liters	0.264	gallons	gal
m^3	cubic meters	35.71	cubic feet	ft^3
m^3	cubic meters	1.307	cubic yards	yd^3
MASS				
g	grams	0.035	ounces	oz
kg	kilograms	2.202	pounds	lb
Mg (or "t")	megagrams (or "metric ton")	1.103	short tons (2000 lb)	T
TEMPERATURE (exact)				
°C	Celsius temperature	1.8°C + 32	Fahrenheit temperature	°F
ILLUMINATION				
lx	lux	0.0929	foot-candles	fc
cd/m^2	candela/m^2	0.2919	foot-Lamberts	fl
FORCE and PRESSURE or STRESS				
N	newtons	0.225	poundforce	lbf
kPa	kilopascals	0.145	poundforce per square inch	lbf/in^2 or psi

* SI is the symbol for the International Symbol of Units. Appropriate rounding should be made to comply with Section 4 of ASTM E380.

(Revised September 1993)

Determining Optimum Thickness for Long-Life Concrete Pavement in Ohio

Prepared by

Shad Sargand, Anwer Al-Jhayyish, Issam Khoury, and Roger Green

Ohio Research Institute for Transportation and the Environment
Russ College of Engineering and Technology
Ohio University
Athens, Ohio 45701-2979

Prepared in cooperation with the
Ohio Department of Transportation
and the
U.S. Department of Transportation, Federal Highway Administration

Final Report
August 2018

Acknowledgements

The authors acknowledge the people who ensured the successful completion of this project, starting with Kelly Nye of the Ohio Department of Transportation's Research Section. Aric Morse, Patrick Bierl and Adam Au served as the subject matter experts, providing guidance on the technical aspects of the project. Mark Pardi and Tom Rozsits of Ohio Concrete are thanked for providing technical comments and cost data. The Ohio Supercomputing Center provided computing resources that enabled the three-dimensional finite element simulations using ABAQUS software to be completed in a reasonable time.

Contents

List of Figures

List of Tables

1 Project Background

The 1993 AASHTO Guide for the Design of Pavement Structures uses equations for concrete pavements based on an empirical analysis of the two-year performance of test sections subjected to 1,114,000 load applications, a value representing 10% to 20% the load applications experienced by a typical interstate route in Ohio during its service life. The AASHTO design equation calculates a pavement thickness that increases as traffic increases. Due to the empirical nature of the 1993 AASHTO design equations, a slab thickness can be selected which will result in a terminal serviceability equal to or greater than the design terminal serviceability for a given reliability, overall standard deviation, concrete elastic modulus, concrete flexural strength, load transfer coefficient, and modulus of subgrade reaction after carrying the design ESAL. However, fatigue testing of concrete beams has shown concrete can endure an unlimited number of loadings if the stress ratio (SR), the total tensile stress due to traffic and environmental loads divided by the concrete modulus of rupture, is less than a critical value [Darter and Barenberg, 1977]. Given the truck configurations and axle loads at a site, the pavement thickness can be designed with a SR which will provide an infinite fatigue life. The minimum such thickness may be less than the thickness determined using the 1993 AASHTO design equations. Any greater thickness results in an overdesigned slab and is not cost effective. In this research, the SR was evaluated for a typical ODOT rigid pavement design, consisting of a doweled jointed plain concrete pavement (JPCP) on a 6 in (150 mm) dense graded aggregate base (DGAB), to determine the minimum thickness which results in a long fatigue life for anticipated truck traffic volume.

In addition, ODOT has adopted a policy to chemically stabilize the subgrade for all new road construction. The modulus of subgrade reaction, k, has never been determined for chemically stabilized soil in Ohio. Research is needed to determine a design value for k for chemically stabilized soil in Ohio.

2 Objectives

The main objective of this study is to provide guidance on the selection of concrete slab thickness required to achieve long term performance considering the effect of slab dimensions, concrete slab support, and climatic conditions on critical stresses. The study will include proposed changes to the design, construction, and material procedures/specifications that, if adopted and implemented, will significantly increase PCC pavement lifetimes and reduce maintenance costs. The estimated impact to the initial construction cost will also be evaluated.

A second objective is to determine a design k value for chemically stabilized subgrade.

The objectives were met by performing the following tasks.

1. Conduct an extensive literature search to identify factors affecting concrete pavement response and behavior, models for predicting concrete pavement response to environmental and truck loading, concrete fatigue performance, and procedures to determine the modulus of subgrade reaction for chemically stabilized subgrade soils.
2. Take the existing data sets from the concrete pavement studies in Ohio (e.g. Long-Term Pavement Performance (LTPP) database) and consolidate into single database. The combined data set will include strains, deflections, surface profiles, temperature, and traffic as collected by various means such as built-in sensors, falling weight deflectometer (FWD), light weight deflectometer (LWD), etc. Collect more recent traffic

and temperature data and necessary information to better understand the conditions rigid pavement experiences throughout its design life.

3. Use the most advanced finite element modeling techniques and finite element software to simulate concrete pavement behavior under Ohio conditions.
4. Validate these finite element models with experimental data in order to capture critical pavement responses under environmental and truck loading conditions.
5. Use the validated finite element model to study the effect of thickness, spacing, and shoulder width on concrete pavement critical responses.
6. Employ the frequently used concrete fatigue models along with predicted critical stresses to determine the optimum concrete slab thickness and joint spacing for pavement designs that would perform long term under severe environmental and truck load conditions in Ohio.
7. Use the AASHTOWare Pavement-ME Design software to study the predicted long-term relative performance of concrete pavement in terms of major distresses such as faulting and transverse cracking and in terms of International Roughness Index (IRI).
8. Evaluate the effect on concrete pavement performance due to Ohio weather using the optimized concrete slab geometry and the Enhanced Integrated Climatic Model (EICM) built into the AASHTOWare program and accompanying data.
9. Propose possible procedures to determine the modulus of subgrade reaction k-value for chemically stabilized subgrade soils.

3 Report Organization

This report contains 18 chapters. Chapter 1 introduces the problem, Chapter 2 states the objectives of the research, and Chapter 3 presents this overview. Chapter 4 contains a literature review on the development of design techniques for rigid pavement, the most advanced modeling techniques, and major causes of concrete pavement failure. Chapter 5 discusses the data on rigid pavements in Ohio and surrounding states from the Long-Term Pavement Performance (LTPP), examining possible trends in the data, followed by data on environmental response of rigid pavements, traffic loads in Ohio, and temperature across the state; these data sets are later used with the finite element model for concrete pavement which is presented and validated in Chapter 6 and Chapter 7. Chapter 8 through Chapter 13 discuss critical stresses and major factors affecting the model followed by the fatigue damage calculations used to determine the optimum slab geometry that ensures a long service life. The long-term performance of concrete pavements as determined by selected distress models and by pavement design software is presented in Chapter 14. The effects of climate are presented in Chapter 15, while Chapter 16 includes a construction cost analysis of various rigid pavement designs. Procedures to determine the k-value for stabilized subgrades is presented in Chapter 17. In Chapter 18, conclusions and recommendations are presented.

4 Literature Review

4.1 Factors Affecting Concrete Pavement Performance

Concrete pavement design is influenced by a variety of factors such as traffic, climate, soil properties, and the structural and mechanical properties of the materials used. Although the early development of pavement thickness design was based on experience, empiricism still plays a vital role. Empirical pavement design is characterized by the ability of pavement to sustain traffic for a given period as given by the Present Serviceability Index (PSI), which is an indicator of ride quality [Huang, 1993]. The concept of PSI was introduced during the AASHO Road test as a rating criterion for pavement performance. According to Yoder and Witczak [1975], the range of PSI is 0 to 5 where 5 indicates superior performance. When a new pavement is opened to traffic, it has an initial serviceability index which decreases to a minimum tolerance at the end of its service life. This minimum PSI is typically 1.5 [AASHTO 1993], while ODOT uses 2.5. The historical data obtained from AASHO Road Test were used to develop empirical design equations for rigid and flexible pavements. However, such equations were developed for a particular pavement structure, climatic region, and design conditions. Any region exhibiting different design conditions would require different design considerations. Therefore, the empirical design method must be adapted to different geographical regions. Furthermore, within a state there may be a great deal of variability in traffic, climate and pavement layer characteristics, and the adaptation that works at one location may not be suitable for another. In the 1970s, the Mechanistic-Empirical (M-E) pavement design method evolved to overcome the limitations associated with purely empirical design procedures [Timm and Barrett, 2005]. The method utilizes solid relationships that characterize material behavior under combinations of loading and traffic conditions. It uses the principles of engineering mechanics to determine pavement responses and relate them to distresses incurred in the pavement throughout its design life [Timm and Barrett, 2005].

Truck traffic is a key parameter in the design of rigid pavement. It is defined as the number of heavy load applications anticipated during the design life. It is expressed in terms of the equivalent number of 18 kip (80 kN) single axle loads (ESALs) [ASHTO 1993]. The concept of ESALs is accepted by design agencies worldwide since it accounts for effect of axles with different loads than 18 kip (80 kN) [Yoder et al, 1975].

Subgrade support is characterized by the modulus of subgrade reaction, also known as the k-value. Different experimental and theoretical procedures were developed over the years to determine the modulus of subgrade reaction. Huang [1993] says k-value is important to determine accurately since it characterizes the support provided by the subgrade and subbase layer under the rigid pavement.

Climate also influences the design and performance of concrete pavement. Seasonal variations of temperature and moisture affect the behavior of the concrete material in many ways. Daily and seasonal temperature variations could cause opening and closing at transverse joints, compromising the load transfer efficiency and accelerating the deterioration of the pavement joints. Upwards and downward curl can be attributed to the temperature difference between the top and the bottom of concrete slab during daytime and night time as shown in Figure 1.

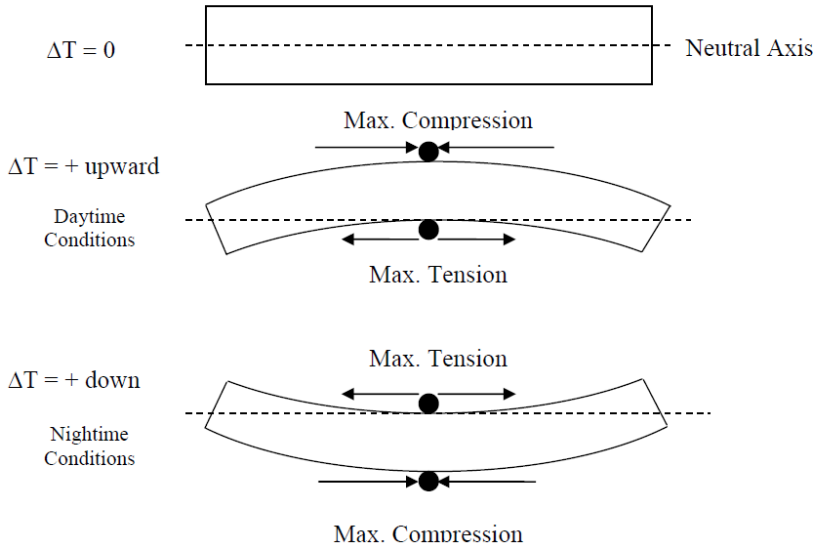

Figure 1. Curling due to temperature difference between the top and bottom of a rigid pavement slab [Timm and William, 2005].

Warping of the concrete slab is a result of seasonal variation in the moisture gradient. Permanent upward curl may happen during the construction due to the dissipation of temperature gradient which originally existed in the pavement while curing. Loss of support beneath the concrete slab could occur due to erosion of base material if it is poorly drained. Freeze-thaw cycles could degrade the pavement, aggregate base, and subgrade. Additionally, dowel bars and tie bars could corrode as a result of water infiltration through cracks, especially in regions where deicing chemicals are routinely used. The effects of climate on the pavement design and construction were identified in the early development of pavement design experiments; however, most of the factors previously described were not fully incorporated. Recent experimental and theoretical studies have been conducted to better understand climate effects so they may be considered in pavement thickness design [Hall, 2000]. The effect of climate was incorporated in the 2002 pavement design guide [ERES, 2002; AASHTO, 2008] through the enhanced integrated climatic model (EICM) which includes recent analytical and field studies and data from across the United States compiled from regional weather stations. The EICM is incorporated in the current version of the MEPDG software, now called AASHTOWare Pavement ME Design.

Concrete material properties such as compressive strength, modulus of elasticity, and flexural strength are key input parameters in the concrete pavement thickness design. The modulus of elasticity describes the stiffness of concrete material and can be either determined experimentally or predicted using concrete 28-day compressive strength from Equation 1, from the American Concrete Institute [ACI Committee 318, 2014]. The flexural strength of concrete is a measure of quality and durability of the concrete material and used as an indicator of fatigue resistance. Based on the AASHTO equations, a higher flexural strength would allow a thinner slab thickness and/or a longer fatigue life. The concrete flexural strength is characterized by 28-day modulus of rupture, which can be determined experimentally from third point loading test of a beam or may be estimated using the 28-day compressive strength as shown in Equation 2, from the American Concrete Institute code [ACI], or Equation 2a, from Sehn [2002].

$$E_c = 57000\sqrt{f'_c} \quad (1)$$

$S_c = 7.5\sqrt{f'_c}$ (2)

$S_c = 5.21(f'_c)^{0.58}$ (2a)

where:

E_c= modulus of elasticity, psi

S_c= modulus of rupture, psi

f'_c= compressive strength, psi

The Long Term Pavement Performance (LTPP) database provides tremendous amount of data on concrete pavement performance from test sections across the United States and Canada. The SPS-2 experiments in the LTPP database were designed to investigate the effects of PCC slab thickness, PCC flexural strength, base type, drainage, lane width, and climate on rigid pavement performance [Chatti et al, 2005]. Several studies have been conducted using the LTPP database to identify factors impacting the response and performance of concrete pavement [Owusu-Antwi et al, 1998; Darter et al, 1997; Darter, 1992; Dempsey, Poblete et al, 1988; and Yu et al, 1997]. Key findings of these studies are presented here. Studies conducted on the effect of slab thickness on pavement performance showed thicker PCC slabs experience reductions in transverse cracking, faulting, spalling, pumping, and edge and corner deflections [Owusu-Antwi et al, 1998; Darter et al, 1997; Darter, 1992]. Other studies investigating the effect of subgrade types on pavement performance showed pavements resting on weak subgrades exhibited increased corner cracking and potentials for voids due to non-uniform support. On the other hand, pavements resting on very stiff subgrades exhibited excessive curling and warping. An average of 23% of slabs resting on a stiff subgrade in Chile cracked prematurely [Chatti et al., 2005]. Additionally, subgrades with high percentage of fines are prone to erosion, swelling, frost heave, and pumping [Dempsey, Poblete et al, 1988]. Pumping under pavements has been studied in Ohio since the second Ohio Department of Highways (precursor to ODOT) research report [ODH, 1951]. Studies which investigated the effect of climate on rigid pavement performance have shown pavements located in regions experiencing more than 70 freeze-thaw cycles and a greater number of wet days exhibited high levels of faulting and spalling [Chatti et al., 2005]. The combination of curling stresses and axle loads increases the potential for transverse cracking. Such stresses are worsened when slabs are resting on stiff bases. Increased roughness was observed in concrete pavements located in freeze zones compared to those located in non-freeze zones [Dempsey, Poblete et al, 1988, Yu et al, 1997].

4.2 Environment

The environment in which a concrete pavement is constructed has a significant impact on its design, construction, and performance. Concrete is a porous material that tends to expand and contract as a result of temperature and moisture variations through the depth of the slab. The influence of the differential expansion and contraction of the concrete pavement has been investigated by many researchers of the past several decades [Hatt, 1925, Carlson, 1934, and Hveem, 1949]. Curling of the concrete slab due to temperature and warping due to moisture differences through the concrete slab were first recognized by Hatt [1925]. Carlson [1934] found through experiments on slab drying that a great deal of moisture loss and shrinkage occurred at the exposed slab surface. In differential expansion, the top of the slab is warmer than the bottom, and the top expands relative to the bottom. Such phenomenon would cause the slab to curl downward leaving a void beneath the middle of the slab, as shown in the convex deformation in Figure 2a. When the top of the slab is cooler than the bottom, the top wants to contract relative to

the bottom, creating upward curl and leaving voids beneath the corners and the edges of the slab, such as the concave curling shown in Figure 2b. Hveem [1949] was the first researcher who studied the failure of curled concrete slab in detail. He defined the curling as "the tendency of a concrete pavement to bend or warp, usually developing high joints". He also stated temperature and moisture of concrete slab vary with depth, and the expansion and contraction are not likely to be confined to horizontal movement only. Hveem [1949] also stated "… It is almost certain that the expansion or contraction will be greater either on the surface or on the underside of the slab with the result that any overall expansion is invariably accompanied by warping or curling of the slabs." He observed the voids beneath the slab as a result of curling and/or warping extended horizontally as much as 3 ft (1 m) away from the joint for California pavements. Curling of a concrete slab in the field is typically restrained by its self-weight, shoulders, dowel and tie bars, friction between the base and slab bottom [Poblete et al., 1987; Rao and Roesler, 2005a]. These restraints are typically different for each slab or even within slab itself depending on its location and connection to adjacent slabs. This variability in restraint may lead to asymmetric curling among the slab edges, resulting in different loss of support between the slab and base as shown in Figure 2c. The loss of support between the concrete slab and the base due to curling would result in increased stresses and deflections, leading to increased slab cracking [Rao and Roesler, 2005b].

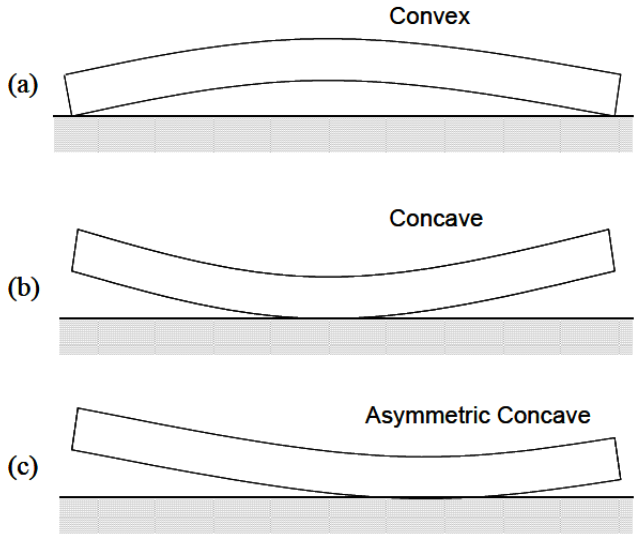

Figure 2. Deformation of slab shape due to curling [Rao and Roesler, 2005].

4.3 Curling of Concrete Slabs

Curling of a concrete pavement slab results from a combination of five different factors. These are temperature gradient through slab depth, moisture gradient through slab depth, drying shrinkage, built-in temperature gradient, and creep. Temperature gradient through the slab depth occurs due to temperature fluctuation between day and night. During the daytime, the top of the slab is typically hotter than the bottom, resulting in positive temperature difference through the slab depth. During nighttime, on the other hand, the slab surface is colder than the bottom which results in negative temperature difference between the top and the bottom. The daily temperature cycle causes different parts the slab to expand and shrink, resulting in slab curling. Field studies

conducted by Armaghani et al. [1986] and Yu et al. [1998] showed temperature gradients through the slab are nonlinear, and temperature fluctuations were greater at the slab surface relative the bottom. It was also shown that these temperature gradients were influenced by solar radiation, air temperature, precipitation, and clouds.

Moisture gradient through slab depth occurs when the surface of the slab, at depth less than 2 in (50 mm), is partially saturated compared to the fully saturated slab bottom [Janssen, 1986, Grasley, 2003, Lim et al., 2004]. The variation in the internal humidity within the concrete pores between the top and bottom causes differential reversible shrinkage strains that leads to slab warping. These shrinkage strains are influenced by several factors such as temperature, relative humidity, rainfall, snow, concrete material, and base drainage. Drying shrinkage is defined, according to Mather [1964] as the reduction in concrete volume as a result of water loss in the concrete after hardening. Janssen [1986] and Suprenant [2002] reported irreversible drying shrinkage happens considerably in concrete pavement surface within approximately 2 in (50 mm) depth. The drying shrinkage is greatly influenced by the curing conditions, and is considerably lower at the slab bottom than at the top as the relative humidity at the slab bottom pores is higher. A special case of drying shrinkage is the autogenous shrinkage that occurs due to self-desiccation when hydration water is insufficient. The irreversible differential shrinkage between the top and the bottom of concrete slab results in permanent shrinkage strain differences through the slab depth, causing permanent slab curling/warping [Rao and Roesler, 2005b].

Built-in temperature gradient occurs when a concrete slab sets while one surface is warmer than the other; typically the top surface is warmer due to the concrete being placed and setting during daytime in the construction season, when there is a positive temperature gradient. As the temperature difference between top and bottom decreases, the slab curls upward. The slab will flatten out only when the temperature gradient matches that at the time of setting, and is expressed as a negative temperature gradient to compensate. The effective built-in temperature gradient is greatly influenced by weather conditions during setting and curing of concrete [Eisenmann and Leykauf, 1990; Yu et al., 1998].

According to Neville and Meyers [1964], creep is defined as the increase in strain over time of concrete under constant stress, and it is inversely related to the concrete strength. The stresses are induced in the concrete due to concrete self-weight and restraints from shoulders and adjacent slabs especially during concrete strength development at early age, resulting in creep strain. The difference in creep strain between the top and bottom of concrete slab helps recover a portion of the permanent built-in curl caused by drying shrinkage and built-in temperature gradient [Schmidt, 2000; Rao et al., 2001]. According to Altoubat and Lange [2001], shrinkage strain is decreased by no less than 50% in the restrained concrete slab by a tensile creep mechanism. The previously described curling components are greatly influenced by concrete material properties such as thermal conductivity, permeability, and thermal expansion coefficient, aggregate type, water content, cement type, cement content, admixtures, etc. [Ytterberg, 1987; Tremper and Spellman, 1963].

Each of the five causes of curling can be expressed as an effective temperature difference between the top and bottom of the slab, and these can be added to compute the total effective linear temperature difference (TELTD):

$$TELTD = \Delta T_{TG} + \Delta T_{MG} + \Delta T_{BI} + \Delta T_{SHR} - \Delta T_{CRP} \quad (3)$$

where the subscripts of the effective temperature differences between top and bottom are: TG for vertical temperature gradient; MG for vertical moisture gradient associated with the reversible differential drying shrinkage; BI for vertical built-in construction temperature gradient; SHR is for irreversible differential drying shrinkage; and CRP is for the creep mechanism. The combined effect of built-in temperature gradients produced by the last four contributions to Equation 3 can be combined into an effective built-in temperature difference (EBITD)[Rao and Roesler, 2005b]. Therefore, Equation (3) can be rewritten as:

$$TELTD = \Delta T_{TG} + EBITD \quad (4)$$

where:

$$EBITD = \Delta T_{MG} + \Delta T_{BI} + \Delta T_{SHR} - \Delta T_{CRP} \quad (5)$$

The EBITD has been traditionally reported by Yu et al. [1998] and Beckemeyer et al. [2002] as "built-in curl", by Eisenmann and Leykauf [1990] as "zero-stress temperature", by Byrum [2000] as "locked-in curvat ure", and by Rao et al. [2001] and Fang [2001] as "equivalent temperature gradient". The 2002 MEPDG [ERES, 2002] defines the EBITD as the sum of "permanent curl" and moisture gradient [Yu et al., 2004]. Typically, EBITD is given a single equivalent temperature gradient value because it is usually stable over a long time compared to the daily and seasonal changes in ΔT_{TG}.

4.4 Determining the Effective Built-in Temperature Difference (EBITD)

One approach several researchers have used to determine the EBITD is to identify the conditions in which slab conforms to the base or reaches no curl condition, and measure the corresponding temperature difference between top and bottom of the slab. In Florida, thermocouples were embedded in 9 in (228 mm) slab, and surface profile measurements were carried on by Armahgani et al. [1986]. They found the slab reached the no-curl conditions when the temperature gradient between the top and bottom was -9°F (-5°C), and they suggested this no-curl temperature gradient is the EBITD. Vandenbossche [2003] calculated the curvature of slabs using Dipsticks in doweled and undoweled concrete pavements, and used the data to develop regression equations for voids beneath the slab due to curling, warping, concrete deflections, and curvature. However, surface profiling techniques may not represent the actual loss of support incurred due to slab curling [Yu et al., 2004]. Fang [2001] used data from 18 in (457 mm) concrete slabs instrumented with thermocouples at Denver International Airport and found EBITD ranged from -8F° (-4.4C°) to -22F° (-12C°) based on multi-depth deflectometer data. The temperature gradients were calculated when PCC slabs come in contact with base. This procedure is impractical when it comes to calculating the EBITD for many slabs because it requires expensive instrumentation and it is difficult to obtain flat slab conditions [Rao and Roesler, 2005b]. Some researchers have used LVDTs and temperature profiling to measure slab corner deflections and temperature profile over a period of 24 hours. Then finite element analyses are performed to estimate EBITD that results in similar corner deflections to those measured by LVDTs [Rao et al., 2001; Beckemeyer et al., 2002; Yu et al., 1998; Rufino, 2004]. Beckemeyer et al. [2002] estimated the EBITD for concrete slabs resting on open-graded granular bases and asphalt-treated permeable bases to be -16F° (-8.8°C) and -13F° (7.2°C), respectively, in Pennsylvania using Yu and Khazanovich [2001] procedure. Rufino [2004] found, based on rolling aircraft deflection data at Denver International Airport, the EBITD ranged from -9 F° (-5 C°) to -14 F° (-7.8 C°). Yu et al. [1998] found the EBITD in a 12 in (305 mm) concrete

slab in Colorado to be -20 F° (-11 C°). In Arizona, Rao et al. [2001], observed EBITD in 14 in (356 mm) doweled concrete slab between -36 F° (-20C°) to -52 F° (-29 C°), 40 days after construction. Finally, the 2002 Design Guide assumes a default value of -10 F° (-5.6 C°) as EBITD.

4.5 Subgrade Stabilization

Fine-grained soils, silts and clays, exist locally in Ohio. Such soils become extremely weak when exposed to moisture. Soil stabilization techniques have been proven to improve the engineering properties of these soils. Chemically stabilized soils are able to provide a strong foundation under the pavement structure to carry traffic loading with reduced deformations [Chou et al. 2004]. Strength improvement of stabilized soils comes as a result of the chemical reaction between soils and the stabilizer, such as cement and lime. However, this chemical reaction varies depending on the soil type, and whether or not the treated soil is responsive to such stabilizer [Chou et al. 2004]. Generally, cement stabilizer is found to react best with sandy and coarse-grained soils, while lime reacts effectively with clays and silty soils. The ODOT *Construction Administration Manual of Procedures* [ODOT, 2017, p. 245] recommends cement stabilization for the following soil classifications: A-3-a, A-4-a, A-4-b, A-6-a, and some A-6-b, while lime stabilization works best with fine-grained soils classified as A-7-6 or A-6-b. A laboratory and experimental field investigation was carried out by Chou et al, [2004] to study the structural benefits of soil stabilization in Ohio. The laboratory results showed chemically stabilized subgrades exhibit higher stiffness and strength than non-stabilized, or natural, subgrades in terms of resilient modulus, unconfined compressive strength, and California bearing ratio (CBR). Also, experimental results obtained in the field using a Dynamic Cone Penetrometer (DCP) showed the strength of stabilized subgrade is higher than natural subgrade after several years of service. Subgrade stabilized with cement gained strength more rapidly than lime stabilized subgrade; within the first seven days about 50% of the 28-day compressive strength is attained for cement stabilized soil. For both types of stabilization, the majority of strength gain occurs within the first 28-day of curing and continues for a long period of time afterwards. Such strength gain in stabilized subgrade soils leads to increases in stiffness and/or elastic modulus of the pavement layers. In many cases, the strength and stiffness increase is so large the stabilized layer can be treated as a structural slab [Little et al, 1995]. The AASHTO 1986 pavement design guide demonstrates the supporting strength of chemically stabilized subgrade impacts the bulk stress invariant and the resilient modulus of the granular base. Little [1994] studied the influence of lime stabilized subgrade on enhancing the resilient modulus of granular base through finite element analysis. He found that under an 18 kip (80 kN) single axle load, the resilient modulus of the base layer increased from 20.3 ksi (140 MPa) when the base layer was directly over non-stabilized subgrade to 28.4 ksi (196 MPa) when the base layer was placed on lime stabilized subgrade.

4.6 Modeling Concrete Pavement

Finite element modelling of concrete pavement is the most robust and widely used method in the analysis of concrete pavement. The advanced computational capabilities of computers nowadays enhanced the analysis and design of concrete pavements to a large extent. Many researchers have developed finite element-based algorithms and programs that aid engineers to address complicated engineering problems in the pavement industry.

4.6.1 Two-dimensional Finite Element Programs

Two and three-dimensional software have been developed over the years. Cheung and Zienkiewicz [1965] were the first to develop an algorithm capable of solving isotropic and orthotropic concrete slab problems on both a semi-infinite elastic continuum and a Winkler foundation. The procedure adopted by Cheung and Zienkiewicz was then used by Huang and Wang [1973] to develop a finite element procedure based on the theory of thin plates on Winkler foundations. However these early methods could not be applied to multi-layer systems. Chou [1984] modified the Huang and Wang model to work on multi-layer systems, and developed a two-dimensional (2D) finite element program called WESLIQID that was capable of handling two-layered pavement system with multiple wheel loads.

Tabatabaie [1978] developed a 2D finite element modeling (FEM) program called ILLISLAB based on theory of medium-thick plate on a Winkler foundation. In the medium-thick plate theory, the plate is thick enough to carry a transverse load by flexure rather than by in-plane forces as in the thin plate theory. Also, the plate thickness was not so great as to have significance of transverse shear deformations. ILLISLAB can evaluate the effect of different load transfer mechanisms. For example, aggregate interlock is modeled using spring elements, and keyway joints are used to transfer shear forces between the adjacent slabs. Doweled joints are modeled using bar element in order to transfer shear forces and moment across the joint. Nasim et al. [1991] modified ILLISLAB by creating influence functions to predict strain time histories at the point of interest. ILLISLAB was further modified to include various subgrade models and temperature loading [Ioannides, 1984, Khazanovich and Ioannides, 1993, Korovesis, 1990]. A more recent version of ILLISLAB is called ILSL2, with the added ability to analyze a separate action of two layers [Khazanovich, 1994]. ISLAB2000 was developed by ERES Consultant in cooperation with Michigan and Minnesota Departments of Transportation, Michigan Technical University, University of Michigan, Michigan State University, and University of Minnesota. ISLAB2000 is revised version of ILSL2 with the ability of modeling more than two layers. Increased numbers of nodes are allowed in ISLAB2000, and the program is capable of modeling mismatched joints. ISLAB2000 provides the ability to obtain a separate action of two pavement layers, linear and nonlinear temperature gradients, and partial depth cracks. ILSL2 and ISLAB2000 have advantages over programs developed specifically for concrete pavements [Khazanovich and Yu, 1998].

JSLAB is another 2D FEM program developed by Tayabji and Colley [1983], which is limited to analyzing a single layer with linear temperature gradient. Several other 2D-FME programs also exist, such as KENELS [Huang, 1974], KENSLABS [Huang, 1985], WESLAYER [Chou, 1981], KENSLAB [Huang, 1993], FEACONS-IV [Choubane and Tia, 1995], and ISLS97 [Roesler and Khazanovich, 1997]. Although the two-dimensional finite element programs have brought about a significant improvement over the conventional pavement analysis methods, they still cannot realistically model some aspects of the behavior of concrete pavement components. For example, the horizontal friction behavior between the pavement layers cannot be accurately modeled, and responses at localized regions such as dowel bar-concrete interface cannot be adequately simulated. Some deficiencies of these 2D finite element programs may be avoided by using three-dimensional (3D) finite element programs.

4.6.2 Three-dimensional Finite Element Programs

The three-dimensional finite element modeling (3D FEM) of concrete pavement evolved to overcome the limitations associated with 2D finite element models (2D FEM) and to better

understand failure modes in concrete pavements. Ioannides and Donelly [1988] used a 3D FEM program called GEOSYS to examine the effect of subgrade conditions on concrete pavement. They developed a simple model which consisted of a concrete slab on a subgrade to study the effect of boundary conditions and subgrade extent on pavement responses. DYNA-SLAB is a 3D FEM software developed by Chatti [1992] as an extension to the 2D-FEM program ILLISLAB. He used DYNA-SLAB to observe the maximum tensile stresses in the concrete pavement take place at the middle of the slab bottom along the free edge and show stress reversal occurs at the transverse joint. Sargand and Beegle [1994] developed a 3D FEM program, OU3D, to validate data from Ohio Strategic Highway Research Program (SHRP) Test Road with mathematical models. The program utilized the elastic theory to characterize material properties of pavement layers, which were modeled using twenty-node hexahedral elements. In this program, the behavior of interface between the concrete slab and subgrade was modeled using a special thin interface element, while beam elements were used to model the dowel and tie bars at the joints. The program is able to predict accurate deflection under thermal loads. The Universities of Washington and Maine, in 1998, in corporation with Washington and Florida Departments of Transportations developed a 3D FEM program, EVERFE. This powerful analysis tool uses a windows-based graphical user interface (GUI) that greatly simplifies model generation and data inputs. Linear and non-linear 3D FEM analysis of jointed concrete pavement can be performed. The concrete layers are modeled with 20-node hexahedral elements, while the base layer is modeled using 8-node brick elements. Embedded beam elements are employed to model the dowel bars. Additionally, the software incorporates linear and nonlinear models for shear transfer by aggregate interlock [EVERFE Manual].

General purpose 3D-FEM packages such as NIKE3D, DYNA3D, TOPAZ3D, ANSYS, and ABAQUS are preferable for rigid pavement analysis because they incorporate advanced modeling features such as interface algorithms and thermal modules. These packages have been in the process of development by private and public organizations since the 1970s, and have been used for different design problems. A detailed 3D FEM of concrete pavement can be created using general purpose finite element programs such as ABAQUS. Such software permits engineers to perform static and dynamic analyses on concrete pavement using advanced material constitutive models, elements, and interfaces. Researchers have shown that a 3D modeling of concrete pavements provides the most realistic representation of the pavement matrix [Chen et al., 2002]. Darter et al. [1995] used ABAQUS to develop a FEM called 3DPAVE. They studied the effect of base support on the response of concrete pavement, and proposed a method to consider pavement support effects in the 1993 AASHTO Design Guide. A 3D finite element model of a jointed concrete pavement was developed by Hammons [1998] using ABAQUS to study the structural response under traffic loads. Shell elements were used to model the concrete slab, hexahedral continuum elements were used for the base layer, and the subgrade was modeled as a Winkler foundation. Hammons [1998] found that model accurately predicted the load transfer efficiency using stresses rather than deflections when compared to experimental data. Masad et al. [1996] employed ABAQUS modeling to study the effect of temperature variation on concrete pavements. Many other researchers have employed ABAQUS to analyze jointed concrete pavements because of the software's advanced capabilities in characterizing pavement materials, interfaces, and boundary conditions, and the program has been used to study concrete pavement responses and performance under a variety of environmental and dynamic and static traffic loads [Jenq et al., 1993; Kuo, 1994; Mallela and George, 1994; Uddin et al., 1994; and Uddin et al., 1995].

4.7 Modeling PCC-Dowel and PCC-Base Interfaces

As a vehicle load travels from one slab of a rigid pavement to the next, the load is transferred across the joint via two major mechanisms, aggregate interlock and dowel bar action [Maitra et al., 2009]. The aggregate interlock mechanism transfer the load through shear interaction at the joint or crack between aggregate particles, and its effective only for small joint width, less than 1.0 mm (39 mil) [Maitra et al., 2009]. Steel dowel bars are placed across transverse joints to provide a means of load transfer without hindering the slab horizontal movements induced by moisture and/or temperature changes. Besides that, dowel bars help keep the concrete slabs aligned in both horizontal and vertical directions [Maitra et al., 2009]. Therefore, realistic modelling of the dowel-concrete interaction in a finite element model is necessary to capture joint behavior and load transfer mechanism under environmental and traffic loads.

In the past, dowel bars were modeled using linear elastic spring elements that connect adjacent slabs at the joint directly, and the joint stiffness is characterized by the shear spring constant [Huang and Wang, 1973]. Mahboub et al. [2004] modeled the dowel bars as nonlinear springs. Tia et al. [1987] used a series of shear and torsional springs to represent the dowel bars across the joints. Tabatabaie and Barenberg [1980] used beam elements to represent the dowel bars, and the interaction between the dowel bar and concrete was modeled using vertical springs, where the stiffness of the springs was used to define the relative displacements between the dowel bars and surrounding concrete. Guo et al. [1995] simulated dowel bars as bending beams embedded in the concrete, and a spring model used for the interaction between the dowels and surrounding concrete. An improvement to this approach was proposed by Zaman and Alvappillai [1995], who introduced contact elements between the dowels and surrounding concrete rather than spring models for the interaction along the length of the dowels. Dere et al. [2006] used beam elements to simulate the dowel bars, and the interaction was captured by using a series of horizontal and vertical springs. Another approach of modeling the dowel bars is by using embedded elements, which permit users to mesh the dowel bars independently of the surrounding concrete [Davids et al., 2003 and Kim and Hjelmstad, 2003]. Davids [2000] used quadratic beam elements to model the dowels, and the interaction was modeled using springs sandwiched between the dowel and concrete.

Typically, dowel bars are coated and lubricated when placed to eliminate dowel-concrete friction so that thermal horizontal movements would not be resisted. However, results from pullout tests showed coating of dowel bars will not completely eliminate friction and therefore it should be considered in the analysis and design of concrete pavements [Khazanovich et al., 2001]. William and Shoukry [2001] used eight-node solid brick elements for the dowel bars, and the dowel-concrete interaction was represented by using a friction coefficient of 0.05. Saxena et al. [2009] also stated that dowel-concrete friction is an important factor that may impact the performance of concrete pavement joints and friction could produce damage to concrete traditionally associated with dowel misalignment.

ABAQUS has the ability to model frictional interfaces between two different materials, using an extended version of the classical isotropic Coulomb friction model. The extensions include an additional limit on the allowable shear stress, anisotropy, and the definition of a secant friction coefficient. In the basic Coulomb friction model, two contacting surfaces can carry shear stresses up to a certain magnitude across their interface before they start sliding relative to one another. When the shear stress is insufficient to cause motion, as shown in the

shaded region at the bottom of the graph in Figure 3, this condition is known as sticking. When the shear stress exceeds the critical value, then there is sliding between the surfaces.

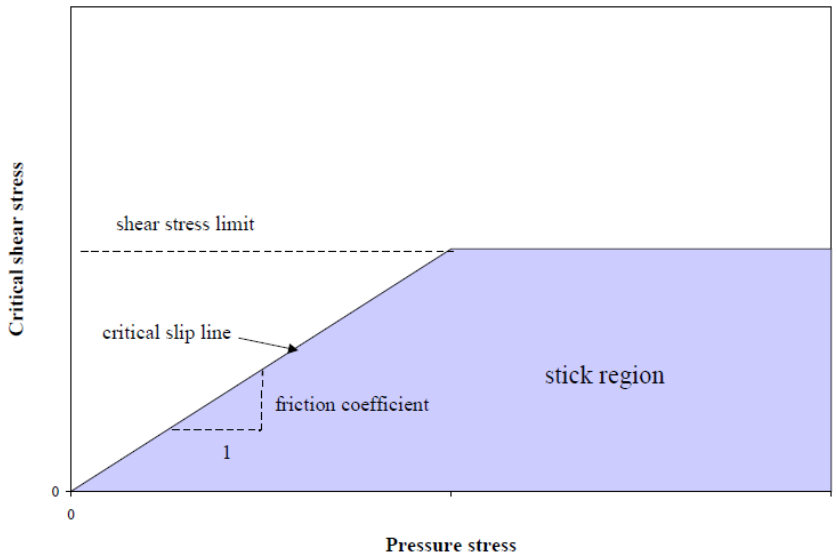

Figure 3. Modified Coulomb friction model [Khazanovich et al., 2001].

Several researchers have used this concept to model dowel-concrete interaction [Khazanovich et al., 2001; William et al., 2001; Maitra et al., 2009; Mackiewicz, 2015; and Luoke et al., 2012]. The friction coefficients used to characterize frictional behavior of dowel-concrete interaction were 0.05 [Maitra et al., 2009; Mackiewicz, 2015; and William et al., 2001], 0.1 [Luoke et al., 2012], 0.3, and 0.5 (both values by Khazanovich et al. [2001]).

The interaction between the concrete slab and base layer is also typically modeled using a friction interface. AASHTO 1993 Pavement Design Guide recommends concrete-base friction coefficients between 0.9 and 2.2. William et al. [2001] modeled the interaction between the concrete and base layer using frictional interface with friction coefficient of 1.5. Luoke et al. [2012] used a friction coefficient of 0.05 between the base and concrete slab.

4.8 Determining the k value of the subgrade

Concrete pavements are typically constructed using Portland cement concrete slabs placed on a granular base resting on a soil subgrade. They are designed to sustain high volume traffic over a design life of 50 years or more for long life concrete. As the foundation on which the entire pavement structure is built, subgrade soil have an impact on the pavement's performance, and are typically included in the design. For research purposes, the subgrade layer is typically modeled as dense liquid Winkler foundation or as a homogenous elastic solid. The Winkler foundation presumes the vertical deflection of any point at the subgrade surface is proportional to the vertical stress acting at that point with no shear transmission [Setiadji, 2009]. The elastic solid model, on the other hand, assumes a vertical load applied to the surface produces an infinite continuous deflection basin. This model was first introduced by Boussinesq in 1885 and considers the subgrade as a homogenous elastic and isotropic material [Huang, 2003]. In concrete pavement design, the Winkler foundation model is regularly used to represent the subgrade soil, which is characterized by a spring constant. Westergaard [1925] was the first to call this spring constant the "modulus of subgrade reaction", known today as the k value.

According to Westergaard, the modulus of subgrade reaction is defined as the applied pressure necessary to produce a unit deflection under a specified loaded area. The k value was first used to characterize the elastic properties of subgrade soil only. However, when a full-scale road test was performed in Arlington, VA, in1930s, k was also used to describe elastic characteristics of other layers such as base and subbase [Darter et al., 1995]. In the early years, concrete pavements consisted of only two layers, with the concrete placed directly on the subgrade, but due to joint pumping issues, this system is no longer used. All concrete pavements built in Ohio today are designed with a base layer between the concrete and subgrade that function as a drainage layer. The drainage layer protects the subgrade and reduces moisture-related problems. In this context, a composite modulus of subgrade reaction was devised to incorporate the effect of the base layer in addition to the subgrade. In the design and rehabilitation of concrete pavements, this composite k-value has become commonly used [AASHTO, 1993; PCA, 1984].

The value of k has been given different names based on the condition and procedure with which the modulus of subgrade reaction is determined. The modulus of subgrade reaction is a term given to the slope of the load deflection curve obtained when a plate-bearing test is performed on very thick homogenous subgrade soil. It can be also estimated by relating the k value to basic material properties and soil classification [The Unified Facilities Criteria, 2001]. Another approach to determine the k value is to use the theory of elasticity of a rigid plate on an elastic foundation [Lysmer and Duncan, 1969]. The equation of deflection is given by Equation 6.

$$\delta = q2a\left(\frac{1-\mu^2}{E}\right)I_\delta \tag{6}$$

where:

q is the pressure on the plate
a is the plate's radius
μ is the Poisson's ratio
E is the Young's modulus
I_δ is influence factor of depth to bedrock, 0.785

The CBR is determined at 0.1 in (2.5 mm) penetration, which is equal to $0.1q$. This gives the relationship between CBR and E shown in Equation 7.

$$CBR = \frac{E}{195.44(1-\mu^2)I_\delta} \tag{7}$$

The relationship between k value and E is then:

$$k = \frac{E}{30(1-\mu^2)I_\delta} \tag{8}$$

By combining Equation 7 and Equation 8, the *CBR-k* relationship can be obtained as shown in Equation 9. Another CBR-k value relationship was recommended by Carlos Gonzalez [Barker and Alexander, 2012] to account for non-cohesive soil types since CBR of cohesive soils is greater than less cohesive soils as shown in Equation 10. Relationships between *CBR* and *k* for other types of soil were not found in the literature.

$$k = 6.5CBR \tag{9}$$

$$k = 20CBR \quad (10)$$

Relationships between the modulus of subgrade reaction k and elastic modulus E also exist. For a partially saturated subgrade soil, the relationship between k value and elastic modulus is shown in Equation 11, and for a stiff material, the relationship would become as shown in Equation 12 [Barker and Alexander, 2012]. The Unified Facilities Criteria [2001] relates the resilient modulus M_r of subgrade soil to modulus of subgrade reaction using Equation 13.

$$k = \frac{E}{19.79} \quad (11)$$

$$k = \frac{E}{19.22} \quad (12)$$

$$M_r = 26\,k^{1.284} \quad (13)$$

The second term, widely used for k value when a base or subbase layer is present, is the composite modulus of subgrade reaction. The composite k value is determined experimentally by performing a plate-loading test on the base or subbase layer. It can be also estimated by relating the k value to the elastic properties of subgrade and subbase layer as well as the thickness of the subbase layer. The AASHTO 1993 Pavement Design Guide uses a regression formula given in Equation 14 to determine the composite modulus of subgrade reaction. This equation is valid only for the case where plate-loading test is performed on the base layer; however, when the thickness of base layer approaches zero, the equation indicates the k value would be 0.05 times the resilient modulus of the subgrade.

$$lnk_{\infty} = -2.807 + 0.1253(lnD_{SB})^2 + 1.062(lnM_R) + 0.1282(lnD_{SB})(lnE_{SB}) - 0.4114(lnD_{SB}) - 0.0581(lnE_{SB}) - 0.1317(lnD_{SB})(lnM_R) \quad (14)$$

where:

k_{∞} = composite modulus of subgrade reaction in pci with no bedrock
D_{SB}= subbase thickness in inches
M_R = resilient modulus of subgrade in psi
E_{SB} = elastic modulus of subbase layer in psi

The effective, also known as equivalent, modulus of subgrade reaction is another term used to describe k value. The k value acts as a modulus of subgrade reaction applied to a layered subgrade support system that would result in similar tensile stresses as if a single homogenous thick layer was substituted. The effective k is typically used with Westergaard model in concrete pavement design and analysis, and it is a function of subgrade modulus, base thickness and quality, concrete pavement properties, and applied load [Barker and Alexander, 2012]. Vesic and Saxena [1974] introduced the concept of effective modulus of subgrade reaction based on interior slab stresses. They developed the following relationship between the effective k and the properties of a concrete slab resting on an elastic foundation.

$$k_{eff} = \left(\frac{E_f}{E}\right)^{\frac{2}{3}} \left(\frac{E_f}{(1-\mu^2)h}\right) \quad (15)$$

where:

E_f = elastic modulus of the foundation
E = concrete modulus of elasticity
μ = Poisson's ratio of concrete
h = concrete slab's thickness.

Over the years, several techniques and procedures have been developed to measure and back-calculate the modulus of subgrade reaction. Procedures of determining k value are available in Hall et al. [1995] and Hall et al. [1997].

5 Data Collection

5.1 Long-Term Pavement Performance (LTPP) database

The Long Term Pavement Performance (LTPP) database provides a tremendous amount of information regarding concrete pavement performance all over the United States and Canada. The SPS-2 experiments in the LTPP database were designed to investigate the effects of PCC slab thickness, PCC flexural strength, base type, drainage, lane width, and climate on rigid pavement performance [Chatti et al, 2005]. Structure and performance data for 60 jointed plain and reinforced concrete sections from Ohio and surrounding states were extracted, including 25 from Ohio, 15 from Michigan, 8 from Indiana, and 7 from Pennsylvania, 2 from Kentucky, and 2 from West Virginia. Many of these sections were excluded after closer inspection because they were not JPCP, being either reinforced concrete or having an overlay applied. This study includes the remaining 45 sections from Ohio (23), Indiana (4), Michigan (15), Pennsylvania (2), and Kentucky (1). The table inset in Figure 4 provides the breakdown of the sections by state.

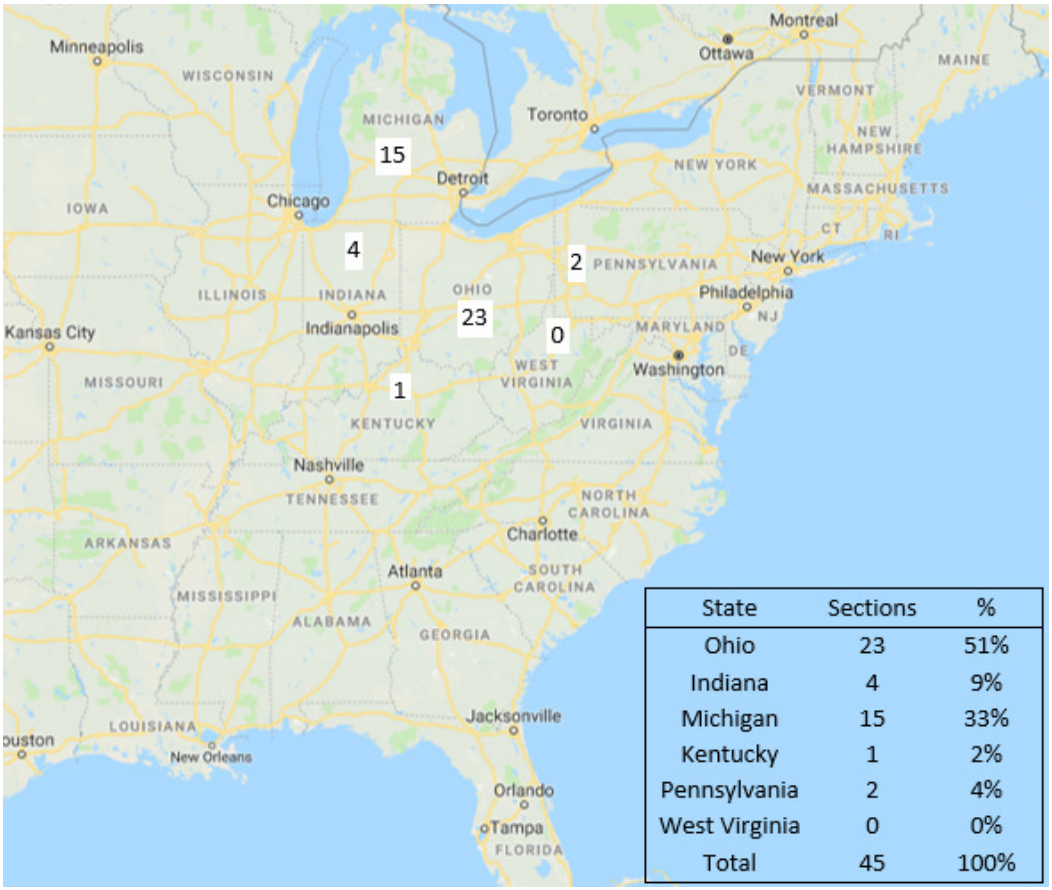

State	Sections	%
Ohio	23	51%
Indiana	4	9%
Michigan	15	33%
Kentucky	1	2%
Pennsylvania	2	4%
West Virginia	0	0%
Total	45	100%

Figure 4. JPCP sections from states sampled in the LTPP database. [Map from Google Maps with numbers inserted]

Figure 5 shows the number of test sections with a given thickness identified by state, while Figure 6 shows the number of test sections with a given slab length.

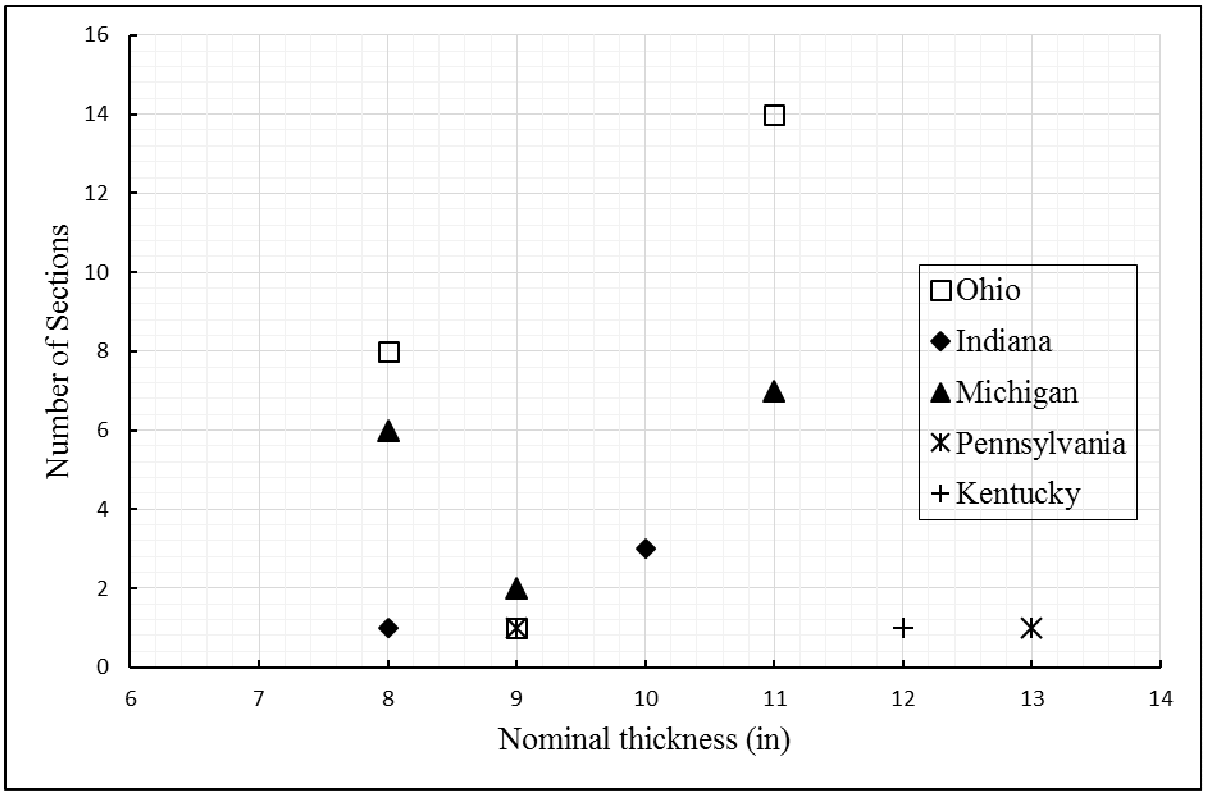

Figure 5. Frequency chart of PCC pavement thicknesses in LTPP database for selected sections (1 in = 25.4 mm).

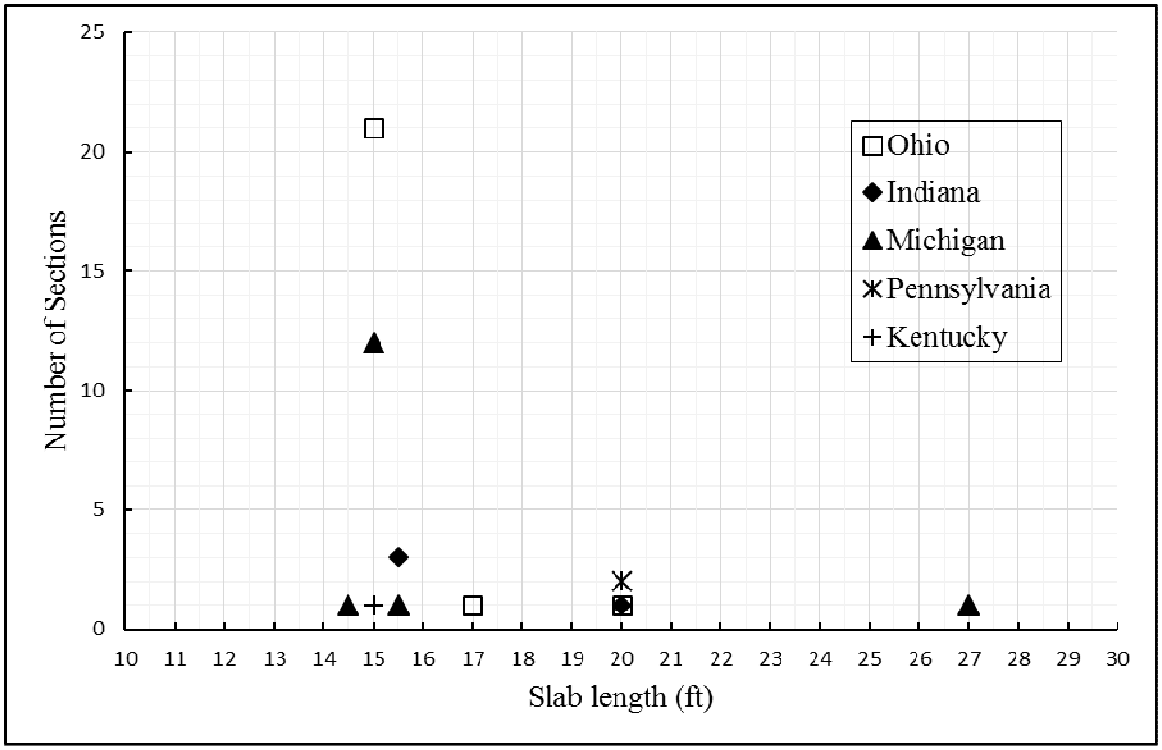

Figure 6. Frequency chart of PCC pavement slab lengths in LTPP database for selected sections (1 ft = 0.305 m).

The age distributions for JPCP sections in Ohio and each adjacent state are presented as Figure 7.

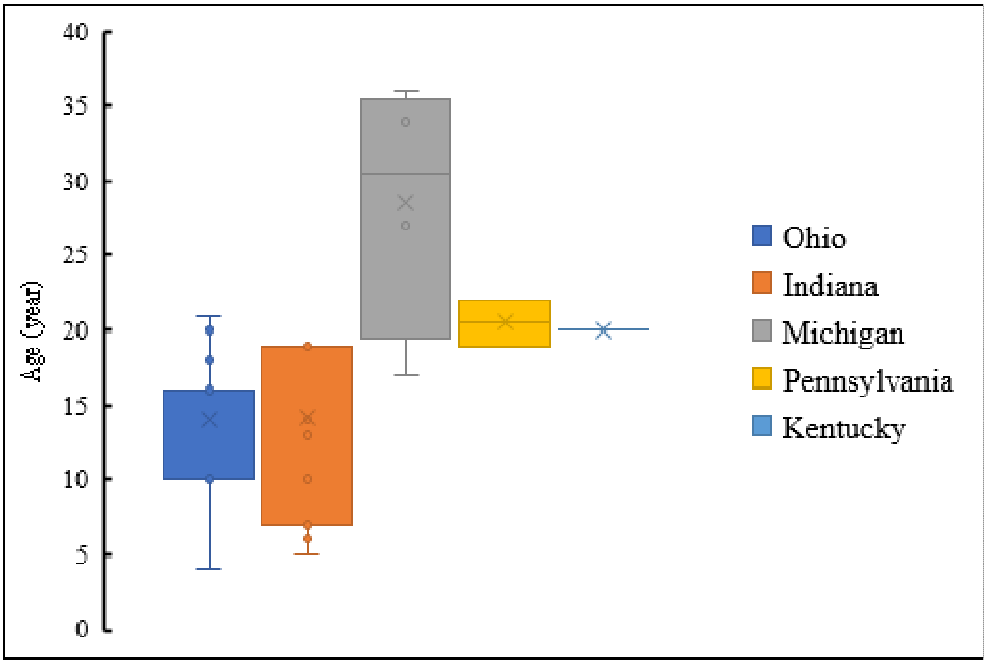

Figure 7. Ages of LTPP concrete test sections by state.

Concrete pavement distress measures such as faulting, transverse cracking, and IRI were reviewed for each state to see how concrete pavements performed in the different states. The whisker box plots in Figure 8 present a review of the distresses in the data by state. The Indiana and Michigan have statistically equal levels of faulting which are higher than the faulting levels in Ohio, Kentucky and Pennsylvania, which are approximately the same. The Kentucky and Pennsylvania sections are performing comparatively well for their age whereas the Indiana sections are performing comparatively poorly for their age in terms of faulting.

The Pennsylvania sections have the highest level of cracking followed by Ohio, Kentucky, Michigan, and Indiana. Statistically, the Michigan and Indiana cracking levels are the same. The Michigan sections are performing comparatively well for their age.

The Michigan sections have a statistically greater roughness than the Ohio sections, and the Michigan, Indiana, and Ohio sections have a statistically greater roughness than those in Pennsylvania. The Kentucky and Pennsylvania sections are performing comparatively well for their age in terms of IRI.

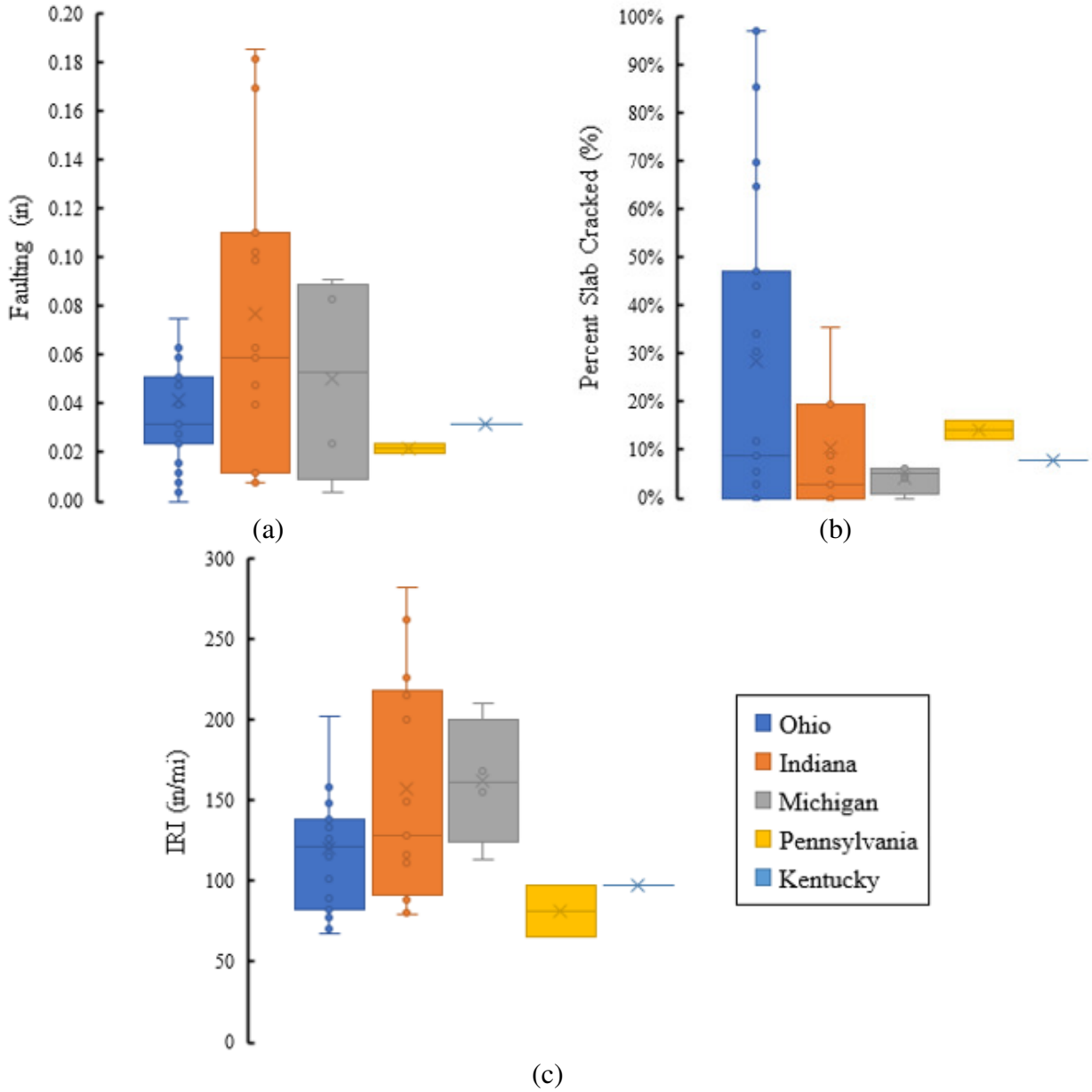

Figure 8. LTPP data on distress measures by state (a) faulting (1 in = 25.4 mm), (b) transverse cracks, and (c) IRI experienced by concrete sections (1 in/mi = 0.016 m/km).

To characterize concrete pavement performance versus age for various pavement thicknesses, the plots in Figure 9 were generated. Figure 10 characterizes performance versus age for various slab lengths. In both figures, the type of shape (square, triangle, circle) indicates the type of base (bound, unbound, combination), and a hollow shape indicates fine subgrade while a solid shape denotes coarse subgrade.

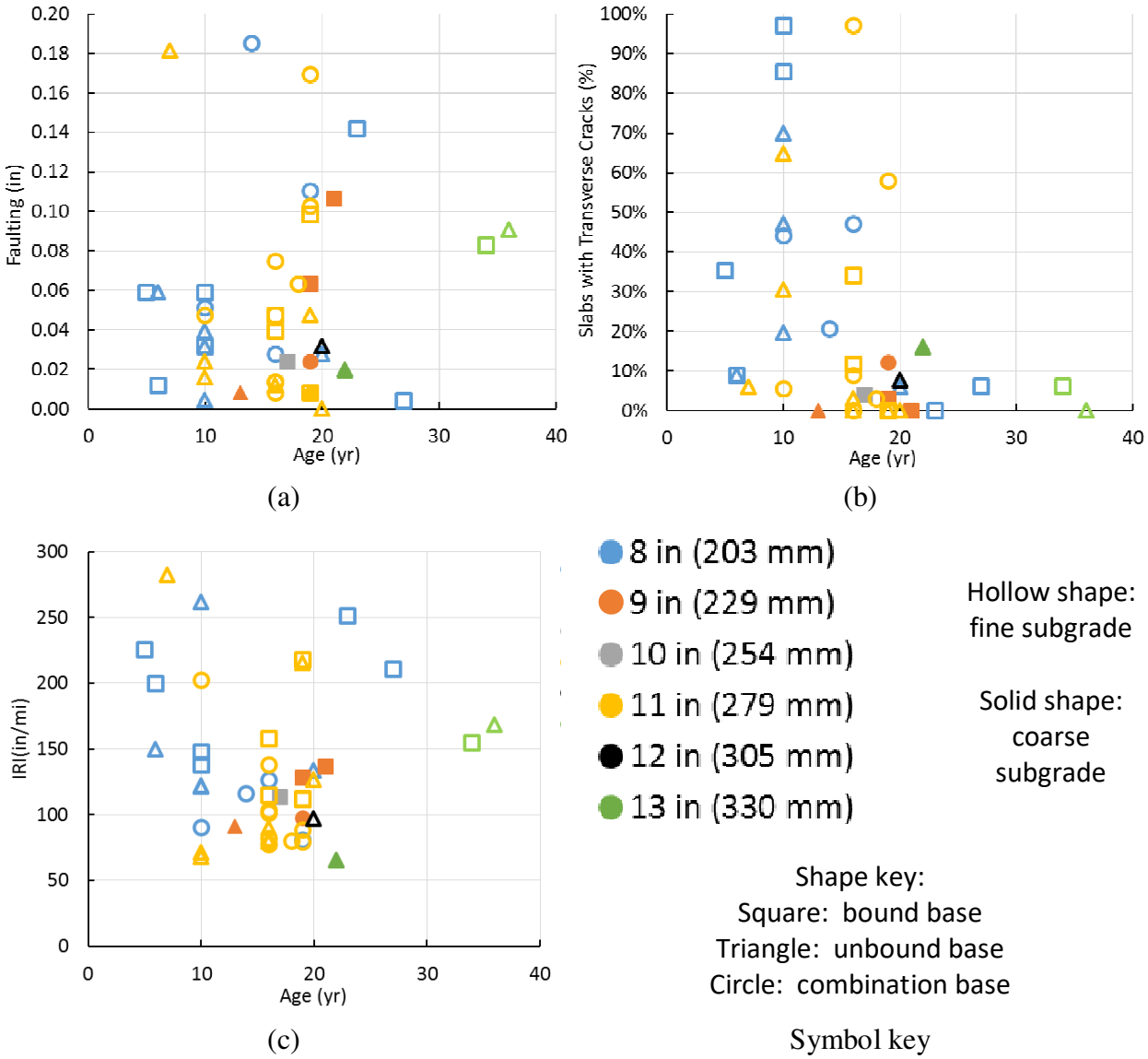

Figure 9. Distress vs. age for various nominal pavement thicknesses, types of base, and types of subgrade. (1 in = 25 mm): (a) Faulting (1 in = 25 mm), (b) Transverse cracks, and (c) IRI (1 in/mi = 0.0156 m/km).

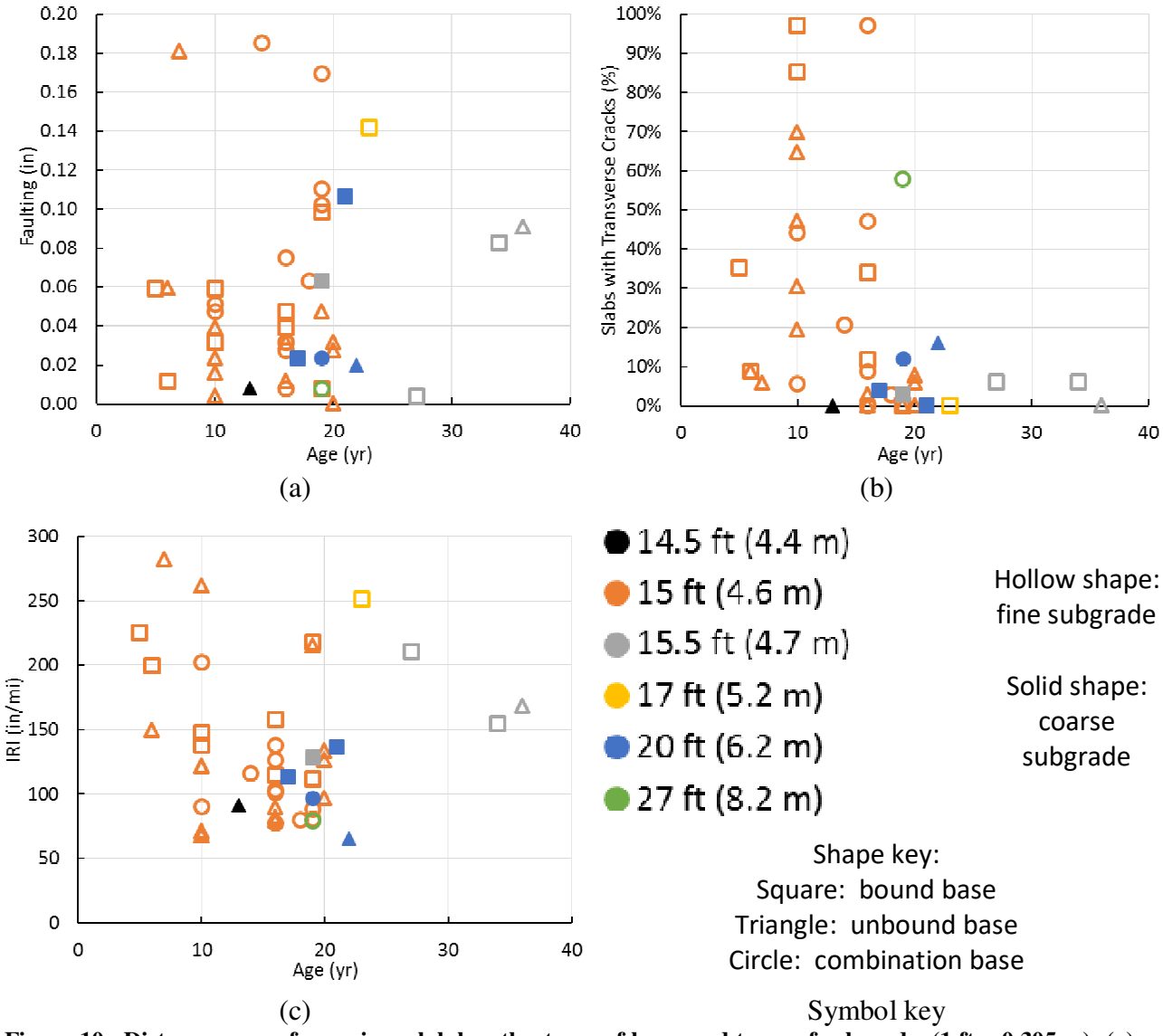

Figure 10. Distress vs. age for various slab lengths, types of base, and types of subgrade. (1 ft = 0.305 m): (a) Faulting (1 in = 25 mm), (b) Transverse cracks, and (c) IRI (1 in/mi = 0.0156 m/km).

The following are observations based on the LTPP data for PCC test sections in Ohio and surrounding states, drawn from inspection of Figure 9 and Figure 10.

- Sections with random joint spacings (average 14.5 ft (4.4 m) and 15.5 ft (4.7 m)) are performing well, none of the five sections have more than 8% of the slabs cracked. These are also among the older sections with age ranging from 13 to 36 years.
- The most extensive cracking is occurring in the sections with 15 ft (4.6 m) long slabs, with 44% of the 34 sections having more than 10% of the slabs cracked.
- On the other hand, 32% of the sections with 15 ft (4.6 m) long slabs have no cracking
- A higher percentage of the 8 in (203 mm) thick pavements, 60%, had greater than 10% cracking when compared to the 11 in (279 mm) thick slabs, which had 29% of sections with greater than 10% cracking.

- For sections less than ten years old, 50% of those with 11 in (279 mm) thick slabs had more than 10% cracking whereas 78% of the sections with 8 in (203 mm) thick slabs had more than 10% cracking
- 91% of the sections had no or low severity faulting as determined by the ODOT pavement condition rating.
- Regarding IRI, 80% of the sections were "acceptable", with IRI ≤ 170 in/mi (2.70 m/km); 37% had a "good", with IRI < 95 in/mi (1.50 m/km). [Bureau of Transportation Statistics 2018; Federal Highway Administration, 2013] The unacceptable sections were approximately evenly distributed between 8 in (203 mm) and 11 in (279 mm) thick pavements.
- Of sections on coarse subgrade, 80% performed well in terms of cracking (< 10% slabs cracked), compared to only 39% of the sections on fine subgrade soil meeting the same criterion.
- Of the sections on a bound base, 43% performed well in terms of cracking (< 10% slabs cracked) compared to 63% of the sections with an unbound base and 64% of the sections with a combined base.

5.2 Accelerated Pavement Load Facility

The Accelerated Pavement Load Facility (APLF), located on the Lancaster Campus of Ohio University, is a state-of-art research facility designed for the study of full-scale pavements under fully controlled environmental and loading conditions. The pit in which experimental sections are constructed is 45 ft (13.7 m) long by 38 ft (11.6 m) wide by 8 ft (2.4 m) deep. On both ends of the building, 14 ft (4.3 m) high by 24 ft (7.3 m) wide doors permit access for equipment typically used to construct pavements. The air temperature in the test bay can be controlled between 10°F (-12°C) to 130°F (54°C), and a wheel load of up to 30,000 lb (133 kN) can be applied with dual or super single tires. The database from *Evaluation of Forces in Dowel Bars under Controlled Conditions* by Sargand, Edwards, and Khoury [2003] is the source of concrete pavement experimental data discussed here. The project focus was to measure the dowel bar and slab responses under controlled conditions on dowelled and undowelled concrete pavements constructed in the APLF, which were constructed in adjacent lanes and not tied to minimize the effect of one lane on the other. The structural responses of a dowelled concrete slab were measured through a period of 188 days within which the pavement was subjected to curing under constant temperature, cycles of temperature, and combined temperature and moving loads. The concrete pavement was constructed in accordance with Ohio Department of Transportation (ODOT) specifications at the time, including Item 452, non-reinforced Portland cement concrete pavement, and Item 304, aggregate base. The 15 ft (4.6 m) long by 12 ft (3.7 m) wide by 10 in (254 mm) thick concrete slabs were constructed on a 6 in (152 mm) thick dense-graded aggregate base (DGAB) supported by A-6 subgrade extending to the bottom of the test pit. This structure is typical for concrete pavement in Ohio. The mix design and physical properties of the concrete slabs are summarized in Table 1.

Table 1. PCC mix and mechanical properties adapted from Sargand, Edwards, and Khoury [2003, Table 2.1 and Table 2.2].

PCC Mix Properties		
Component	**density**	**unit weight**

Fine Aggregate	762 kg/m^3	1285 lb/yd^3
Coarse Aggregate (#57 Limestone)	967 kg/m^3	1630 lb/yd^3
Cement	356 kg/m^3	600 lb/yd^3
Water	178 kg/m^3	300 lb/yd^3
Water / Cement Ratio	0.5	0.5
Air Entrainment (6%)	0.49 kg/m^3	13.2 oz/yd^3

PCC Mechanical Properties

Property	**Metric Units**	**English units**
Density/Unit Weight of concrete	2.3 kg /m^3	143.6 pcf
Poisson's Ratio	0.22	0.22
Coefficient of Thermal Expansion	1.20E-05 C$^{\circ\,-1}$	6.66E-06 F$^{\circ-1}$
2-Day Compressive Strength	13.6 MPa	1.97 ksi
7-Day Compressive Strength	30.5 MPa	4.43 ksi
14-Day Compressive Strength	32.9 MPa	4.77 ksi
28-Day Compressive Strength	37.3 MPa	5.41 ksi
391-Day Compressive Strength	49.9 MPa	7.24 ksi
28-Day Modulus of Rupture	3.6 MPa	0.52 ksi
2-Day Young's Modulus	16,000 MPa	2,320 ksi
7-Day Young's Modulus	21,300 MPa	3,085 ksi
28-Day Young's Modulus	23,500 MPa	3,415 ksi

The concrete slabs were instrumented with strain gauges and thermocouples during concrete placement to measure strain and temperature. Linear Variable Displacement Transformers (LVDTs) were mounted along the pavement edges after concrete placement to monitor vertical displacement at slab corner and edges. Vibrating Wire (VW) strain gauges were embedded 1 in (25 mm) from the top and bottom of the end slabs along the centerline to monitor environmentally-induced strains caused by controlled temperature change. TML PMR-60 three-axis rosettes were also embedded 1 in (25 mm) from the top and bottom of middle slab to measure strains caused by rolling wheel and temperature change. LVDTs were also used during the combined temperature and dynamic loadings. The wheel travelled along five different paths. The slab layout and instrumentation is as illustrated in Figure 11.

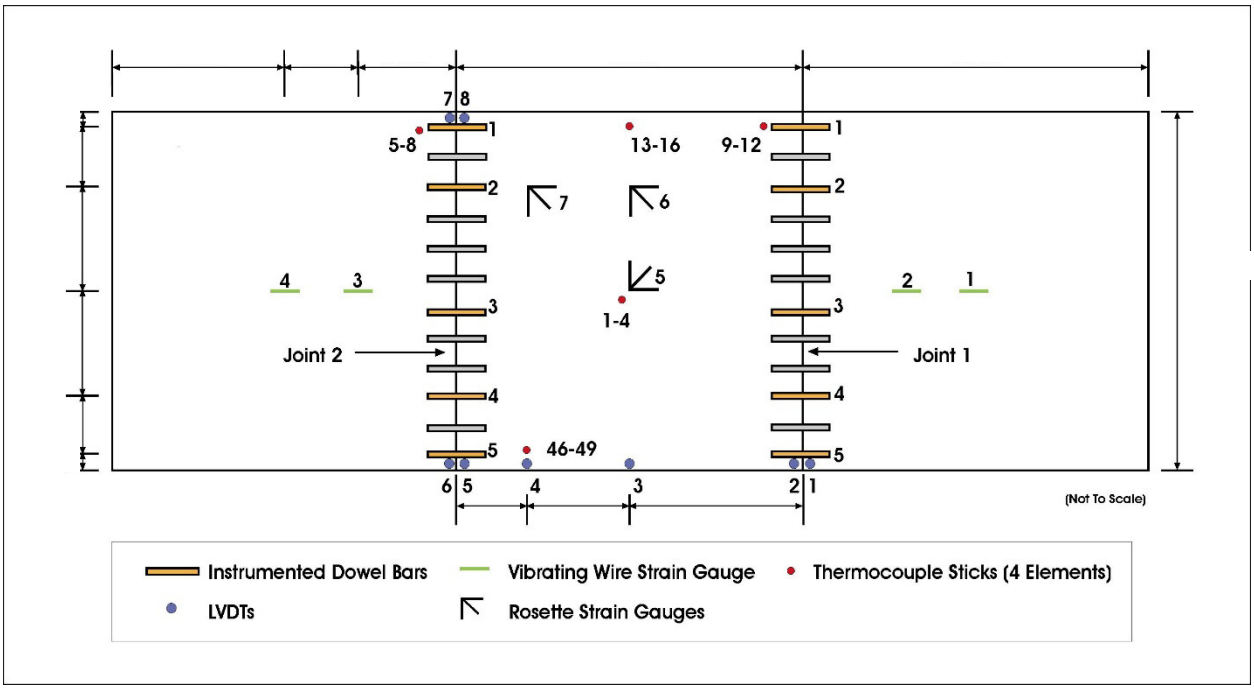

Figure 11. Pavement instrumentation layout with dimensions in m (1 ft = 0.305 m). Adapted from [Sargand, Edwards, and Khoury, 2003]

A Dipstick was used to obtain slab profiles by measuring vertical elevations to a thousandth of an inch at 12 in (305 mm) intervals. The Dipstick consists of an LCD display, two footpads, and a main body housing an inclinometer positioned so its axis and a line passing through the footpads are co-planar. Slab profiles were monitored periodically along a fixed path to determine the environmental response of the pavement during curing and temperature changes. The path, consisted of a rectangle 11 ft by 14 ft (3.36 m by 4.27 m) and one diagonal across the rectangle, and was traversed on the middle slab of both pavements as shown in Figure 12. All data collection and processing was completed by a mini notebook computer attached to the Dipstick handle.

The pavement testing in APLF was conducted in three stages. The first stage included the curing period continued to five weeks under constant temperature, followed by a stage of controlled temperature changes lasting three weeks. In the second stage, the temperature was changed from 68°F (20°C) to 97°F (35°C) for one week, from 97°F (35°C) to 41°F (5°C) for three days, and finally returned to 70°F (21°C). Finally, the third stage included rolling wheel loads of 9,000 lb (40kN), 12,000 lb (53kN), and 15,000 lb (67kN) at 5 mph (8 km/h) and tire pressure of 110 psi (758 kPa). The wheel loads were applied under different controlled environmental conditions, which are: uniform temperatures of 70°F (21°C), 97°F (35°C), and 41°F (5°C) and temperature changes from 68°F (20°C) to 97°F (35°C), from 97°F (35°C) to 72°F (22°C), from 72°F (22°C) to 41°F (5°C), from 41°F (5°C) to 70°F (21°C), from 40°F (4°C) to 97°F (35°C), and from 97°F (35°C) to 41°F (5°C). The thermocouples were removed after the end of Stage II, and at the same time the rosette strain gauges were instrumented to measure the load induced strains in Stage III. LVDTs and vibrating wire strain gauges were installed over the entire testing period. Vibrating wire strain gauges provided temperature gradient and strains due to environmental loading through the entire time of testing.

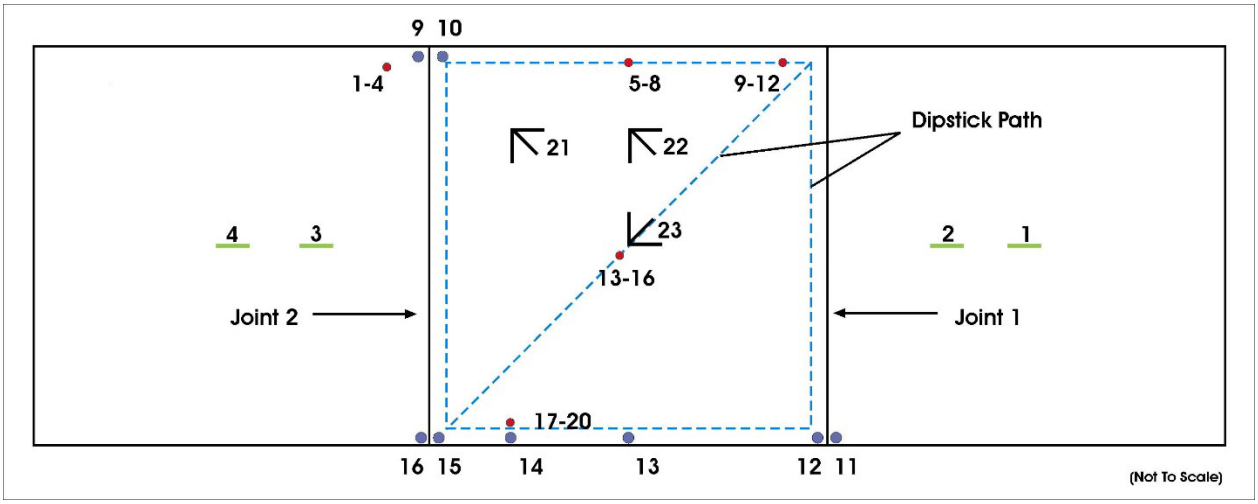

Figure 12. Dipstick path traversed on the pavement. For key of sensor symbols, see Figure 11. [Sargand, Edwards, and Khoury, 2003]

Figure 13 shows the slab temperature gradient during the full test time as measured by vibrating wire strain gauges. The slab top and bottom strains due to environmental changes are shown in Figure 14 through Figure 17 for strain gauges 1, 2, 3, and 4, respectively. The temperature and strain data were recorded from the vibrating wire strain gauges every 30 minutes. The slab corner and edge deflections up to the end of Stage II, as measured by LVDTs, are also presented in Figure 18 and Figure 19, respectively. The positive reading indicates an upward deflection. An LVDT reading was obtained every 15 minutes. The corner deflection is the average of LVDTs 1, 2, 5, 6, 7, and 8, while the edge deflection is the average of LVDTs 2, 3, 4, and 5. For comparison purposes, Figure 20 shows the temperature difference across the slab thickness at its center through the end of Stage II as measured by the thermocouples. Thermocouple data were recorded every 30 minutes. The slight difference between Figure 19 and Figure 12 for the same time period is because the thermocouples were installed at the top and the bottom of the slab, while the vibrating wire strain gauge were placed 1 in (25 mm) above the bottom and 1 in (25 mm) below the top of the slab. Detailed experimental data will be presented together with the finite element modeling data in the next chapter.

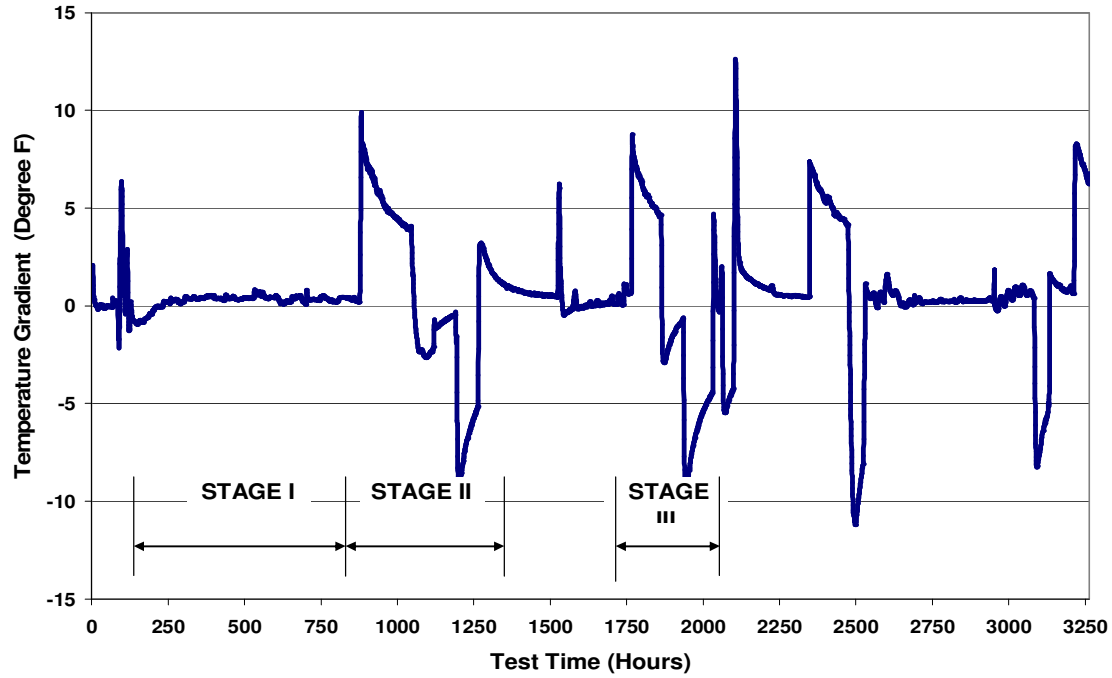

Figure 13. Average temperature difference (labelled Temperature Gradient) between top and bottom of slab measured by vibrating wire strain gauges (1F° = 0.55C°). [Sargand and Abdalla, 2006]

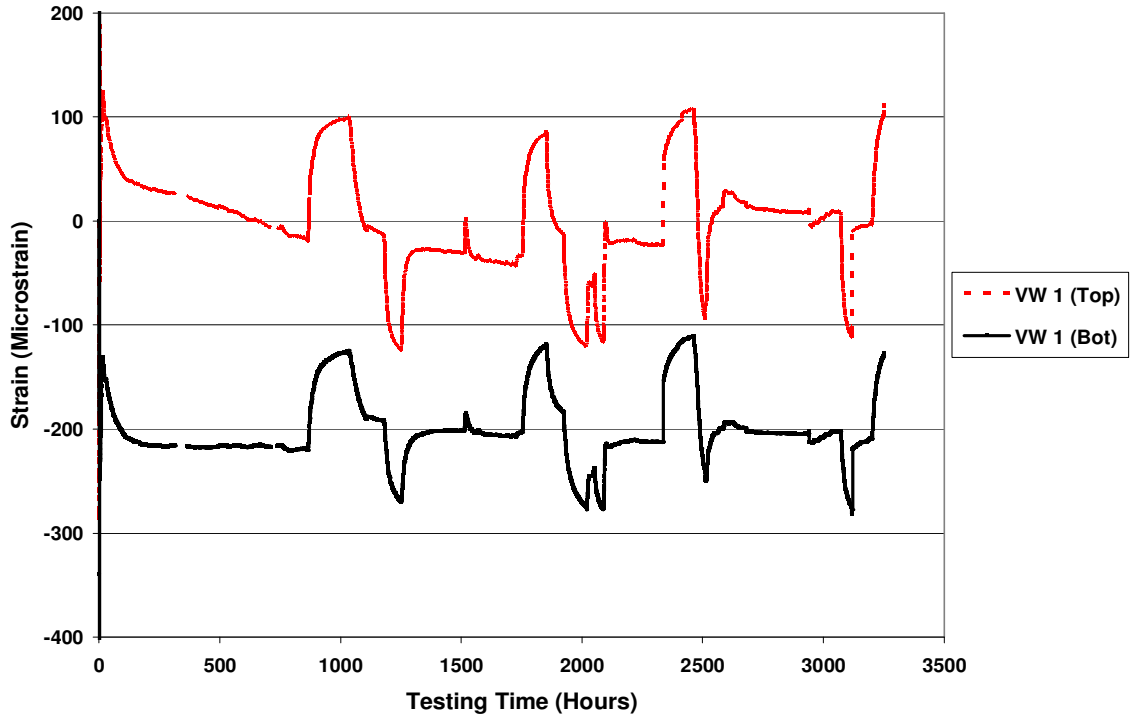

Figure 14. Top and Bottom Strain Development at Vibrating Wire Strain Gauge Location # 1. [Sargand and Abdalla. 2006]

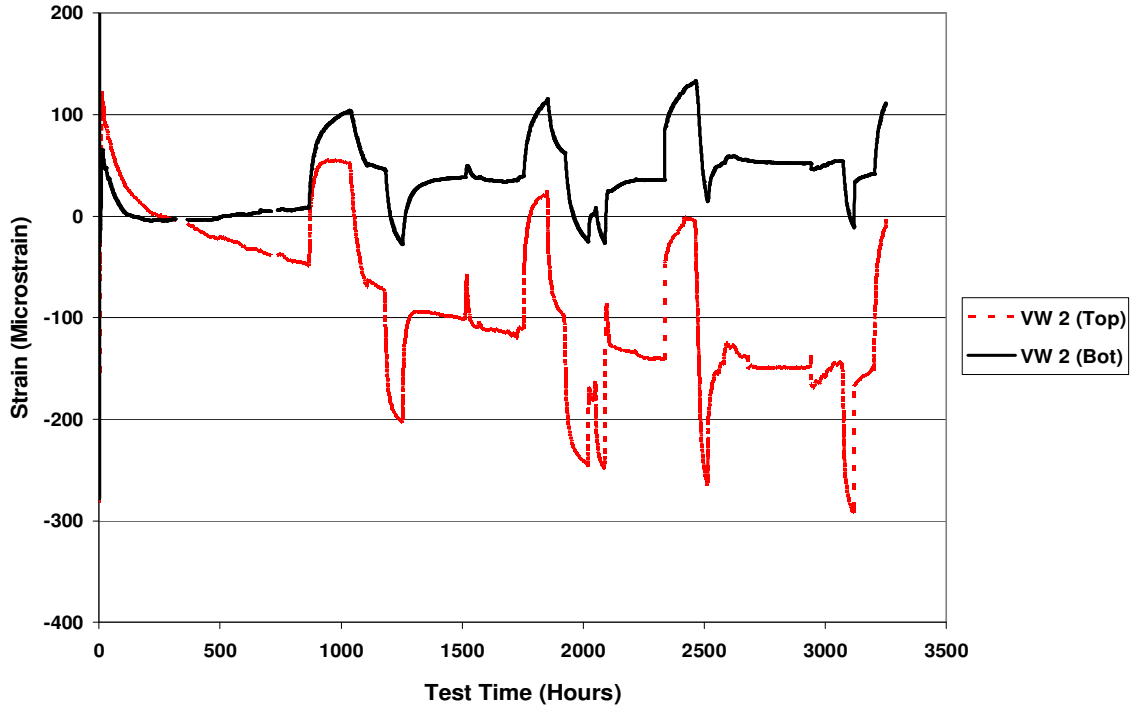

Figure 15. Top and Bottom Strain Development at Vibrating Wire Strain Gauge Location # 2. [Sargand and Abdalla, 2006]

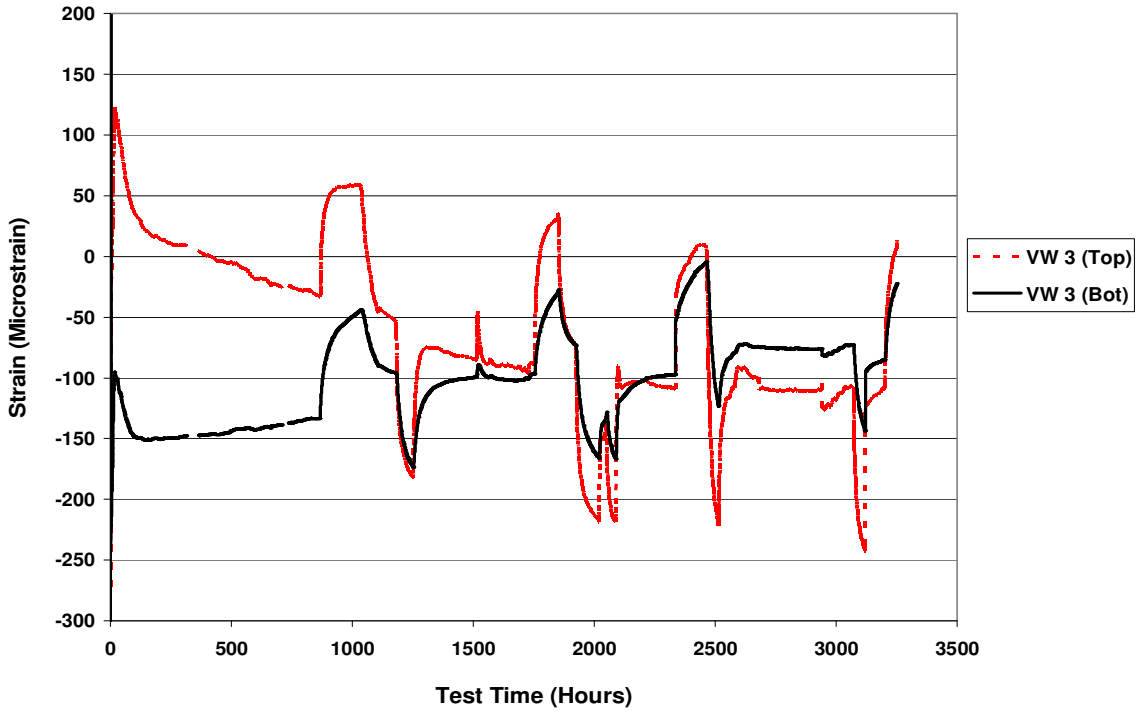

Figure 16. Top and Bottom Strain Development at Vibrating Wire Strain Gauge Location # 3. [Sargand and Abdalla, 2006]

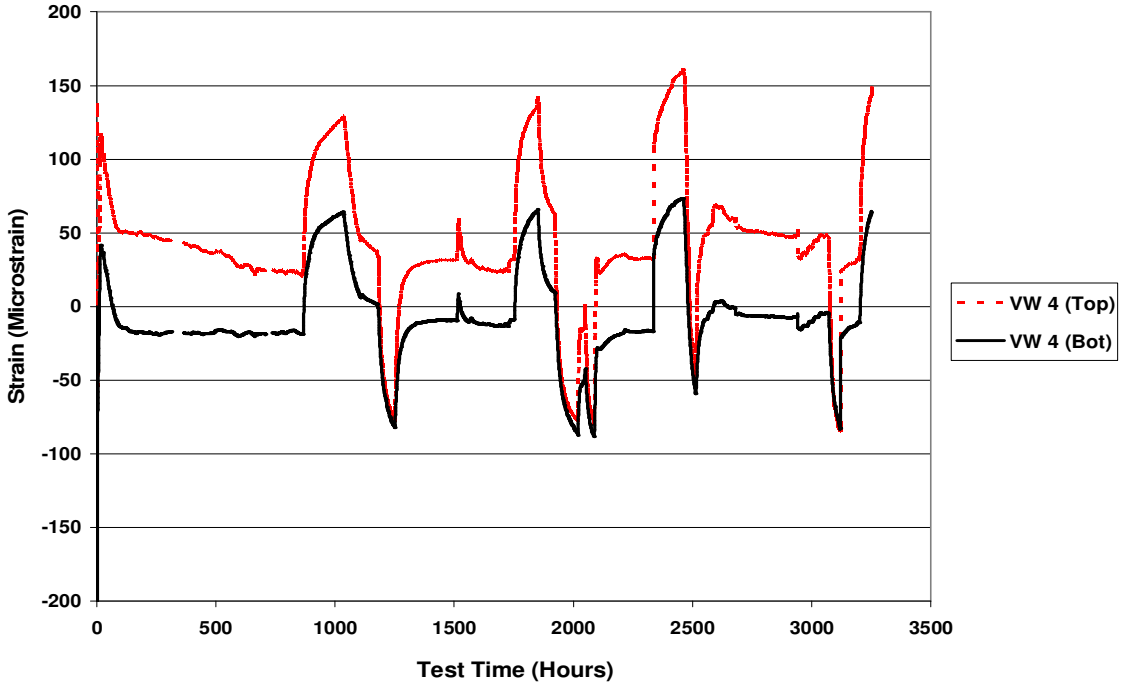

Figure 17. Top and Bottom Strain Development at Vibrating Wire Strain Gauge Location # 4. [Sargand and Abdalla, 2006]

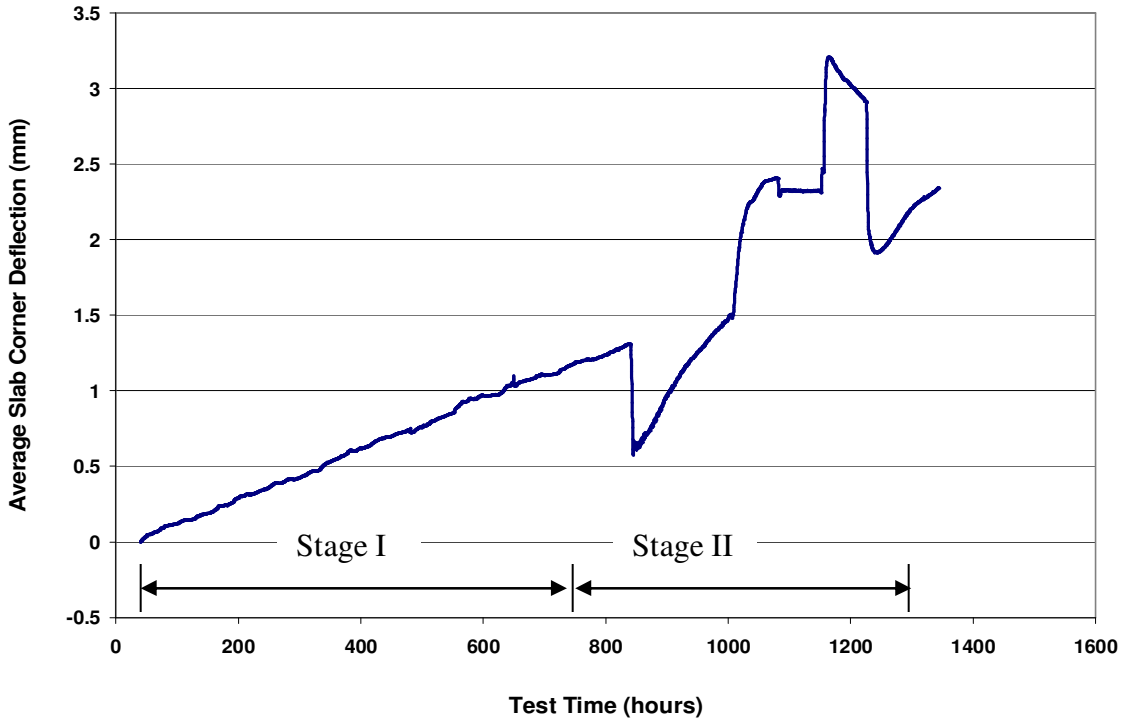

Figure 18. Average Slab Corner Deflection during Stages I and II (1 mm = 39 mil). [Sargand and Abdalla, 2006]

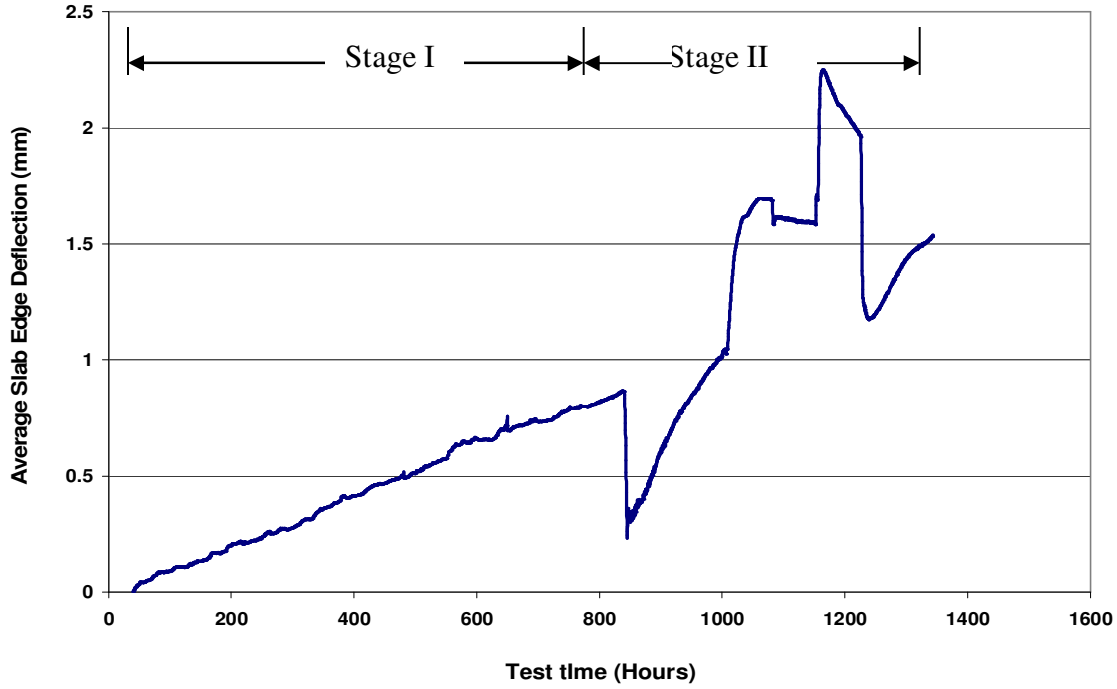

Figure 19. Average Slab Edge Deflection during Stages I and II (1 mm = 39 mil). [Sargand and Abdalla, 2006]

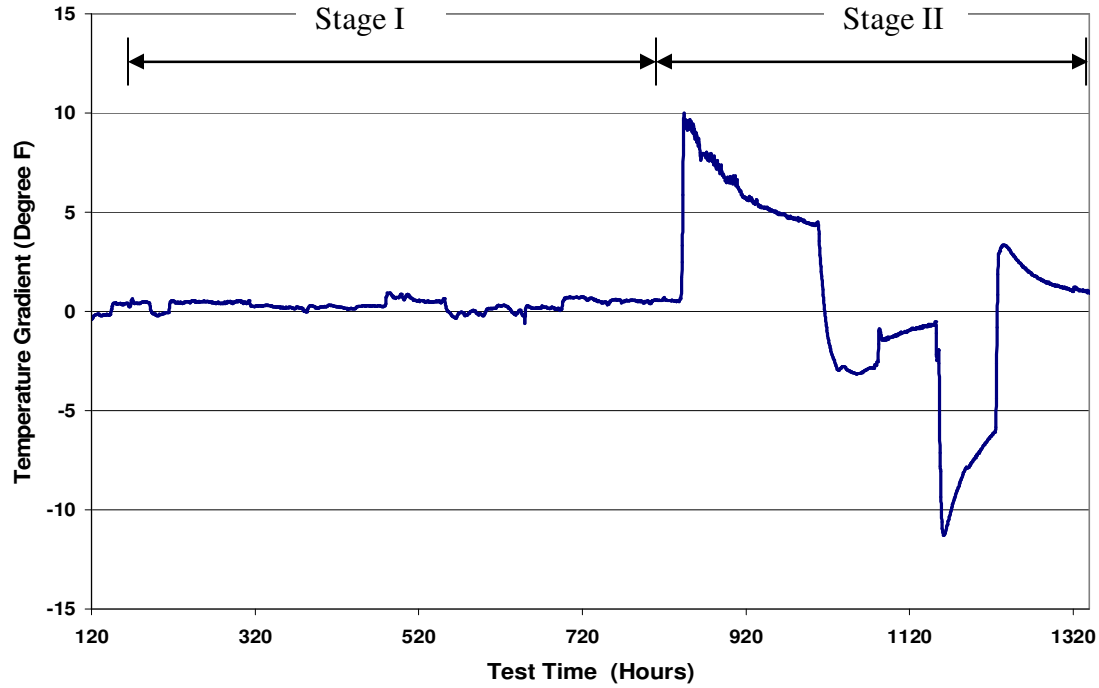

Figure 20. Temperature difference (labelled Temperature Gradient) between top and bottom of slab at the center as measured by thermocouples (1F° = 0.55C°). [Sargand and Abdalla, 2006]

5.3 Traffic data

Traffic is a key parameter directly impacting the design and analysis of concrete pavements. Therefore, it is important to have an insight on the type, weight, and the amount of traffic expected to travel on a typical highway pavement every year. The Ohio Department of Transportation (ODOT) Office of Technical Services (OTS) has an advanced Traffic Count Database System (TCDS) which provides tremendous amount of hourly traffic count data such as volume, speed, class, and Weigh-in-Motion (WIM) data for major roads in the state. Based on discussions with ODOT, a section of Interstate 70 near Reynoldsburg was selected as representative of Ohio traffic on a highly traveled interstate of Functional Class 1 (FC1). An aerial view of I-70 and maps showing its location are in Figure 21.

Figure 21. Interstate 70, east of Reynoldsburg, Ohio. [Google Maps, 2018]

Weigh In Motion (WIM) data from a site (Location ID 30645) on I-70 east of Reynoldsburg was provided to the research team. The last three years of data were averaged to determine the current AADTT. ODOT's Transportation Data Management System (TDMS) reports the 2017 AADT for I-70 was 59,075 vehicles, and the AADTT was 11,023 trucks, which includes all the FHWA vehicle classes shown in Figure 22 excluding Classes 1, 2, and 3. I-70 is classified as Truck Traffic Classification TTC1 route, with predominantly Class 9 (5 axle tractor-trailer) trucks; it is labelled an Urban Interstate by TDMS. Class 9 trucks are by far the most common large vehicle, comprising about 77% of the total annual truck traffic, as shown in Figure 23. The spectrum of vehicle types was determined using software from a report by the University of Akron [Abbas and Frankhouser, 2012] and found to be very similar to the default MEPDG traffic database used nationwide. Because the class distribution determined from the I-70 data was very similar to the MEPDG default for TTC1, the concerns voiced by Abbas and Frankhouser [2012] regarding the default value of Class 9 vehicles do not apply. A linear

growth model with was adopted in this analysis [Lu, Zhang, and Henry, 2007; ERES, 2004], in part because it was adopted by ODOT [Abbas and Frankhouser, 2012, p. 144]. The growth rate was 3%, the average of the previous three years from TDMS.

In modeling rigid pavement damage, it is important to consider the critical vehicle locations on the concrete slab shown in Figure 24, where the first and second axles simultaneously apply loads on opposite ends of a single slab. In other words, the spacing between the first and second axle (whether single or tandem) will be a bit less than the joint spacing or slab length.

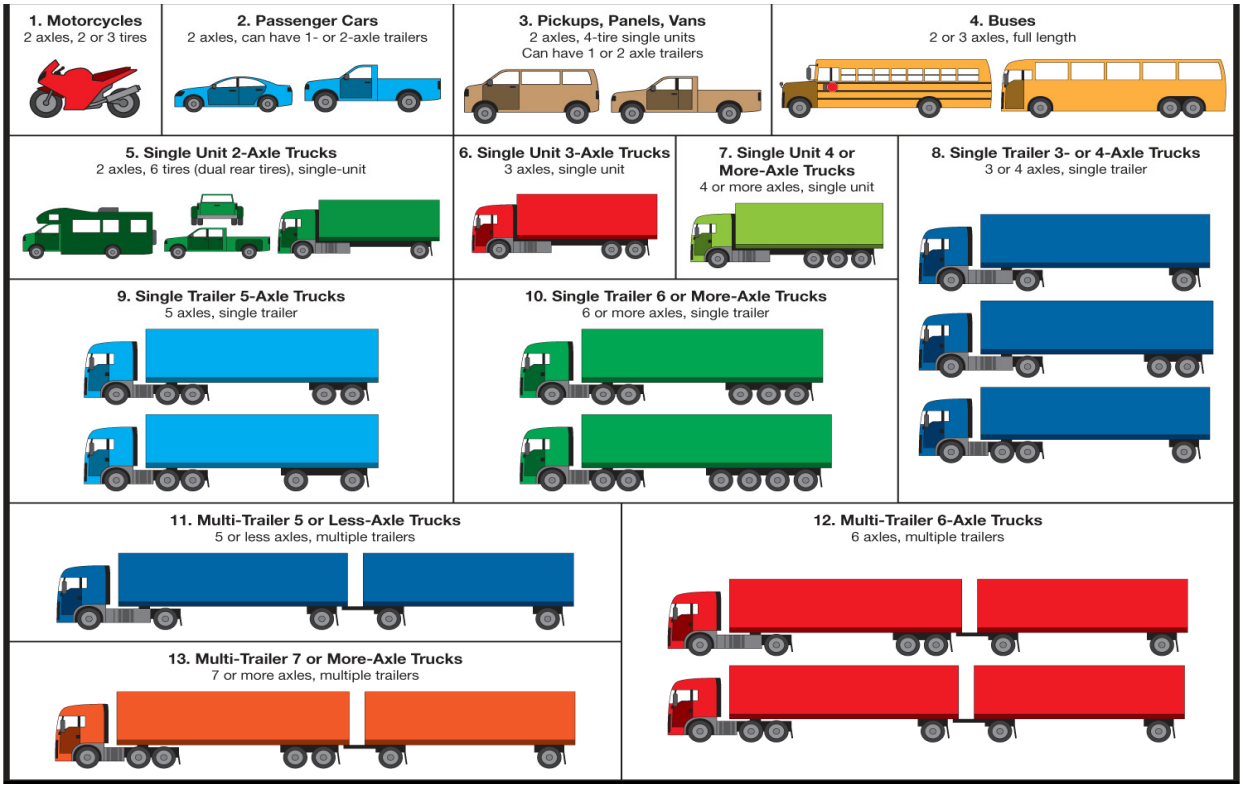

Figure 22. FHWA Vehicle classifications. [TXDOT, 2012]

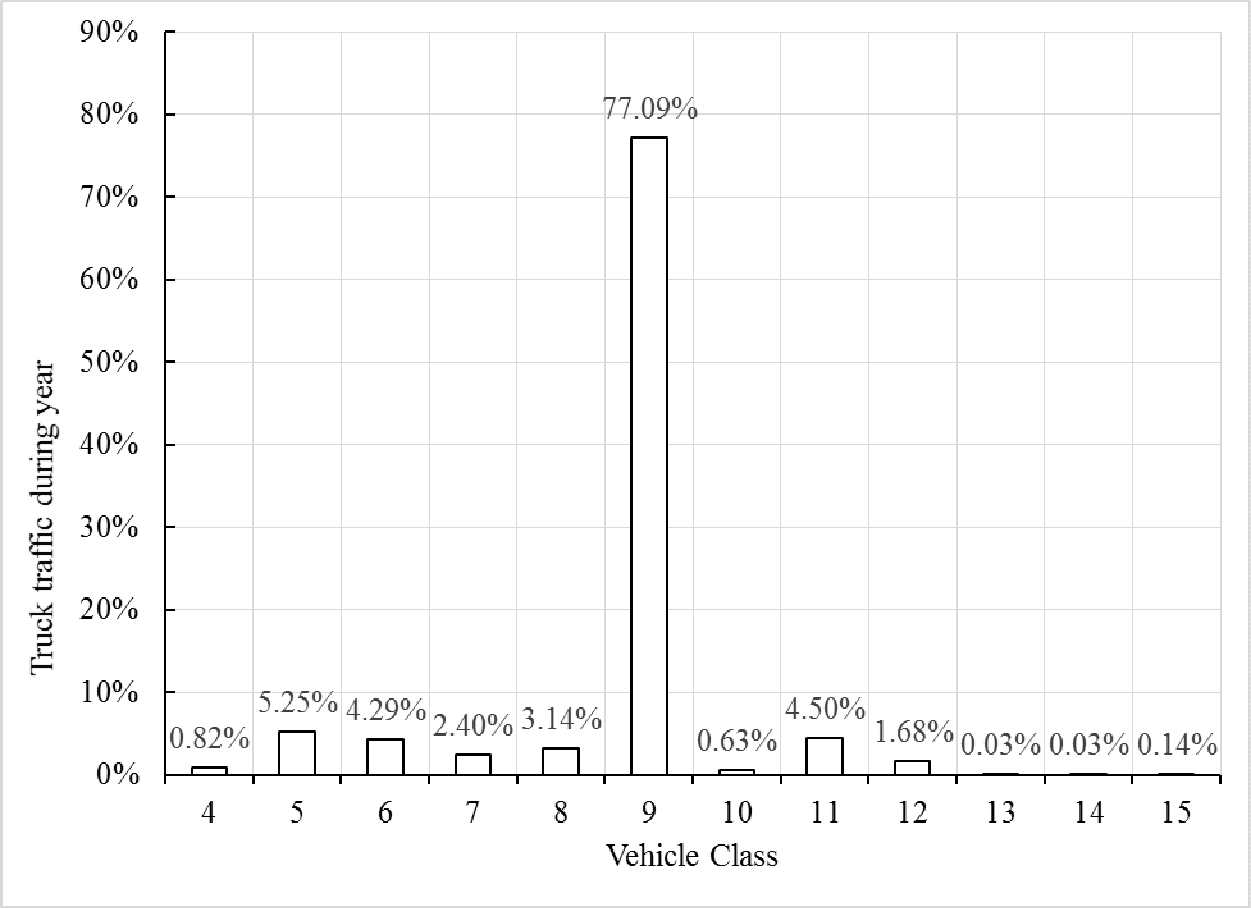

Figure 23. Percentage of AADTT count for each vehicle class on I-70 based on one year of data from I-70.

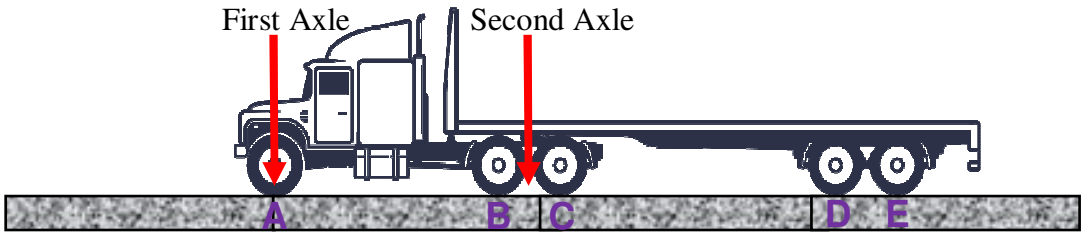

Figure 24. Critical vehicle location on concrete pavement, indicated by position of first and second axle (a tandem axle is pictured) at opposite ends of the same slab. Tire contact points are labelled A-E in violet.

The I-70 data include counts and weight data for Class 5 through Class 15, all of which are included in the analysis of WIM data. The annual number of passes for each first and second spacing and their weights, is presented Table 2 and Table 3. Tire Contact Point A is where the tire meets the road under the steering axle at the front of the truck, identified as "First Axle" in Figure 24; Contact Point B is the front tire of the first tandem axle group at the rear of the cab (labelled "Second Axle"), and Contact Point C is the rear tire of the same tandem axle group at the rear of the cab. The first wheel spacing is measured between Contact Point A and Contact Point B, and the second spacing is measured between Contact Point B and Contact Point C. The data were also plotted in Figure 25. Average weight on front tire (Contact Point A) is 10 kip (44 kN), weight on Contact Points B+C (Tandem Group 1) combined is 32 kip (142 kN).

Table 2. Total annual vehicle count and average weight of first and second axle versus axle spacing (English units).

Axle Spacing (ft)	Count	%	Max.WT.A (kip)	Ave.WT.A (kip)	Max.WT.B (kip)	Ave.WT.B (kip)	Max.WT.C (kip)	Ave.WT.C (kip)	Tandem Axle Max (kip)	Tandem Axle Ave (kip)	Ave. Tandem Spacing (ft)
9	1976	0.19%	24.69	13	23.15	6.83	27.34	7.61	50	14	7.27
10	10044	0.96%	22.49	10	24.25	10.89	24.91	10.61	49	21	5.17
11	42481	4.05%	24.69	10	28.00	11.59	28.00	11.06	56	23	5.17
12	64852	6.18%	21.61	10	32.63	12.81	33.29	11.79	66	25	11.06
13	64267	6.13%	23.59	10	30.20	13.44	27.12	12.35	57	26	17.33
14	29498	2.81%	23.81	10	29.54	11.66	27.12	10.73	57	22	11.51
15	88069	8.40%	28.44	11	28.44	12.37	27.34	12.07	56	24	4.87
16	146579	13.98%	25.79	12	27.34	12.90	29.76	12.63	57	26	4.53
17	326343	31.12%	23.81	12	28.44	13.07	26.23	12.81	55	26	4.48
18	82883	7.90%	22.93	12	28.00	13.81	27.78	13.51	56	27	4.77
19	73862	7.04%	24.25	11	27.78	13.22	27.12	13.22	55	26	4.44
20	65302	6.23%	25.35	12	30.42	14.14	27.34	13.91	58	28	4.42
21	27935	2.66%	24.91	10	26.23	13.48	26.46	13.32	53	27	4.53
22	9018	0.86%	21.83	10	26.68	13.41	24.25	13.07	51	26	4.59
23	6917	0.66%	22.27	10	29.54	13.85	27.12	12.68	57	27	4.61
24	2536	0.24%	18.96	11	28.44	14.78	27.12	10.60	56	25	4.90
25	3268	0.31%	19.84	12	26.90	15.36	24.03	10.79	51	26	4.64
26	2745	0.26%	21.83	14	29.10	18.50	26.01	12.33	55	31	4.22

Table 3. Total annual vehicle count and average weight of first and second axle versus axle spacing (metric units).

Axle Spacing (m)	Count	%	Max.WT.A (kN)	Ave.WT.A (kN)	Max.WT.B (kN)	Ave.WT.B (kN)	Max.WT.C (kN)	Ave.WT.C (kN)	Tandem Axle Max (kN)	Tandem Axle Ave (kN)	Ave. Tandem Spacing (m)
2.7	1976	0.19%	110	60	103	30	122	34	225	64	2.22
3.0	10044	0.96%	100	43	108	48	111	47	219	96	1.58
3.4	42481	4.05%	110	45	125	52	125	49	249	101	1.58
3.7	64852	6.18%	96	46	145	57	148	52	293	109	3.37
4.0	64267	6.13%	105	44	134	60	121	55	255	115	5.28
4.3	29498	2.81%	106	43	131	52	121	48	252	100	3.51
4.6	88069	8.40%	127	50	127	55	122	54	248	109	1.49
4.9	146579	13.98%	115	51	122	57	132	56	254	114	1.38
5.2	326343	31.12%	106	52	127	58	117	57	243	115	1.37
5.5	82883	7.90%	102	52	125	61	124	60	248	121	1.45
5.8	73862	7.04%	108	51	124	59	121	59	244	118	1.35
6.1	65302	6.23%	113	52	135	63	122	62	257	125	1.35
6.4	27935	2.66%	111	46	117	60	118	59	234	119	1.38
6.7	9018	0.86%	97	45	119	60	108	58	227	118	1.40
7.0	6917	0.66%	99	46	131	62	121	56	252	118	1.40
7.3	2536	0.24%	84	50	127	66	121	47	247	113	1.49
7.6	3268	0.31%	88	52	120	68	107	48	227	116	1.41
7.9	2745	0.26%	97	62	129	82	116	55	245	137	1.28

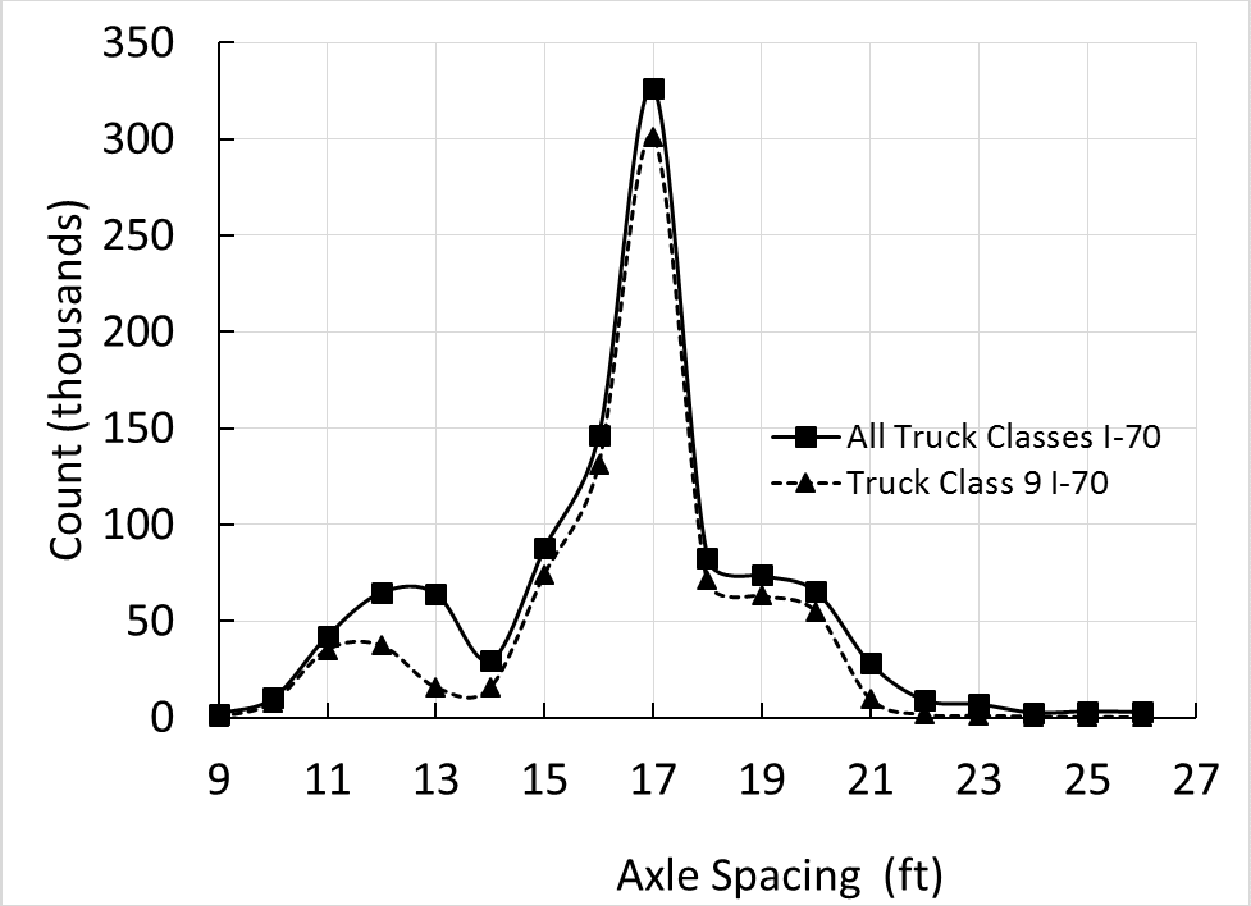

Figure 25. Annual vehicle passes on I-70 for each axle spacing (1 ft = 0.305 m).

The most frequent axle spacing recorded is 17 ft (5.2 m). It should be noticed the first axle is typically lighter than the second axle. The average first axle weight was found to be about 10 kip (44 kN) and the average tandem axle weight was about 32 kip (142 kN). These estimates are based on the reported by Abbas et al. [2012, p. 129-133]. More details about axle spacing and weight selection will be provided in Chapter 6.

5.4 Temperature data

The temperature at which a concrete pavement is constructed has a significant impact on its performance. Concrete is a porous material which expands and contracts as a result of temperature and moisture variations through its depth. Therefore, using actual temperature data in the design and analysis of concrete pavements would be more representative of field conditions. Route 23 in Delaware County, Ohio contains several concrete test sections instrumented with thermocouples and other sensors which collect temperature data on daily basis. Temperature data of two concrete test sections on Route 23 was used to find the maximum negative and positive temperature gradients through their depth, namely, Section 201 and Section 204. Section 201 is 8 in (203 mm) PCC on 6 in (152 mm) DGAB, and Section 204 is 11 in (279 m) PCC on 6 in (152 mm) DGAB. Temperature data for these two sections were analyzed to find the maximum negative and positive temperature gradients experienced during a typical year. The results showed the maximum negative temperature gradient was found in section 201 on

December, 2000 to be -1.29 C°/in (-0.51C°/cm or -2.32 F°/in), and the maximum positive temperature gradient happened in April, 2000 with a value of 2.24 C°/in (0.88C°/cm or 4.0 F°/in). The negative and positive temperature gradients of the two sections during 1996-2001 are presented in Figure 26 through Figure 31.

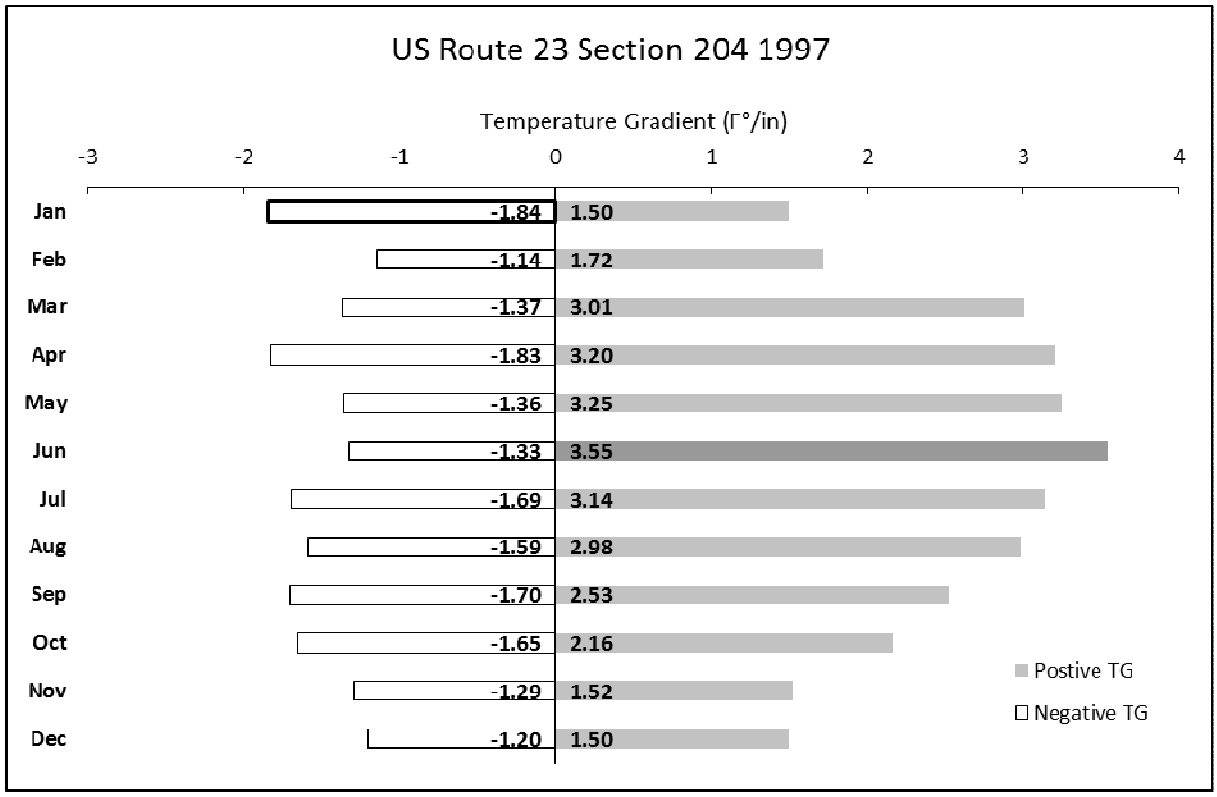

Figure 26. Maximum negative and positive temperature gradient in Section 204 Route 23 during 1997. (1 F°/in = 0.22 C°/cm)

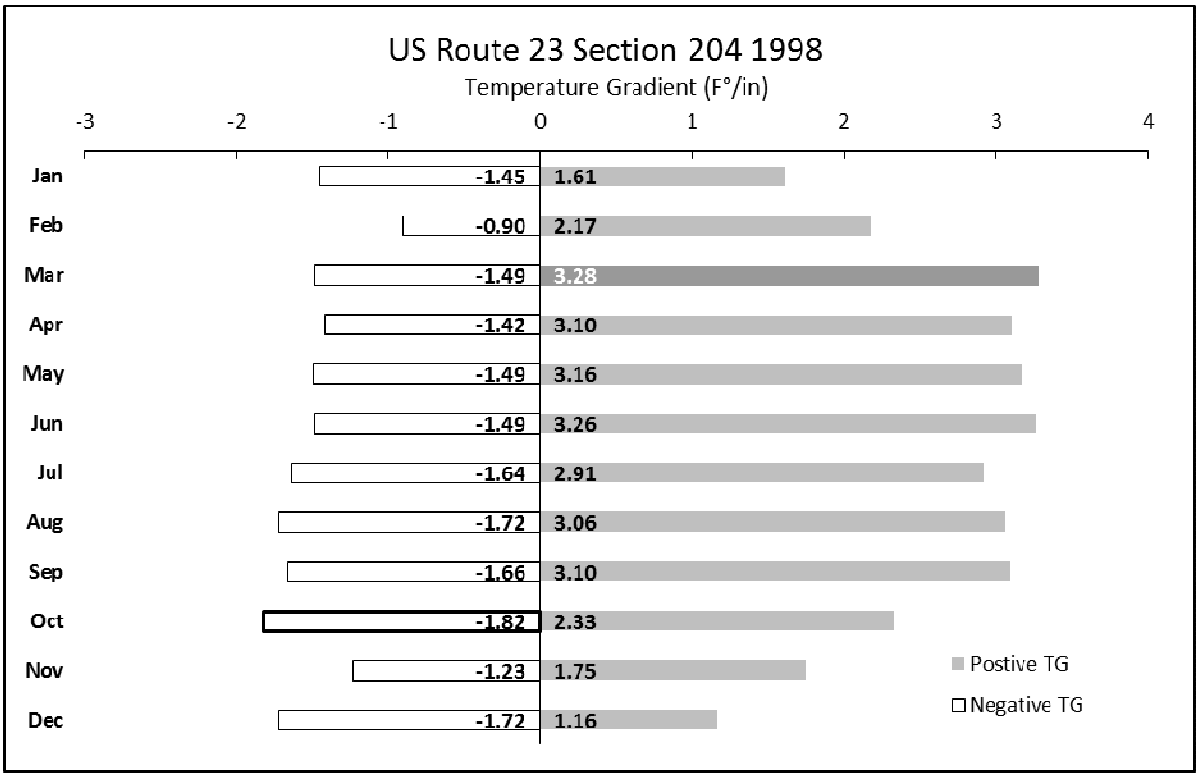

Figure 27. Maximum negative and positive temperature gradient in Section 204 Route 23 during 1998. (1 F°/in = 0.22 C°/cm)

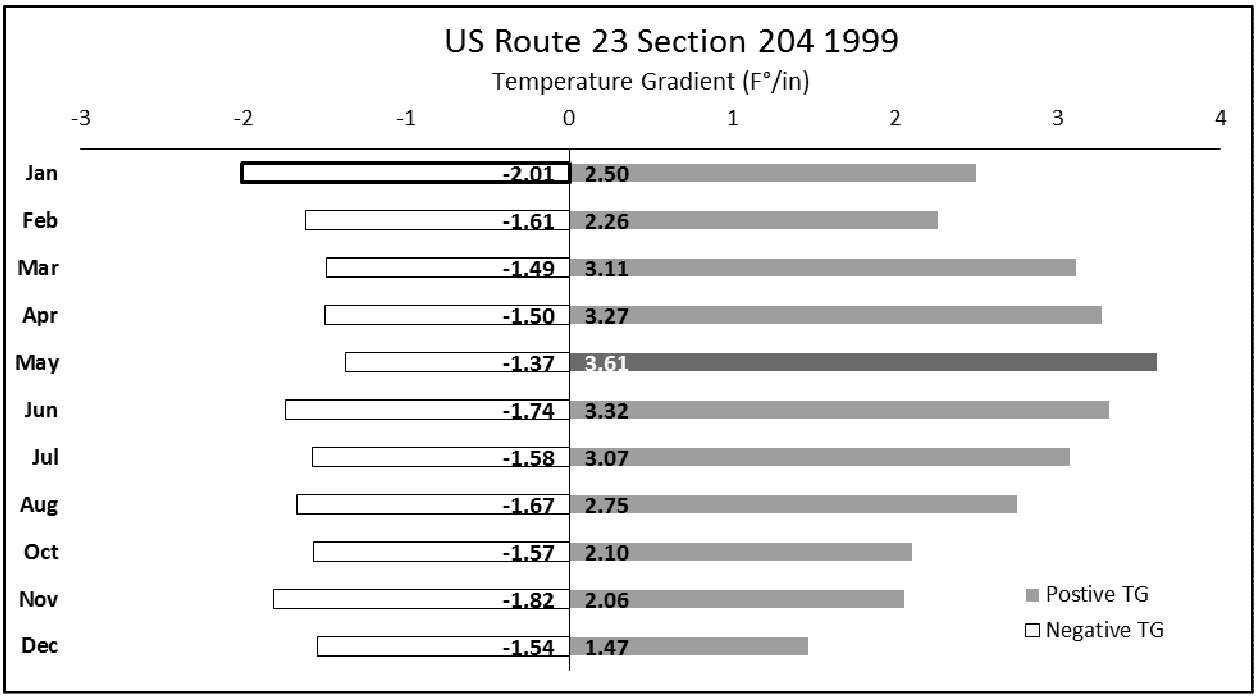

Figure 28. Maximum negative and positive temperature gradient in Section 204 Route 23 during 1999. (1 F°/in = 0.22 C°/cm)

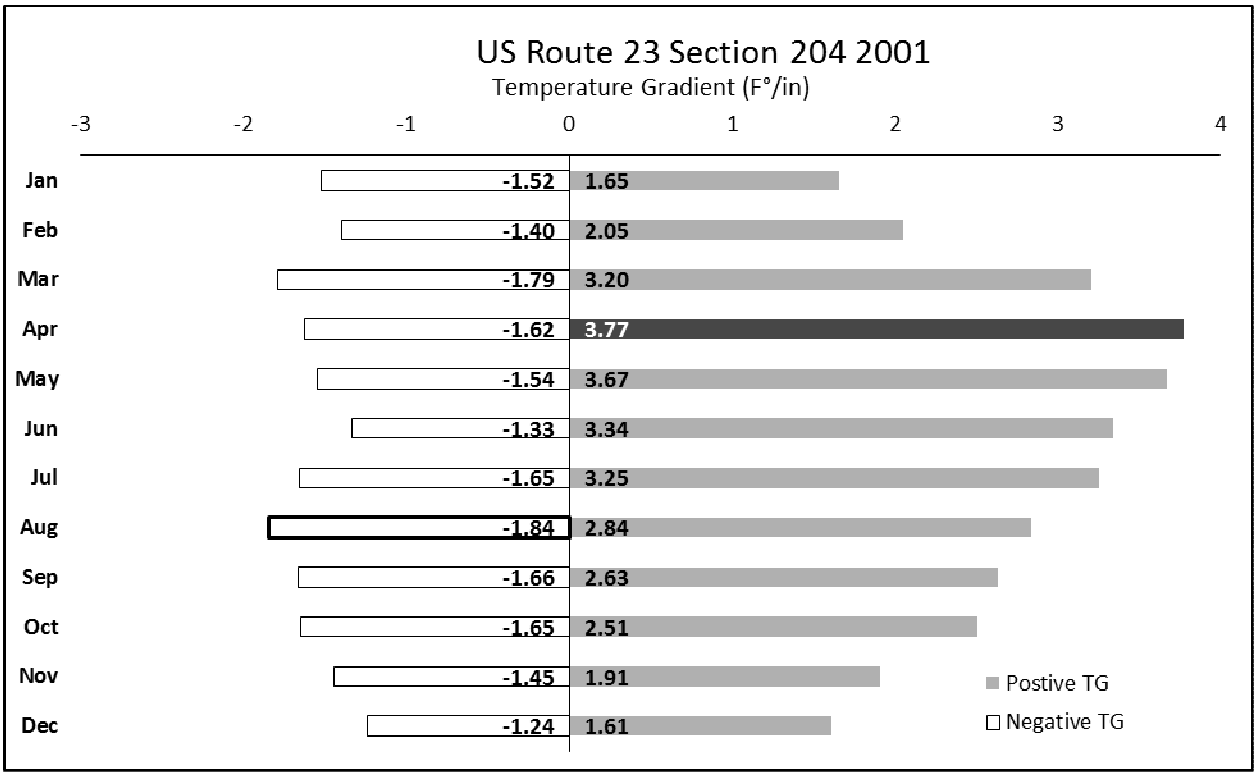

Figure 29. Maximum negative and positive temperature gradient in Section 204 Route 23 during 2001. (1 F°/in = 0.22 C°/cm)

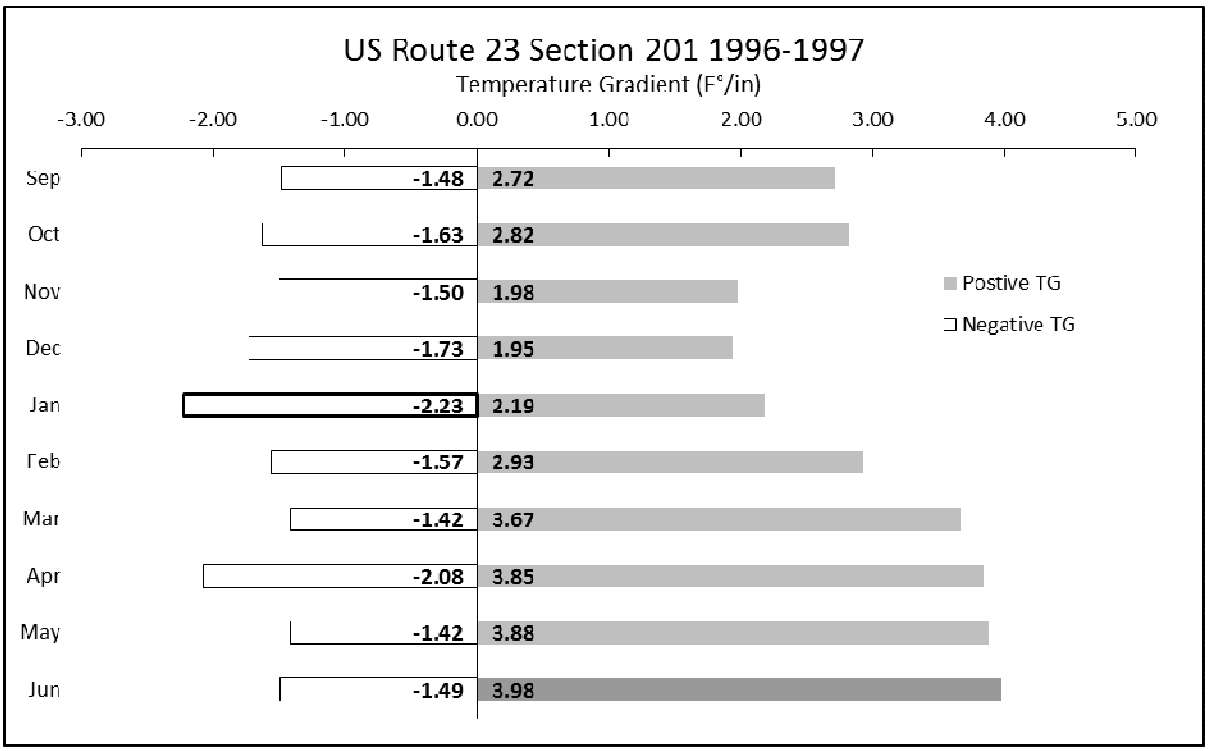

Figure 30. Maximum negative and positive temperature gradient in Section 201 Route 23 during 1996-1997. (1 F°/in = 0.22 C°/cm)

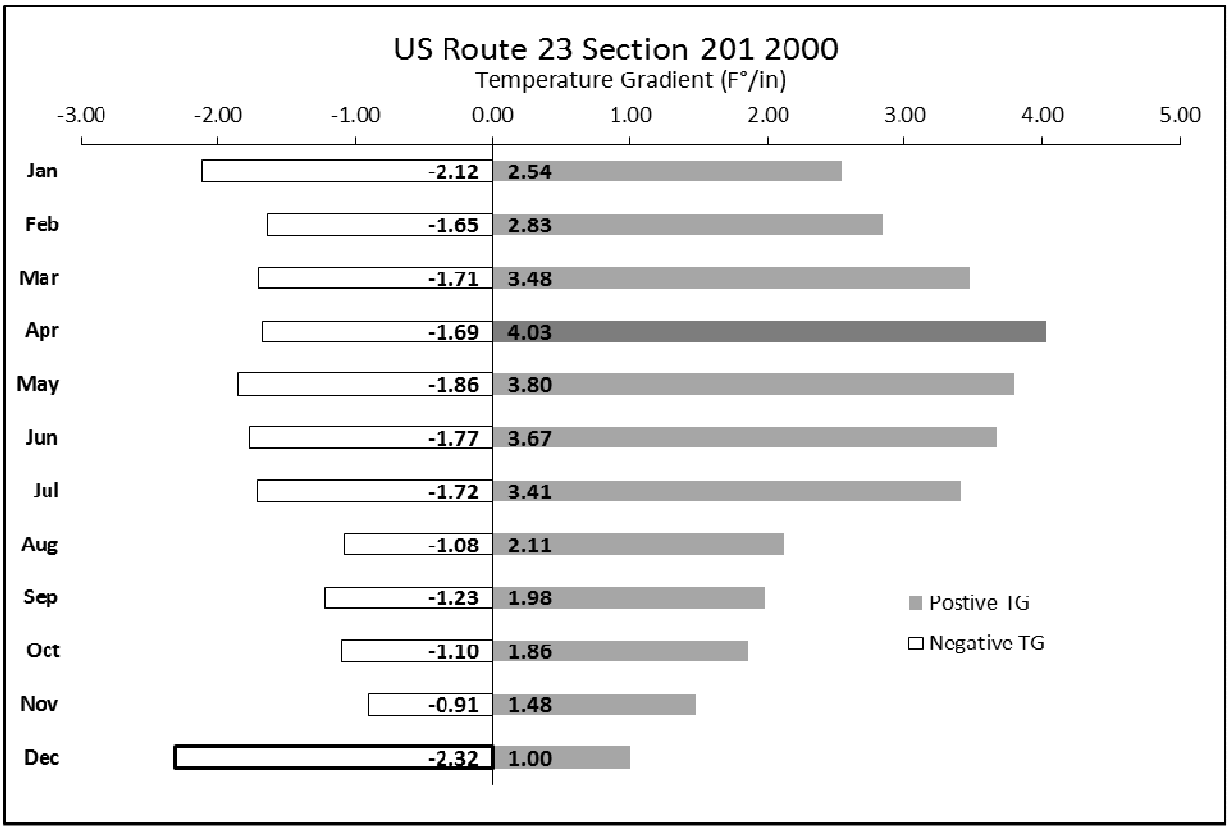

Figure 31. Maximum negative and positive temperature gradient in Section 201 Route 23 during 2000. (1 F°/in = 0.22 C°/cm)

6 Finite Element Modeling (FEM)

Finite element modeling (FEM) of concrete pavement is the most robust and widely used method for the analysis of concrete pavement. The advanced computational capabilities of computers have greatly enhanced the analysis and design of concrete pavements. Although there are ready-made FEM programs specialized for concrete pavement design, commercial 3D finite element software can model concrete pavement more realistically. ABAQUS is one program capable of modelling concrete pavements in three-dimensions with different complex behavioral aspects and boundary conditions specialized concrete pavement modeling programs fail to include. Therefore, it was decided to use ABAQUS v. 6.14 as the analytical tool in this FEM.

6.1 APLF 3D FEM

This FEM was created to simulate the concrete section tested in the Accelerated Pavement Load Facility (APLF) since response data are available for verification. The model consisted of three concrete slabs having length 15 ft (4.6 m), width 12 ft (3.7 m), and thickness 10 in (254 mm). The slabs are connected in the transverse direction with 1.5 in (38 mm) diameter and 18 in (457 mm) length dowel bars at the joints. A total of 12 steel dowel bars with 12 in (305 mm) spacing were used to provide load transfer between adjacent slabs. The concrete slabs rest on a 6 in (152 mm) thick DGAB layer supported by a 12 in (305 mm) thick layer of chemically stabilized subgrade and 70 in (1800 mm) thick natural subgrade. This structure is a typical concrete pavement design for ODOT since they recently started a policy of global stabilization for all newly constructed pavements. The subgrade was modeled as solid elastic medium rather than the traditional Winkler foundation since it provides continuity and more accurate responses [Luoke et al., 2012]. The model geometry is presented in Figure 32.

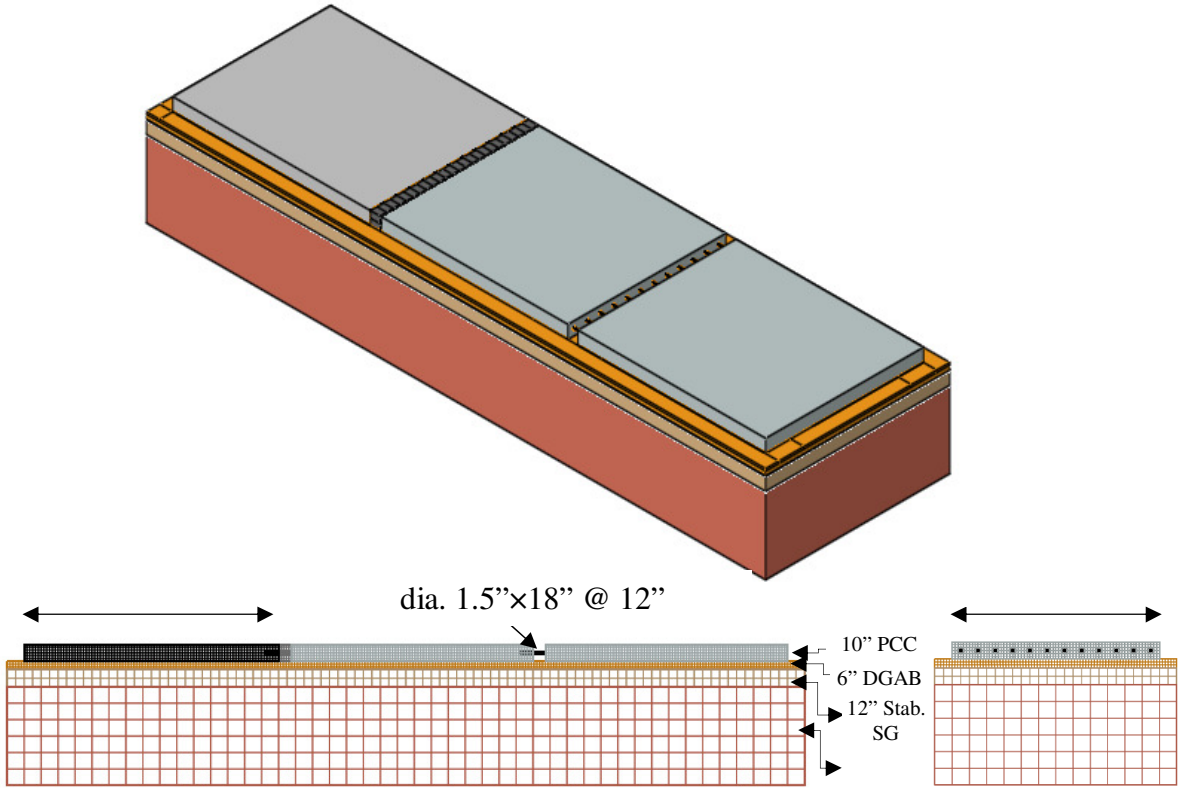

Figure 32. Single lane model geometry and mesh (1” = 1 in = 25 mm, 1’= 1ft = 0.305 m).

A fine mesh was applied to the concrete slab, dowel bars, and base layer, while a coarse mesh was used for the stabilized and natural subgrade layers. An 8-node brick element was adopted throughout the mesh. The slab supporting layers were extended to avoid edge effects. A linear elastic behavior was assumed for all layers and dowel bars. The PCC-dowel interaction was modeled using frictional interface on one slab with friction coefficient 0.05 with full embedment on the other slab. The interface between the concrete and base layer was also modeled as frictional, with friction coefficient 0.9. The interactions between stabilized subgrade and base and between stabilized subgrade and subgrade layer were modeled as fully bonded. The boundary conditions were applied to the sides of supporting layers by forbidding horizontal movement. The boundary conditions at the bottom of subgrade layer were applied by preventing the horizontal and vertical movements, and assuming there is negligible vertical displacement below a certain subgrade depth. The frictional interfaces between the concrete and dowel bars and between the concrete and base layer were modeled in terms of tangential behavior and normal behavior with no tension. When the concrete slab is curled upward, it will be fully separate without pulling up base material. A gap of 0.25 in (6.4 mm) was used to separate the adjacent slabs at the joints. This eliminated any aggregate interlock, and all load transfer between adjacent slabs was through the dowels. However, a normal behavior was applied in case concrete slabs come in contact due to thermal expansion in order to transfer the horizontal responses at the joints. The material properties of the model components are presented in Table 4. The elastic parameters of concrete material, shown in Table 1, were obtained experimentally by Sargand, Edwards, and Khoury [2003]. The material parameters used in the elastic model for the

supporting layers were selected initially from Sargand and Abdalla [2006] and then refined by an iterative back calculation until the simulation results matched empirical measurements in the indoor facility. The boundary conditions were also applied in a way that best simulated the slab constraints in the APLF. Different boundary conditions were tried until the model response matched data from the APLF.

Table 4. Verified elastic material parameters for the FEM.

Concrete Material		
Young's Modulus	3.42E+06 psi	23.6 GPa
Poisson's Ratio	0.22	
Coefficient of Thermal Expansion	6.70E-06 /F°	12.06E-06 /C°
Unit Weight | Density	144 pcf	2300 kg/m^3
Base Material		
Young's Modulus	40000 psi	276 MPa
Poisson's Ratio	0.35	
Stabilized Subgrade Material		
Young's Modulus	25000 psi	172 MPa
Poisson's Ratio	0.35	
Subgrade Material		
Young's Modulus	6000 psi	41 MPa
Poisson's Ratio	0.4	
Dowel Bar Material		
Young's Modulus	2.90E+06 psi	200 GPa
Poisson's Ratio	0.3	

6.2 Effective Built-in Temperature Difference During Slab Curing

Portland cement concrete shrinks as it dries, essentially because water evaporates while the cement paste hardens. Moisture gradients in concrete pavements cause differential shrinkage between the top and the bottom of the pavement. Shrinkage causes upward warping, as moisture is lost primarily from the top of the slab. This leads to corner uplift and curling which results in the top of the pavement experiencing tension and the bottom of the pavement experiencing compression. During the curing period, which lasted for five weeks, the air temperature in the APLF was kept constant. The temperature gradient within the slab thickness was approximately zero after 5 days (120 hours). Meanwhile, the average corner upward warping due to the moisture gradient was observed to be 0.052 in (1.321 mm) at the end of the fifth week (Figure 18). This amount of warping can be simulated as a built-in negative temperature difference (EBITD). Using ABAQUS, a number of temperature differences were tried until the calculated curling matched the measured curling. A residual temperature difference of -22F° (-12.2C°) gave a good match. This value is close to those obtained by Yu et al. [1995] (-20F° = -11.1C°) and Sargand, Edwards, and Khoury [2003]. This upward curl would cause a permanent loss of support to the pavement. The trial built-in temperature differences and the corresponding amount of curl are presented in Table 5.

Table 5. Trial residual temperature differences and computed corner deflections.

Built-in Temperature Difference	**(F°)**	-10	-12	-16	-18	-20	**-22**	-24
	(C°)	-5.6	-6.7	-8.9	-10.0	-11.1	**-12.2**	-13.3
Corner Deflection	**(mil)**	15	21	33	39	45	**52**	59
	(mm)	0.38	0.53	0.84	0.99	1.14	**1.32**	1.50

6.3 Modeling Loss of Support Due to Slab Curling/Warping

At the end of curing period, concrete slabs experienced a permanent built-in curl, which would result in a permanent loss of support along the slabs edges and corners. This loss of support can be estimated using the Dipstick data recorded at the end of the curing period which lasted for 838 hours. The Dipstick data across the slab diagonal measured after 838 and 1167 hours of test time is shown in Figure 33. The slab deflections along the slab diagonal shown in Figure 34 were referenced to the deflection of the corner as a base line; however, deflections should be referenced to zero deflection line. The horizontal distance of 38 ft (11.6 m) represents the slab diagonal being measured twice, forward and backward. The horizontal dotted line at 0.052 in (1.32 mm) represents the zero-deflection line. It is shown the upward lift along the diagonal extends 3.5 ft (1.07 m) from the corner. As a sign convention, upward curling has a positive sign, and downward curling has a negative sign. Using simple geometry, and assuming symmetrical uplift, the upward curling area can be found as 2.2 ft (0.67 m) in the longitudinal direction by 2.7 ft (0.82 m) in the transverse direction, as shown in Figure 34. Assuming a uniform rectangular loss of support along the slab edges, the unsupported areas under the concrete slab would be as shown as the hatched regions in Figure 35.

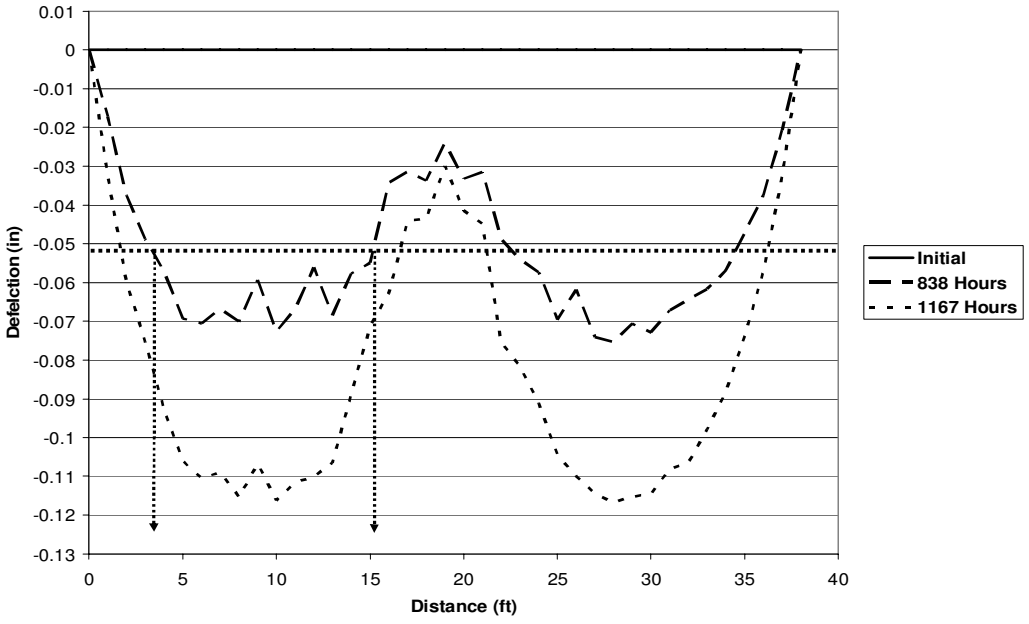

Figure 33. Dipstick Profile along Diagonal Path on Slab (1 in = 25.4 mm; 1 ft = 0.305 m).

Figure 34. Extent of upward curling along the diagonal (left in English units, right in metric units).

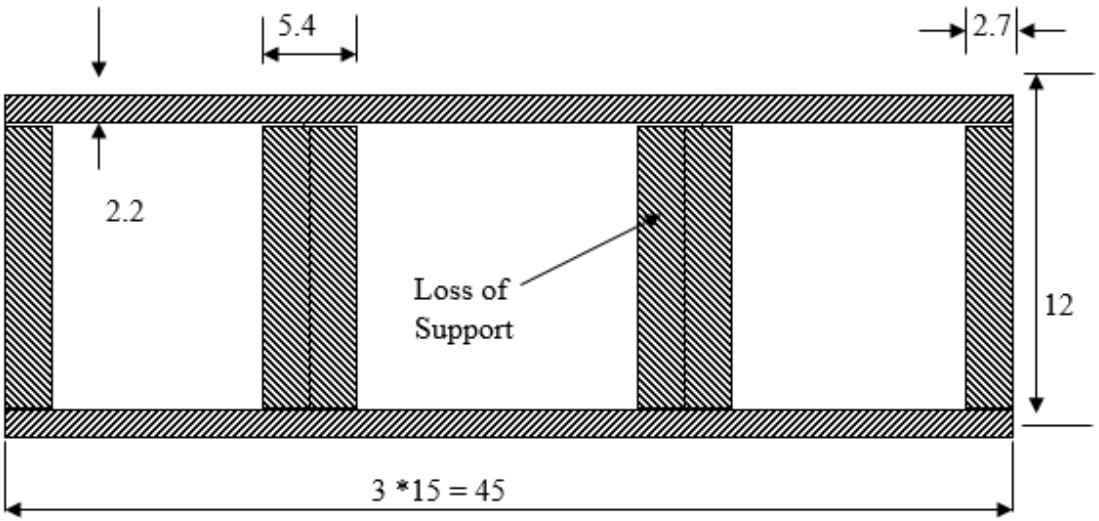

Figure 35. Measured loss of support (Dimensions in feet, 1 ft = 0.305 m).

From the FEM under negative temperature difference of -22F° (-12.2C°) over a 10 in (254 mm) thickness (i.e. -2.2 F°/in = -0.48 C°/cm) associated with upward curl of at 0.052 in (1.321 mm), the amount of loss of support by assuming a rectangular loss of support area was found to be 3.36 ft (1.02 m) along the diagonal, or 2.67 ft (0.81 m) in the longitudinal direction by 2.04 ft (0.62 m) in the transverse direction. This agrees with loss of support obtained from the Dipstick data. The loss of support area obtained from the FEM is shown in the hatched regions of Figure 36.

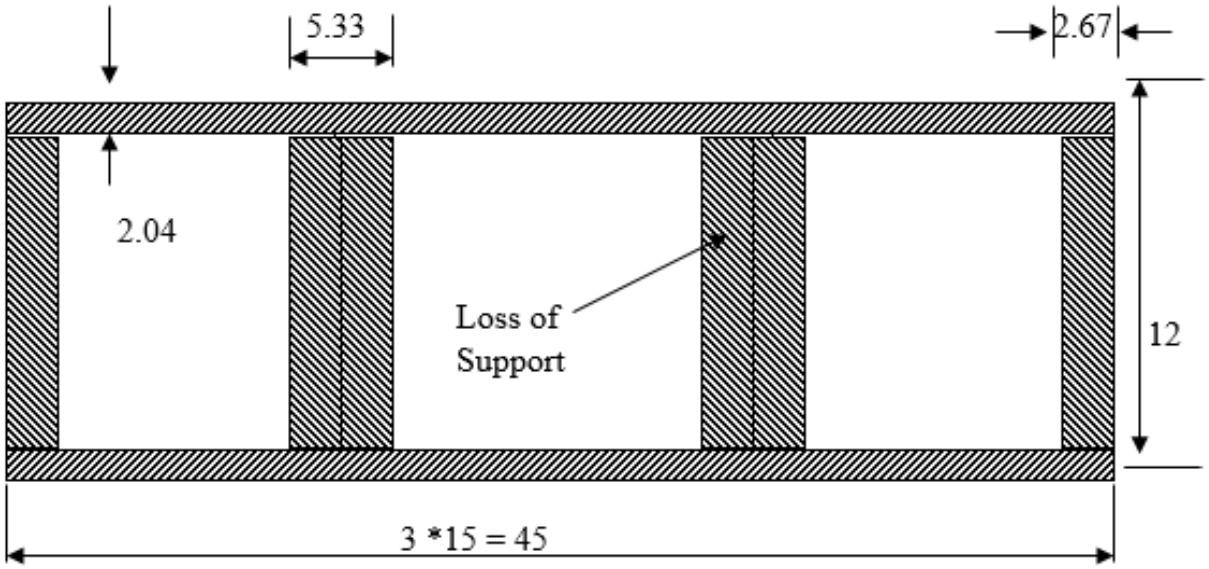

Figure 36. Loss of support as determined form FEM (Dimensions in feet, 1 ft = 0.305 m).

There are three ways in which loss of support can be modeled in ABAQUS. The first method is to assume a flat slab conditions and using the effective built-in temperature difference (EBITD) as a reference. For instance, if a temperature difference of +12 F° (6.7 C°) is to be applied to the flat slab, the EBITD would be added to determine the net temperature difference on the warped slab: -22 F° + 12 F° = -10 F° (-12.2 C° + 6.7 C° = -5.5 C°). The second method is by modeling the concrete slab in its deformed shape at the end of curing period. In this case the full temperature difference, as obtained experimentally, should be applied. The problem associated with first method is when a negative temperature difference is applied along with EBITD, the slab responses would be much higher than those experimentally obtained during the controlled temperature stage. When the temperature difference is added to the EBITD, the residual responses associated with EBITD would be added to the responses obtained from the applied temperature difference, thus resulting in greater values for deflection and strain responses than those measured. The second approach, on the other hand, models the slab conditions better and results in closer agreement with measured responses. However, one problem associated with modeling deformed shapes in ABAQUS is the mesh and dowel bars. It is complicated to obtain a uniform structured mesh with the deformed shape modeled in ABAQUS, and the appropriate element type could not be used. In addition, the dowel bars would not be straight and the exact dowel bars deformed shape and looseness is unknown. The third approach which can be used to model the loss of support is assuming a flat slab condition and in the areas experiencing loss of support under concrete slabs, the base layer under the pavement is replaced by a weak material with an elastic modulus of 1 psi (6.89 kPa) and a Poisson's ratio of 0.35. The base layer in this case is modeled using two different materials, namely original base material and weak material. The weak material extends only under the regions where the concrete slab is not in contact with base material as shown in Figure 37. Since this method resulted in good agreement with measured responses and overcomes the issues associated with first two methods, it was used in this study. In addition, the extent of loss of support was determined experimentally.

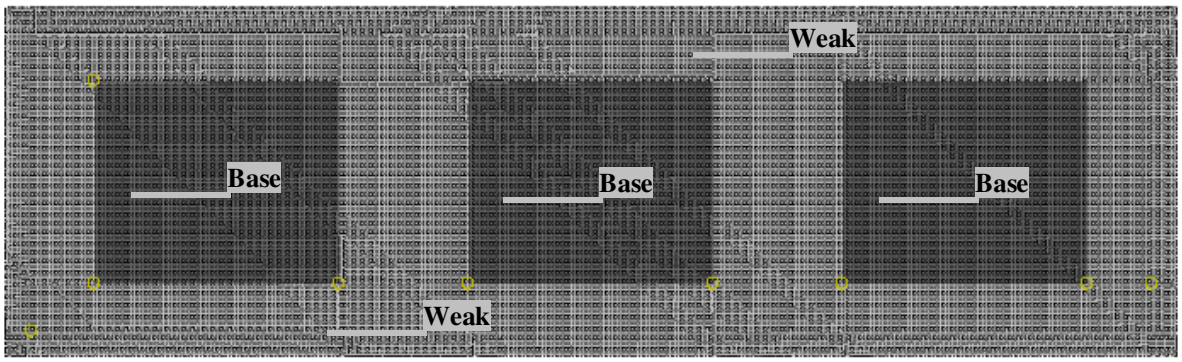

Figure 37. Modeling loss of support as weak material at the top of base layer.

7 Finite Element Model Validation

To obtain realistic responses from the FEM, it must be verified and validated, using deflection and strain data obtained from APLF from three stages of the experiment. First, the model was calibrated to compute deflection and loss of support values in agreement with those measured during the curing period, by running the model with different material properties and boundary conditions until agreement was reached. Then the data from the controlled temperature stage (Stage II) and from the combined temperature and wheel load (Stage III) were used to validate the model.

7.1 Validation under Controlled Temperature Cycles

After the period of curing, a period of controlled temperature changes was applied from the fifth week to the eighth week. During this period, the air temperature was raised from 68°F (20°C) to 97°F (35°C) for one week starting after the pavement cured for 838 hours, decreased within 2 days back to 72°F (22°C) for 3 days, decreased further to 41°F (5°C) for 3 days, and eventually returned to 70°F (21°C) and held constant to the end of the experiment. The maximum temperature gradient along the slab depth occurred within a few hours after the air temperature was changed. In order to simplify the validation process, the corner deflections were predicted at seven key points in time representing the inflections in the temperature time series shown in Figure 38.

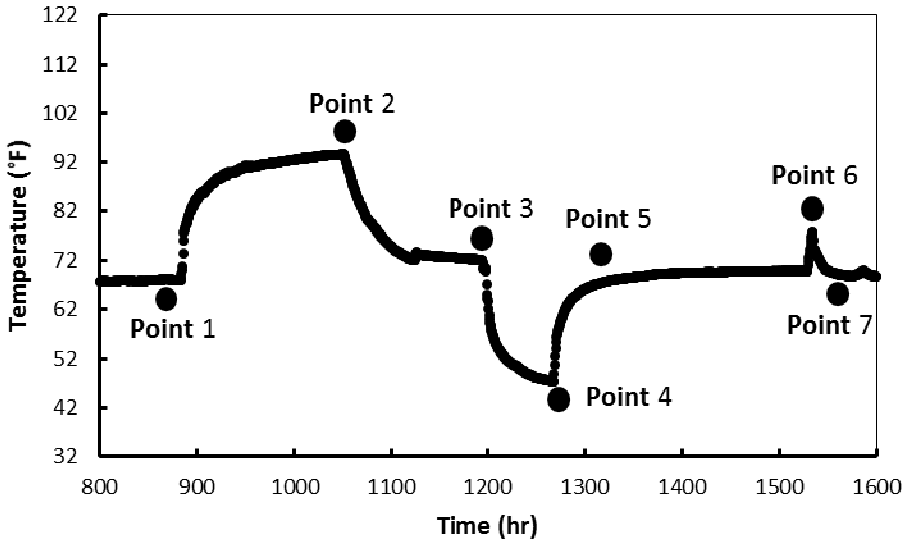

Figure 38. Slab center temperature in APLF during Stage II with selected key points (T(°C) = (T(°F)-32)5/9).

The measured corner deflection during Stage II, shown earlier in Figure 17, compared to Figure 19 implies although the temperature differences at the beginning and end of Stage II are close, the deflection at the corners is significantly different. This discrepancy is due to a combination of two influences. On one hand, there is an ongoing moisture loss through the top pavement surface during Stage II causing an additional rise of the corners. On the other hand, the computed deflection is based on the boundary conditions in terms of aggregate interlock in the transverse joints. The higher the absolute temperature of the pavement, the more aggregate interlock occurs, and the more the slab warping is restrained. When comparing the predicted

corner deflections to the measured values, the relative differences in temperature and deflection should be considered instead of absolute initial and final temperature values. Therefore, the temperature gradient of Point 1 was applied in the FEM as the initial temperature state and Point 2 was applied as final temperature state. Similarly, when moving the next point, Point 2 was applied as the initial temperature state and Point 3 as the final state and so on. This approach simulates the actual change in temperature differences the pavement experienced. The actual temperature differences as well as average actual and relative corner deflections measured from LVDTs 1, 2, 5, 6, 7, 8 and the average predicted corner deflections from ABAQUS are listed in Table 6. The relative measured and predicted corner deflections are also shown in Figure 39.

Table 6. Temperature differences with measured and predicted relative corner deflections at key points during experiment.

Point	Time	Temp. Diff. through slab		Corner deflection					
				Absolute Measured		Relative Measured		Relative Predicted	
	(hr)	(C°)	(F°)	(mil)	(mm)	(mil)	(mm)	(mil)	(mm)
1	870	0.31	0.56	51.83	1.316	0	0	0	0
2	888	5.13	9.23	24.23	0.615	-27.6	-0.701	-27.91	-0.709
3	1193	-0.4	-0.72	92.46	2.348	68.23	1.733	33	0.838
4	1205	-6.3	-11.27	126.6	3.216	34.14	0.867	35.53	0.902
5	1270	0.47	0.85	105.89	2.690	-20.71	-0.526	-35.46	-0.901
6	1534	3.92	7.06	77.54	1.970	-28.35	-0.720	-21.24	-0.539
7	1558	-0.3	-0.52	105.02	2.668	27.47	0.698	21.34	0.542

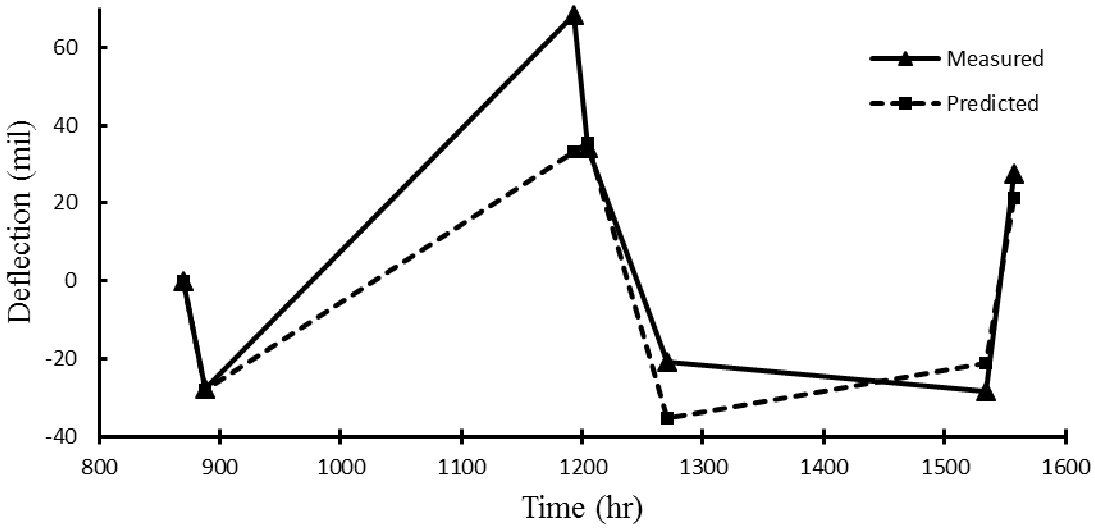

Figure 39. Predicted and measured average corner deflection versus test time. (1 mil =0.0254 mm)

In general, the finite element modeling using the loss of support areas described earlier showed good agreement with the measured deflections. The differences between measured and predicted values can be justified by the combination of two factors. First, as mentioned earlier, there is an ongoing warping process during Stage II, which caused an additional rise in corner deflection as clearly shown in the values measured at Point 3. Second, the loss of support defined in Figure 37 was used in all the seven points. However, when the slab was subjected to a

positive TG, the pavement experienced a smaller loss of support. This is clearly shown in the disagreement of deflection at Point 5.

A similar approach was used to validate the FEM against measured strain. However, in this case, slab temperature measured by Vibrating Wire (VW) strain gauges was used instead of the temperature measured by thermocouples because of the difference in recording times. Although the loss of support was derived from measuring corner deflections, it is still appropriate to use the same loss of support area for strain validation. For the purpose of strain validation, the comparisons were made at seven key points as shown in Figure 40. Also, the total temperature of slab at the key points was applied since top and bottom strain values in the slab are to be compared. Better agreement between the measured and predicted strains was obtained following this approach. The top and bottom temperatures were determined by averaging the temperature data obtained from all strain gauges embedded in the side slabs. The relative measured and predicted top and bottom strain values at the slab center (average of Location 1 and Location 4) and the slab third point (average of Location 2 and Location 3) are shown in Table 7. The calculated and measured strains are in fairly good agreement in terms of value and general trends. The small discrepancies may be attributed to the ongoing moisture loss and the difference between the estimated and actual amount of loss of support.

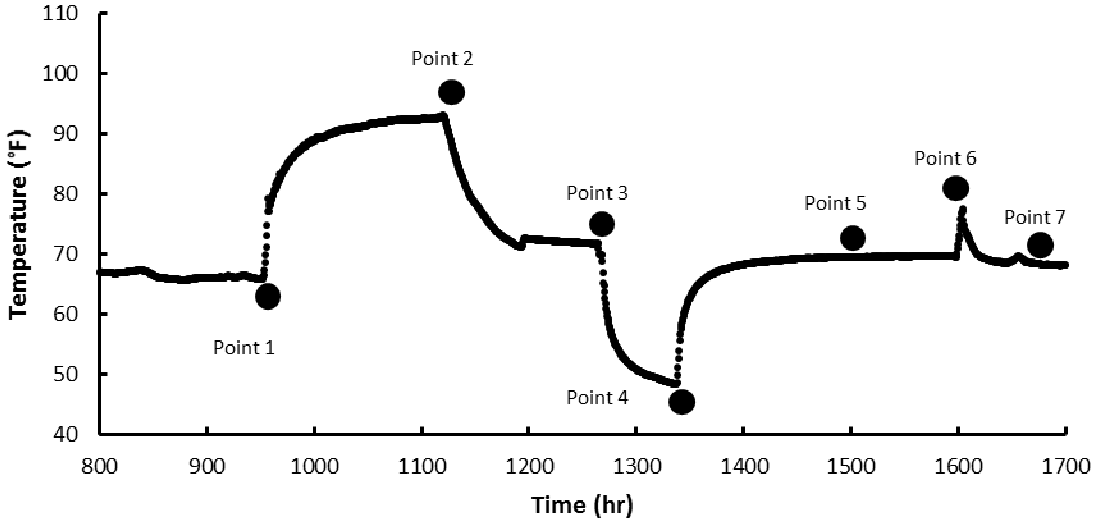

Figure 40. Slab temperature on the top of slab center (VW1) with the selected key points in the strain validation (T(°C) = (T(°F)-32)5/9).

Table 7. The relative measured and predicted top and bottom strain values at the slab center (average of location # 1 and 4) and the slab third point (average of location # 2 and 3).

								Relative Measured Strain				Relative FEM Strain			
Point	Time	Temperature at top of slab		Temperature at bottom of slab		ΔT		VW1&4		VW2&3		VW1&4		VW2&3	
								top	bottom	top	bottom	top	bottom	top	bottom
	(hr)	(°F)	(°C)	(°F)	(°C)	(F°)	(C°)	(με)	(με)	(με)	(με)	(με)	(με)	(με)	(με)
1	935	67.52	19.73	67.22	19.57	0.31	0.17	0	0	0	0	0	0	0	0
2	1125	76.72	24.84	68.51	20.28	8.21	4.56	108.82	85.78	87.53	93.05	115.07	109.43	106.23	100.35
3	1262	73.03	22.79	74.23	23.46	-1.2	-0.67	-99.25	-62.16	-109.9	-55.15	-86.83	-85.62	-80.43	-78.31
4	1337	57.54	14.19	66.93	19.41	-9.4	-5.22	-113.6	-82.16	-130.6	-77.29	-111.2	-106	-103.5	-96.6
5	1575	67.68	19.82	66.27	19.04	1.4	0.78	102.02	71.45	101.47	70.36	100.85	89.3	94.24	80.89
6	1605	71.32	21.84	69.03	20.57	2.29	1.27	29.95	16.2	36.22	10.89	22.84	15.26	21.82	13.35
7	1700	68.36	20.20	68.2	20.11	0.17	0.09	-37.08	-19.31	-45.21	-12.94	-25.87	-22.88	-24.75	-20.25

7.1.1 Deflection and Strain Validation under Combined Temperature and Load application

In Stage III of the APLF experiment, the test pavement was subjected to a temperature gradient and a rolling wheel load. The pavement response was measured by the strain gauges (both rosettes and VW gauges) and the LVDTs. A set of representative cases of combined temperature and wheel load were selected for simulation. Figure 41 shows an overhead view of the test section indicating the location of relevant sensors and the paths (numbered 1-5) along which the live load could be applied. Two of the paths were used for the validation of deflection; Path 1 (P1), which ran along the pavement edge and over LVDT2, LVDT4, and LVDT5; and Path 2 (P2) located 30 in (0.76 m) towards the center and representing a typical location for a truck load to be applied. The applied load on Path 1 was always 12,000 lb (53 kN), while on Path 2 the load was always 15,000 lb (67 kN), and both loads were applied with the wheel rolling at the slow speed of 5 mph (8 km/h). Deflection data used in the validation were collected on Path 1 and Path 2 during each of four temperature cases: Case 1, air temperature raised from 70°F (21°C) to 100°F (38°C) with the run occurring at a time when the temperature difference ΔT between top and bottom of the slab was 9.43 F° (5.24 C°), Case 2, air temperature raised held at 100°F (38°C) with the run occurring at a time when the temperature difference ΔT between top and bottom of the slab was 5.40 F° (3.00 C°), Case 3, air temperature reduced from 70°F (21°C) to 40°F (4.4°C) with the run occurring at a time when the temperature difference ΔT between top and bottom of the slab was -8.90 F° (-4.94 C°) (i.e. the top was colder than the bottom), and Case 4, air temperature held at 40°F (4.4°C) with the run occurring at a time when the temperature difference ΔT between top and bottom of the slab was -5.05 F° (-2.81 C°). Since the expected deflection is downward, a positive value means downward deflection, while a negative value means upward deflection. No Dipstick data were available to determine the actual loss of support, so a reasonable estimated loss of support (LOS) had to be assumed. Since the tire speed was very low (5 mph = 8 km/h), the situation was treated as if the load was static for estimating the LOS. The simulation results agreed well with measured deflections for both paths on the four cases. The peaks where the tire was directly above the LVDTs were predicted by FEM. The discrepancies can be attributed to the non-uniformity in the materials, construction,

corner lift, and uncertainties in estimating the loss of support. The results, temperature cases, and load cases are presented in Table 8 (Table 9) and Table 10 (Table 11) in English (metric) units.

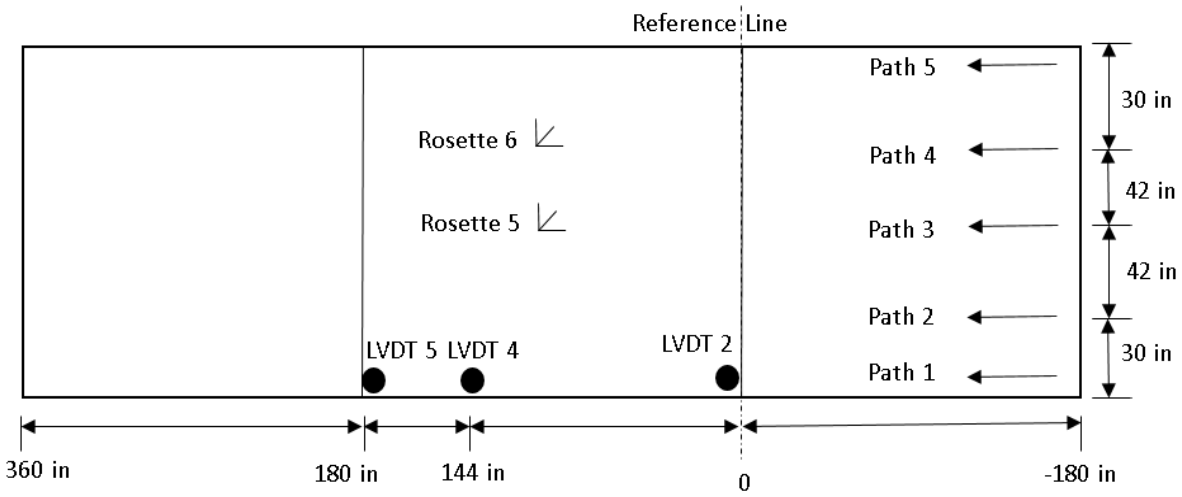

Figure 41. Load paths and sensor locations used for validation (1 in = 25 mm).

Table 8. Measured and predicted deflections under combined temperature and wheel loads for Case1 and Case 2 (English units).

CASE	PATH	Load	Loss of Support		Air Temp.	ΔT	LVDT2			LVDT4			LVDT5		
			long.	trans.			dist.	meas.	FEM	dist.	meas.	FEM	dist.	meas.	FEM
		(lb)	(ft)	(ft)	(°F)	(F°)	(in)	(mil)	(mil)	(in)	(mil)	(mil)	(in)	(mil)	(mil)
CASE 1	P1	12000	2.0	1.5	70-100	9.43	-90	19.60	22.10	0	9.80	16.10	0	7.38	24.31
							-45	35.30	31.20	45	16.70	20.30	45	16.21	25.55
							0	45.80	49.70	90	27.70	28.10	90	30.81	29.33
							45	44.30	34.00	144	45.00	50.80	144	51.20	47.08
							90	33.10	23.50	180	49.00	44.20	180	51.54	59.83
							144	20.20	23.60	225	41.70	34.00	225	48.19	41.61
							180	11.60	22.70	270	28.80	29.50	270	37.33	32.38
	P2	15000	2.0	1.5	70-100	9.43	-90	23.71	21.91	0	9.90	15.87	0	10.15	24.15
							-45	34.95	31.30	45	15.32	20.05	45	20.49	25.29
							0	43.02	49.58	90	22.67	27.56	90	35.76	29.12
							45	40.03	34.07	144	35.46	37.74	144	50.41	42.78
							90	35.36	23.39	180	37.92	32.97	180	51.31	55.35
							144	24.75	19.09	225	34.49	22.55	225	43.09	37.51
							180	14.98	18.25	270	26.50	17.61	270	40.85	27.95
CASE 2	P1	12000	2.0	1.5	100	5.40	-90	7.82	13.57	0	4.29	11.89	0	3.14	15.88
							-45	24.41	22.67	45	9.16	15.73	45	9.86	17.20
							0	35.71	41.10	90	16.22	23.21	90	20.08	20.99
							45	35.60	25.48	144	30.62	34.78	144	37.85	34.46
							90	25.26	15.06	180	34.76	28.79	180	42.07	47.16
							144	19.50	10.81	225	29.47	18.22	225	37.59	28.97
							180	12.05	9.83	270	21.58	13.43	270	29.81	19.68
	P2	15000	2.0	1.5	100	5.40	-90	16.05	13.38	0	7.61	11.43	0	7.27	15.71
							-45	24.47	22.83	45	13.14	15.45	45	16.25	16.95
							0	34.46	40.96	90	19.17	22.96	90	27.10	20.84
							45	31.40	25.32	144	30.95	33.02	144	39.30	34.50
							90	25.35	14.81	180	33.13	28.21	180	40.95	46.68
							144	17.54	10.56	225	27.46	17.95	225	34.40	28.84
							180	11.59	9.68	270	19.46	13.11	270	29.68	19.36

Table 9. Measured and predicted deflections under combined temperature and wheel loads for Case1 and Case 2 (metric units).

CASE	PATH	Load	Loss of Support		Air Temp.	ΔT	LVDT2			LVDT4			LVDT5		
			long.	trans.			dist.	meas.	FEM	dist.	meas.	FEM	dist.	meas.	FEM
		(kN)	(m)	(m)	(°C)	(C°)	(m)	(mm)	(mm)	(m)	(mm)	(mm)	(m)	(mm)	(mm)
CASE 1	P1	53.4	0.61	0.46	21-38	5.24	-2.29	0.4978	0.5613	0.00	0.2489	0.4089	0.00	0.1875	0.6175
							-1.14	0.8966	0.7925	1.14	0.4242	0.5156	1.14	0.4117	0.6490
							0.00	1.1633	1.2624	2.29	0.7036	0.7137	2.29	0.7826	0.7450
							1.14	1.1252	0.8636	3.66	1.1430	1.2903	3.66	1.3005	1.1958
							2.29	0.8407	0.5969	4.57	1.2446	1.1227	4.57	1.3091	1.5197
							3.66	0.5131	0.5994	5.72	1.0592	0.8636	5.72	1.2240	1.0569
							4.57	0.2946	0.5766	6.86	0.7315	0.7493	6.86	0.9482	0.8225
	P2	66.7	0.61	0.46	21-38	5.24	-2.29	0.6022	0.5565	0.00	0.2515	0.4031	0.00	0.2578	0.6134
							-1.14	0.8877	0.7950	1.14	0.3891	0.5093	1.14	0.5204	0.6424
							0.00	1.0927	1.2593	2.29	0.5758	0.7000	2.29	0.9083	0.7396
							1.14	1.0168	0.8654	3.66	0.9007	0.9586	3.66	1.2804	1.0866
							2.29	0.8981	0.5941	4.57	0.9632	0.8374	4.57	1.3033	1.4059
							3.66	0.6287	0.4849	5.72	0.8760	0.5728	5.72	1.0945	0.9528
							4.57	0.3805	0.4636	6.86	0.6731	0.4473	6.86	1.0376	0.7099
CASE 2	P1	53.4	0.61	0.46	38	3.00	-2.29	0.1986	0.3447	0.00	0.1090	0.3020	0.00	0.0798	0.4034
							-1.14	0.6200	0.5758	1.14	0.2327	0.3995	1.14	0.2504	0.4369
							0.00	0.9070	1.0439	2.29	0.4120	0.5895	2.29	0.5100	0.5331
							1.14	0.9042	0.6472	3.66	0.7777	0.8834	3.66	0.9614	0.8753
							2.29	0.6416	0.3825	4.57	0.8829	0.7313	4.57	1.0686	1.1979
							3.66	0.4953	0.2746	5.72	0.7485	0.4628	5.72	0.9548	0.7358
							4.57	0.3061	0.2497	6.86	0.5481	0.3411	6.86	0.7572	0.4999
	P2	66.7	0.61	0.46	38	3.00	-2.29	0.4077	0.3399	0.00	0.1933	0.2903	0.00	0.1847	0.3990
							-1.14	0.6215	0.5799	1.14	0.3338	0.3924	1.14	0.4128	0.4305
							0.00	0.8753	1.0404	2.29	0.4869	0.5832	2.29	0.6883	0.5293
							1.14	0.7976	0.6431	3.66	0.7861	0.8387	3.66	0.9982	0.8763
							2.29	0.6439	0.3762	4.57	0.8415	0.7165	4.57	1.0401	1.1857
							3.66	0.4455	0.2682	5.72	0.6975	0.4559	5.72	0.8738	0.7325
							4.57	0.2944	0.2459	6.86	0.4943	0.3330	6.86	0.7539	0.4917

Table 10. Measured and predicted deflections under combined temperature and wheel loads for Case3 and Case 4 (English units).

CASE	PATH	Load	Loss of Support		Air Temp.	ΔT	LVDT2			LVDT4			LVDT5		
			long.	trans.			dist.	meas.	FEM	dist.	meas.	FEM	dist.	meas.	FEM
		(lb)	(ft)	(ft)	(°F)	(F°)	(in)	(mil)	(mil)	(in)	(mil)	(mil)	(in)	(mil)	(mil)
CASE 3	P 1	12000	2.7	2.2	70-40	-8.90	-90	-5.63	-9.70	0	-1.83	-7.26	0	-11.45	-16.72
							-45	1.94	1.56	45	1.34	-2.52	45	-8.61	-14.34
							0	19.10	20.22	90	8.50	5.98	90	-4.00	-8.96
							45	4.79	3.19	144	18.19	18.32	144	7.83	6.35
							90	-4.08	-9.03	180	19.03	12.40	180	18.10	20.13
							144	-9.73	-15.15	225	8.01	1.77	225	0.44	1.96
							180	-11.43	-16.99	270	-6.74	-4.22	270	-6.88	-9.36
	P2	15000	2.7	2.2	70-40	-8.90	-90	-6.61	-10.09	0	3.12	-7.60	0	-7.36	-17.02
							-45	-4.24	1.54	45	7.46	-2.62	45	-3.22	-14.68
							0	18.09	19.81	90	10.64	5.94	90	4.21	-9.14
							45	5.27	2.80	144	15.56	16.73	144	16.86	6.35
							90	-2.27	-9.54	180	14.45	11.95	180	22.96	19.59
							144	-11.88	-15.74	225	3.64	1.65	225	0.41	1.80
							180	-16.42	-17.50	270	1.08	-4.35	270	-7.33	-9.71
CASE 4	P 1	12000	2.7	2.2	40	-5.05	-90	-2.29	-0.35	0	3.22	-0.88	0	0.15	-5.22
							-45	2.21	8.86	45	6.63	3.11	45	2.40	-3.53
							0	23.84	27.02	90	13.52	10.74	90	7.48	0.65
							45	11.99	11.31	144	19.27	22.32	144	18.55	14.25
							90	5.85	0.75	180	19.82	16.46	180	22.51	26.96
							144	2.92	-3.97	225	9.36	5.94	225	11.39	9.14
							180	1.24	-5.26	270	1.51	1.08	270	3.91	-0.22
	P2	15000	2.7	2.2	40	-5.05	-90	-1.67	-0.72	0	1.31	-1.04	0	-0.83	-5.54
							-45	2.19	8.87	45	5.87	3.32	45	1.04	-3.91
							0	22.26	26.70	90	11.96	11.19	90	5.65	0.40
							45	17.29	10.96	144	18.18	20.76	144	16.68	14.19
							90	9.05	0.29	180	18.91	15.41	180	23.78	26.40
							144	2.95	-4.48	225	2.82	5.61	225	4.58	8.98
							180	1.13	-5.67	270	0.19	0.93	270	1.57	-0.60

Table 11. Measured and predicted deflections under combined temperature and wheel loads for Case 3 and Case 4 (metric units).

CASE	PATH	Load	Loss of Support		Air Temp.	ΔT	LVDT2			LVDT4			LVDT5		
			long.	trans.			dist.	meas.	FEM	dist.	meas.	FEM	dist.	meas.	FEM
		(kN)	(m)	(m)	(°C)	(C°)	(m)	(mm)	(mm)	(m)	(mm)	(mm)	(m)	(mm)	(mm)
CASE 3	P 1	53.4	0.82	0.67	21-4.4	-4.94	-2.29	-0.1430	-0.2464	0.00	-0.0465	-0.1844	0.00	-0.2908	-0.4247
							-1.14	0.0493	0.0396	1.14	0.0340	-0.0640	1.14	-0.2187	-0.3642
							0.00	0.4851	0.5136	2.29	0.2159	0.1519	2.29	-0.1016	-0.2276
							1.14	0.1217	0.0810	3.66	0.4620	0.4653	3.66	0.1989	0.1613
							2.29	-0.1036	-0.2294	4.57	0.4834	0.3150	4.57	0.4597	0.5113
							3.66	-0.2471	-0.3848	5.72	0.2035	0.0450	5.72	0.0112	0.0498
							4.57	-0.2903	-0.4315	6.86	-0.1712	-0.1072	6.86	-0.1748	-0.2377
	P2	66.7	0.82	0.67	21-4.4	-4.94	-2.29	-0.1679	-0.2563	0.00	0.0792	-0.1930	0.00	-0.1869	-0.4323
							-1.14	-0.1077	0.0391	1.14	0.1895	-0.0665	1.14	-0.0818	-0.3729
							0.00	0.4595	0.5032	2.29	0.2703	0.1509	2.29	0.1069	-0.2322
							1.14	0.1339	0.0711	3.66	0.3952	0.4249	3.66	0.4282	0.1613
							2.29	-0.0577	-0.2423	4.57	0.3670	0.3035	4.57	0.5832	0.4976
							3.66	-0.3018	-0.3998	5.72	0.0925	0.0419	5.72	0.0104	0.0457
							4.57	-0.4171	-0.4445	6.86	0.0274	-0.1105	6.86	-0.1862	-0.2466
CASE 4	P 1	53.4	0.82	0.67	4.4	-2.81	-2.29	-0.0582	-0.0089	0.00	0.0818	-0.0224	0.00	0.0038	-0.1326
							-1.14	0.0561	0.2250	1.14	0.1684	0.0790	1.14	0.0610	-0.0897
							0.00	0.6055	0.6863	2.29	0.3434	0.2728	2.29	0.1900	0.0165
							1.14	0.3045	0.2873	3.66	0.4895	0.5669	3.66	0.4712	0.3620
							2.29	0.1486	0.0191	4.57	0.5034	0.4181	4.57	0.5718	0.6848
							3.66	0.0742	-0.1008	5.72	0.2377	0.1509	5.72	0.2893	0.2322
							4.57	0.0315	-0.1336	6.86	0.0384	0.0274	6.86	0.0993	-0.0056
	P2	66.7	0.82	0.67	4.4	-2.81	-2.29	-0.0424	-0.0183	0.00	0.0333	-0.0264	0.00	-0.0211	-0.1407
							-1.14	0.0556	0.2253	1.14	0.1491	0.0843	1.14	0.0264	-0.0993
							0.00	0.5654	0.6782	2.29	0.3038	0.2842	2.29	0.1435	0.0102
							1.14	0.4392	0.2784	3.66	0.4618	0.5273	3.66	0.4237	0.3604
							2.29	0.2299	0.0074	4.57	0.4803	0.3914	4.57	0.6040	0.6706
							3.66	0.0749	-0.1138	5.72	0.0716	0.1425	5.72	0.1163	0.2281
							4.57	0.0287	-0.1440	6.86	0.0048	0.0236	6.86	0.0399	-0.0152

The experimental instrumentation to measure the strain due to a moving load on a curled slab included three rosette locations. For strain validation of combined temperature and wheel load, data collected from rosettes in Location six (Rosette 6) were used when a wheel load travelled Path 4 shown in Figure 41. Temperature Case 1, with loads of 9 kip (40 kN) and 12 kip (53 kN), and Temperature Case 2 with loads of 12 kip (53 kN) and 15 kip (67 kN) were employed. The temperature gradients and loss of support used were the same as for Case 1 and Case 2 in Table 8. The computed longitudinal and transverse strains at the top and bottom were compared to the values measured by the top and bottom rosettes at Location 6. The measured

strains show the strain reversals increased as the temperature dropped, while the peak strain value was not affected by the temperature variations. Thus when the tire is directly on the rosette gauge, the slab is in full contact with the base at that location. The validation results are presented in Figure 42 to Figure 45; a positive strain value indicates tension.

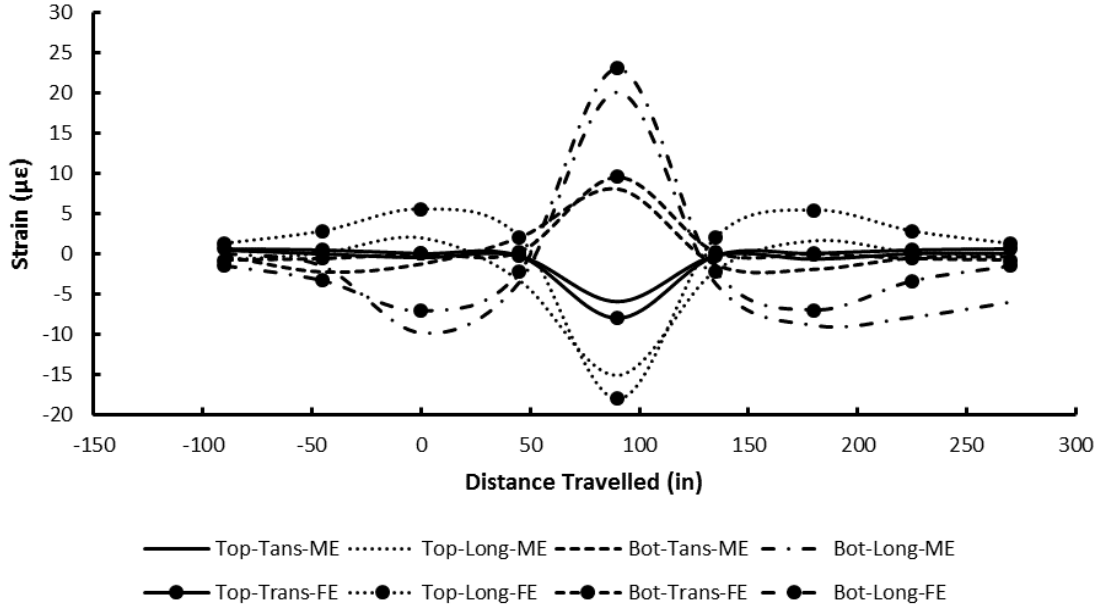

Figure 42. Longitudinal and transverse predicted and measured strain for Case 1 at top and bottom of slab along wheel path 4 at a load of 9000 lb (40 kN) (1 in = 25 mm). FE = Finite element model (FEM), ME = measured by strain gauges.

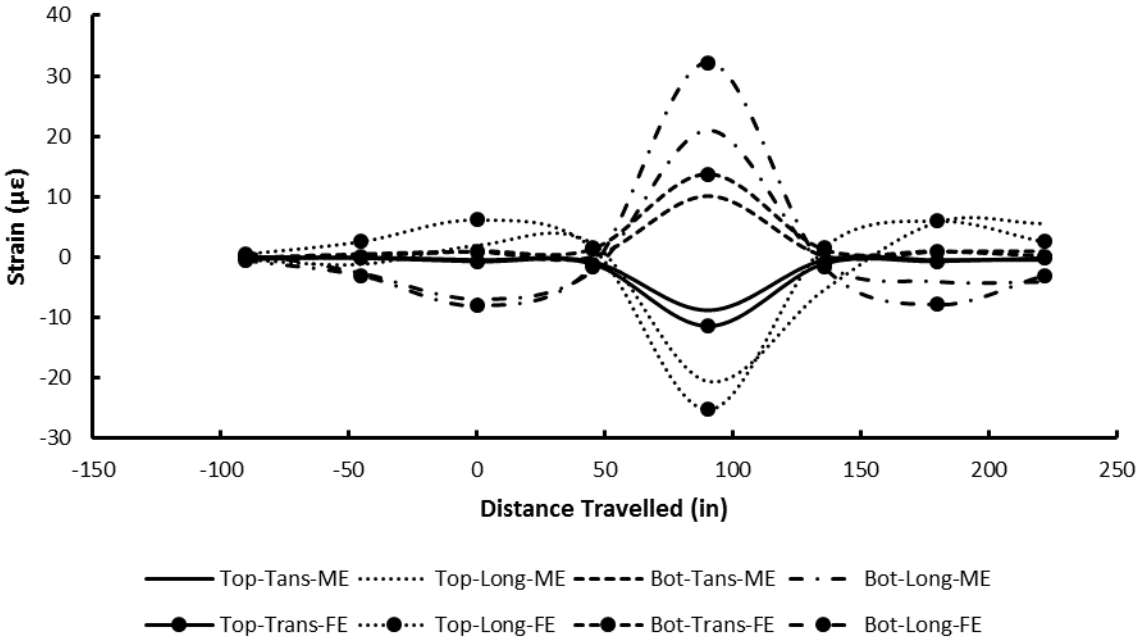

Figure 43. Longitudinal and transverse predicted and measured strain for Case 1 at top and bottom of slab along wheel path 4 at a load of 12000 lb (53 kN) (1 in = 25 mm). FE = Finite element model (FEM), ME = measured by strain gauges.

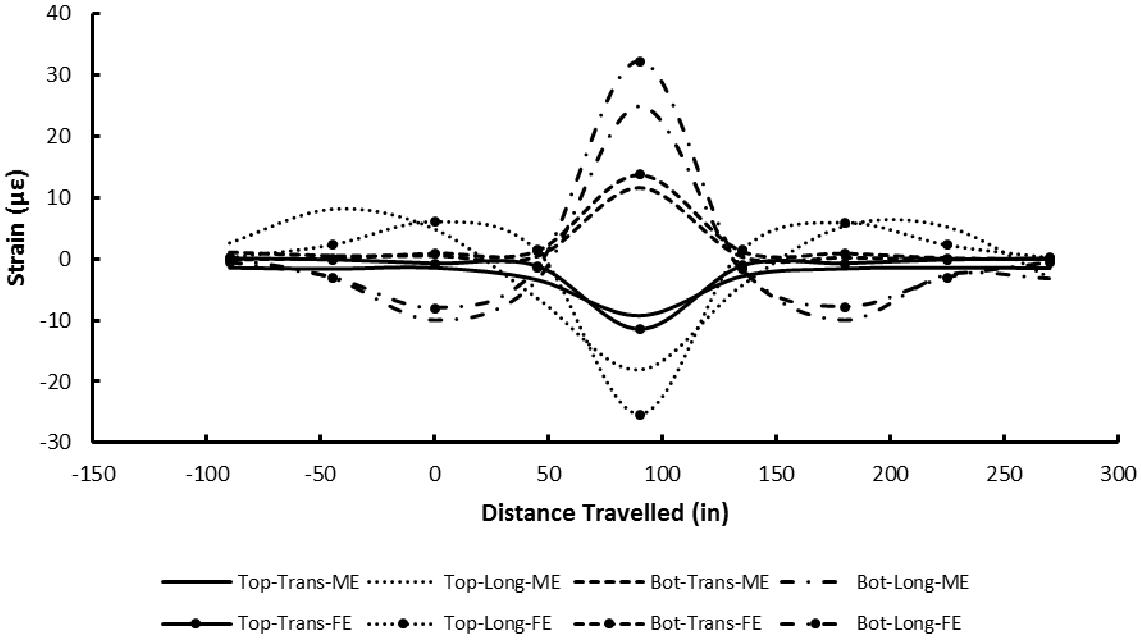

Figure 44. Longitudinal and transverse predicted and measured strain for Case 2 at top and bottom of slab along wheel path 4 at a load of 12000 lb (53 kN) (1 in = 25 mm). FE = Finite element model (FEM), ME = measured by strain gauges.

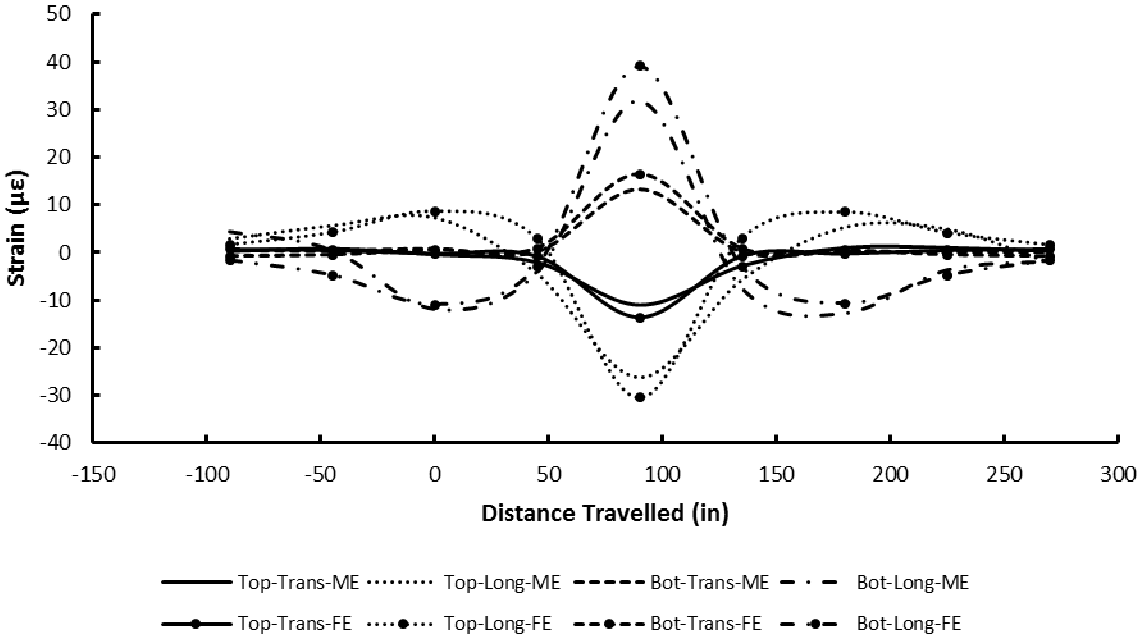

Figure 45. Longitudinal and transverse predicted and measured strains for Case 2 at top and bottom of slab along wheel path 4 at a load of 15000 lb (67 kN) (1 in = 25 mm). FE = Finite element model (FEM), ME = measured by strain gauges.

The predicted peak strains in the longitudinal and transverse directions were always higher than the measured strain, due to the inaccuracy in estimating the loss of support (LOS) in

the model. Moreover, the rosette measured the strain 1 in (25 mm) below the top and 1 in (25 mm) above the bottom of the slab, while the FEM reported the strain at the top and bottom surfaces of the slab, i.e. at points 1 in (25 mm) higher and 1 in (25 mm) lower than the rosette elevations. However, the model with the LOS as described above showed the same general trends as the empirical data. A proper selection of LOS will improve the predictions of deflections and strains due to combined temperature and wheel loads.

7.2 Finite Element Model Validation for Route 23 Concrete Sections

As another method of validating the finite element model (FEM) of concrete pavement developed in this study, performance data from concrete sections of the SHRP Test Road on US Route 23 in Delaware County (3902XX section numbers) were selected to compare to FEM outputs. Performance data for 19 concrete sections including number of cracks observed in each section (as reported in the LTPP database) are available as well as the failure (terminal PSI $\leq$ 2.5) predicted by AASHTO 1993 Design Guide [AASHTO, 1993], both shown in Table 12. The sections are ranked from 1 to 19, with 1 being most severely cracked and 19 the least cracked. The validation of the model would be assessed by the ability of finite element model to reproduce the ranking.

FEMs were developed for each of the 19 sections using ABAQUS 6.14, and the model analyzed for performance under environmental and truck loads. Each model included three concrete slabs in length and the width included two lanes and AC shoulders. The transverse joints were connected by 18 in (457 mm) dowel bars spaced at 12 in (305 mm), while the longitudinal joints were tied with 30 in (762 mm) #5 tie bars spaced at 30 in (760 mm). 5 ft (1.5 m) and 10 ft (3.0 m) asphalt shoulders were also modeled at the left and right of each pavement section. The model and details of dowel and tie bars are as shown in Figure 46 and Figure 47. Measured actual material properties were used to characterize all pavement layers [Masada and Sargand, 2002]. The pavement structure for each section are listed in Table 13 and the material properties are in Table 14 and Table 15.

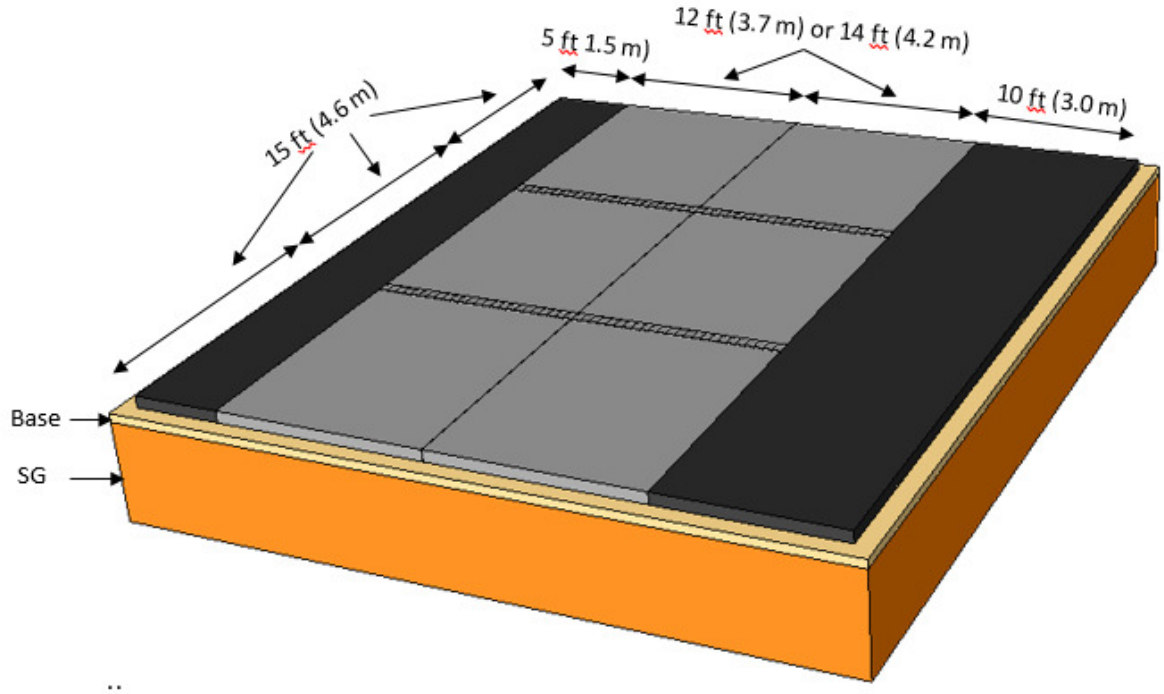

Figure 46. Finite element model geometry used to simulate PCC sections on DEL-23.

Table 12. Dimensions and rank data for Route 23 Sections.

Section	Slab thickness (in)	Slab thickness (mm)	Dowel diameter (in)	Dowel diameter (mm)	Slab length (ft)	Slab length (m)	Slab width (ft)	Slab width (m)	Base type	AASHTO 1993 predicted rank	Crack count 2005	Crack rank	Begin Station	End Station
390201	8	203	1.25	32	15	4.6	12	3.7	DGAB	1	48	5	342	349
390202	8	203	1.25	32	15	4.6	14	4.3	DGAB	4	94	2	318	325
390203	11	279	1.5	38	15	4.6	14	4.3	DGAB	6	0	13	383	390
390204	11	279	1.5	38	15	4.6	12	3.7	DGAB	9	64	4	274	269
390205	8	203	1.25	32	15	4.6	12	3.7	LCB	2	97	1	335	342
390206	8	203	1.25	32	15	4.6	14	4.3	LCB	5	88	3	325	335
390207	11	279	1.5	38	15	4.6	14	4.3	LCB	7	0	14	390	397
390208	11	279	1.5	38	15	4.6	12	3.7	LCB	10	3	10	397	404
390209	8	203	1.25	32	15	4.6	12	3.7	ATFDB	3	15	9	349	356
390210	8	203	1.25	32	15	4.6	14	4.3	ATFDB	8	36	6	302	309
390211	11	279	1.5	38	15	4.6	14	4.3	ATFDB	11	0	15	369	375
390212	11	279	1.5	38	15	4.6	12	3.7	ATFDB	18	21	8	293	302
390259	11	279	1.5	38	15	4.6	12	3.7	DGAB	17	27	7	256	274
390260	11	279	1.5	38	15	4.6	12	3.7	ATFDB	13	0	16	309	318
390261	11	279	1.5	38	15	4.6	14	4.3	CTFDB	19	0	17	356	365
390262	11	279	1.5	38	15	4.6	12	3.7	CTFDB	14	0	18	404	412
390263	11	279	1.5	38	15	4.6	14	4.3	DGAB	16	0	19	412	421
390264	11	279	1.5	38	15	4.6	12	3.7	DGAB	12	3	11	422	434
390265	11	279	1.5	38	15	4.6	12	3.7	ATFDB	15	3	12	375	383

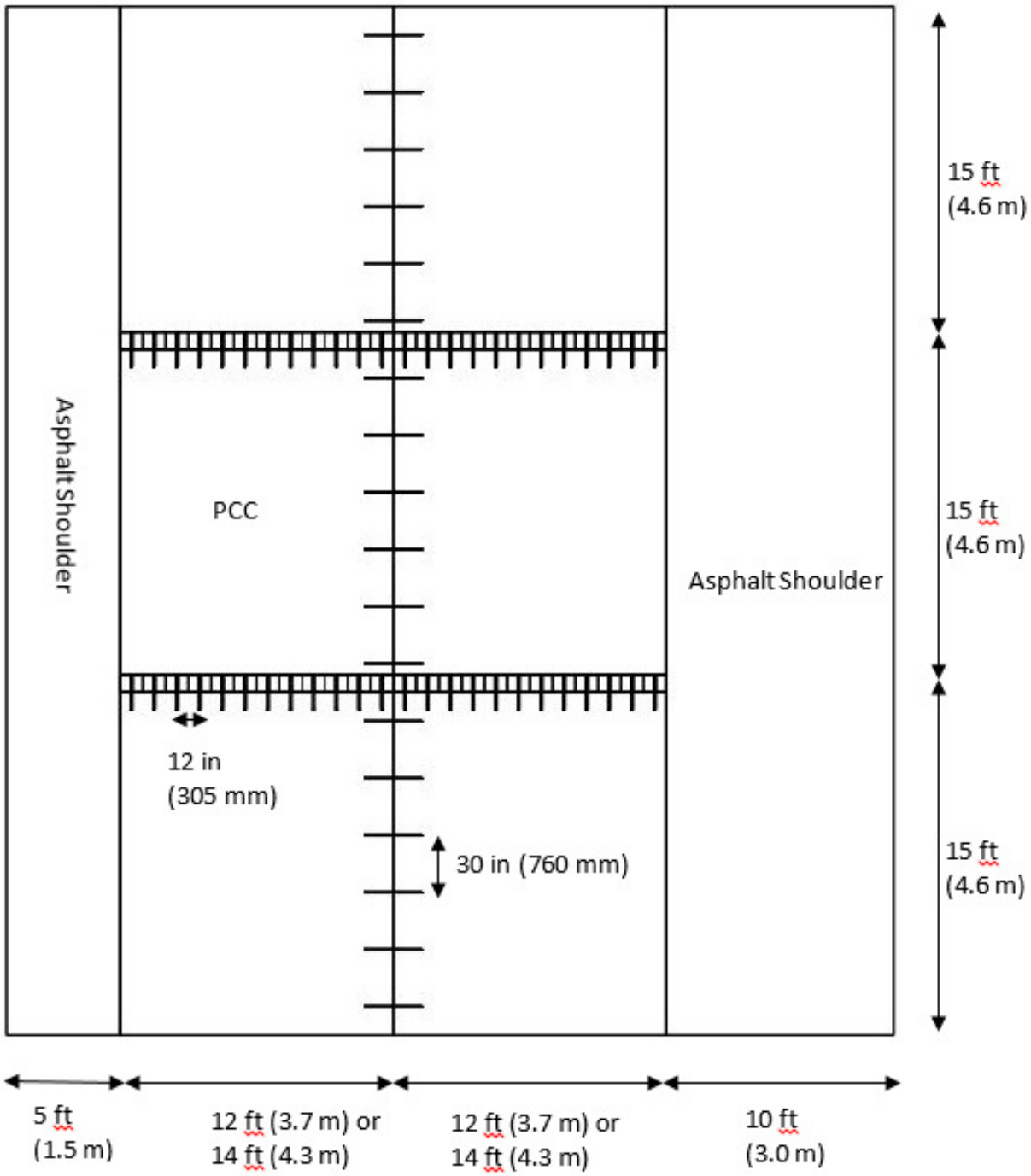

Figure 47. Dowel bar and tie bar configurations used in FEM of DEL-23.

Table 13. Structural build-up of DEL-23 concrete test sections.

									Base type and thickness									
	Slab thickness		Dowel diameter		Slab length		Slab width		ATFDB		CTFDB		LCB		DGAB		Total	
Section	(in)	(mm)	(in)	(mm)	(ft)	(m)	(ft)	(m)	(in)	(mm)	(in)	(mm)	(in)	(mm)	(in)	(mm)	(in)	(mm)
390201	8	203	1.25	32	15	4.6	12	3.7							6	152	6	152
390202	8	203	1.25	32	15	4.6	14	4.3							6	152	6	152
390203	11	279	1.5	38	15	4.6	14	4.3							6	152	6	152
390204	11	279	1.5	38	15	4.6	12	3.7							6	152	6	152
390205	8	203	1.25	32	15	4.6	12	3.7					6	152			6	152
390206	8	203	1.25	32	15	4.6	14	4.3					6	152			6	152
390207	11	279	1.5	38	15	4.6	14	4.3					6	152			6	152
390208	11	279	1.5	38	15	4.6	12	3.7					6	152			6	152
390209	8	203	1.25	32	15	4.6	12	3.7	4	102					4	102	8	203
390210	8	203	1.25	32	15	4.6	14	4.3	4	102					4	102	8	203
390211	11	279	1.5	38	15	4.6	14	4.3	4	102					4	102	8	203
390212	11	279	1.5	38	15	4.6	12	3.7	4	102					4	102	8	203
390259	11	279	1.5	38	15	4.6	12	3.7							6	152	6	152
390260	11	279	1.5	38	15	4.6	12	3.7	4	102					4	102	8	203
390261	11	279	1.5	38	15	4.6	14	4.3			4	102			4	102	8	203
390262	11	279	1.5	38	15	4.6	12	3.7			4	102			4	102	8	203
390263	11	279	1.5	38	15	4.6	14	4.3							6	152	6	152
390264	11	279	1.5	38	15	4.6	12	3.7							6	152	6	152
390265	11	279	1.5	38	15	4.6	12	3.7	4	102					4	102	8	203

Table 14. Material Properties for each concrete section on Route 23 (English units).

Section	Portland Cement Concrete					ATFDB		CTFDB		LCB		DGAB		Subgrade	
	E (psi)	ν	γ (pci)	α °F^{-1}	S_c (psi)	E (psi)	ν	E (psi)	ν	E (psi)	ν	E (psi)	ν	E (psi)	ν
390201	4355934	0.22	0.0825	6.28E-06	549							54100	0.35	9051	0.4
390202	3700000	0.235	0.0805	6.44E-06	705							34400	0.35	17900	0.4
390203	3000000	0.165	0.0822	6.28E-06	580							69600	0.35	14941	0.4
390204	3900000	0.204	0.0822	6.28E-06	578							69600	0.35	29780	0.4
390205	4400000	0.201	0.0833	6.28E-06	544					2904489	0.25			9327	0.4
390206	4700000	0.21	0.0822	6.28E-06	425					2182288	0.25			12736	0.4
390207	2900000	0.179	0.0839	6.28E-06	382					2380000	0.19			17087	0.4
390208	2900000	0.166	0.0822	6.44E-06	377					2680000	0.25			16348	0.4
390209	4300000	0.18	0.0833	6.28E-06	427	630820	0.25					74200	0.35	10386	0.4
390210	5051821	0.18	0.0840	6.44E-06	413	1108457	0.25					48300	0.35	10313	0.4
390211	2500000	0.181	0.0814	6.28E-06	490	676916	0.25					25000	0.35	15854	0.4
390212	4300000	0.291	0.0834	6.44E-06	656	656546	0.25					54144	0.35	20438	0.4
390259	4000000	0.175	0.0819	6.44E-06	459							66369	0.35	11459	0.4
390260	3500000	0.232	0.0833	6.28E-06	467	884131	0.25					60944	0.35	14723	0.4
390261	2600000	0.181	0.0833	6.28E-06	462			1661000	0.271			64616	0.35	18001	0.4
390262	2600000	0.18	0.0822	6.28E-06	475			1661000	0.271			66475	0.35	15637	0.4
390263	2600000	0.133	0.0822	6.28E-06	488							35110	0.35	13592	0.4
390264	3900000	0.169	0.0824	6.28E-06	481							45627	0.35	4975	0.4
390265	4200000	0.29	0.0828	6.28E-06	449	1901532	0.25					43553	0.35	12866	0.4

Table 15. Material Properties for each concrete section on Route 23 (metric units).

Section	Portland Cement Concrete					ATFDB		CTFDB		LCB		DGAB		Subgrade	
	E (MPa)	ν	γ (kg/m^3)	α °C^{-1}	S_c (MPa)	E (MPa)	ν	E (MPa)	ν	E (MPa)	ν	E (MPa)	ν	E (MPa)	ν
390201	30033	0.22	2284	1.13E-05	3.79							373	0.35	62.4	0.4
390202	25511	0.235	2228	1.16E-05	4.86							237	0.35	123.4	0.4
390203	20684	0.165	2275	1.13E-05	4.00							480	0.35	103.0	0.4
390204	26890	0.204	2275	1.13E-05	3.99							480	0.35	205.3	0.4
390205	30337	0.201	2306	1.13E-05	3.75					20026	0.25			64.3	0.4
390206	32405	0.21	2275	1.13E-05	2.93					15046	0.25			87.8	0.4
390207	19995	0.179	2323	1.13E-05	2.63					16410	0.19			117.8	0.4
390208	19995	0.166	2275	1.16E-05	2.60					18478	0.25			112.7	0.4
390209	29647	0.18	2307	1.13E-05	2.94	4349	0.25					512	0.35	71.6	0.4
390210	34831	0.18	2326	1.16E-05	2.85	7643	0.25					333	0.35	71.1	0.4
390211	17237	0.181	2252	1.13E-05	3.38	4667	0.25					172	0.35	109.3	0.4
390212	29647	0.291	2308	1.16E-05	4.52	4527	0.25					373	0.35	140.9	0.4
390259	27579	0.175	2267	1.16E-05	3.16							458	0.35	79.0	0.4
390260	24132	0.232	2307	1.13E-05	3.22	6096	0.25					420	0.35	101.5	0.4
390261	17926	0.181	2307	1.13E-05	3.19			11452	0.271			446	0.35	124.1	0.4
390262	17926	0.18	2275	1.13E-05	3.28			11452	0.271			458	0.35	107.8	0.4
390263	17926	0.133	2275	1.13E-05	3.36							242	0.35	93.7	0.4
390264	26890	0.169	2279	1.13E-05	3.32							315	0.35	34.3	0.4
390265	28958	0.29	2291	1.13E-05	3.10	13111	0.25					300	0.35	88.7	0.4

Each section was subjected to an effective negative temperature gradient of 4.52 F°/in (21.9 C°/m), which is a combination of maximum measured temperature gradient and EBITD, and axle loads at the two ends of the slab (10 kip (44 kN) single and 33 kip (147 kN) dual axle). The maximum tensile stresses at the top and near the center of each slab were determined as shown in Table 3.

Table 16. The stress level at the top center of each section under combined environmental and truck loads (σ_{max}) as well as under environmental load (σ_{Temp}) only.

Section	Slab thickness		Dowel diameter		Slab length		Slab width		Base Type	σ_{max}		σ_{Temp}	
	(in)	(mm)	(in)	(mm)	(ft)	(m)	(ft)	(m)		(psi)	(kPa)	(psi)	(kPa)
390201	8	203	1.25	32	15	4.6	12	3.7	DGAB	357.63	2465.8	176.31	1215.6
390202	8	203	1.25	32	15	4.6	14	4.3	DGAB	364.55	2513.5	208.83	1439.8
390203	11	279	1.5	38	15	4.6	14	4.3	DGAB	274.73	1894.2	151.66	1045.7
390204	11	279	1.5	38	15	4.6	12	3.7	DGAB	249.75	1722.0	117.07	807.2
390205	8	203	1.25	32	15	4.6	12	3.7	LCB	372.53	2568.5	221.16	1524.8
390206	8	203	1.25	32	15	4.6	14	4.3	LCB	390.98	2695.7	232.92	1605.9
390207	11	279	1.5	38	15	4.6	14	4.3	LCB	248.06	1710.3	144.74	997.9
390208	11	279	1.5	38	15	4.6	12	3.7	LCB	296.84	2046.6	176.65	1218.0
390209	8	203	1.25	32	15	4.6	12	3.7	ATFDB	356.22	2456.1	182.66	1259.4
390210	8	203	1.25	32	15	4.6	14	4.3	ATFDB	380.33	2622.3	198.16	1366.3
390211	11	279	1.5	38	15	4.6	14	4.3	ATFDB	261.24	1801.2	148.5	1023.9
390212	11	279	1.5	38	15	4.6	12	3.7	ATFDB	342.21	2359.5	170.38	1174.7
390259	11	279	1.5	38	15	4.6	12	3.7	DGAB	290.97	2006.2	140.77	970.6
390260	11	279	1.5	38	15	4.6	12	3.7	ATFDB	299.19	2062.8	153	1054.9
390261	11	279	1.5	38	15	4.6	14	4.3	CTFDB	273.79	1887.7	159.42	1099.2
390262	11	279	1.5	38	15	4.6	12	3.7	CTFDB	268.63	1852.1	145.25	1001.5
390263	11	279	1.5	38	15	4.6	14	4.3	DGAB	253.16	1745.5	142.07	979.5
390264	11	279	1.5	38	15	4.6	12	3.7	DGAB	246.39	1698.8	114.96	792.6
390265	11	279	1.5	38	15	4.6	12	3.7	ATFDB	310.95	2143.9	152.91	1054.3

The stress levels obtained from the finite element analysis were also ranked from 1 to 19 based on the severity of stresses developed due to combined truck and environmental loads. The results then were compared to performance data to verify if the model developed for each section was able to mimic the ranking of the field measures as shown in Table 17. The AASHTO column represents the order in which the sections were predicted to fail based on the 1993 AASHTO Guide for Design of Pavement Structures. The Crack column represents the order of observed cracking with 1 representing the sections with the most transverse cracking. A Match was designated when the FEM rank was within 1 of either of the other ranks.

Table 17. Maximum FEM stress and failure rank from finite element and performance data.

	FEM Stress		Rank			
Section	(psi)	(kPa)	FEM	AASHTO	Crack	State
390201	357.63	2465.8	5	1	5	Match
390202	364.55	2513.5	4	4	2	Match
390203	274.73	1894.2	12	6	13	Match
390204	249.75	1722.0	17	9	4	
390205	372.53	2568.5	3	2	1	Match
390206	390.98	2695.7	1	5	3	Match
390207	248.06	1710.3	18	7	14	
390208	296.84	2046.6	10	10	10	Match
390209	356.22	2456.1	6	3	9	
390210	380.33	2622.3	2	8	6	
390211	261.24	1801.2	15	11	15	Match
390212	342.21	2359.5	7	18	8	Match
390259	290.97	2006.2	11	17	7	
390260	299.19	2062.8	9	13	16	
390261	273.79	1887.7	13	19	17	
390262	268.63	1852.1	14	14	18	Match
390263	253.16	1745.5	16	16	19	Match
390264	246.39	1698.8	19	12	11	Match
390265	310.95	2143.9	8	15	12	

Table 17 has Match marked for 11 out 19 sections, where the field failure rank was predicted by FEM. This agreement further confirms the validity of the FEM. The non-Match state of the remaining sections may be attributed the quality of material properties used to characterize each section as well as the conditions of the section in the site such drainage and base type.

8 Determining Optimum Thickness and Joint Spacing

Traditionally, joint spacing (or slab length) is a function of the minimum thickness determined to meet specific structural requirements. Such a procedure may result in long slab length, but longer slab lengths have been found to have limited service lives [Darter et al., 1995; Guo et al., 1997; Parsons, 2003; Sargand and Abdalla, 2006] and are subject to greater faulting and more transverse cracking [Smith et al., 1990]. Thicker slabs have been shown to perform better, while the slab width, regardless of the presence of shoulders, has no significant effect on concrete pavement life. Previous studies [including Darter et al., 1995; Guo et al., 1997; Parson et al., 2003] have found joint spacing in rigid pavement has a major effect on slab cracking and faulting. However, there is no standard procedure to determine optimum slab length and thickness together which minimizes the critical stresses induced in the slab under given cycles of environmental and truck loads. The performance of concrete pavement is significantly influenced by several factors such as temperature variations, loss of support, built-in curl, slab length and thickness, base stiffness, truck axle spacing and frequency of load applications, dowel bars, the presence of shoulders, and others. Considering these factors in the analysis of concrete pavements would help determining the critical stress levels the pavement experience during its design life. Therefore, the experimental and field data collected for this study along with the validated finite element model will be employed to determine the critical stresses as functions of both slab thickness and slab length and thereby determine the optimum slab geometry to sustain environmental and truck load applications over a long service life of at least 50 years.

9 Concrete Pavement Stress Analysis

The analysis of concrete pavement critical stresses was conducted on three different slab lengths and thicknesses. The selected slab lengths are 13 ft (4.0 m), 15 ft (4.6 m), and 17 ft (5.2 m), and the selected slab thicknesses are 9 in (229 mm), 12 in (305 mm), and 15 in (381 mm). These geometries were selected because they are frequently used in high volume interstates in the state of Ohio. For each slab length and thickness, three axle spacings and loads were used. Typically, when the axle spacing is similar to slab length, maximum tensile stresses are induced near the center of the slab. However, maximum tensile stresses can also be generated around the center when axle spacing is smaller or larger than the slab length. This can be seen in Figure 48 where different axle spacings were applied to the same slab length. A concrete pavement of 13 ft (4.0 m) long by 12 ft (3.6m) wide by 9 in (229 mm) thick was used to determine the stresses induced by different axle spacings. Since the differences in stress levels are small, it was decided to use axle spacings of 13 ft (4.0 m), 15 ft (4.6 m), and 17 ft (5.2 m), as they are the most frequently observed in the traffic data analyzed for this study.

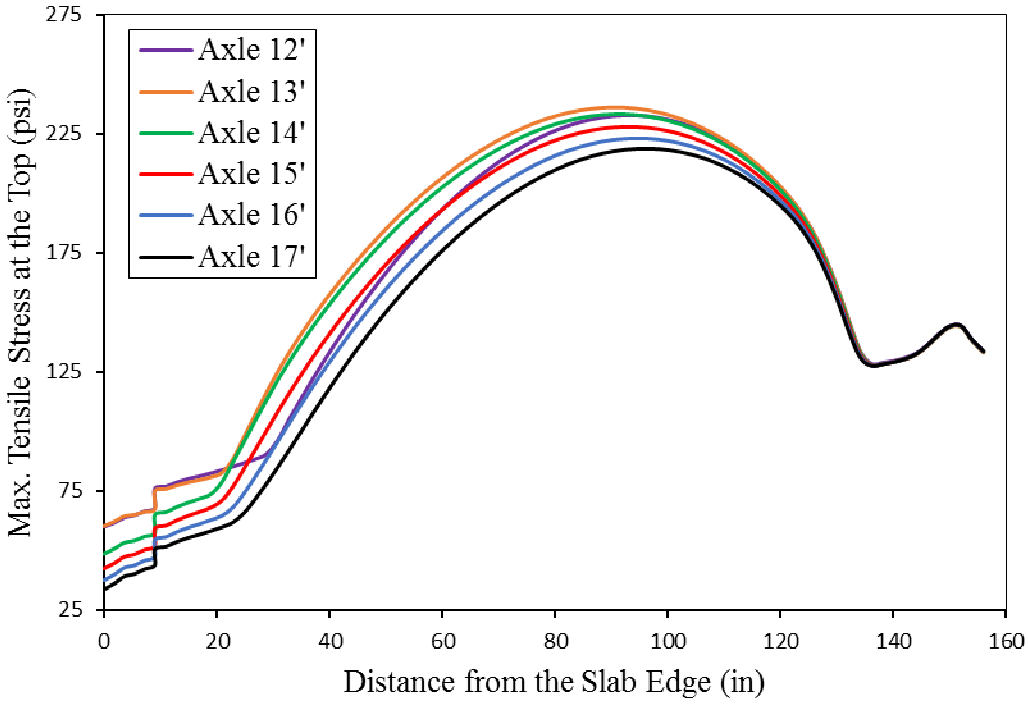

Figure 48. Tensile stresses induced near the center line by loads applied with different axle spacings (1 in = 25.4 mm, 1' = 1 ft = 0.305 m, 1psi = 6.89 kPa).

The first and second axle weights were applied to the middle slab in the FEM on the wheel path using AASHTO LRFD fatigue load configuration shown in Figure 49. A rectangular footprint of 20 in (508 mm) × 10 in (254 mm) was used for the dual tires in the tandem axles (Contact Points B, C, D, E), while a square footprint of 10 in (254 mm) was used for single tires in the steering axle (Contact Point A).

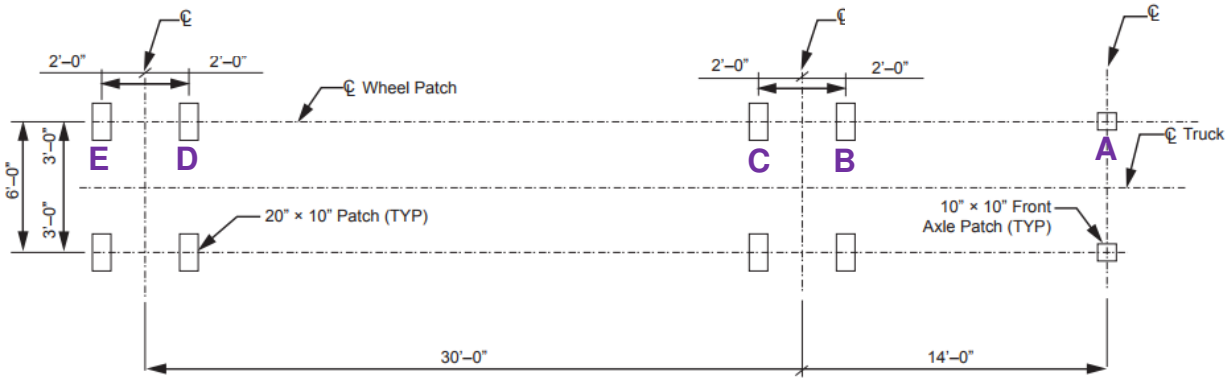

Figure 49. Fatigue load configuration with contact areas of tires at points marked A-E for design truck (1" = 1 in = 0.0254 m, 1' = 1 ft = 0.305 m) [adapted from AASHTO LRFD, 2012]

The temperature data obtained from US Route 23 in Delaware County were also used to account for the actual environmental load concrete pavements experience in Ohio. The recorded maximum negative temperature gradient was -1.29 C°/in (= -0.51 C°/cm = -2.32 F°/in), and the maximum positive temperature gradient was +2.24 C°/in (= +0.88 C°/cm = +4.03 F°/in). The

temperature distribution is also found to be linear in the two sections. Therefore, a linear temperature distribution was assumed. The EBITD was applied to pavement in two ways. The first approach was by assuming there are no residual stresses in the deformed slab shape, and the loss of support was modeled using the weak material method described earlier. In this case, only the maximum temperature gradient obtained from US Route 23 data was used in the stress calculations. The second approach was by applying the EBITD of -2.2 F°/in (-0.48C°/cm) to account for loss of support plus the maximum negative temperature gradient. In this case, the stresses would include residual stresses due to EBITD, stresses due to the maximum negative temperature gradient, and stresses from truck loads. In this case, no weak material was used under the slab edges and corners since the EBITD will cause the slab to curl up, leaving areas of no contact between the slab and base layer. It still controversial to account for stresses induced by the permanent built-in curl during the curing period as some of stresses will be relieved later by creep. Concrete pavements undergo shrinkage and creep throughout its lifetime, and it typically starts simultaneously during concrete placement [Kovler, 1999] as depicted in Figure 50. Upon shrinkage, tensile stresses are induced in the concrete due to self-weight and other constraints such as adjacent slabs or shoulders. Such stresses would be enough to cause creep which counteracts shrinkage deformation [Jeong and Zollinger, 2005]. As the concrete pavement is constructed during day time, drying shrinkage will occur due to rapid surface drying caused by high ambient temperature. Consequently, creep induced simultaneously during concrete drying will tend to reduce the upward curing and warping. Also, the amount of built-curl in the slab will decrease over time as a result of creep while the concrete is an extremely viscous fluid and not completely hardened [Lederle et al., 2011; Rao et al., 2001; Yu and Khaznovich, 2001]. Not only during concrete placement, but also over the entire service life, creep can influence the curling of rigid pavement [Lederle et al., 2011; Nantung, 2011]. Creep can also cause stress relaxation, defined as time-dependent stress decrease under constant change in strain, in the pavement, thus inducing partial recovery from stress at the top of the slab and reducing the built-in curl over time [Nassiri, 2011; Rao et al., 2001; Lederle et al., 2011; Park et al., 2015].

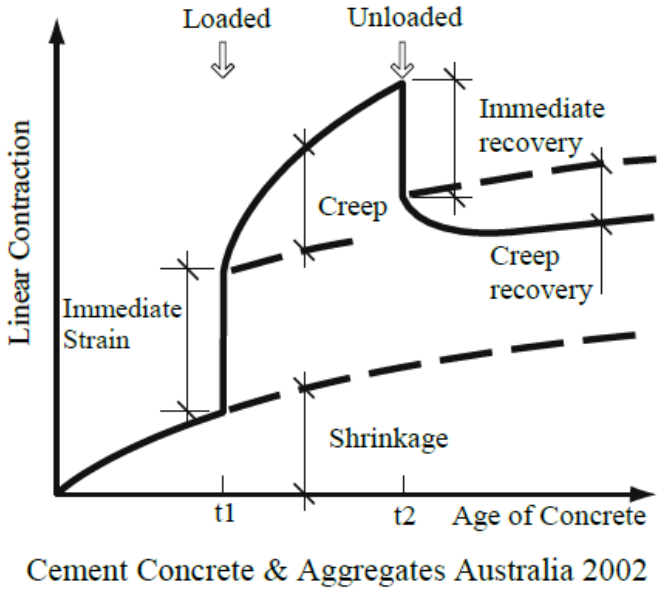

Figure 50. Creep and shrinkage of concrete pavement [Ceylan et al, 2016]

However, AASHTOWare assigns a -10 F° (-5.5 C°) to account for "Permanent Curl" and moisture gradient in the software regardless of the slab thickness. Although, tensile stress generated from the permanent built-in curl may not be large enough to cause fatigue cracking, the combined effect of built-in curl, temperature gradient, and traffic load can increase the level of stresses significantly [Lee and Darter, 1994a and 1994b; Yoder and Witczak, 1975]. Typically, when the concrete pavement is subjected to a positive temperature gradient, the damage mode would be bottom-up cracking when combined with traffic load. With presence of built-in curl, on the other hand, the top-down cracking mode will be predominant when combined with traffic load and daily temperature variation. Curling can also result in loss of support between the slab and supporting layers, increasing the tensile stresses in the slab and promoting slab failure under repeated truck loads [Channakeshava et al., 1993; Rao and Roesler, 2005b]. Therefore, the stresses in concrete pavement were calculated in this study using two approaches. The first included the built-in curl as loss of support only with zero EBITD. The second approach augments the built-in curl with an EBITD of -2.2 F°/in (-0.48C°/cm), accounting for both loss of support and associated residual stresses. The stresses calculated from the first approach would result in lower maximum tensile stresses than the second approach, thereby providing a range of responses.

Although concrete pavement may experience a high positive temperature gradient during its service life, it will never experience a downward curl or be in full contact with underlying base layer due to the permanent built-in curl [Bordelon and Roesler, 2009]. This implies the upward lifting of slab edges remains even in the warm seasons, a fact measured experimentally in the APLF. This phenomenon was also investigated in this study by using the validated FEM to determine the level of stresses developed by a positive temperature gradient and comparing it with negative temperature gradient effect. Two cases were considered on 15 ft (4.6 m) × 12 ft (3.7 m) × 12 in (305 mm) slab. The first case includes negative temperature gradient of -2.32 F°/in (-0.51C°/cm) with axle loads of 10 kip (44 kN) and 33 kip (147 kN) applied at the two ends of the slab. Loss of support was modeled as a weak material under slab edge and corners, and no EBITD were applied. The stresses were calculated along the top of slab center in the longitudinal direction. The second case involved positive temperature gradient of +2.32 F°/in (+0.51C°/cm) and axle load of 33 kip (147 kN) positioned at the slab center along the wheel path. The loss of support was modeled as in the first case, and again without EBITD. For the second case, the stresses were calculated at the slab bottom along the wheel path. The results are shown in Figure 51.

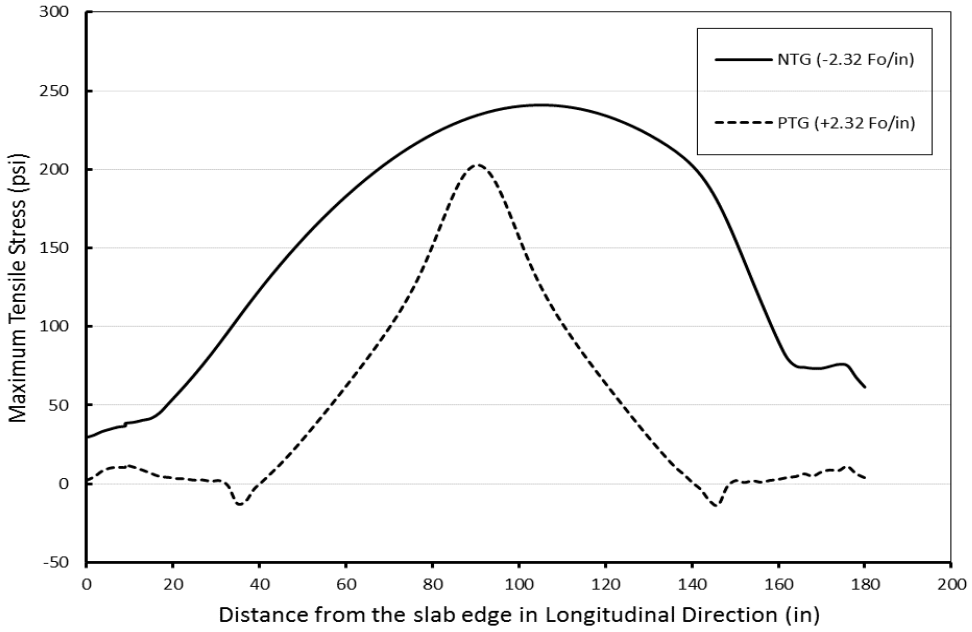

Figure 51. Stresses as a function of distance from the slab edge due to truck load with negative temperature gradient (NTG = -2.32F°/in = -0.51C°/cm) and positive temperature gradient (PTG = +2.32F°/in = +0.51C°/cm), assuming no EBITD (1 in =25.4 mm, 1 psi = 6.89 kPa).

Figure 51 shows the one with negative temperature gradient produces higher maximum tensile stress. Also, the stresses under negative temperature gradient extend to a greater area around the center than the case of positive temperature gradient where the maximum stress is more localized. Therefore, the fatigue life would be affected more by a negative temperature gradient and axle spacing than by a positive temperature gradient of the same magnitude.

10 Determining the Amount of Loss of Support Due to Built-In Curl

One would expect different amount of loss of support under different slab lengths and thicknesses since the loss of support was determined experimentally only for slab length of 15 ft (4.6 m) and thickness of 10 in (254 mm). For this study, the analysis included slab lengths of 12 ft (3.7 m) to 17 ft (5.2 m) in 1 ft (0.305 m) increments and thicknesses of 8 in (203 mm) to 15 in (381 mm). The amount of loss of support under each slab geometry was determined by applying the EBITD of -2.2 F°/in (-0.48 C°/cm) determined experimentally to each slab length and thickness using the validated FEM. The results are presented in Table 18. It seems longitudinal loss of support is significantly influenced by slab length, while transverse loss of support is influenced by slab thickness. This can also be seen in Figure 52 and Figure 53.

Table 18. Loss of support area due to built-in curl EBITD of -2.2 F°/in (-0.48 C°/cm) for each slab length and thickness.

Slab dimensions						Loss of Support			
Thickness		Length		Width		Longitudinal		Transverse	
(in)	(mm)	(ft)	(m)	(ft)	(m)	(in)	(mm)	(in)	(mm)
8	203	12	3.7	12	3.7	22.4	569	25.8	655
8	203	13	4.0	12	3.7	25.1	638	25.8	655
8	203	14	4.3	12	3.7	26.7	678	25.2	640
8	203	15	4.6	12	3.7	29.7	754	25.9	658
8	203	16	4.9	12	3.7	31.7	805	25.9	658
8	203	17	5.2	12	3.7	33.5	851	25.9	658
9	229	12	3.7	12	3.7	23.0	584	25.4	645
9	229	13	4.0	12	3.7	26.0	660	25.3	643
9	229	14	4.3	12	3.7	28.9	734	25.3	643
9	229	15	4.6	12	3.7	31.5	800	25.2	640
9	229	16	4.9	12	3.7	34.0	864	25.2	640
9	229	17	5.2	12	3.7	36.3	922	25.2	640
10	254	12	3.7	12	3.7	22.7	577	24.6	625
10	254	13	4.0	12	3.7	25.9	658	24.6	625
10	254	14	4.3	12	3.7	29.0	737	24.6	625
10	254	15	4.6	12	3.7	32.0	813	24.5	622
10	254	16	4.9	12	3.7	34.8	884	24.5	622
10	254	17	5.2	12	3.7	37.4	950	24.4	620
11	279	12	3.7	12	3.7	22.2	564	23.9	607
11	279	13	4.0	12	3.7	25.6	650	23.9	607
11	279	14	4.3	12	3.7	29.1	739	23.8	605
11	279	15	4.6	12	3.7	32.3	820	23.7	602
11	279	16	4.9	12	3.7	35.4	899	23.6	599
11	279	17	5.2	12	3.7	38.3	973	23.6	599
12	305	12	3.7	12	3.7	21.8	554	23.0	584
12	305	13	4.0	12	3.7	25.3	643	23.0	584
12	305	14	4.3	12	3.7	28.8	732	22.9	582
12	305	15	4.6	12	3.7	32.2	818	22.8	579
12	305	16	4.9	12	3.7	35.5	902	22.6	574
12	305	17	5.2	12	3.7	38.8	986	22.5	572
13	330	12	3.7	12	3.7	21.1	536	22.1	561
13	330	13	4.0	12	3.7	24.7	627	22.1	561
13	330	14	4.3	12	3.7	28.5	724	22.0	559
13	330	15	4.6	12	3.7	32.0	813	21.8	554
13	330	16	4.9	12	3.7	35.2	894	21.8	554
13	330	17	5.2	12	3.7	38.5	978	21.7	551
14	356	12	3.7	12	3.7	20.1	511	21.0	533
14	356	13	4.0	12	3.7	24.0	610	21.3	541
14	356	14	4.3	12	3.7	27.7	704	21.2	538
14	356	15	4.6	12	3.7	31.1	790	21.0	533
14	356	16	4.9	12	3.7	34.7	881	20.9	531
14	356	17	5.2	12	3.7	38.1	968	20.7	526
15	381	12	3.7	12	3.7	20.3	516	21.5	546
15	381	13	4.0	12	3.7	23.9	607	21.3	541
15	381	14	4.3	12	3.7	27.5	699	21.2	538
15	381	15	4.6	12	3.7	31.1	790	21.0	533
15	381	16	4.9	12	3.7	34.7	881	20.9	531
15	381	17	5.2	12	3.7	38.2	970	20.7	526

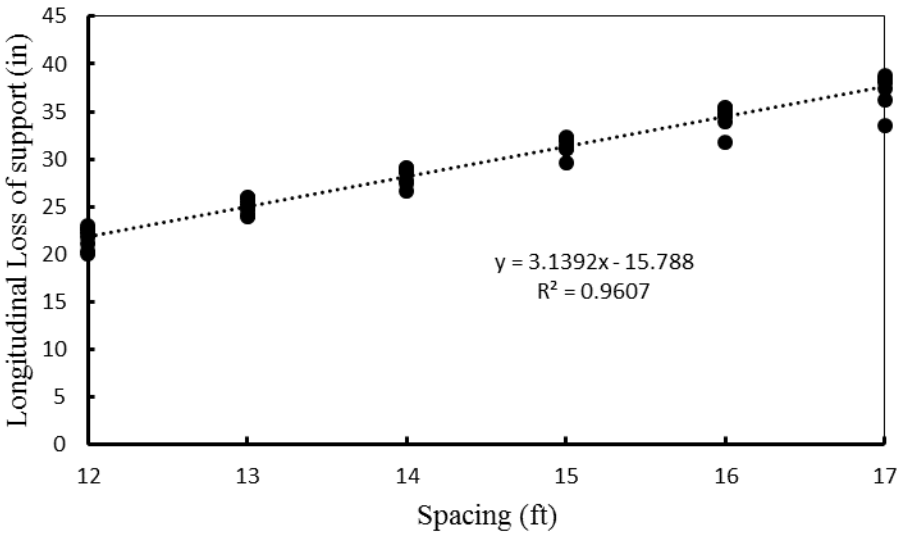

Figure 52. Longitudinal loss of support for each slab length due to built-in curl EBITD of -2.2 F°/in (-0.48 C°/cm) (1 in = 25 mm, 1 ft = 0.305 m).

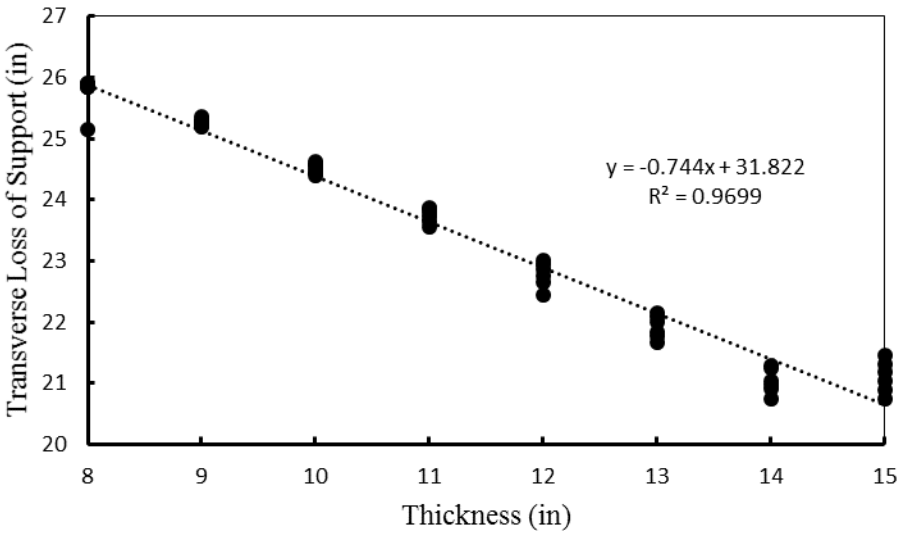

Figure 53. Transverse loss of support for each slab thickness due to built-in curl EBITD of -2.2 F°/in (-0.48 C°/cm) (1 in = 25 mm, 1 ft = 0.305 m).

The longitudinal loss of support increases as the slab length increases, while transverse loss of support decreases as slab thickness increases. The estimated loss of support for the studied slab geometries was used to model the amount of loss of support under each slab the in FEM in order to obtain the desired stresses.

11 The Results of Stress Calculations

Considering all the concepts described above and using the validated FEM and truck load and temperature data, the maximum tensile stresses each slab length and thickness was determined. As mentioned earlier, the stresses were calculated using two approaches by considering LOS with no built-in curl residual stresses (i.e. Zero EBITD) and by including the EBITD and the associated residual stresses. Table 19 (Table 20) presents the maximum tensile

stresses at the top of the slab under the negative temperature gradient (NTG) in combination with the truck load or EBITD or both in English (metric) units. These results are also plotted in Figure 54 and Figure 55. The 13 ft (4.0 m) slab length exhibits the lowest tensile stresses under all load conditions. Also, thicker slabs produce lower tensile stresses. Including the EBITD in the stresses calculation increases the stress level by 56% under negative temperature gradient and by 46% under negative temperature gradient and truck load; verifying the importance of including the permanent built-in curl in the stress calculations. Maximum stresses occur when the axle spacing matches the slab length with the axles located at both ends of the slab.

Table 19. Maximum tensile stress at top of slab for each load condition (English units).

Thickness (in)	Joint spacing (ft)	Axle spacing (ft)	Maximum Tensile Stress at the Top of Slab (psi)			
			Truck+NTG	NTG	Truck+NTG+EBITD	NTG+EBITD
9	13	13	236.3	115.6	347.4	185.2
		15	228.2	115.6	335.0	185.2
		17	219.0	115.6	318.6	185.2
	15	13	246.7	137.0	369.4	216.1
		15	249.5	137.0	377.2	216.1
		17	243.0	137.0	366.5	216.1
	17	13	255.8	156.9	388.0	246.8
		15	257.7	156.9	396.1	246.8
		17	256.9	156.9	399.5	246.8
12	13	13	201.6	95.6	289.8	151.2
		15	194.8	95.6	280.2	151.2
		17	185.5	95.6	266.6	151.2
	15	13	218.8	115.4	320.6	178.6
		15	227.3	115.4	332.6	178.6
		17	220.6	115.4	323.2	178.6
	17	13	235.3	137.4	348.7	207.9
		15	243.5	137.4	362.4	207.9
		17	248.9	137.4	371.5	207.9
15	13	13	163.8	78.5	228.6	124.1
		15	158.7	78.5	221.6	124.1
		17	151.5	78.5	211.3	124.1
	15	13	183.7	96.5	259.2	148.3
		15	192.0	96.5	269.4	148.3
		17	186.8	96.5	262.3	148.3
	17	13	203.3	117.1	288.3	174.9
		15	212.8	117.1	301.7	174.9
		17	219.3	117.1	310.3	174.9

Table 20. Maximum tensile stress at top of slab for each load condition (metric units).

Thickness (mm)	Joint spacing (m)	Axle spacing (m)	Maximum Tensile Stress at the Top of Slab (kPa)			
			Truck+NTG	NTG	Truck+NTG+EBITD	NTG+EBITD
229	4.0	4.0	1629	797	2395	1277
		4.6	1573	797	2310	1277
		5.2	1510	797	2197	1277
	4.6	4.0	1701	945	2547	1490
		4.6	1720	945	2601	1490
		5.2	1675	945	2527	1490
	5.2	4.0	1764	1082	2675	1702
		4.6	1777	1082	2731	1702
		5.2	1771	1082	2754	1702
305	4.0	4.0	1390	659	1998	1042
		4.6	1343	659	1932	1042
		5.2	1279	659	1838	1042
	4.6	4.0	1509	796	2210	1231
		4.6	1567	796	2293	1231
		5.2	1521	796	2228	1231
	5.2	4.0	1622	947	2404	1433
		4.6	1679	947	2499	1433
		5.2	1716	947	2561	1433
381	4.0	4.0	1129	541	1576	856
		4.6	1094	541	1528	856
		5.2	1045	541	1457	856
	4.6	4.0	1267	665	1787	1022
		4.6	1324	665	1857	1022
		5.2	1288	665	1808	1022
	5.2	4.0	1402	807	1988	1206
		4.6	1467	807	2080	1206
		5.2	1512	807	2139	1206

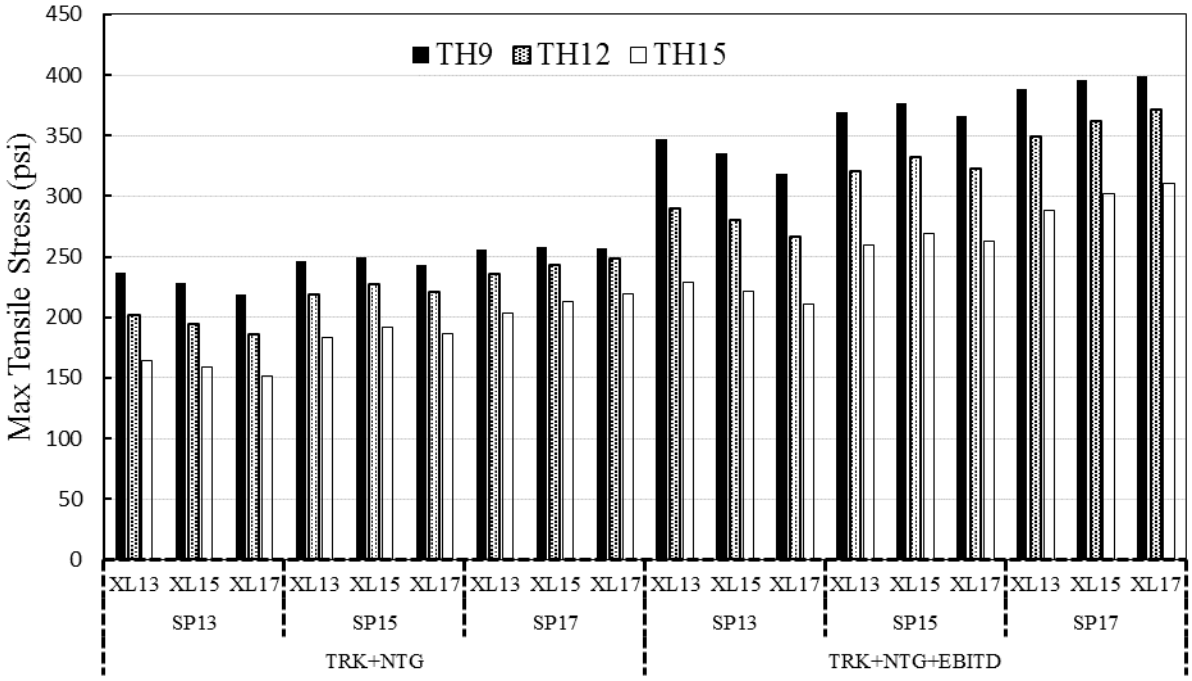

Figure 54. Maximum tensile stress (1 psi = 6.89 kN) for each axle spacing (XL), slab length (SP), and slab thickness (TH) under combined negative temperature gradient (NTG) and truck load with and without EBITD.

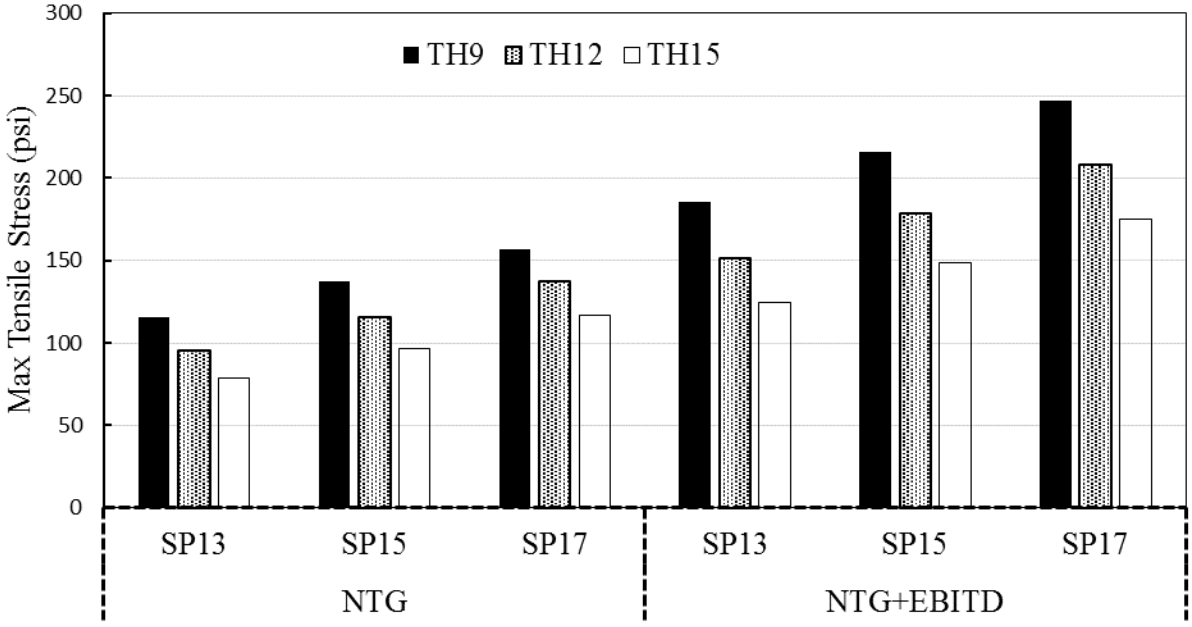

Figure 55. Maximum tensile stress (1 psi = 6.89 kN) under negative temperature gradient (NTG) with and without EBITD for each slab length (SP) and thickness (TH).

For the loading cases used in this study, with steering and second axles positioned at opposite ends of the same slab, the location of maximum tensile stress would occur near the center of slab top, but slightly closer to the heavier second axle as shown in Figure 56 where the second axle is on the right.

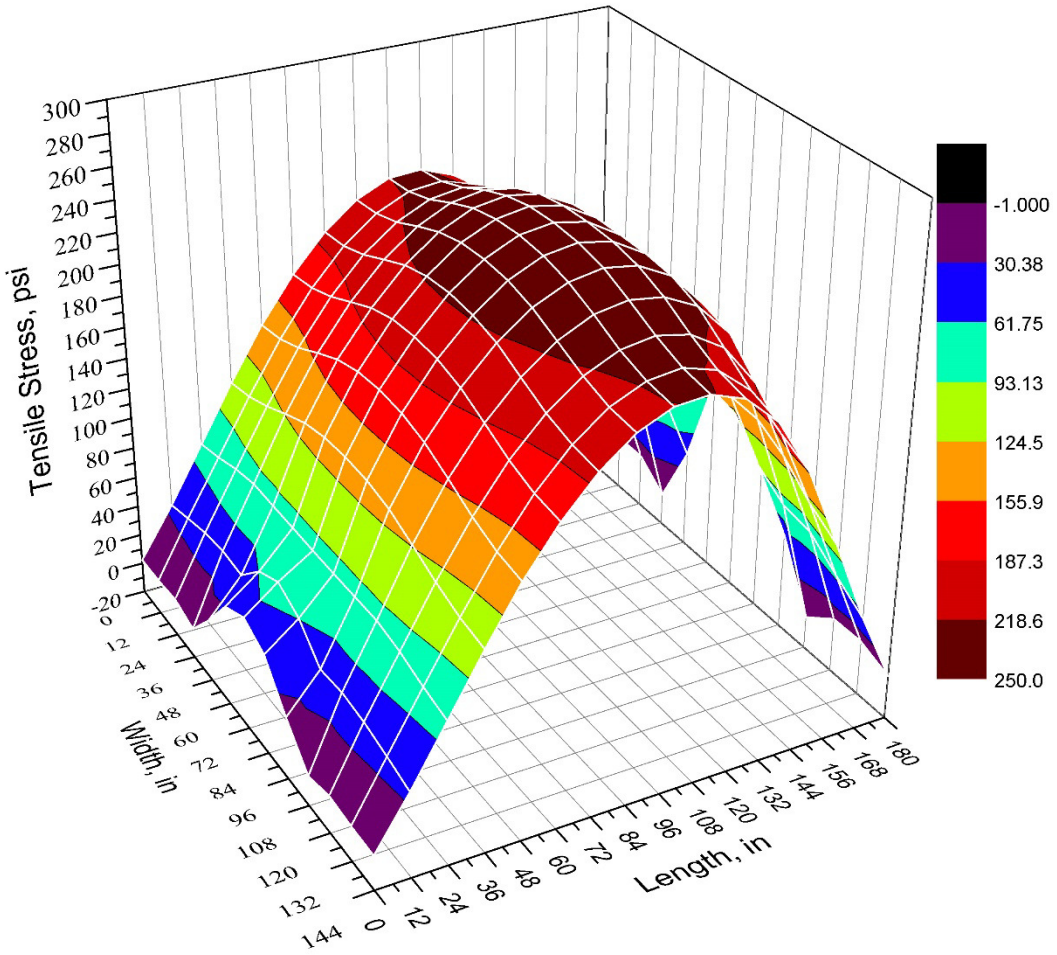

Figure 56. Maximum tensile stress location at the slab top due to load and negative temperature gradient (1 in = 0.0254 m, 1 psi = 6.89 kN).

12 Effect of Shoulders on the Maximum Stresses

In the field, single lane concrete pavement is rare. Most rigid pavements include at least two lanes tied together along the central longitudinal joint with tie bars, and typically with shoulders at the roadway edge. The shoulder could be either tied concrete or asphalt. According to the ODOT Pavement Design Manual [ODOT, 2014], shoulders are used to accommodate disabled vehicles, provide lateral support for the base and surface courses, improve the safety of a highway, and to maintain traffic operations during lane closures. They are constructed with the same thickness and joint spacing as the driving lanes, except the transverse joints in the shoulders are not dowelled. Concrete shoulders are typically tied to driving lanes using mild steel tie bars. Tying concrete shoulders to the driving lanes provides lateral support and spreads the load over a greater area, thus reducing the stresses induced in the driving lane slabs under environmental and traffic loads. Flexible shoulders are not tied to the driving lane. They may provide some lateral support to the concrete pavement. In this study, the effect of shoulders on concrete pavement performance was also considered. Therefore, the validated one-lane concrete pavement FEM was extended to include a second driving lane and a 10 ft (3.0 m) wide concrete shoulder. The slab length and thickness of the shoulder matched those of the driving lane. The tie bar diameter, length, and spacing were obtained from ODOT Standard Drawing BP-2.1 (version dated 7-17-2015) titled "Longitudinal Pavement Joints" where the 5×30 (16 mm diameter × 762 mm length) deformed bar was used with 30 in (0.76 m) spacing across the longitudinal joints. The 3D FEM geometry with second lane and concrete shoulder, including dowel and tie bars is shown in Figure 57. The corresponding model with an asphalt shoulder is shown in Figure 58.

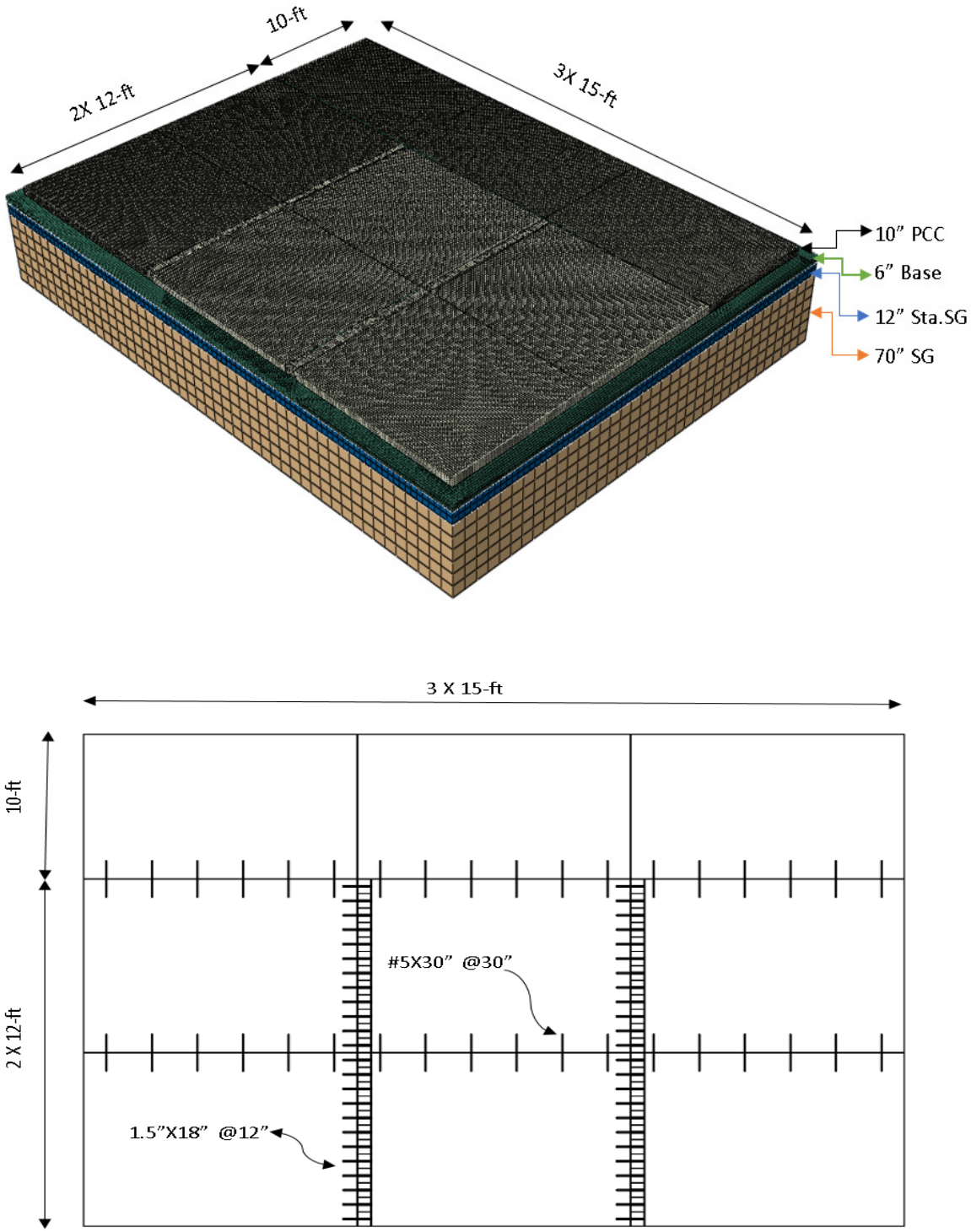

Figure 57. 3D FEM geometry with second lane and PCC shoulders with details of dowel and tie bars (1" = 1 in =25.4 mm, 1' = 1 ft = 0.305 m).

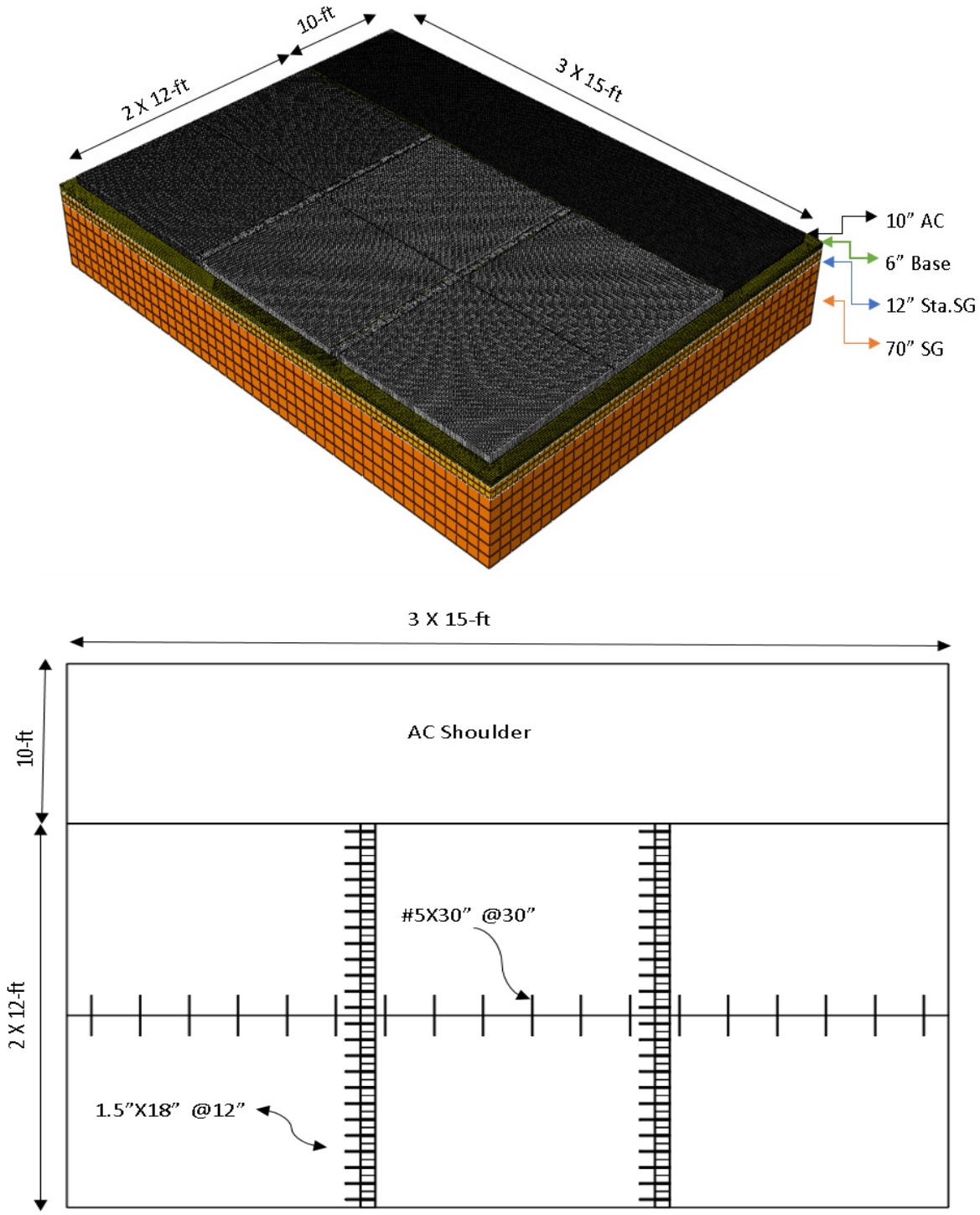

Figure 58. 3D FEM geometry with second travel lane and AC shoulders with details of dowel and tie bars (1" = 1 in =25.4 mm, 1' = 1 ft = 0.305 m).

In these models, the PCC material properties in the shoulder and second lane are the same as in the driving lane, while the properties for the asphalt shoulder were taken from Masada et al. [2004] and AASHTO MEPDG 2002; the AC elastic modulus was 5.0E5 psi (3.4 GPa), Poisson's

ratio was 0.37, the density was 140 pcf (2240 kg/m^3), and the coefficient of thermal expansion was 5.0E-6 F$^{\circ -1}$ (2.8E-5 C$^{\circ -1}$).

Using these models with the slab lengths and thicknesses previously considered in the single lane model, the maximum tensile stresses at the top of the middle panel under combined temperature and truck loads were determined. The results for PCC pavements with PCC shoulders are presented in Table 21 (Table 22) in English (metric) units, while those for PCC pavements with AC shoulders are presented in Table 23 (Table 24) in English (metric) units, and they are plotted in Figure 59 in comparison for the simulation with no shoulder. Including PCC tied shoulders reduced the stresses induced in the concrete slab by 9%, 13%, and 15% respectively for slab thicknesses of 9 in (229 mm), 12 in (305 mm), and 15 in (381 mm) under combined temperature and truck loads. With asphalt shoulders, the stresses decreased by 4%, 6%, and 8% respectively for slab thicknesses of 9 in (229 mm), 12 in (305 mm), and 15 in (381 mm) under combined temperature and truck loads. No significant reduction in stress was observed for either shoulder under temperature load only. Tied PCC shoulders provided more lateral support to the pavement than AC shoulders, which resulted in more stress reduction under combined loading. Also, the thicker concrete slabs exhibited more stress reduction.

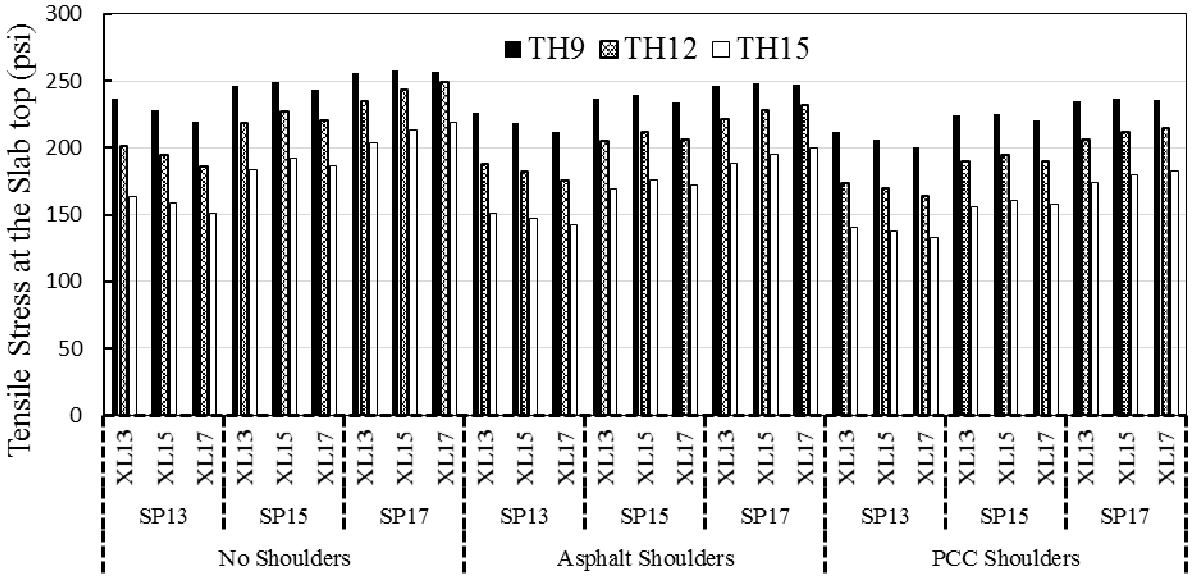

Figure 59. The effect of shoulders on tensile stress (1 psi = 6.89 kN) at the top of the concrete slab for each axle spacing (XL), slab length (SP), and slab thickness (TH).

Table 21. Maximum Tensile Stress at top center of the PCC slab with second lane and PCC Shoulders under Truck and Temperature loads (English units).

Thickness (in)	Spacing (ft)	Axle spacing (ft)	Maximum Tensile Stress at the Top of Slab (psi)			
			Truck+NTG	NTG	Truck+NTG+EBITD	NTG+EBITD
9	13	13	212.0	117.7	312.5	187.8
		15	206.1	117.7	303.9	187.8
		17	199.9	117.7	293.9	187.8
	15	13	224.0	138.7	334.7	218.0
		15	225.4	138.7	339.4	218.0
		17	220.7	138.7	332.0	218.0
	17	13	235.3	159.1	356.5	249.7
		15	236.5	159.1	361.8	249.7
		17	235.7	159.1	363.7	249.7
12	13	13	173.7	97.0	248.6	153.1
		15	169.2	97.0	242.7	153.1
		17	163.9	97.0	235.2	153.1
	15	13	189.4	117.1	274.3	181.1
		15	194.4	117.1	281.3	181.1
		17	190.1	117.1	275.6	181.1
	17	13	206.5	139.3	300.3	210.9
		15	211.5	139.3	308.1	210.9
		17	214.3	139.3	312.9	210.9
15	13	13	140.3	80.9	199.0	127.5
		15	137.2	80.9	195.0	127.5
		17	133.2	80.9	189.6	127.5
	15	13	156.2	98.8	222.7	151.5
		15	161.1	98.8	228.6	151.5
		17	158.0	98.8	224.8	151.5
	17	13	173.8	119.3	247.5	177.8
		15	179.3	119.3	254.6	177.8
		17	182.7	119.3	259.1	177.8

Table 22. Maximum Tensile Stress at top center of the PCC slab with second lane and PCC Shoulders under Truck and Temperature loads (metric units).

Thickness (mm)	Spacing (m)	Axle spacing (m)	Maximum Tensile Stress at the Top of Slab (kPa)			
			Truck+NTG	NTG	Truck+NTG+EBITD	NTG+EBITD
229	4.0	4.0	1462	812	2155	1295
		4.6	1421	812	2095	1295
		5.2	1378	812	2026	1295
	4.6	4.0	1544	956	2308	1503
		4.6	1554	956	2340	1503
		5.2	1522	956	2289	1503
	5.2	4.0	1622	1097	2458	1722
		4.6	1631	1097	2495	1722
		5.2	1625	1097	2508	1722
305	4.0	4.0	1198	669	1714	1056
		4.6	1167	669	1673	1056
		5.2	1130	669	1622	1056
	4.6	4.0	1306	807	1891	1249
		4.6	1340	807	1939	1249
		5.2	1311	807	1900	1249
	5.2	4.0	1424	960	2070	1454
		4.6	1458	960	2124	1454
		5.2	1478	960	2157	1454
381	4.0	4.0	967	558	1372	879
		4.6	946	558	1344	879
		5.2	918	558	1307	879
	4.6	4.0	1077	681	1535	1045
		4.6	1111	681	1576	1045
		5.2	1089	681	1550	1045
	5.2	4.0	1198	823	1706	1226
		4.6	1236	823	1755	1226
		5.2	1260	823	1786	1226

Table 23. Maximum Tensile Stress at top center of the PCC slab with second lane and AC Shoulders under Truck and Temperature loads (English units).

Thickness (in)	Spacing (ft)	Axle spacing (ft)	Maximum Tensile Stress at the Top of Slab (psi)			
			Truck+NTG	NTG	Truck+NTG+EBITD	NTG+EBITD
9	13	13	226.0	115.5	331.8	184.4
		15	218.9	115.5	321.5	184.4
		17	211.4	115.5	309.0	184.4
	15	13	237.1	136.6	354.3	215.3
		15	239.3	136.6	360.7	215.3
		17	233.6	136.6	352.1	215.3
	17	13	246.7	156.8	374.5	246.2
		15	248.2	156.8	381.1	246.2
		17	247.5	156.8	383.9	246.2
12	13	13	187.5	94.9	267.4	150.3
		15	182.0	94.9	260.3	150.3
		17	175.1	94.9	250.8	150.3
	15	13	204.7	114.9	295.5	177.6
		15	211.4	114.9	304.9	177.6
		17	206.1	114.9	297.8	177.6
	17	13	221.7	136.9	322.9	207.1
		15	228.2	136.9	333.2	207.1
		17	232.4	136.9	340.1	207.1
15	13	13	151.3	78.0	212.3	123.3
		15	147.5	78.0	207.6	123.3
		17	142.5	78.0	201.0	123.3
	15	13	169.3	96.0	239.1	147.6
		15	175.7	96.0	246.7	147.6
		17	171.9	96.0	241.9	147.6
	17	13	188.1	116.3	266.1	174.0
		15	195.4	116.3	275.4	174.0
		17	200.2	116.3	281.6	174.0

Table 24. Maximum Tensile Stress at top center of the PCC slab with second lane and AC Shoulders under Truck and Temperature loads (metric units).

Thickness (mm)	Spacing (m)	Axle spacing (m)	Maximum Tensile Stress at the Top of Slab (kPa)			
			Truck+NTG	NTG	Truck+NTG+EBITD	NTG+EBITD
229	4.0	4.0	1558	796	2288	1271
		4.6	1509	796	2217	1271
		5.2	1458	796	2130	1271
	4.6	4.0	1635	942	2443	1484
		4.6	1650	942	2487	1484
		5.2	1611	942	2428	1484
	5.2	4.0	1701	1081	2582	1697
		4.6	1711	1081	2628	1697
		5.2	1706	1081	2647	1697
305	4.0	4.0	1293	654	1844	1036
		4.6	1255	654	1795	1036
		5.2	1207	654	1729	1036
	4.6	4.0	1411	792	2037	1225
		4.6	1458	792	2102	1225
		5.2	1421	792	2053	1225
	5.2	4.0	1529	944	2226	1428
		4.6	1573	944	2297	1428
		5.2	1602	944	2345	1428
381	4.0	4.0	1043	538	1464	850
		4.6	1017	538	1431	850
		5.2	983	538	1386	850
	4.6	4.0	1167	662	1649	1018
		4.6	1211	662	1701	1018
		5.2	1185	662	1668	1018
	5.2	4.0	1297	802	1835	1200
		4.6	1347	802	1899	1200
		5.2	1380	802	1942	1200

12.1 The Effect of Slab Width on Tensile Stress

Sometimes concrete pavements are constructed with a 14 ft (4.3 m) slab width to provide a continuous shoulder to pavement lane. This widened slab width has been reported in the literature to have an insignificant effect on the concrete pavement performance [Darter et al., 1995; Guo et al., 1997; Parsons, 2003; Sargand and Abdalla, 2006]. However, when considering built-in curl, the slab width may have an impact on long-term concrete pavement performance. Therefore, in this study, 14 ft (4.3 m) slab width was used with the various slab lengths and thicknesses to study the impact of slab width on pavement stresses under combined temperature and truck loads. The validated FEM was updated to have a slab width of 14 ft (4.3 m) as shown in Figure 60; the EBITD was modeled as previously described. The results are presented in Table 25 (Table 26) in English (metric) units and compared to those from the 12 ft (3.7 m) slab width in Figure 61.

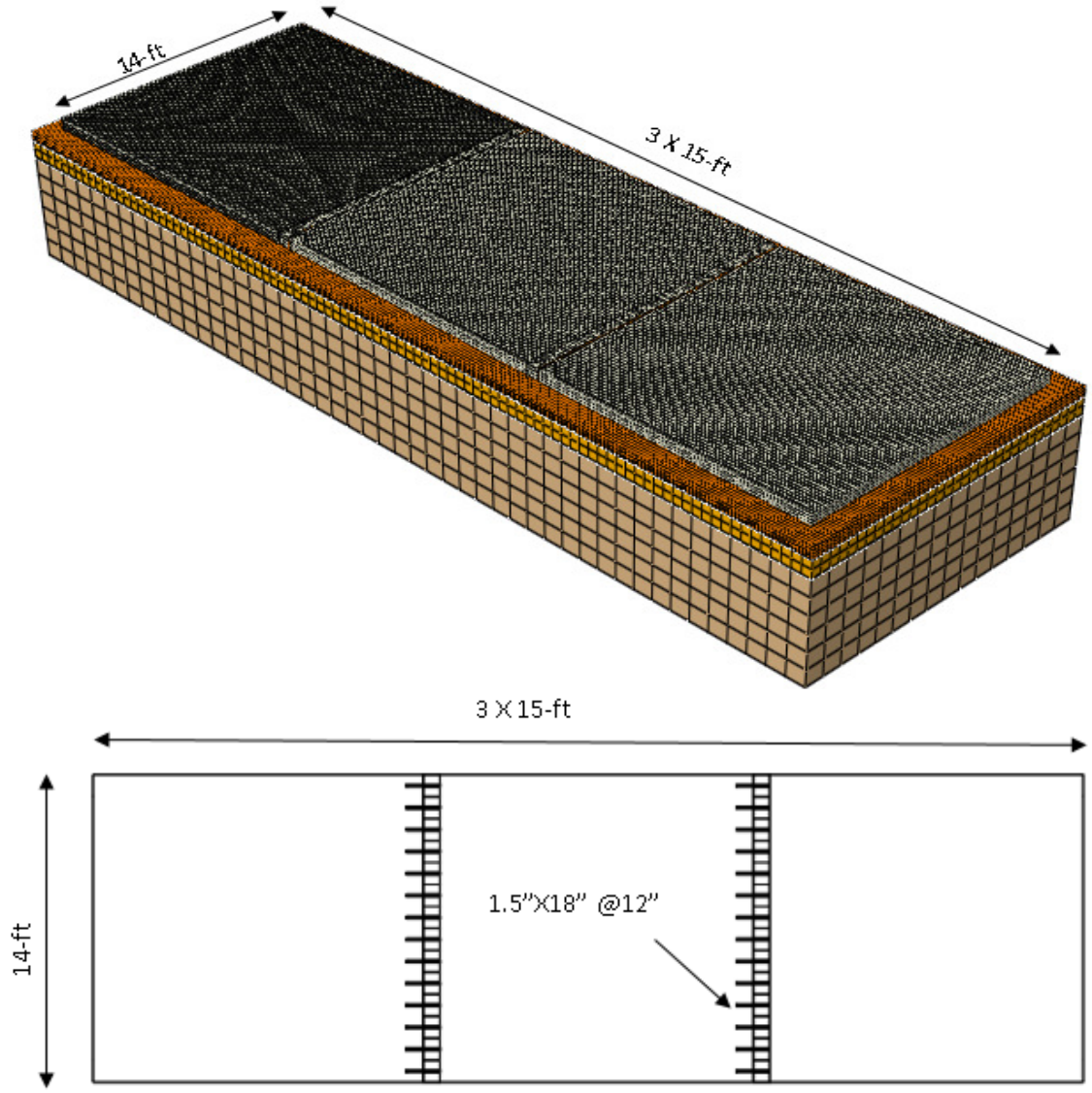

Figure 60. 3D FEM of 14 ft (4.3 m) slab width (1" = 1 in = 25.4 mm, 1 ft = 0.305 m).

Table 25. Maximum Tensile Stress at the top of mid PCC slab with 14 ft (4.3 m) slab width under negative temperature gradient (NTG) with truck loads (TRK) and/or EBITD (English units).

Thickness (in)	Spacing (ft)	Axle spacing (ft)	Maximum Tensile Stress at the Top of Slab (psi)			
			Truck+NTG	NTG	Truck+NTG+EBITD	NTG+EBITD
9	13	13	219.4	120.0	340.2	192.6
		15	211.9	120.0	329.0	192.6
		17	202.9	120.0	314.5	192.6
	15	13	230.7	141.3	365.1	224.3
		15	233.4	141.3	371.3	224.3
		17	227.4	141.3	361.6	224.3
	17	13	239.1	161.4	383.2	255.0
		15	241.8	161.4	390.9	255.0
		17	241.7	161.4	394.4	255.0
12	13	13	189.1	98.6	278.4	156.9
		15	182.9	98.6	269.9	156.9
		17	174.5	98.6	258.0	156.9
	15	13	205.1	118.6	307.3	184.8
		15	213.0	118.6	318.2	184.8
		17	207.1	118.6	309.9	184.8
	17	13	221.4	140.5	334.9	214.5
		15	229.2	140.5	347.5	214.5
		17	234.4	140.5	355.8	214.5
15	13	13	160.6	81.6	230.4	130.2
		15	153.8	81.6	221.3	130.2
		17	147.3	81.6	212.4	130.2
	15	13	176.6	99.3	256.2	153.9
		15	187.5	99.3	270.2	153.9
		17	180.4	99.3	260.5	153.9
	17	13	196.3	119.7	286.6	180.3
		15	204.4	119.7	297.1	180.3
		17	213.8	119.7	310.1	180.3

Table 26. Maximum Tensile Stress at the top of mid PCC slab with 14 ft (4.3 m) slab width under negative temperature gradient (NTG) with truck loads (TRK) and/or EBITD (metric units).

Thickness (mm)	Spacing (m)	Axle spacing (m)	Maximum Tensile Stress at the Top of Slab (kPa)			
			Truck+NTG	NTG	Truck+NTG+EBITD	NTG+EBITD
229	4.0	4.0	1513	827	2346	1328
		4.6	1461	827	2268	1328
		5.2	1399	827	2168	1328
	4.6	4.0	1591	974	2517	1546
		4.6	1609	974	2560	1546
		5.2	1568	974	2493	1546
	5.2	4.0	1649	1113	2642	1758
		4.6	1667	1113	2695	1758
		5.2	1666	1113	2719	1758
305	4.0	4.0	1304	680	1920	1082
		4.6	1261	680	1861	1082
		5.2	1203	680	1779	1082
	4.6	4.0	1414	818	2119	1274
		4.6	1469	818	2194	1274
		5.2	1428	818	2137	1274
	5.2	4.0	1526	969	2309	1479
		4.6	1580	969	2396	1479
		5.2	1616	969	2453	1479
381	4.0	4.0	1107	563	1589	898
		4.6	1060	563	1526	898
		5.2	1016	563	1464	898
	4.6	4.0	1218	685	1766	1061
		4.6	1293	685	1863	1061
		5.2	1244	685	1796	1061
	5.2	4.0	1353	825	1976	1243
		4.6	1409	825	2048	1243
		5.2	1474	825	2138	1243

Maximum tensile stresses at the top of 14 ft (4.3 m) wide concrete slab were reduced by an average of 5% from the case of 12 ft (3.7m) wide slab under combined temperature and truck loads. This percentage was reduced to 2% when EBITD was added to the applied negative temperature gradient. Tensile stresses under temperature loading only, on the other hand, was increased by an average of 3% when using 14 ft (4.3 m) slab width. The reduction in tensile stresses under combined loading decreases with increased slab thickness. In the FEM analysis, the reduction in tensile stress with 14 ft (4.3 m) slab width is small compared to the effect of

having shoulders, but it may contribute to the pavement performance and ultimately increase the pavement life.

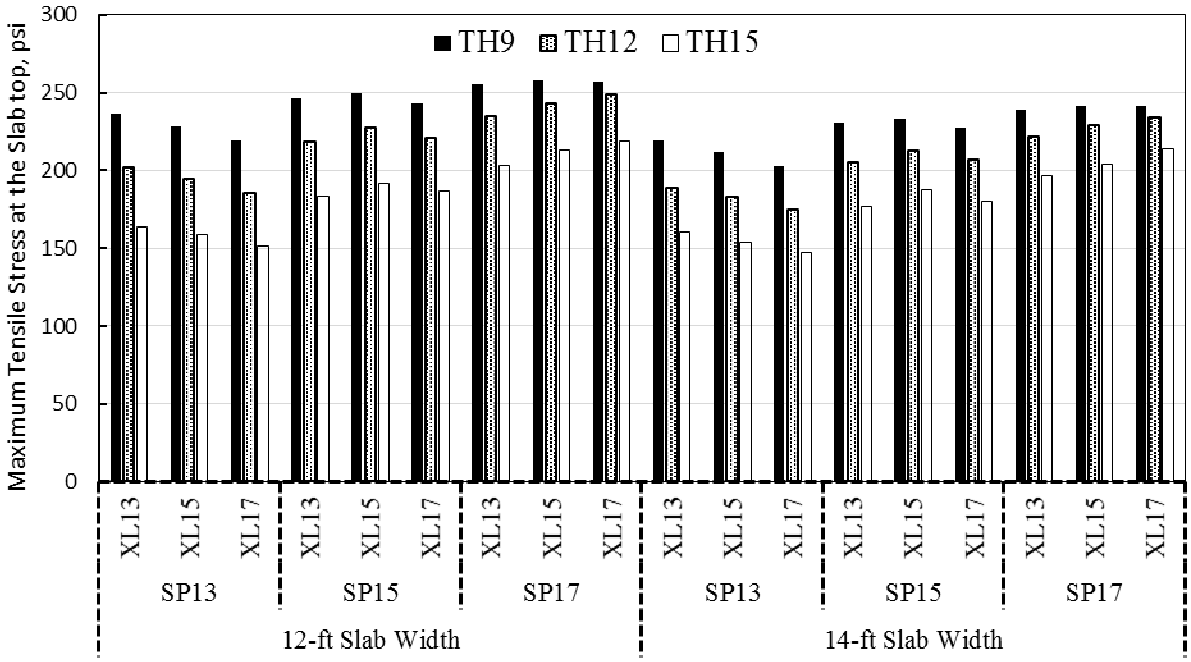

Figure 61. Maximum tensile stress (1 psi = 6.89 kN) at top of 12 ft (3.7 m) slab width versus 14 ft (4.3 m) slab width for each axle spacing (XL), slab length (SP), and slab thickness (TH).

12.2 Effect of Dowel Bars on Slab Response

The 3D FEM with slab geometry (12 in (305 mm) thick and 13 ft (4.0 m) long) was utilized to study the effect of the diameter and spacing of dowel bars on slab response under combined truck load and curling/warping temperature gradient. Dowel bar diameters of 1.0 in (25 mm), 1.25 in (32 mm), and 1.5 in (38 mm) and spacings of 8.0 in (203 mm), 12.0 in (305 mm), and 16 in (406 mm) were used for this study. 3D FEMs for the selected dowel bar diameters and spacings were developed using ABAQUS. The 3D FEMs included two 12 ft (3.7 m) wide lanes of rigid pavement with 10 ft (3.0 m) wide tied concrete shoulder, and each lane had three 13 ft (4.0 m) long slabs. No.5 deformed mild steel tie bars with diameter 0.625 in (16 mm) were used to tie the shoulders to the pavement and the longitudinal joint between the lanes. The main purpose of the modeling was to find the dowel bar diameter and spacing that would result in minimum slab tensile stresses at mid-slab and the corresponding load transfer efficiency (LTE) and stress concentration. The results are as presented in Table 27.

Table 27. Dowel bar spacings and diameters with associated stresses and load transfer efficiency (LTE).

Spacing		Diameter		Tensile Stress		Stress Concentration		LTE
(in)	(mm)	(in)	(mm)	(psi)	(kPa)	(psi)	(kPa)	(%)
8	203	1	25	230.5	1589	277.2	1911	90
12	305	1	25	224.7	1549	227.1	1566	87
16	406	1	25	221.1	1524	224.5	1548	85
8	203	1.25	32	241.2	1663	327.7	2259	91
12	305	1.25	32	232.3	1601	330.8	2281	89
16	406	1.25	32	226.5	1562	330.4	2278	88
8	203	1.5	38	255.5	1762	429.2	2959	93
12	305	1.5	38	242.8	1674	436.2	3008	91
16	406	1.5	38	235.0	1620	433.9	2992	90

The results were also plotted in Figure 62 through Figure 64. The dowel bar diameter of 1.0 in (25 mm) and spacing of 16 in (406 mm) has the lowest tensile stresses at the mid-slab as shown in Figure 62. However, the LTE associated with dowel bar diameter of 1.0 in (25 mm) and spacing of 16 in (406 mm) was lower than for the other diameter and spacing combinations. Larger dowel diameters and closer spacing would produce higher LTE as shown in Figure 63. Dowel bars stress concentrations at the transverse joints were not affected much by the dowel spacing, but were affected by the dowel diameter, with larger diameters producing higher levels of stress concentration, as shown in Figure 64.

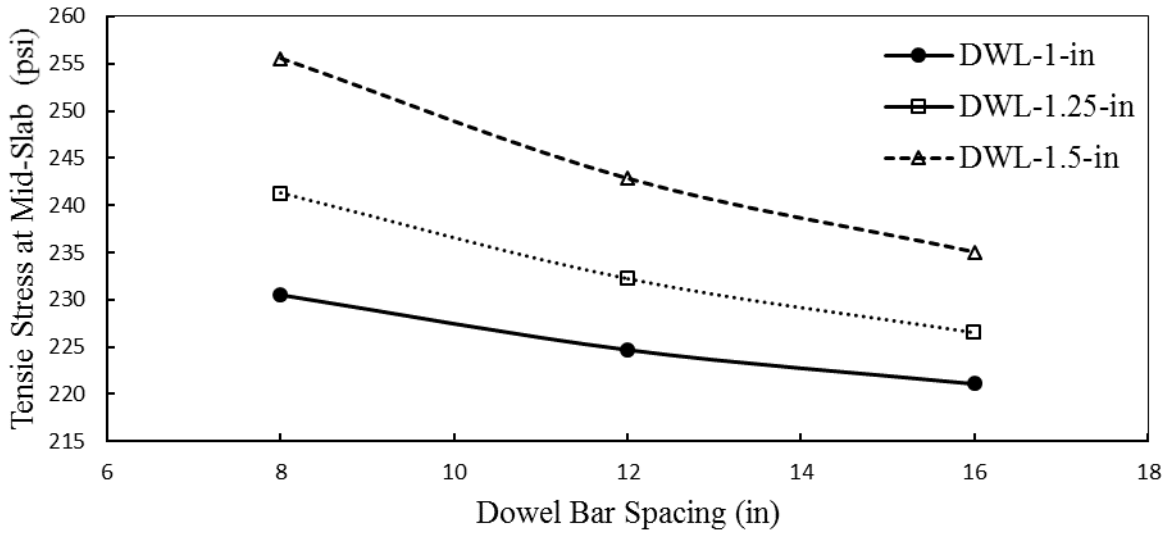

Figure 62. Mid-slab tensile stress as a function of dowel bar diameter and spacing. (1 in = 25.4 mm, 1 psi = 6.89 kPa)

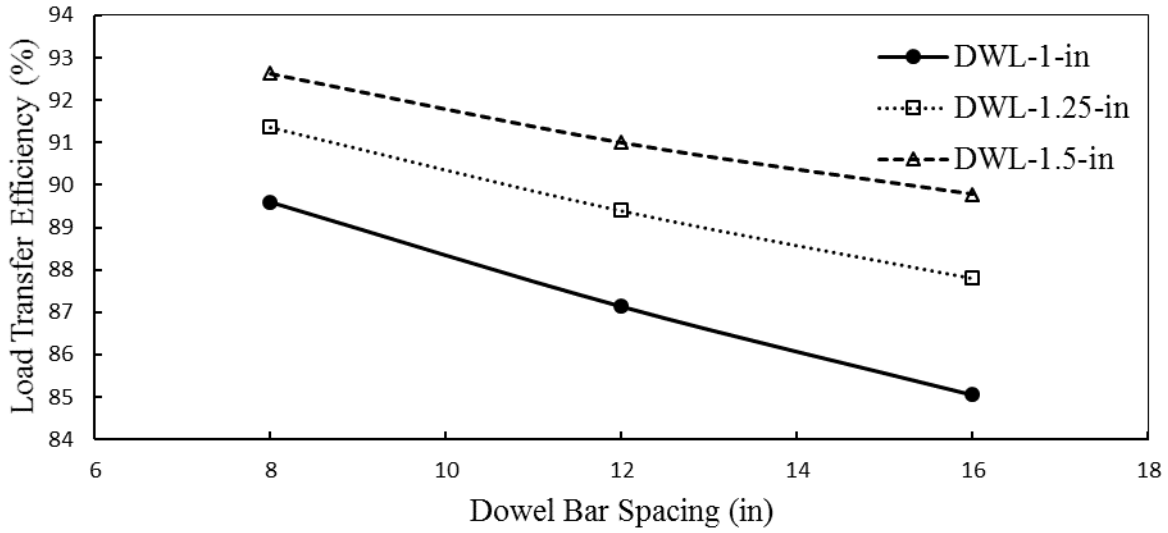

Figure 63. Load transfer efficiency (LTE) for each dowel bar diameter and spacing. (1 in = 25.4 mm)

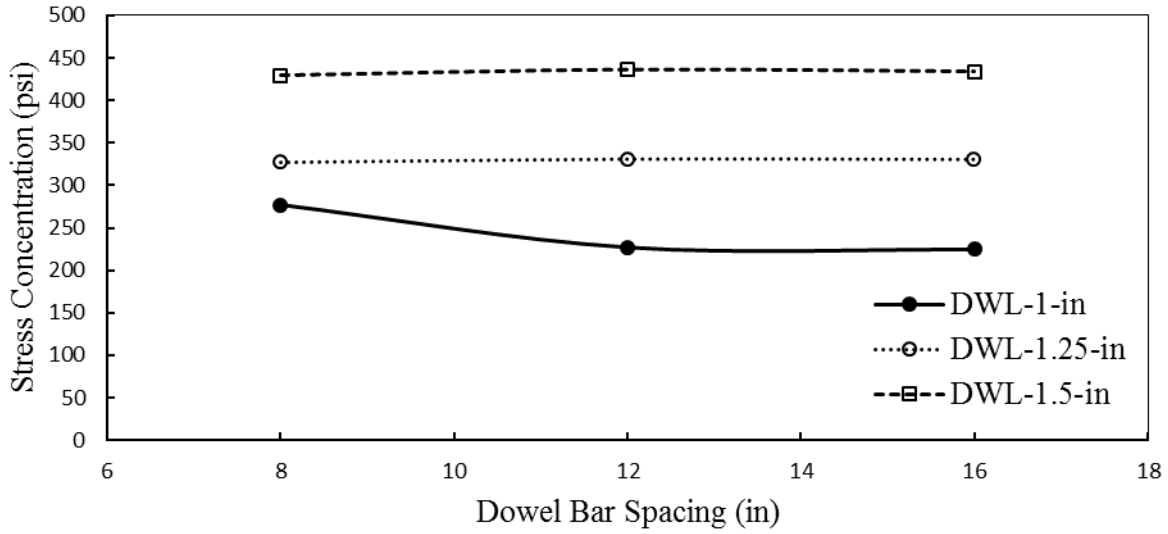

Figure 64. Stress concentration around dowel bars at transverse joints for each dowel spacing and diameter. (1 in = 25.4 mm, 1 psi = 6.89 kPa)

12.3 Effect of tie bars on slab response

The 3D FEM with slab thicknesses 9 in (229 mm) to 15 in (381 mm) thick was utilized to study the effect of the number/spacing of tie bars on slab response under combined truck load and curling/warping temperature gradient. The 3D FEM in ABAQUS included two 12 ft (3.7 m) wide lanes of rigid pavement with 10 ft (3.0 m) wide tied concrete shoulder, and each lane had three slabs of length and thickness which were varied. Dowel bars had diameters of 1.5 in (38 mm) with standard spacing. No.5 deformed mild steel tie bars with diameter 0.625 in (16 mm) were used to tie the shoulders to the pavement and the longitudinal joint between the lanes

following ODOT specifications. The main purpose of the modeling was to find the maximum slab tensile stresses at mid-slab as a function of slab length with tie bars included.

The maximum tensile stress at the pavement surface in the center of the slab area for each geometry are presented in Figure 65 and Table 28 (English units) and Table 29 (metric units). From the figure it can be seen how when the slab length is increased in 0.5 ft (152 mm) increments from 13 ft (4.0 m) to 15 ft (4.6 m) and following ODOT specifications on the number and spacing of tie bars, the stress curves shift by varying amounts. The maximum stress at the center of the slab shifts up a small amount for the increment from 13 ft (4.0 m) to 13.5 ft (4.1 m), then a larger amount when the length goes from 13.5 ft (4.1 m) to 14 ft (4.3 m). This is because in the first 0.5 in (12 mm) increment the number of tie bars along the slab length remains the same as before, while in the second increment an additional tie bar is specified for each slab. These results show how tie bars have a significant impact on the maximum stress observed in the PCC pavement slab.

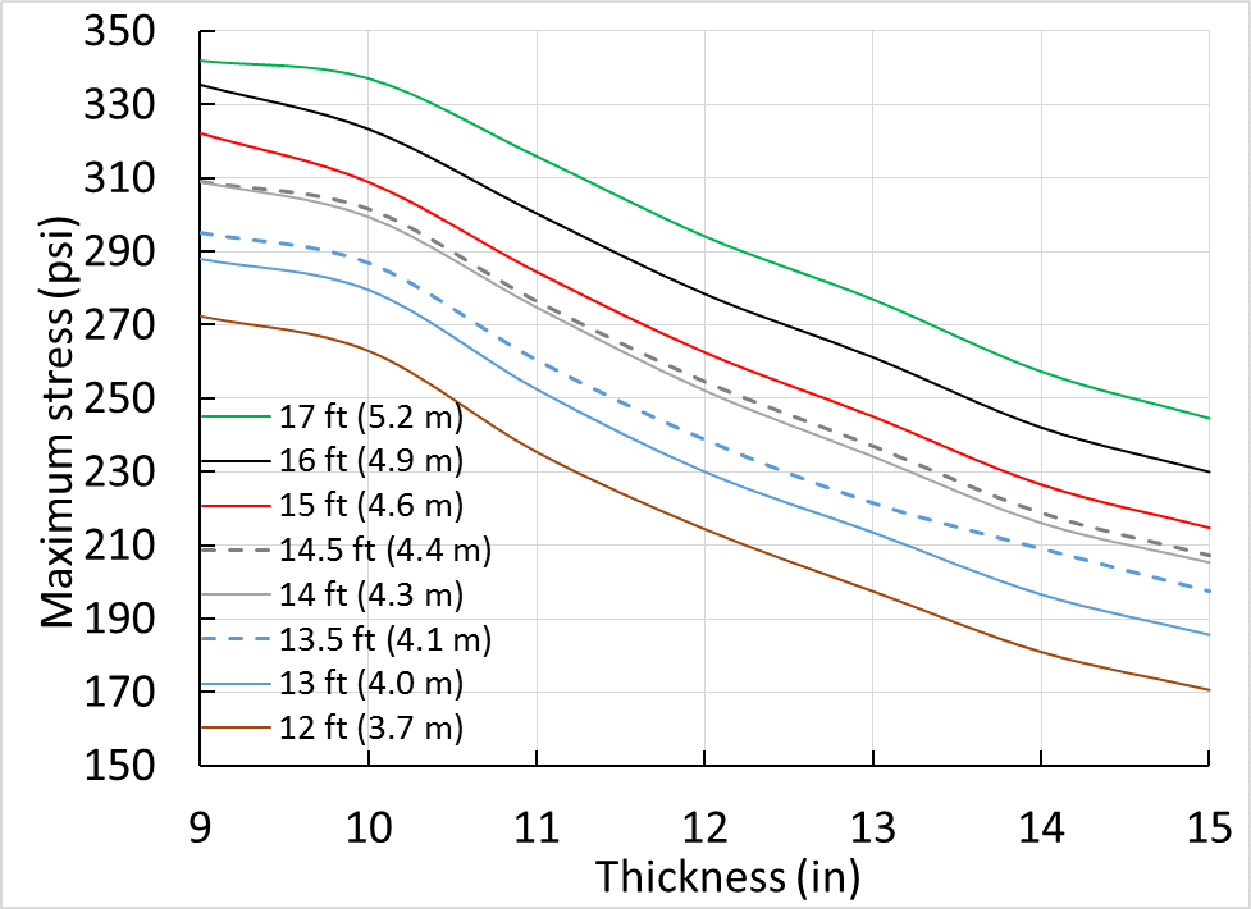

Figure 65. Maximum stress at pavement surface near center of the pavement slab as a function of thickness and slab length with tie bars placed following ODOT specifications (1 in =25.4 m, 1 psi = 6.89 kPa).

Table 28. Maximum stress in slab versus thickness and length with tie bars placed per ODOT specifications (English units).

Maximum stress (psi)								
Thickness	Slab length (ft)							
(in)	12	13	13.5	14	14.5	15	16	17
9	272.4	288.0	295.0	309.0	309.1	322.2	335.4	342.0
10	262.9	279.5	286.8	299.4	301.6	308.9	323.3	337.1
11	235.4	252.5	260.4	274.8	276.5	284.5	300.3	315.9
12	214.4	230.0	238.8	252.1	254.6	262.5	278.4	294.1
13	197.5	213.5	221.5	234.2	237.1	245.0	261.2	276.9
14	181.0	196.6	209.1	216.1	218.9	226.5	242.1	257.3
15	170.6	185.7	197.5	205.3	207.3	214.8	230.0	244.6
No. tie bars	5	5	5	6	6	6	6	7

Table 29. Maximum stress in slab versus thickness and length with tie bars placed per ODOT specifications (metric units)

Maximum stress (kPa)								
Thickness	Slab length (m)							
(mm)	3.7	4.0	4.1	4.3	4.4	4.6	4.9	5.2
229	1878	1986	2034	2130	2131	2222	2312	2358
254	1813	1927	1978	2064	2080	2130	2229	2324
279	1623	1741	1795	1895	1906	1961	2071	2178
305	1478	1586	1646	1738	1755	1810	1920	2028
330	1361	1472	1527	1615	1634	1690	1801	1909
356	1248	1356	1442	1490	1509	1562	1669	1774
381	1177	1280	1362	1416	1429	1481	1586	1686
No. tie bars	5	5	5	6	6	6	6	7

12.4 Interaction of dowels and tie bars

FEM was used to investigate how the spacing of tie bars affected the distribution of stresses at localized regions of a PCC slab, such as the corner, where a tie bar on longitudinal joint and a dowel bar on the transverse joint come closest to each other. A 15 ft (4.6 m) long by 12 ft (3.7 m) wide by 12 in (305 mm) thick slab geometry was used. Dowels of 1.5 in (38 mm) diameter were modeled spaced at 12 in (305 mm) along the transverse joint, with the first dowel positioned 6 in (152 mm) from the corner. Standard No. 5 tie bars of 30 in (760 mm) length were placed connecting the pavement to the shoulders and along the longitudinal joint between the lanes, following ODOT specifications. Tie bar spacing was set at 15 in (381 mm), 20 in (508 mm), 25 in (635 mm), and 30 in (762 mm), with the first bar at 15 in (381 mm), 20 in (508 mm), 25 in (635 mm), and 30 in (762 mm) from the corner. The FEM slab was subjected to combined loads from negative temperature gradient (NTG) and EBITD plus a truck load placed on the wheel path, slab edge, or slab corner.

Figure 66 represents the worst case situation, with the wheel path load and 30 in (760 mm) tie bar spacing, which had the highest stresses under the corner tie bar (564 psi, 3887 kPa) and

almost the highest stress under the dowel bars (428 psi, 2948 kPa). The maximum principal stresses under the dowels and tie bars are shown in Figure 67 and in Table 30 (English units) and Table 31 (metric units). The maximum stress under the dowel bars was unaffected by the tie bar spacing (less than 1% change), while under the tie bars, a decrease in the maximum principal stress of 26% to 30% was noticed as the tie bar spacing decreased to half its original value, as shown in Table 30 (English units) and Table 31 (metric units).

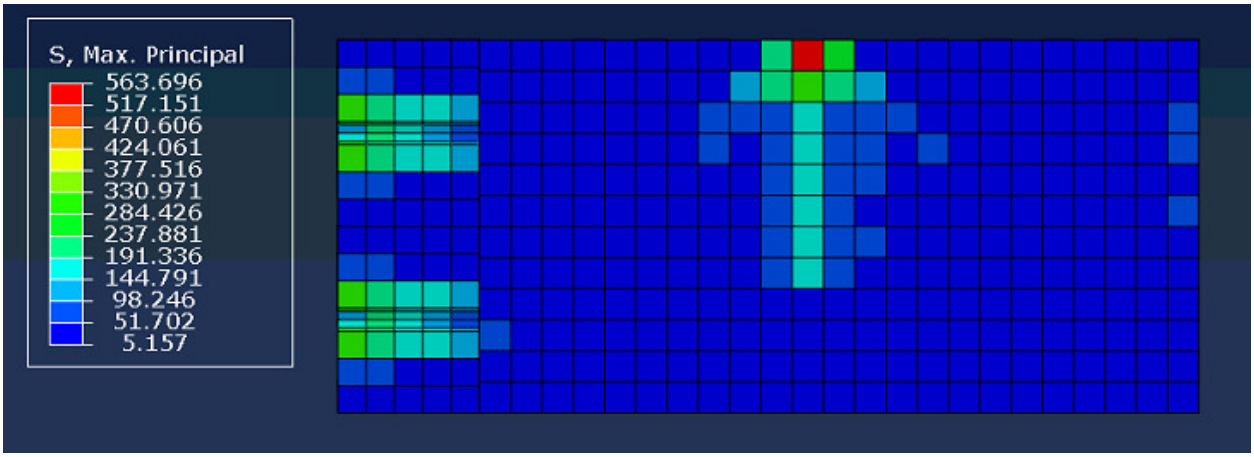

Figure 66. Stress distribution under dowels and tie bars at corner of PCC pavement slab with 30 in (760 mm) tie bar spacing and truck load on wheel path.

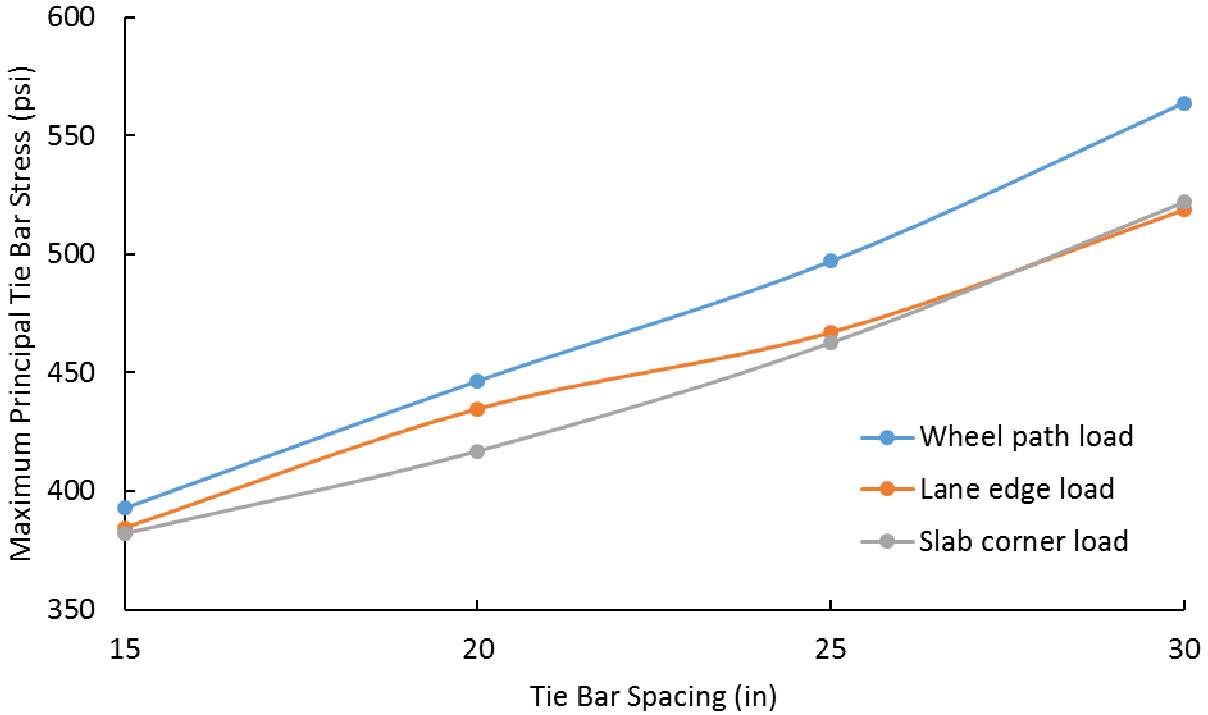

Figure 67. Maximum principal stress versus tie bar spacing due to wheel path, lane edge, and corner load (Truck) combined with NTG and EBITD for 1.5 in (38 mm) dowel diameter and 12 in (305 mm) dowel spacing in a 15 ft (4.6 m) long by 12 ft (3.7 m) wide by 12 in (305 mm) thick PCC pavement slab. (1 in = 25.4 mm, 1 psi = 6.89 kPa)

Table 30. Maximum principal stress versus tie bar spacing due to wheel path, lane edge, and corner load (Truck) combined with NTG and EBITD for 1.5 in dowel diameter and 12 in dowel spacing in a 15 ft long by 12 ft wide by 12 in thick PCC pavement slab. (English units)

Load position	Wheel Path			Lane Edge			Slab Corner		
Tie bar spacing (in)	Maximum stress Dowel (psi)	Tie (psi)	Tie bar stress decrease	Maximum stress Dowel (psi)	Tie (psi)	Tie bar stress decrease	Maximum stress Dowel (psi)	Tie (psi)	Tie bar stress decrease
30	428	564	0%	398	519	0%	395	522	0%
25	430	497	12%	400	467	10%	397	463	11%
20	430	446	21%	402	435	16%	398	417	20%
15	431	393	30%	402	385	26%	398	382	27%

Table 31. Maximum principal stress versus tie bar spacing due to wheel path, lane edge, and corner load (Truck) combined with NTG and EBITD for 38 mm dowel diameter and 305 mm dowel spacing in a 4.6 m long by 3.7 m wide by 305 mm thick PCC pavement slab. (metric units)

Load position	Wheel Path			Lane Edge			Slab Corner		
Tie bar spacing (mm)	Maximum stress Dowel (kPa)	Tie (kPa)	Tie bar stress decrease	Maximum stress Dowel (kPa)	Tie (kPa)	Tie bar stress decrease	Maximum stress Dowel (kPa)	Tie (kPa)	Tie bar stress decrease
762	2948	3887	0%	2743	3575	0%	2723	3598	0%
635	2963	3426	12%	2761	3219	10%	2737	3189	11%
508	2968	3078	21%	2773	2997	16%	2742	2874	20%
381	2973	2708	30%	2770	2652	26%	2744	2634	27%

13 Concrete Fatigue Calculations

Cracking occurs in concrete pavements due to fatigue of concrete slabs caused by repeated truck and environmental loads or by material related issues. In the case of repeated loads, tensile stresses in the concrete pavement are critical and therefore the primary consideration in concrete pavement thickness design. Fatigue damage is also used to evaluate the performance of concrete pavements. Fatigue damage is determined according to Miner's [1945] hypothesis of linear accumulation of damage under repeated loads as given in following expression:

$$Fatigue\ Damage\ (FD) = \sum \frac{n_i}{N_i} = 1.0 \quad (16)$$

where:

n_i = The actual number of load applications under condition i

N_i = The allowable number of load applications to failure under condition i.

According to the hypothesis, fatigue damage under different truck and environmental loads can be summed together, and the material is fractured if the accumulated fatigue damage reaches1.0. However, the accumulated damage under a calibrated system with a given reliability does not have to be 1.0 [Zollinger and Barenberg, 1989]. Hilsdorf and Kesler [1976] reported Miner's hypothesis may result in inaccurate fatigue strength predictions; additional studies indicated deviations from Miner's hypothesis were insignificant due to the large variability of strength and fatigue life of typical concrete materials [Ballinger, 1972].

13.1 Fatigue models

Most of the available fatigue models utilized the concept of stress ratio (SR) to determine the fatigue life of concrete pavement. The stress ratio a concrete pavement experiences is typically related to the logarithm of loads necessary to cause fatigue failure. The stress ratio is defined as the ratio of tensile bending stresses induced in the concrete slab to the concrete modulus of rupture.

$$SR = \frac{\sigma_{total}}{MR} \quad (17)$$

where:

σ = Total tensile stress under traffic and environmental loads at critical locations.

MR = Modulus of rupture obtained from third-point loading of beams after 28 days of curing.

Roesler [1998] observed the flexural strength and modulus of rupture of plain concrete tested in a fully supported slab configuration be as much as 30% greater than those of the same concrete tested in a beam configuration. Also, Roesler et al. [2003] and Littleton [2003] showed the flexural strength of the concrete slab is dependent on the geometry, material properties, and boundary conditions, and the slab flexural strength is twice the beam flexural strength.

Several types of fatigue models have been developed to estimate the permissible number of load repetitions to failure for a given stress level in concrete pavement. The most frequently

used models are the Zero-Maintenance fatigue model, the PCA Beam Fatigue model, the MEPDG fatigue model, and the Tepfers and Kutti [1979] fatigue model. These fatigue models are not expected to produce similar results as they were developed under different assumptions and different performance equations for relating fatigue damage to slab cracking in field.

The Zero-Maintenance fatigue model was proposed by Darter and Barenberg [1977] and is expressed in equation (18), where *N* is the number of load repetitions, and *SR* is the stress ratio. The model was derived by compiling several laboratory beam fatigue tests into a single equation at 50% probability of failure.

$$\log N = 17.61 - 17.61\,SR \tag{18}$$

The PCA Beam Fatigue model [Packard, 1973; Packard and Tayabji, 1983] was developed using concrete beams with 5% complete beam fractures. The stresses used to develop the model were calculated at the bottom of the beam using the bending equation. The model suggests a beam with SR < 0.45 will carry unlimited load applications. The model is given in the following expressions.

$$\begin{aligned} &\log N = 11.737 - 12.077\,SR \quad for\ SR \geq 0.55 \\ &\mathrm{N} = \left[\frac{4.2577}{SR - 0.4325}\right]^{3.268} \quad for\ 0.45 < SR < 0.55 \\ &\mathrm{N} = unlimited \quad for\ SR \leq 0.45 \end{aligned} \tag{19}$$

The Mechanistic-Empirical Pavement Design Guide (MEPDG) uses the fatigue model developed by Darter et al. [2001] and Yu et al. [2004] using several highway databases to determine the number of load repetitions to failure with 50% slab cracking. The load and temperature stresses were determined using ISLAB2000 at lane-shoulder joint edge. The model can be expressed as follows:

$$logN = 2.0\ SR^{-1.22} \tag{20}$$

The Tepfers and Kutti [1971] fatigue model utilizes the concept of stress range to calculate the fatigue life of concrete pavement rather than just maximum critical stresses. Stress range has been reported to have a significant influence on the fatigue life of concrete pavement [Murdock and Kesler, 1958; Awad and Hilsdorf, 1974; Tepfers, 1979; and Tepfers and Kutti, 1979]. Rufino [2003] reported the use of the maximum stress concept in the airfield rigid pavement design may not be the best approach since the actual stresses which cause fatigue damage could be incorrectly estimated. The residual stresses caused by EBITD and temperature variation can be considered in the fatigue damage calculation with the concept of stress range. The stress range-based model proposed by Tepfers and Kutti [1971] can be expressed in the following equation.

$$\log_{10} N = \frac{1 - \frac{\sigma_{max}}{MOR}}{\beta\,(1 - R)} \tag{21}$$

where:

N = The number of load applications to failure at 50% reliability

σ_{max} = The maximum tensile stress under temperature and load cycle

MOR = The modulus of rupture
β = Calibration coefficient, 0.0685 for concrete by Tepfers (1979a)
$R = \sigma_{min} / \sigma_{max}$
σ_{min} = Residual tensile stress under temperature effect only

Domenichini and Machionna [1981] modified the Tepfers and Kutti equation by modifying the calibration factor from 0.0685 to 0.0954 to account for factors not included in beam fatigue testing such as rest period, variability in the environmental stresses, and variability of concrete thickness and modulus of rupture. Rao and Roesler [2004] and Rao [2005] found, based on accelerated pavement testing in California, the concept of stress range in fatigue analysis best predicted the location of crack initiation in the concrete slab.

Once the allowable number of load applications is determined, the fatigue damage can be estimated using Equation 22, which resembles Miner's [1945] Equation (Equation 16), except the sum is not set equal to 1.

$$FD = \sum_i \frac{n_i}{N_i} \tag{22}$$

In Equation 22, fatigue damage is related to the percentage of cracked slabs in the field using calibrated models. These models are highly dependent on the quality of data used for calibration, such as material properties, traffic, and geometry [Bordelon and Roesler, 2009]. In the MEPDG, fatigue damage is related to percent slabs cracking P_{cr} at 50% and 95% reliability by:

$$P_{cr}^{50\%} = \frac{100}{1 + FD^{-1.98}} \tag{23}$$

$$P_{cr}^{95\%} = P_{cr}^{50\%} + 1.64\, Se \tag{24}$$

$$Se = \left(5.3116\, P_{cr}^{50\%}\right)^{0.3903} + 2.99 \tag{25}$$

where Se is the standard deviation obtained from national calibration of the MEPDG. In this project, data are used from the national calibration of AASHTOWare Pavement ME Design in lieu of a calibration specific to Ohio.

The above cracking equations were developed primarily by using LTPP data on cracked JPCP pavement sections observed in test sections.

13.2 Damage Calculations

The fatigue models presented earlier were used to calculate the ultimate number of load applications until failure for each slab thickness and length. Since most rigid pavement highways are constructed with tied PCC shoulders, the maximum tensile stress at the top of the concrete slab on a pavement with tied PCC shoulders was utilized to estimate accumulated damage. The maximum tensile stress was found by considering the EBITD as negative temperature gradient of -2.2 F°/in (-0.48 C°/cm), which was added to the maximum negative temperature gradient found in Route 23 -2.32 F°/in (-0.51 C°/cm) in the stress calculations along with truck load. This

represents the worst case scenario for the pavement. The slab lengths considered in this analysis were 12 ft (3.7 m), 13 ft (4.0 m), 13.5 ft (4.1 m), 14 ft (4.3 m), 14.5 ft (4.4 m), 15 ft (4.6 m), 16 ft (4.9 m), and 17 ft (5.2 m). For each slab length, the following PCC thicknesses were considered: 9 in (229 mm), 10 in (254 mm), 11 in (279 mm), 12 in (305 mm), 13 in (330 mm), 14 in (356 mm), and 15 in (381 mm). The ultimate number of such load applications for each slab thickness and spacing are shown in Table 32 and Table 33.

Table 32. The ultimate number of load applications Nf predicted by each damage model for each slab length and slab thickness. (inf. = infinity)

Slab length		PCC thickness		S max		S max T		Zero-Maintenance	MEPDG	Tepfers and Kutti	PCA
(ft)	(m)	(in)	(mm)	(psi)	(kPa)	(psi)	(kPa)	Log Nf	Log Nf	Log Nf	Log Nf
12	3.7	9	229	272	1878	173	1191	9.6	5.2	21.8	7.5
		10	254	263	1813	176	1213	9.9	5.5	24.8	inf.
		11	279	235	1623	153	1054	10.7	6.3	25.3	inf.
		12	305	214	1478	140	965	11.3	7.0	27.0	inf.
		13	330	197	1361	131	902	11.8	7.8	29.0	inf.
		14	356	181	1248	122	844	12.3	8.6	31.5	inf.
		15	381	171	1177	117	807	12.6	9.3	33.3	inf.
13	4.0	9	229	288	1986	188	1296	9.2	4.9	21.9	6.4
		10	254	280	1927	191	1315	9.4	5.1	24.5	6.9
		11	279	252	1741	166	1147	10.2	5.7	24.8	inf.
		12	305	231	1593	154	1059	10.8	6.4	26.8	inf.
		13	330	213	1472	142	981	11.3	7.1	28.2	inf.
		14	356	197	1356	133	915	11.8	7.8	30.2	inf.
		15	381	186	1280	128	880	12.2	8.4	32.2	inf.
13.5	4.1	9	229	295	2034	196	1348	9.0	4.8	22.0	6.1
		10	254	287	1978	198	1365	9.2	4.9	24.6	6.4
		11	279	260	1795	174	1196	10.0	5.5	24.8	inf.
		12	305	239	1646	160	1106	10.6	6.2	26.8	inf.
		13	330	221	1527	149	1026	11.1	6.7	28.1	inf.
		14	356	209	1442	139	955	11.5	7.2	28.2	inf.
		15	381	198	1362	133	918	11.8	7.8	30.1	inf.
14	4.3	9	229	309	2130	202	1395	8.5	4.5	20.5	5.6
		10	254	299	2064	204	1403	8.8	4.7	22.8	5.9
		11	279	275	1895	180	1244	9.5	5.2	23.0	7.3
		12	305	252	1738	167	1151	10.2	5.8	25.1	inf.
		13	330	234	1615	155	1066	10.7	6.3	26.2	inf.
		14	356	216	1490	145	996	11.3	7.0	28.2	inf.
		15	381	205	1416	140	966	11.6	7.4	30.2	inf.

Table 33. The ultimate number of load applications Nf predicted by each damage model for each slab length and slab thickness. (inf. = infinity) (ctd)

Slab length		PCC thickness		S max		S max T		Zero-Maintenance	MEPDG	Tepfers and Kutti	PCA
(ft)	(m)	(in)	(mm)	(psi)	(kPa)	(psi)	(kPa)	Log Nf	Log Nf	Log Nf	Log Nf
14.5	4.4	9	229	309	2131	211	1453	8.5	4.5	22.3	5.6
		10	254	302	2080	213	1466	8.8	4.6	24.6	5.8
		11	279	276	1906	188	1298	9.5	5.1	24.7	7.1
		12	305	255	1755	174	1202	10.1	5.7	26.7	inf.
		13	330	237	1634	162	1118	10.7	6.2	28.0	inf.
		14	356	219	1509	151	1044	11.2	6.8	30.1	inf.
		15	381	207	1429	146	1004	11.5	7.3	32.1	inf.
15	4.6	9	229	322	2222	218	1501	8.2	4.3	20.8	5.3
		10	254	309	2130	220	1517	8.5	4.5	24.6	5.6
		11	279	284	1961	196	1348	9.3	5.0	24.6	6.6
		12	305	263	1810	181	1250	9.9	5.5	26.5	inf.
		13	330	245	1690	169	1165	10.4	6.0	27.8	inf.
		14	356	227	1562	158	1088	11.0	6.6	29.9	inf.
		15	381	215	1481	152	1045	11.3	7.0	31.8	inf.
16	4.9	9	229	335	2312	233	1610	7.8	4.1	21.2	5.0
		10	254	323	2229	235	1622	8.1	4.3	24.7	5.2
		11	279	300	2071	211	1454	8.8	4.7	24.5	5.9
		12	305	278	1920	196	1352	9.4	5.1	26.4	7.0
		13	330	261	1801	184	1266	9.9	5.5	27.8	inf.
		14	356	242	1669	171	1181	10.5	6.1	29.8	inf.
		15	381	230	1586	164	1134	10.9	6.4	31.6	inf.
17	5.2	9	229	342	2358	250	1723	7.6	4.0	23.3	4.9
		10	254	337	2324	250	1726	7.7	4.0	24.8	5.0
		11	279	316	2178	227	1562	8.3	4.4	24.4	5.4
		12	305	294	2028	211	1455	9.0	4.8	26.3	6.1
		13	330	277	1909	198	1367	9.5	5.1	27.7	7.1
		14	356	257	1774	186	1279	10.1	5.6	29.9	inf.
		15	381	245	1686	178	1227	10.4	6.0	31.7	inf.

The 12 ft (3.7 m) long slab would sustain a great amount of combined temperature and load applications, and the number increases as the thickness of pavement increases. Slab thickness of 10 in (254 mm) might be enough to sustain around ten billion (10^{10}) load applications based on the zero-maintenance model. The PCA model suggests this design will sustain an unlimited number of load applications, based on 600 psi (4.1 MPa) flexural strength, which is the value required by ODOT to open a road to traffic. The MEPDG model resulted in lower Nf-values; however, this model was developed from LTPP databases. The best way to

evaluate this model is through the use of the AASHTOWare Pavement ME-Design program, which was used and is discussed later in this report, though the AASHTOWare program presents different results than the calculation presented here because the program uses a different approach to computing damage, which involves monthly and daily traffic distributions and seasonal and daily temperature fluctuations based on the selected weather station.

Using the ultimate number of load applications obtained from Zero-Maintenance and PCA fatigue damage models, the fatigue damage of concrete pavements after 50 years of combined temperature and load applications using Equation 16 was estimated. The Tepfers model consistently over predicted Nf, implying unrealistically long pavement life; therefore the model was dropped from subsequent analysis. The 50 years of traffic data were generated by AASHTOWare Pavement ME Design v. 2.2 using the average of the most recent three years (2015-2017) of I-70 AADTT data obtained from ODOT's Transportation Data Management System (TDMS). The average growth rate (3%) on I-70 from the past three years on TDMS was used in the linear growth model following typical ODOT practice and the recommendations of Abbas and Frankhouser [2012]. These traffic data were then used along with Nf to calculate the cumulative damage occurring in 50 years of combined axle and negative temperature gradient loads using Equation 16. Also, the percent cracking at 50% reliability was obtained using Equation 23. The results are shown in Table 34 and Table 35, which expresses the percentages with two digits, and in scientific notation since in some cases the computed values were extremely low.

The minimum thicknesses required for a given slab length for a service life of 50 years and infinity for each fatigue model, except Tepfers and Kutti, are shown in Table 36. The thickness needed for a 15 ft (4.6 m) slab length to obtain a 50 year life based on fatigue cracking was 12.2 in (310 mm), 10.3 in (262 mm), and 16.8 in (427 mm) for the PCA, Zero Maintenance, and MEPDG models respectively. The thicknesses needed for an infinite life for the same slab length are 13 in (330 mm) and 11 in (279 mm) for the PCA and Zero Maintenance models, while the MEPDG model does not provide an infinite life value.

Table 34. Cumulative damage after 50 years of combined axle and negative temperature gradient loads using different fatigue models. Red values indicate failure due to transverse cracking within 50 years.

Slab length		PCC thickness		S max		S max T		50-yr Percent Slab Cracking at 50% Reliability					
(ft)	(m)	(in)	(mm)	(psi)	(kPa)	(psi)	(kPa)	Zero-Maintenance		MEPDG		PCA	
12	3.7	9	229	272	1878	173	1191	2.87E-01	0.29%	1.00E+02	100.00%	9.77E+01	97.72%
		10	254	263	1813	176	1213	8.13E-02	0.08%	1.00E+02	100.00%	4.99E-02	0.05%
		11	279	235	1623	153	1054	2.04E-03	0.00%	1.00E+02	99.99%	4.99E-02	0.05%
		12	305	214	1478	140	965	1.23E-04	0.00%	9.97E+01	99.75%	4.99E-02	0.05%
		13	330	197	1361	131	902	1.28E-05	0.00%	9.31E+01	93.14%	4.99E-02	0.05%
		14	356	181	1248	122	844	1.40E-06	0.00%	2.04E+01	20.35%	4.99E-02	0.05%
		15	381	171	1177	117	807	3.52E-07	0.00%	1.35E+00	1.35%	4.99E-02	0.05%
13	4.0	9	229	288	1986	188	1296	2.27E+00	2.27%	1.00E+02	100.00%	9.74E+01	97.45%
		10	254	280	1927	191	1315	7.44E-01	0.74%	1.00E+02	100.00%	2.55E-03	0.00%
		11	279	252	1741	166	1147	2.01E-02	0.02%	1.00E+02	100.00%	2.55E-03	0.00%
		12	305	231	1593	154	1059	1.13E-03	0.00%	1.00E+02	99.98%	2.55E-03	0.00%
		13	330	213	1472	142	981	1.09E-04	0.00%	9.97E+01	99.70%	2.55E-03	0.00%
		14	356	197	1356	133	915	1.14E-05	0.00%	9.19E+01	91.89%	2.55E-03	0.00%
		15	381	186	1280	128	880	2.63E-06	0.00%	4.62E+01	46.24%	0.00E+00	0.00%
13.5	4.1	9	229	295	2034	196	1348	5.63E+00	5.63%	1.00E+02	100.00%	1.00E+02	100.00%
		10	254	287	1978	198	1365	1.95E+00	1.95%	1.00E+02	100.00%	1.00E+02	99.98%
		11	279	260	1795	174	1196	5.79E-02	0.06%	1.00E+02	100.00%	4.99E-02	0.05%
		12	305	239	1646	160	1106	3.20E-03	0.00%	1.00E+02	100.00%	4.99E-02	0.05%
		13	330	221	1527	149	1026	3.18E-04	0.00%	9.99E+01	99.93%	4.99E-02	0.05%
		14	356	209	1442	139	955	6.04E-05	0.00%	9.93E+01	99.33%	4.99E-02	0.05%
		15	381	198	1362	133	918	1.28E-05	0.00%	9.32E+01	93.21%	4.99E-02	0.05%
14	4.3	9	229	309	2130	202	1395	2.79E+01	27.86%	1.00E+02	100.00%	1.00E+02	100.00%
		10	254	299	2064	204	1403	9.68E+00	9.68%	1.00E+02	100.00%	1.00E+02	100.00%
		11	279	275	1895	180	1244	3.95E-01	0.40%	1.00E+02	100.00%	9.92E+01	99.23%
		12	305	252	1738	167	1151	1.91E-02	0.02%	1.00E+02	100.00%	4.99E-02	0.05%
		13	330	234	1615	155	1066	1.73E-03	0.00%	1.00E+02	99.99%	4.99E-02	0.05%
		14	356	216	1490	145	996	1.54E-04	0.00%	9.98E+01	99.82%	4.99E-02	0.05%
		15	381	205	1416	140	966	3.66E-05	0.00%	9.86E+01	98.60%	4.99E-02	0.05%

Table 35. Cumulative damage after 50 years of combined axle and negative temperature gradient loads using different fatigue models. Red values indicate failure due to transverse cracking within 50 years. (ctd)

Slab length		PCC thickness		S max		S max T		50-yr Percent Slab Cracking at 50% Reliability					
(ft)	(m)	(in)	(mm)	(psi)	(kPa)	(psi)	(kPa)	Zero-Maintenance		MEPDG		PCA	
14.5	4.4	9	229	309	2131	211	1453	2.81E+01	28.07%	1.00E+02	100.00%	1.00E+02	100.00%
		10	254	302	2080	213	1466	1.26E+01	12.57%	1.00E+02	100.00%	1.00E+02	100.00%
		11	279	276	1906	188	1298	4.96E-01	0.50%	1.00E+02	100.00%	9.96E+01	99.61%
		12	305	255	1755	174	1202	2.66E-02	0.03%	1.00E+02	100.00%	4.99E-02	0.05%
		13	330	237	1634	162	1118	2.55E-03	0.00%	1.00E+02	99.99%	4.99E-02	0.05%
		14	356	219	1509	151	1044	2.24E-04	0.00%	9.99E+01	99.89%	4.99E-02	0.05%
		15	381	207	1429	146	1004	4.77E-05	0.00%	9.91E+01	99.05%	4.99E-02	0.05%
15	4.6	9	229	322	2222	218	1501	6.93E+01	69.34%	1.00E+02	100.00%	1.00E+02	100.00%
		10	254	309	2130	220	1517	2.76E+01	27.63%	1.00E+02	100.00%	1.00E+02	100.00%
		11	279	284	1961	196	1348	1.43E+00	1.43%	1.00E+02	100.00%	1.00E+02	99.97%
		12	305	263	1810	181	1250	7.69E-02	0.08%	1.00E+02	100.00%	4.99E-02	0.05%
		13	330	245	1690	169	1165	7.43E-03	0.01%	1.00E+02	100.00%	4.99E-02	0.05%
		14	356	227	1562	158	1088	6.24E-04	0.00%	1.00E+02	99.97%	4.99E-02	0.05%
		15	381	215	1481	152	1045	1.29E-04	0.00%	9.98E+01	99.77%	4.99E-02	0.05%
16	4.9	9	229	335	2312	233	1610	9.29E+01	92.95%	1.00E+02	100.00%	1.00E+02	100.00%
		10	254	323	2229	235	1622	7.25E+01	72.46%	1.00E+02	100.00%	1.00E+02	100.00%
		11	279	300	2071	211	1454	1.08E+01	10.81%	1.00E+02	100.00%	1.00E+02	100.00%
		12	305	278	1920	196	1352	6.42E-01	0.64%	1.00E+02	100.00%	9.98E+01	99.81%
		13	330	261	1801	184	1266	6.42E-02	0.06%	1.00E+02	100.00%	4.99E-02	0.05%
		14	356	242	1669	171	1181	4.99E-03	0.00%	1.00E+02	100.00%	4.99E-02	0.05%
		15	381	230	1586	164	1134	9.91E-04	0.00%	1.00E+02	99.98%	4.99E-02	0.05%
17	5.2	9	229	342	2358	250	1723	9.70E+01	96.95%	1.00E+02	100.00%	1.00E+02	100.00%
		10	254	337	2324	250	1726	9.43E+01	94.33%	1.00E+02	100.00%	1.00E+02	100.00%
		11	279	316	2178	227	1562	4.93E+01	49.33%	1.00E+02	100.00%	1.00E+02	100.00%
		12	305	294	2028	211	1455	5.01E+00	5.01%	1.00E+02	100.00%	1.00E+02	100.00%
		13	330	277	1909	198	1367	5.27E-01	0.53%	1.00E+02	100.00%	9.97E+01	99.67%
		14	356	257	1774	186	1279	3.83E-02	0.04%	1.00E+02	100.00%	4.99E-02	0.05%
		15	381	245	1686	178	1227	6.99E-03	0.01%	1.00E+02	100.00%	4.99E-02	0.05%

Table 36. Minimum thickness needed for 50 year life and infinite life for each damage model.

PCA					
Slab Length (ft)	Minimum 50 year thickness (in)	Minimum infinite life thickness (in)	Slab Length (m)	Minimum 50 year thickness (mm)	Minimum inifinite life thickness (mm)
12	9.5	10	3.7	241	254
13	10.5	11	4.0	267	279
13.5	10.9	12	4.1	277	305
14	11.6	13	4.3	295	330
14.5	11.7	13	4.4	297	330
15	12.2	13	4.6	310	330
16	13.0	14	4.9	330	356
17	13.8	15	5.2	351	381
Zero-Maintenance					
12	7.6	9	3.7	193	229
13	8.5	9	4.0	216	229
13.5	8.9	9	4.1	226	229
14	9.7	10	4.3	246	254
14.5	9.8	10	4.4	249	254
15	10.3	11	4.6	262	279
16	11.1	12	4.9	282	305
17	11.8	12	5.2	300	305
MEPDG					
12	14.5	15	3.7	368	381
13	15.3	X	4.0	389	X
13.5	15.9	X	4.1	404	X
14	16.3	X	4.3	414	X
14.5	16.5	X	4.4	419	X
15	16.8	X	4.6	427	X
16	17.7	X	4.9	450	X
17	18.8	X	5.2	478	X

14 Evaluation of Long Term Pavement Performance of Concrete Pavement

There is more than one mechanism by which concrete pavements fail, depending on the pavement structure, material properties, base type, subgrade type, and environment. The Mechanistic-Empirical Pavement Design Guide uses three criteria for failure of rigid pavements: International Roughness Index (IRI), faulting, and percent slabs cracked; the AASHTOWare program computes and plots values for each measure at a selected reliability level and compares to the failure criteria. A good pavement design is one that minimizes all of these major distresses throughout its design life. AASHTOWare. The failure criteria used are: IRI ≥ 160 in/mi (2.50 m/km), faulting ≥ 0.16 in (4.1 mm), and fatigue cracking ≥ 10%; the selected reliability level is 50%. AASHTOWare Pavement ME-Design v. 2.4 was used in this study.

No calibration exists for Ohio, though guidelines were prepared by Applied Research Associates [Mallela et al., 2009]. Mallela et al. [2012, p. 76] concluded the national calibration factors for cracking and faulting were sufficient for use in Ohio and local calibration may not be necessary. There was good correlation between the measured and predicted IRI but there is a bias of unknown origin; their local calibration indicated joint spacing was the only factor which had a significant effect [Mallela et al, 2012, p. 76]. However, the effect of IRI is less significant, so emphasis was placed on the cracking and faulting results using the national calibration.

ODOT baseline values were used for the material properties of PCC layer [Mallela et al, 2012, p. 76] assuming limestone aggregate, and the material properties of the supporting layers were kept constant to eliminate any possible bias from altered material characteristics. In particular, E for concrete was 5,000,000 psi (34.5 GPa) with coefficient of thermal expansion 5.4×10^{-6} $F^{\circ-1}$ (9.7×10^{-6} $C^{\circ-1}$), and M_R was 600 psi (4.14 MPa). The modeled pavement structure consisted of a given thickness of PCC placed on 6 in (152 mm) DGAB, 12 in (305 mm) stabilized subgrade, and untreated subgrade as considered earlier in this study. The PCC slab thickness was set to values from 9 in (229 mm) to 15 in (381 mm) in 1 in (25.4 mm) intervals. The slab length was set to 12 ft (3.7 m), 13 ft (4.0 m), 13.5 ft (4.1 m), 14 ft (4.3 m), 14.5 ft (4.4 m), 15 ft (4.6 m), 16 ft (4.9 m), or 17 ft (5.2 m). Tied PCC shoulders were included, with dowel bars of 1.5 in (38 mm) diameter spaced at 12 in (305 mm) were used for all pavement structures. The design life was set at 50 years, and climate data were derived from stored data in the software from weather stations in Columbus (Station 04804) and Cincinnati (Station 93812); the 36 years of weather data stored in the database (from January 1, 1979 through June 30, 2015 in the latest version) were cycled through 1.39 times to simulate 50 years of weather. The default permanent built-in temperature difference was also applied to account for pavement curling and warping. The station in Columbus was chosen as representative of average conditions and was near the section of I-70 where traffic data were collected, and the station in Cincinnati was representative of stations with higher freeze-thaw cycles.

The initial AADTT value was 10672, the average AADTT of the previous three years (2015-2017) on I-70 data in ODOT's Transportation Data Management System (TDMS). Of the three growth rate models presented in the MEPDG [ERES, 2004]. The linear growth model [ERES, 2004] currently used by ODOT [Abbas and Frankhouser, 2012, p. 114] was adopted in this analysis with a 3% annual growth rate calculated by averaging the last three years of I-70 data in ODOT's TDMS. The software accompanying the Akron report was used to generate a statewide MEPDG input traffic database for use in AASHTOWare.

Abbas and Fankhouser [2012] indicated the segment of I-70 from which data were collected is classified as a Truck Traffic Classification TTC1 route. The software generated truck distribution data were similar to the TTC1 data in the AASHTOWare program for nationwide values. Abbas and Frankhouser [2012] were concerned the default value of Class 9 in the MEPDG was not represented correctly, but the statewide results generated from the report program for this project showed that the class distribution on I-70 is almost identical to the national default. The nationwide data in the software were selected for the modeling.

An example of program output is shown for illustrative purposes in Figure 68, for a 12 ft (3.7 m) long slab with 11 in (279 mm) thick PCC. Reliability level was set to 50%.

Results of the AASHTOWare runs with 50 year values of IRI, faulting, and transverse cracking, are tabulated in Table 37 and Table 38 (English units) and in Table 39 and Table 40 (metric units). Results in red shaded cells indicate a failed design criterion. Generally speaking, shorter slab lengths and thicker pavements tended to perform better. The minimum thicknesses to meet all three criteria were 12 in (305 mm) for 12 ft (3.7 m), 13 ft (4.0 m) and 13.5 ft (4.1 m) slab lengths, when considering both Columbus (04804) and Cincinnati (93812) weather stations.

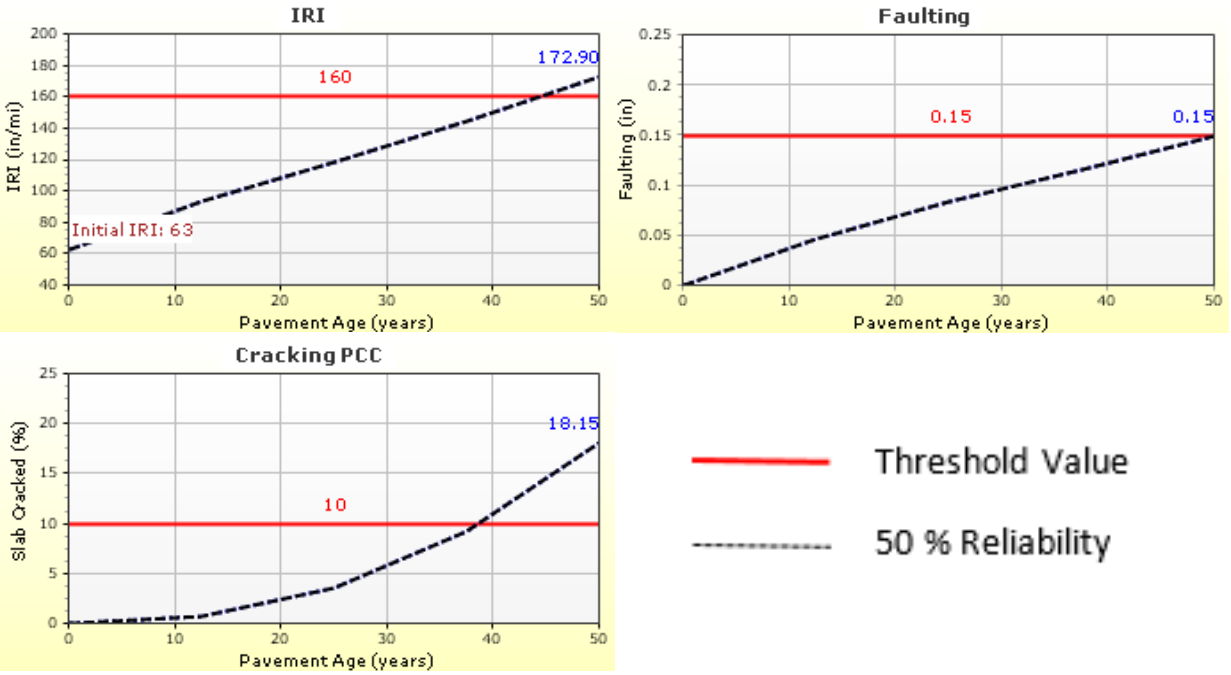

Figure 68. IRI, faulting, and cracking for 12 ft (3.7 m) slab length and 11 in (279 mm) slab thickness computed by AASHTOWare Pavement ME Design program. (1 in/mi = 0.016 m/km, 1 in =25.4 mm)

Table 37. AASHTOware computed 50 year values for design criteria for various slab length and thickness designs. Shaded cells indicate failed designs. (English units)

Station		Cincinnati			Columbus		
Slab length (ft)	PCC Thickness (in)	IRI (in/mi)	Faulting (in)	Transverse cracking (%)	IRI (in/mi)	Faulting (in)	Transverse cracking (%)
12	9	214.6	0.14	66.6	212.3	0.14	61.0
	10	169.2	0.14	12.6	168.2	0.14	9.7
	11	160.0	0.14	1.0	157.3	0.13	0.9
	12	156.0	0.14	0.2	152.8	0.13	0.1
	13	152.1	0.13	0.0	152.1	0.13	0.0
	14	150.3	0.13	0.0	149.2	0.12	0.0
	15	150.2	0.13	0.0	150.2	0.13	0.0
13	9	239.4	0.15	96.1	240.9	0.16	95.0
	10	212.0	0.15	65.2	208.4	0.15	59.0
	11	172.9	0.15	18.2	167.8	0.14	14.4
	12	156.1	0.15	1.5	153.8	0.14	1.7
	13	152.2	0.14	0.6	152.5	0.14	0.4
	14	150.5	0.14	0.1	150.2	0.13	0.1
	15	143.2	0.13	0.0	141.9	0.12	0.0
13.5	9	240.7	0.16	96.8	242.3	0.16	95.8
	10	212.7	0.16	65.3	209.2	0.16	59.1
	11	173.5	0.16	18.2	168.5	0.151	14.4
	12	156.9	0.15	1.5	154.8	0.15	1.7
	13	153.4	0.15	0.6	153.8	0.15	0.4
	14	152.2	0.15	0.1	151.9	0.14	0.1
	15	153.1	0.15	0.0	149.1	0.14	0.0
14	9	242.1	0.17	97.7	243.9	0.17	96.8
	10	213.7	0.17	65.6	210.2	0.16	59.3
	11	174.4	0.16	18.2	169.5	0.16	14.4
	12	158.0	0.16	1.5	156.0	0.151	1.7
	13	154.9	0.16	0.6	155.3	0.151	0.4
	14	154.1	0.15	0.1	153.9	0.15	0.1
	15	155.5	0.16	0.0	154.1	0.15	0.0
Failure criteria		160	0.16	10%	160	0.16	10%

Table 38. AASHTOware computed 50 year values for design criteria for various slab length and thickness designs. Shaded cells indicate failed designs. (English units) (ctd)

Station		Cincinnati			Columbus		
Slab length (ft)	PCC Thickness (in)	IRI (in/mi)	Faulting (in)	Transverse cracking (%)	IRI (in/mi)	Faulting (in)	Transverse cracking (%)
14.5	9	244.6	0.18	99.9	247.0	0.18	99.8
	10	239.9	0.17	96.4	240.5	0.17	95.3
	11	224.1	0.17	77.4	218.0	0.17	72.2
	12	184.8	0.17	32.6	178.6	0.16	27.6
	13	160.5	0.16	5.4	161.1	0.16	5.5
	14	157.6	0.16	2.0	157.0	0.16	1.5
	15	158.5	0.17	0.7	157.0	0.16	0.5
15	9	245.2	0.18	99.9	247.6	0.18	99.9
	10	240.7	0.18	96.4	241.4	0.18	95.4
	11	225.1	0.18	77.5	219.1	0.17	72.2
	12	186.1	0.18	32.6	179.9	0.17	27.6
	13	162.1	0.17	5.4	162.6	0.17	5.5
	14	159.6	0.17	2.0	159.0	0.17	1.5
	15	160.9	0.18	0.7	159.3	0.17	0.5
16	9	246.0	0.2	100.0	248.4	0.2	100.0
	10	244.8	0.2	99.6	246.2	0.19	99.5
	11	243.0	0.2	97.0	240.5	0.19	96.1
	12	230.2	0.19	83.5	224.4	0.18	79.0
	13	198.8	0.19	46.8	194.3	0.19	40.8
	14	172.0	0.19	13.1	168.7	0.19	9.4
	15	169.3	0.2	6.0	166.7	0.19	4.6
17	9	246.6	0.21	100.0	249.0	0.21	100.0
	10	246.2	0.21	100.0	247.8	0.21	100.0
	11	246.8	0.21	99.6	245.0	0.2	99.5
	12	243.9	0.21	97.7	241.2	0.2	96.9
	13	235.9	0.21	89.1	233.6	0.2	85.7
	14	210.8	0.21	57.0	208.3	0.21	54.4
	15	193.3	0.22	31.3	185.4	0.21	23.5
Failure criteria		160	0.16	10%	160	0.16	10%

Table 39. AASHTOware computed 50 year values for design criteria for various slab length and thickness designs. Shaded cells indicate failed designs. (metric units)

Station		Cincinnati			Columbus		
Slab length (m)	PCC Thickness (mm)	IRI (m/km)	Faulting (mm)	Transverse cracking (%)	IRI (m/km)	Faulting (mm)	Transverse cracking (%)
3.7	229	3.347	3.6	66.6	3.311	3.6	61.0
	254	2.640	3.6	12.6	2.624	3.6	9.7
	279	2.496	3.6	1.0	2.454	3.3	0.9
	305	2.433	3.6	0.2	2.383	3.3	0.1
	330	2.373	3.3	0.0	2.372	3.3	0.0
	356	2.345	3.3	0.0	2.328	3.0	0.0
	381	2.343	3.3	0.0	2.343	3.3	0.0
4.0	229	3.734	3.8	96.1	3.759	4.1	95.0
	254	3.307	3.8	65.2	3.251	3.8	59.0
	279	2.697	3.8	18.2	2.617	3.6	14.4
	305	2.435	3.8	1.5	2.400	3.6	1.7
	330	2.375	3.6	0.6	2.379	3.6	0.4
	356	2.348	3.6	0.1	2.343	3.3	0.1
	381	2.234	3.3	0.0	2.213	3.0	0.0
4.1	229	3.755	4.1	96.8	3.780	4.1	95.8
	254	3.319	4.1	65.3	3.263	4.1	59.1
	279	2.706	4.1	18.2	2.629	3.8	14.4
	305	2.447	3.8	1.5	2.414	3.8	1.7
	330	2.393	3.8	0.6	2.399	3.8	0.4
	356	2.374	3.8	0.1	2.370	3.6	0.1
	381	2.388	3.8	0.0	2.326	3.6	0.0
4.3	229	3.777	4.3	97.7	3.804	4.3	96.8
	254	3.334	4.3	65.6	3.278	4.1	59.3
	279	2.720	4.1	18.2	2.645	4.1	14.4
	305	2.465	4.1	1.5	2.434	3.8	1.7
	330	2.416	4.1	0.6	2.422	3.8	0.4
	356	2.404	3.8	0.1	2.401	3.8	0.1
	381	2.426	4.1	0.0	2.404	3.8	0.0
Failure criteria		2.496	4.1	0.1	2.496	4.1	0.1

Table 40. AASHTOware computed 50 year values for design criteria for various slab length and thickness designs. Shaded cells indicate failed designs. (metric units) (ctd)

Station		Cincinnati			Columbus		
Slab length (m)	PCC Thickness (mm)	IRI (m/km)	Faulting (mm)	Transverse cracking (%)	IRI (m/km)	Faulting (mm)	Transverse cracking (%)
4.4	229	3.815	4.6	99.9	3.853	4.6	99.8
	254	3.742	4.3	96.4	3.752	4.3	95.3
	279	3.495	4.3	77.4	3.401	4.3	72.2
	305	2.883	4.3	32.6	2.786	4.1	27.6
	330	2.503	4.1	5.4	2.513	4.1	5.5
	356	2.459	4.1	2.0	2.450	4.1	1.5
	381	2.473	4.3	0.7	2.449	4.1	0.5
4.6	229	3.824	4.6	99.9	3.862	4.6	99.9
	254	3.755	4.6	96.4	3.766	4.6	95.4
	279	3.512	4.6	77.5	3.418	4.3	72.2
	305	2.903	4.6	32.6	2.807	4.3	27.6
	330	2.528	4.3	5.4	2.537	4.3	5.5
	356	2.489	4.3	2.0	2.480	4.3	1.5
	381	2.510	4.6	0.7	2.485	4.3	0.5
4.9	229	3.838	5.1	100.0	3.876	5.1	100.0
	254	3.818	5.1	99.6	3.841	4.8	99.5
	279	3.791	5.1	97.0	3.752	4.8	96.1
	305	3.591	4.8	83.5	3.501	4.6	79.0
	330	3.102	4.8	46.8	3.032	4.8	40.8
	356	2.682	4.8	13.1	2.631	4.8	9.4
	381	2.641	5.1	6.0	2.600	4.8	4.6
5.2	229	3.846	5.3	100.0	3.884	5.3	100.0
	254	3.841	5.3	100.0	3.865	5.3	100.0
	279	3.850	5.3	99.6	3.823	5.1	99.5
	305	3.805	5.3	97.7	3.763	5.1	96.9
	330	3.681	5.3	89.1	3.644	5.1	85.7
	356	3.288	5.3	57.0	3.250	5.3	54.4
	381	3.015	5.6	31.3	2.893	5.3	23.5
Failure criteria		2.496	4.1	0.1	2.496	4.1	0.1

15 Evaluation of Effect of Weather in Ohio on Performance

The temperature and moisture variations during pavement life can significantly change the material properties of pavement layers and affect pavement response and performance. The Enhanced Integrated Climatic Model (EICM) is a one-dimensional coupled heat and moisture flow model developed to simulate and predict the variation in behavior and properties of pavement and unbound materials under different environmental conditions over the service life [Zapata and Houston, 2008]. The EICM was first developed under NCHRP Project 1-37A for FHWA, then incorporated in the MEPDG, and now is embedded in AASHTOWare Pavement ME Design [Zapata and Houston, 2008]. Since there no stand-alone EICM software available, the evaluation was conducted using the current version of AASHTOWare, Build 2.4. The evaluation consisted of simulating an optimum pavement geometry (12 in (305 mm) slab thickness and 13 ft (4.0 m) slab length) in the software under Ohio weather, which is characterized by 20 weather stations spread across the state using data collected from June 1979 through May 2015 (36 years) as of the time of this simulation; for a 50 year simulation, data were cycled 1.39 times.

The evaluation compared distress results of the selected slab geometry for each weather station in Ohio, looking for significant changes in pavement performance. ODOT baseline values were used for the material properties of PCC layer, and the material properties and structures of the supporting layers were also kept constant to eliminate any possible bias from altered material characteristics. The only variable in this analysis was the climate as determined by selecting a weather stations. Table 41 (Table 42) lists the 20 weather stations with the weather input data for each in English (metric) units: mean annual air temperature, mean annual precipitation, freezing index, and mean annual number of freeze/thaw cycles. The AASHTOWare program predictions at 50% reliability of IRI, faulting, and cracking are also included in the table for each station for the optimum slab geometry are also included in the table, along with the mean, standard deviation, and (where applicable) the coefficient of variation for each column of data.

Table 41. Climate inputs and 50 year output distresses corresponding to each weather station for slab thickness of 12 in (305 mm) and length 13 ft (4.0 m). (English units)

Weather Station	Mean annual air temperature (°F)	Mean annual precipitation (in)	Freezing index (°F - days)	Average annual number of freeze/thaw cycles	IRI (in/mi)	Faulting (in)	Transverse cracking (%)
AKRON, OH-14813	49.29	37.34	692.29	63.11	159.48	0.14	2.77
AKRON, OH-14895	51.01	36.79	538.74	70.94	154.11	0.14	1.49
CINCINNATI, OH-93812	53.71	40.33	391.10	61.77	159.08	0.15	1.49
CLEVELAND, OH-14820	50.21	34.32	631.71	56.42	156.17	0.14	2.62
CLEVELAND, OH-04854	50.21	34.32	631.71	56.42	156.17	0.14	2.62
COLUMBUS, OH-04804	51.46	35.99	569.12	59.48	153.83	0.14	1.72
COLUMBUS, OH-14821	51.46	35.99	569.12	59.48	153.79	0.14	1.67
COVINGTON/CINCINNATI, OH-93814	54.81	42.42	329.82	63.59	153.2	0.14	1.32
DAYTON, OH-93815	51.56	38.38	598.31	57.14	153.71	0.14	1.66
DEFIANCE, OH-04851	51.06	34.89	661.30	63.25	156.18	0.14	1.46
FINDLAY, OH-14825	51.24	34.38	636.42	61.85	155.89	0.14	2.23
HAMILTON, OH-53855	52.66	38.94	483.73	66.54	155.83	0.14	2.02
MANSFIELD, OH-14891	49.51	37.55	718.68	59.54	158.46	0.14	2.33
MARION, OH-04855	51.00	37.31	640.38	59.91	157.88	0.14	2.23
NEW PHILADELPHIA, OH-04852	51.01	36.79	538.74	70.94	154.38	0.14	1.67
NEWARK, OH-04858	52.16	38.34	449.91	69.51	155.83	0.14	1.29
TOLEDO, OH-04848	50.09	33.75	707.37	63.51	157.62	0.14	1.77
WILMINGTON, OH-13841	52.87	39.82	464.05	64.57	154.68	0.14	1.2
WOOSTER, OH-04842	49.50	36.83	686.33	62.14	159.23	0.14	3.05
ZANESVILLE, OH-93824	51.76	37.17	474.27	69.39	156.17	0.14	1.66
Mean	**51.33**	**37.08**	**570.66**	**62.98**	**156.08**	**0.14**	**1.91**
Standard Deviation	**1.35**	**2.12**	**104.53**	**4.34**	**1.89**	**0.00**	**0.51**
Coefficient of Variation	**2.63%**	**5.73%**	**18.32%**	**6.89%**	**1.21%**	**1.51%**	**26.81%**

Table 42. Climate inputs and 50 year output distresses corresponding to each weather station for slab thickness of 12 in (305 mm) and length 13 ft (4.0 m). (metric units)

Weather Station	Mean annual air temperature (°C)	Mean annual precipitation (mm)	Freezing index (°C - days)	Average annual number of freeze/thaw cycles	IRI (m/km)	Faulting (mm)	Transverse cracking (%)
AKRON, OH-14813	9.61	948.4	384.61	63.11	2.49	3.6	2.77
AKRON, OH-14895	10.56	934.5	299.30	70.94	2.40	3.6	1.49
CINCINNATI, OH-93812	12.06	1024.4	217.28	61.77	2.48	3.8	1.49
CLEVELAND, OH-14820	10.12	871.7	350.95	56.42	2.44	3.6	2.62
CLEVELAND, OH-04854	10.12	871.7	350.95	56.42	2.44	3.6	2.62
COLUMBUS, OH-04804	10.81	914.1	316.18	59.48	2.40	3.6	1.72
COLUMBUS, OH-14821	10.81	914.1	316.18	59.48	2.40	3.6	1.67
COVINGTON/CINCINNATI, OH-93814	12.67	1077.5	183.23	63.59	2.39	3.6	1.32
DAYTON, OH-93815	10.87	974.9	332.39	57.14	2.40	3.6	1.66
DEFIANCE, OH-04851	10.59	886.2	367.39	63.25	2.44	3.6	1.46
FINDLAY, OH-14825	10.69	873.3	353.57	61.85	2.43	3.6	2.23
HAMILTON, OH-53855	11.48	989.1	268.74	66.54	2.43	3.6	2.02
MANSFIELD, OH-14891	9.73	953.8	399.27	59.54	2.47	3.6	2.33
MARION, OH-04855	10.56	947.7	355.77	59.91	2.46	3.6	2.23
NEW PHILADELPHIA, OH-04852	10.56	934.5	299.30	70.94	2.41	3.6	1.67
NEWARK, OH-04858	11.20	973.8	249.95	69.51	2.43	3.6	1.29
TOLEDO, OH-04848	10.05	857.3	392.98	63.51	2.46	3.6	1.77
WILMINGTON, OH-13841	11.59	1011.4	257.81	64.57	2.41	3.6	1.2
WOOSTER, OH-04842	9.72	935.5	381.29	62.14	2.48	3.6	3.05
ZANESVILLE, OH-93824	10.98	944.1	263.48	69.39	2.44	3.6	1.66
Mean	**10.74**	**941.90**	**317.03**	**62.98**	**2.43**	**3.57**	**1.91**
Standard Deviation	**0.75**	**53.94**	**58.07**	**4.34**	**0.03**	**0.05**	**0.51**
Coefficient of Variation	**6.97%**	**5.73%**	**18.32%**	**6.89%**	**1.21%**	**1.51%**	**26.81%**

The variation in the predicted distresses for the same slab design constructed at different locations indicates the software is sensing the climate variations for different regions within Ohio. For the evaluation of long term pavement performance in Chapter 14 with AASHTOWare Pavement ME Design, the weather stations used were Columbus (04804), representing a typical climate, and Cincinnati (93812), representing a climate with a higher number of freeze-thaw cycles.

16 Economic Analysis

The FEM and AASHTOWare results identified several slab thickness and length combinations that have superior predicted service life. A cost analysis was performed to determine the optimal thickness and length combination.

Material costs for PCC pavement were obtained from Mark Pardi at Ohio Concrete. A standard pavement mix of concrete goes for $90 per cubic yard ($118/m^3). Dowel baskets for joints are estimated at $8 per linear foot ($26/m), so a joint on a 12 ft (3.66 m) wide lane would cost $96. Based on these inputs, the material cost per lane-mile (lane-km) has been computed and is shown in Table 43 and Table 44 (Table 45 and Table 46) for English (metric) units, all based on 12 ft (3.7 m) slab width.

The cost of the concrete has a larger influence on the cost than the cost of the dowel basket. The minimum cost pavements that pass all three performance criteria for each slab length are highlighted in the yellow rows of Table 43 (Table 45 for metric units). The 13.5 ft (4.3 m) long by 12 in (305 mm) thick slab size has the least cost, by about 0.58%, or $1444 per lane-mile ($897 per lane-km). Given the small margin, the least costly design is sensitive to relatively small changes in the cost of materials.

This analysis assumes the materials used are durable enough to survive 50 years. The results of previous research regarding alternative dowel bars [e.g. Larson and Smith, 2011] and concrete pavement performance [e.g. Sargand et. al., 2017] should be considered and specifications revised accordingly prior to implementation of a 50 year design.

Table 43. Cost per lane-mile comparison for various slab geometries, all with 12 ft wide lanes. (English units)

Slab length (ft)	Thickness (in)	Lane width (ft)	Concrete cost ($/lane-mile)	Basket cost ($/lane-mile)	Total ($/lane-mile)
12	9	12	$158,400	$42,240.00	$200,640
	10	12	$176,000	$42,240.00	$218,240
	11	12	$193,600	$42,240.00	$235,840
	12	12	$211,200	$42,240.00	$253,440
	13	12	$228,800	$42,240.00	$271,040
	14	12	$246,400	$42,240.00	$288,640
	15	12	$264,000	$42,240.00	$306,240
13	9	12	$158,400	$38,990.77	$197,391
	10	12	$176,000	$38,990.77	$214,991
	11	12	$193,600	$38,990.77	$232,591
	12	12	$211,200	$38,990.77	$250,191
	13	12	$228,800	$38,990.77	$267,791
	14	12	$246,400	$38,990.77	$285,391
	15	12	$264,000	$38,990.77	$302,991
13.5	9	12	$158,400	$37,546.67	$195,947
	10	12	$176,000	$37,546.67	$213,547
	11	12	$193,600	$37,546.67	$231,147
	12	12	$211,200	$37,546.67	$248,747
	13	12	$228,800	$37,546.67	$266,347
	14	12	$246,400	$37,546.67	$283,947
	15	12	$264,000	$37,546.67	$301,547
14	9	12	$158,400	$36,205.71	$194,606
	10	12	$176,000	$36,205.71	$212,206
	11	12	$193,600	$36,205.71	$229,806
	12	12	$211,200	$36,205.71	$247,406
	13	12	$228,800	$36,205.71	$265,006
	14	12	$246,400	$36,205.71	$282,606
	15	12	$264,000	$36,205.71	$300,206
14.5	9	12	$158,400	$34,957.24	$193,357
	10	12	$176,000	$34,957.24	$210,957
	11	12	$193,600	$34,957.24	$228,557
	12	12	$211,200	$34,957.24	$246,157
	13	12	$228,800	$34,957.24	$263,757
	14	12	$246,400	$34,957.24	$281,357
	15	12	$264,000	$34,957.24	$298,957

Table 44. Cost per lane-mile comparison for various slab geometries, all with 12 ft wide lanes. (English units) (ctd)

Slab length (ft)	Thickness (in)	Lane width (ft)	Concrete cost ($/lane-mile)	Basket cost ($/lane-mile)	Total ($/lane-mile)
15	9	12	$158,400	$33,792.00	$192,192
	10	12	$176,000	$33,792.00	$209,792
	11	12	$193,600	$33,792.00	$227,392
	12	12	$211,200	$33,792.00	$244,992
	13	12	$228,800	$33,792.00	$262,592
	14	12	$246,400	$33,792.00	$280,192
	15	12	$264,000	$33,792.00	$297,792
16	9	12	$158,400	$31,680.00	$190,080
	10	12	$176,000	$31,680.00	$207,680
	11	12	$193,600	$31,680.00	$225,280
	12	12	$211,200	$31,680.00	$242,880
	13	12	$228,800	$31,680.00	$260,480
	14	12	$246,400	$31,680.00	$278,080
	15	12	$264,000	$31,680.00	$295,680
17	9	12	$158,400	$29,816.47	$188,216
	10	12	$176,000	$29,816.47	$205,816
	11	12	$193,600	$29,816.47	$223,416
	12	12	$211,200	$29,816.47	$241,016
	13	12	$228,800	$29,816.47	$258,616
	14	12	$246,400	$29,816.47	$276,216
	15	12	$264,000	$29,816.47	$293,816

Table 45. Cost per lane-km comparison for various slab geometries, all with 3.7 m wide lanes. (metric units)

Slab length (m)	Thickness (mm)	Lane width (m)	Concrete cost ($/lane-km)	Basket cost ($/lane-km)	Total ($/lane-km)
3.7	229	3.7	$98,425	$26,247	$124,672
	254	3.7	$109,361	$26,247	$135,608
	279	3.7	$120,297	$26,247	$146,544
	305	3.7	$131,233	$26,247	$157,480
	330	3.7	$142,169	$26,247	$168,416
	356	3.7	$153,106	$26,247	$179,352
	381	3.7	$164,042	$26,247	$190,288
4.0	229	3.7	$98,425	$24,228	$122,653
	254	3.7	$109,361	$24,228	$133,589
	279	3.7	$120,297	$24,228	$144,525
	305	3.7	$131,233	$24,228	$155,461
	330	3.7	$142,169	$24,228	$166,397
	356	3.7	$153,106	$24,228	$177,333
	381	3.7	$164,042	$24,228	$188,269
4.1	229	3.7	$98,425	$23,330	$121,755
	254	3.7	$109,361	$23,330	$132,691
	279	3.7	$120,297	$23,330	$143,628
	305	3.7	$131,233	$23,330	$154,564
	330	3.7	$142,169	$23,330	$165,500
	356	3.7	$153,106	$23,330	$176,436
	381	3.7	$164,042	$23,330	$187,372
4.3	229	3.7	$98,425	$22,497	$120,922
	254	3.7	$109,361	$22,497	$131,858
	279	3.7	$120,297	$22,497	$142,794
	305	3.7	$131,233	$22,497	$153,730
	330	3.7	$142,169	$22,497	$164,667
	356	3.7	$153,106	$22,497	$175,603
	381	3.7	$164,042	$22,497	$186,539
4.4	229	3.7	$98,425	$21,721	$120,146
	254	3.7	$109,361	$21,721	$131,082
	279	3.7	$120,297	$21,721	$142,019
	305	3.7	$131,233	$21,721	$152,955
	330	3.7	$142,169	$21,721	$163,891
	356	3.7	$153,106	$21,721	$174,827
	381	3.7	$164,042	$21,721	$185,763

Table 46. Cost per lane-km comparison for various slab geometries, all with 3.7 m wide lanes. (metric units) (ctd)

Slab length (m)	Thickness (mm)	Lane width (m)	Concrete cost ($/lane-km)	Basket cost ($/lane-km)	Total ($/lane-km)
4.6	229	3.7	$98,425	$20,997	$119,422
	254	3.7	$109,361	$20,997	$130,358
	279	3.7	$120,297	$20,997	$141,295
	305	3.7	$131,233	$20,997	$152,231
	330	3.7	$142,169	$20,997	$163,167
	356	3.7	$153,106	$20,997	$174,103
	381	3.7	$164,042	$20,997	$185,039
4.9	229	3.7	$98,425	$19,685	$118,110
	254	3.7	$109,361	$19,685	$129,046
	279	3.7	$120,297	$19,685	$139,982
	305	3.7	$131,233	$19,685	$150,918
	330	3.7	$142,169	$19,685	$161,854
	356	3.7	$153,106	$19,685	$172,791
	381	3.7	$164,042	$19,685	$183,727
5.2	229	3.7	$98,425	$18,527	$116,952
	254	3.7	$109,361	$18,527	$127,888
	279	3.7	$120,297	$18,527	$138,824
	305	3.7	$131,233	$18,527	$149,760
	330	3.7	$142,169	$18,527	$160,697
	356	3.7	$153,106	$18,527	$171,633
	381	3.7	$164,042	$18,527	$182,569

17 Determining the k-value for Chemically Stabilized Subgrades

The subgrade under a rigid pavement is typically modeled as a dense liquid Winkler foundation, which is characterized by a spring constant. The Winkler foundation presumes the vertical deflection of any point at the subgrade surface is proportional to the vertical stress acting at that point with no shear [Setiadji, 2009]. Westergaard [1925] was the first to introduce the term "modulus of subgrade reaction", known today as the k value. According to Westergaard, the modulus of subgrade reaction is defined as the applied pressure necessary to produce a unit deflection under a specified loaded area. The k value was first used to characterize the elastic properties of subgrade soil only. However, later when a full-scale road test performed in Arlington, Virginia, in the 1930s, k was also used to describe elastic characteristics of other layers such as base and subbase [Darter et al., 1995]. Early, concrete pavements consisted of concrete placed on the subgrade, but rigid pavements are presently designed with an intervening base layer to provide drainage and prevent joint pumping. In this pavement system, a composite modulus of subgrade reaction was used to incorporate the effect of base layer in combination with the subgrade. In the design and rehabilitation of concrete pavements, the concept of composite modulus of subgrade reaction k has become commonly used [AASHTO, 1993; Packard, 1984]. ODOT recently adopted a policy of stabilization of subgrade soils for all new construction. However, there is no standard procedure to determine the k value for chemically stabilized subgrade soils. To fill this gap, nondestructive field tests such as Falling Weight Deflectometer (FWD), Light Weight Deflectometer (LWD), and German Plate Test (GPT, also called the Plate Bearing Test) were conducted on three sites in Ohio to determine the k-value for stabilized subgrade soils.

17.1 Field Data Analysis

The FWD, LWD, and GPT field tests were performed on three sites in Ohio, HAM-75-6.75, ALL-75-0.21-N, and HAM-75-2.30-N. On HAM-75-6.75, the tests were conducted directly on the subgrade soil, while on ALL-75-0.2-N1, the tests were performed on the stabilized subgrade. On HAM-75-2.30-N, the testing was conducted on the base layer. ALL-75-0.21-N had a 12 in (305 mm) layer of cement stabilized subgrade. The base and cement stabilized subgrade soil thicknesses in HAM-75-2.30-N were 6 in (152 mm) and 16 in (406 mm), respectively. The raw data obtained from the three tests were used to calculate the stiffness and modulus of tested layers at each site. According to AASHTO [1986], the modulus of subgrade reaction, k-value, is calculated from Plate Bearing Test (or GPT) using the following equation.

$$k = \frac{p}{d} \tag{26}$$

Where:

p is the static pressure in psi

d is the displacement of the rigid plate in inches

AASHTO also defines the k-value, as the applied load divided by the volume displaced beneath the plate in Figure 69. In this case, the plate need not be considered rigid, and the k-value is determined using the elastic layer theory using Equation 27.

$$k = \frac{P}{V} \quad (27)$$

Where:

P is the magnitude of the applied load in pounds

V is the volume displaced directly beneath the load plate in cubic inches

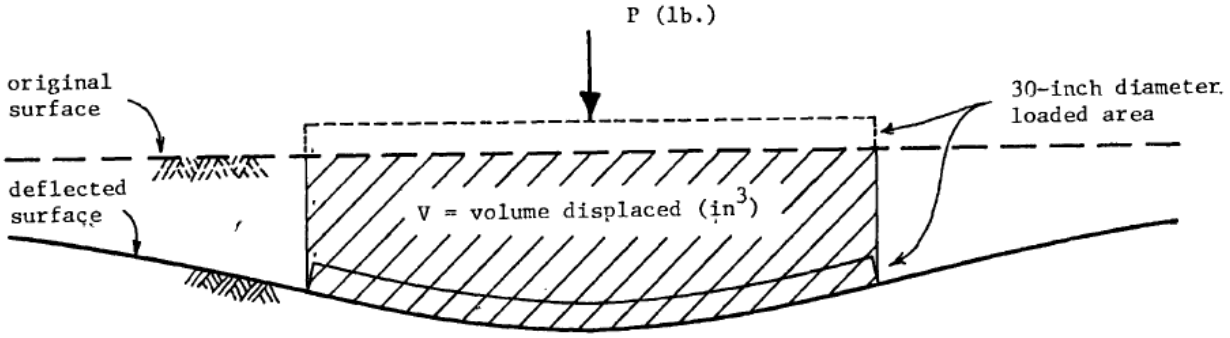

Figure 69. AASHTO alternative method for estimating k-value using the elastic layer theory with the assumption the plate is not necessarily rigid [AASHTO, 1986].

The modulus of subgrade reaction is related to the elastic modulus by the following equation, assuming a rigid plate test again:

$$k = \frac{2E}{\pi(1-\mu^2)a} \quad (28)$$

Where:

E is the elastic surface modulus in psi

μ is the Poisson's Ratio

a is the rigid plate radius in inches

The elastic modulus of a semi-infinite half space can be calculated form the deflection at the center of the circular rigid plate using the following equation:

$$E = \frac{(1-\mu^2)P}{2\,a\,d_o} \quad (29)$$

Where d_0 is the deflection at the center of the rigid plate in inches

AASHTO [1993] relates the modulus of subgrade reaction to the subgrade resilient modulus using the following equation:

$$k = \frac{M_R}{19.4} \quad (30)$$

Equation 30 applies when the plate test is conducted on the top of a base layer or subbase, the measured stiffness is a composite of the stiffnesses of the base layer and the subgrade, and is called the composite modulus of subgrade reaction. The AASHTO 1993 design guide uses

Equation 14 to determine the composite modulus of subgrade reaction, which presupposes knowing the elastic moduli of the base and subgrade. The test data gathered for this project were used to back-calculate the layer moduli for the sites containing stabilized and base layers.

For two and three layer systems, a closed-form solution exists to estimate the surface deflections directly under loading plates in conjunction using the method of equivalent thickness of Odemark and Boussinesq [Ullidtz 1987]. For a uniformly distributed load, the deflection at any depth below the center line of circular plate can be determined from Equation 31. For loads transferred via a rigid circular plate, the deflection below the circular plate at any depth can be calculated using Equation 32 [Ullidtz 1987].

$$d_z = \frac{(1+\mu)\sigma_0 a}{E}\left[\frac{1}{\left(1+\left(\frac{z}{a}\right)^2\right)^{\frac{1}{2}}} + (1-2\mu)\left(\left(1+\left(\frac{z}{a}\right)^2\right)^{\frac{1}{2}} - \frac{z}{a}\right)\right] \quad (31)$$

$$d_z = \frac{(1+\mu)\sigma_0 a}{2E}\left[(1-\mu)\left(\pi - 2arctan\left(\frac{z}{a}\right)\right) + \frac{\left(\frac{z}{a}\right)}{1+\left(\frac{z}{a}\right)^2}\right] \quad (32)$$

where z is the depth where the deflection is calculated.

The base and stabilized layer should be transformed to an equivalent thickness of the subgrade layer via the transformation in Figure 70 using the following equation.

$$h_e = f h_1 \sqrt[3]{\frac{E_1}{E_2}} \quad (33)$$

where:

h_e is the equivalent thickness

f is the correction factor of 0.8, except for first interface of two-layer system where a factor of 0.9 is used and 1.0 for multi-layer system.

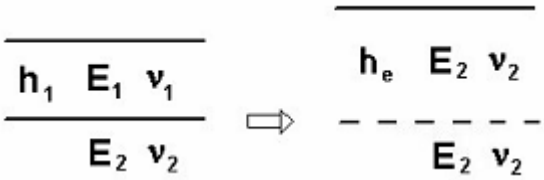

Figure 70. Odemark's transformation of a layered system, from ELMOD QuickStart Manual [Dynatest International, 2010].

The deflection of each layer in a multi-layer system is calculated from the compression of the transformed layer, which is basically determined from the difference between the deflection at the top and bottom of the transformed layer. Then, the total deflection from all layers is equal to the surface deflection directly below the centerline of the circular plate. Using this approach, the deflections measured directly below the loading plate with FWD, LWD, and GPT were used to determine the elastic moduli of the base, stabilized subgrade, and subgrade layers. The elastic

moduli were determined iteratively by selecting values for the elastic moduli and applying Equation 32 until the calculated surface deflections matched the measured deflections.

Equations 27, 28, and 30 were used to calculate the modulus of subgrade reaction for site on which testing was performed directly on the subgrade HAM-75-6.75. Equation 27 and Equation 28 were used to determine the composite modulus of subgrade reaction which includes the stabilized subgrade and subgrade for site ALL-75-0.21-N and base, stabilized subgrade, and subgrade for site HAM-75-2.30-N. Also, Equation 14 was used to determine the composite modulus of subgrade reaction on HAM-75-2.30-N and compare it with the other equations.

17.2 Analysis Results of k-value

Table 47 (Table 48) shows the modulus of subgrade reaction required to support the load applied directly to the subgrade on a rigid circular plate in English (metric) units. Table 49 (Table 50) presents the composite modulus of subgrade reaction of stabilized subgrade and subgrade layer required to support the applied load in English (metric) units, and Table 51 (Table 52) shows the composite modulus subgrade reaction of base, stabilized subgrade, and subgrade layers required to support the applied load in English (metric) units. The back calculated elastic moduli are also presented in the tables for the applicable layers. The composite elastic modulus represents the surface modulus of the entire system calculated directly from the surface deflection below the center of loading plate using Equation 29. The modulus of subgrade reaction significantly increased when the stabilized subgrade layer was added, and when the system also includes a base layer it exhibits an even higher composite modulus. AASHTO [1993] provides a graph to calculate the composite modulus of subgrade reaction based on the elastic modulus of subgrade, modulus of base, and thickness of base as shown in Figure 71.

Table 47. The modulus of subgrade reaction, k-value, and resilient modulus MR for HAM-75-6.75, where tests were performed directly on the subgrade (English units).

STATION	Load (lb)	D_o (mil)	M_R (psi)	k value Eq. 28 (lb/in^3)	k value AASHTO (lb/in^3)	k value Eq. 27 (lb/in^3)
FWD (Normalized load)						
1	9000	68.51	9593	615	495	762
2	9000	93.36	6868	440	354	561
3	9000	68.05	9420	604	486	745
4	9000	87.69	7353	471	379	568
5	9000	100.25	6382	409	329	509
6	9000	102.53	6240	400	322	493
7	9000	136.44	4755	305	245	355
8	9000	112.72	5699	365	294	446
9	9000	52.98	12152	779	626	963
10	9000	64.82	9947	638	513	788
Average		**88.73**	**7841**	**503**	**404**	**619**
LWD						
1	1868	16.78	10611	680	547	871
2	1865	31.84	4213	270	217	349
3	1869	16.38	8322	534	429	679
4	1887	10.85	12389	794	639	1003
5	1849	9.03	15984	1025	824	1266
6	1842	11.67	11224	720	579	902
7	1765	24.03	5230	335	270	411
8	1815	17.98	7660	491	395	611
9	1778	6.73	18892	1211	974	1485
10	1862	13.2	18758	1203	967	1493
Average		**15.85**	**11328**	**726**	**584**	**907**
GPT						
1	4725	59.49	5645	362	291	362
2	4097	58.52	4975	319	256	319
3	4690	80.48	4142	266	213	266
4	4058	78.27	3684	236	190	236
5	4678	83.35	3989	256	206	256
6	4134	85.1	3452	221	178	221
7	4834	47.86	7177	460	370	460
8	4035	46.51	6166	395	318	395
Average		**67.45**	**4904**	**314**	**253**	**314**
FWD/LWD		**5.6**	**0.7**	**0.7**	**0.7**	**0.7**
FWD/GPT		**1.3**	**1.6**	**1.6**	**1.6**	**2**
LWD/GPT		**0.2**	**2.3**	**2.3**	**2.3**	**2.9**

Table 48. The modulus of subgrade reaction, k-value, and resilient modulus MR for HAM-75-6.75, where tests were performed directly on the subgrade (metric units).

				k value		
STATION	**Load** (kN)	**D_o** (mm)	**M_R** (MPa)	**Eq. 28** (MN/m^3)	**AASHTO** (MN/m^3)	**Eq. 27** (MN/m^3)
FWD (Normalized load)						
1	40	1.740	66.14	166.9	134.4	206.8
2	40	2.371	47.35	119.4	96.1	152.3
3	40	1.728	64.95	164.0	131.9	202.2
4	40	2.227	50.70	127.9	102.9	154.2
5	40	2.546	44.00	111.0	89.3	138.2
6	40	2.604	43.02	108.6	87.4	133.8
7	40	3.466	32.78	82.8	66.5	96.4
8	40	2.863	39.29	99.1	79.8	121.1
9	40	1.346	83.79	211.5	169.9	261.4
10	40	1.646	68.58	173.2	139.3	213.9
Average		**2.254**	**54.06**	**136.5**	**109.7**	**168.0**
LWD						
1	8.31	0.426	73.16	184.6	148.5	236.4
2	8.30	0.809	29.05	73.3	58.9	94.7
3	8.31	0.416	57.38	145.0	116.5	184.3
4	8.39	0.276	85.42	215.5	173.5	272.3
5	8.22	0.229	110.21	278.2	223.7	343.7
6	8.19	0.296	77.39	195.4	157.2	244.8
7	7.85	0.610	36.06	90.9	73.3	111.6
8	8.07	0.457	52.81	133.3	107.2	165.9
9	7.91	0.171	130.26	328.7	264.4	403.1
10	8.28	0.335	129.33	326.6	262.5	405.3
Average		**0.403**	**78.10**	**197.1**	**158.5**	**246.2**
GPT						
1	21.02	1.511	38.92	98.3	79.0	98.3
2	18.22	1.486	34.30	86.6	69.5	86.6
3	20.86	2.044	28.56	72.2	57.8	72.2
4	18.05	1.988	25.40	64.1	51.6	64.1
5	20.81	2.117	27.50	69.5	55.9	69.5
6	18.39	2.162	23.80	60.0	48.3	60.0
7	21.50	1.216	49.48	124.9	100.4	124.9
8	17.95	1.181	42.51	107.2	86.3	107.2
Average		**1.713**	**33.81**	**85.2**	**68.7**	**85.2**
FWD/LWD		**5.6**	**0.7**	**0.7**	**0.7**	**0.7**
FWD/GPT		**1.3**	**1.6**	**1.6**	**1.6**	**2**
LWD/GPT		**0.2**	**2.3**	**2.3**	**2.3**	**2.9**

Table 49. The composite modulus of subgrade reaction, k-value, and corresponding elastic modulus E for ALL-75-0.21-N, where testing was performed directly on stabilized subgrade above natural subgrade (English units).

				k value		
STATION	**Load** (lb)	**D_o** (mil)	**M_R** (psi)	**Eq. 28** (lb/in^3)	**AASHTO** (lb/in^3)	**Eq. 27** (lb/in^3)
FWD (Normalized load)						
1	9000	31.12	20556	1318	1570	16533
2	9000	88.34	7317	469	549	3757
3	9000	20.66	30974	1986	2506	24984
4	9000	19.45	32894	2109	2704	28120
5	9000	28.72	22274	1428	1829	18278
6	9000	31.15	20535	1317	1678	14816
7	9000	12.32	51972	3332	4228	44541
8	9000	15.94	40473	2595	3382	33989
9	9000	17.68	36172	2319	3021	28328
10	9000	20.58	31081	1993	2603	24190
Average		**28.6**	**29425**	**1887**	**2407**	**23754**
LWD						
1	1888	6.00	22410	1437	1778	16731
2	1913	11.36	12176	781	907	9365
3	1931	5.05	28439	1823	2418	21413
4	1958	7.46	18915	1213	1594	14275
5	1899	10.38	14054	901	1179	11075
6	1973	6.52	48077	3083	3763	33541
7	1988	4.94	29146	1869	2439	21892
8	1953	3.12	46407	2976	3901	31640
9	1914	6.43	26672	1710	2244	21517
10	1955	6.47	22257	1427	1876	18408
Average		**6.77**	**26855**	**1722**	**2210**	**19986**
GPT						
1	4184	24.7	12040	772	772	5114
2	3517	27.5	9089	583	583	3984
3	4797	66.34	5139	330	330	2249
4	4156	68.46	4314	277	277	1898
5	5394	39.25	9766	626	626	4406
6	4138	35.91	8189	525	525	3444
Average		**43.69**	**8089**	**519**	**519**	**3516**
FWD/LWD		**4.22**	**1.1**	**1.1**	**1.09**	**1.19**
FWD/GPT		**0.65**	**3.64**	**3.64**	**4.64**	**6.76**
LWD/GPT		**0.16**	**3.32**	**3.32**	**4.26**	**5.68**

Table 50. The composite modulus of subgrade reaction, k-value, and corresponding elastic modulus E for ALL-75-0.21-N, where testing was performed directly on stabilized subgrade above natural subgrade (metric units).

STATION	Load (kN)	D_o (mm)	M_R (MPa)	k value		
				Eq. 28 (MN/m^3)	AASHTO (MN/m^3)	Eq. 27 (MN/m^3)
FWD (Normalized load)						
1	40	0.790	141.73	357.8	426.2	4487.8
2	40	2.244	50.45	127.3	149.0	1019.8
3	40	0.525	213.56	539.1	680.2	6781.8
4	40	0.494	226.80	572.5	734.0	7633.1
5	40	0.729	153.57	387.6	496.5	4961.5
6	40	0.791	141.58	357.5	455.5	4021.8
7	40	0.313	358.33	904.5	1147.7	12090.5
8	40	0.405	279.05	704.4	918.0	9226.2
9	40	0.449	249.40	629.5	820.0	7689.6
10	40	0.523	214.30	541.0	706.6	6566.3
Average		**0.726**	**202.88**	**512.2**	**653.4**	**6448.0**
LWD						
1	8.40	0.152	154.51	390.1	482.6	4541.6
2	8.51	0.289	83.95	212.0	246.2	2542.1
3	8.59	0.128	196.08	494.8	656.4	5812.5
4	8.71	0.189	130.41	329.3	432.7	3874.9
5	8.45	0.264	96.90	244.6	320.0	3006.3
6	8.78	0.166	331.48	836.9	1021.5	9104.6
7	8.84	0.125	200.95	507.3	662.1	5942.5
8	8.69	0.079	319.96	807.8	1058.9	8588.6
9	8.51	0.163	183.90	464.2	609.1	5840.7
10	8.70	0.164	153.46	387.4	509.2	4996.8
Average		**0.172**	**185.16**	**467.4**	**599.9**	**5425.1**
GPT						
1	18.61	0.627	83.01	209.6	209.6	1388.2
2	15.64	0.699	62.67	158.3	158.3	1081.4
3	21.34	1.685	35.43	89.6	89.6	610.5
4	18.49	1.739	29.74	75.2	75.2	515.2
5	23.99	0.997	67.33	169.9	169.9	1196.0
6	18.41	0.912	56.46	142.5	142.5	934.9
Average		**1.110**	**55.77**	**140.9**	**140.9**	**954.4**
FWD/LWD		**4.22**	**1.1**	**1.1**	**1.09**	**1.19**
FWD/GPT		**0.65**	**3.64**	**3.64**	**4.64**	**6.76**
LWD/GPT		**0.16**	**3.32**	**3.32**	**4.26**	**5.68**

Table 51. The composite modulus of subgrade reaction, k-value, and equivalent elastic modulus E for HAM-75-2.30-N, where testing was performed directly on the base and the system included stabilized and natural subgrade (English units).

STATION	Load (lb)	D_o (mil)	M_R (psi)	k value		
				Eq. 28 (lb/in^3)	AASHTO (lb/in^3)	Eq. 27 (lb/in^3)
FWD (Normalized load)						
1	9000	7.84	81760	5242	6097	28490
2	9000	11.38	56251	3607	4203	22229
3	9000	9.38	68332	4381	5119	26433
4	9000	10.59	60379	3871	4636	25731
5	9000	11.57	55336	3548	4149	20389
6	9000	32.59	19968	1280	1638	15915
7	9000	43.06	16407	1052	1254	18826
8	9000	17.76	36140	2317	2808	11191
9	9000	15.24	42118	2701	3171	20438
10	9000	11.49	55708	3572	4155	20001
Average		**17.09**	**49240**	**3157**	**3723**	**20964**
LWD						
1	2020	2.39	65553	4203	5028	32320
2	1837	1.91	70701	4533	5208	35972
3	1841	4.57	29178	1871	2360	12060
4	1848	4.68	28319	1816	2308	11628
5	1886	2.81	48022	3079	3706	20547
6	1838	2.94	47726	3060	3352	22366
7	1905	6.12	23019	1476	1875	9561
8	1835	5.04	38782	2487	2935	16914
9	1918	4.36	35109	2251	2799	14451
10	1874	2.92	46919	3008	3589	20074
Average		**3.77**	**43333**	**2778**	**3316**	**19589**
GPT						
1	4709	8.7	38452	2465	2465	9859
2	3912	9.92	28037	1798	1798	3675
3	4793	5.07	67237	4311	4311	19275
4	4007	4.1	69442	4452	4452	20431
5	4736	48.96	6875	441	441	1751
6	4019	53.94	5294	339	339	1042
7	4771	20.73	16357	1049	1049	3006
8	4032	26.26	10914	700	700	3030
Average		**22.21**	**30326**	**1944**	**1944**	**7759**
FWD/LWD		**4.53**	**1.14**	**1.14**	**1.12**	**1.07**
FWD/GPT		**0.77**	**1.62**	**1.62**	**1.91**	**2.7**
LWD/GPT		**0.17**	**1.43**	**1.43**	**1.71**	**2.52**

Table 52. The composite modulus of subgrade reaction, k-value, and equivalent elastic modulus E for HAM-75-2.30-N, where testing was performed directly on the base and the system included stabilized and natural subgrade (metric units).

STATION	Load (kN)	D_o (mm)	M_R (MPa)	k value Eq. 28 (MN/m^3)	k value AASHTO (MN/m^3)	k value Eq. 27 (MN/m^3)
FWD (Normalized load)						
1	40	0.199	563.72	1422.9	1655.0	7733.5
2	40	0.289	387.84	979.1	1140.9	6034.0
3	40	0.238	471.13	1189.2	1389.5	7175.2
4	40	0.269	416.30	1050.8	1258.4	6984.6
5	40	0.294	381.53	963.1	1126.2	5534.5
6	40	0.828	137.67	347.5	444.6	4320.1
7	40	1.094	113.12	285.6	340.4	5110.3
8	40	0.451	249.18	628.9	762.2	3037.8
9	40	0.387	290.39	733.2	860.8	5547.8
10	40	0.292	384.09	969.6	1127.9	5429.2
Average		**0.434**	**339.50**	**857.0**	**1010.6**	**5690.6**
LWD						
1	8.99	0.061	451.97	1140.9	1364.8	8773.2
2	8.17	0.049	487.47	1230.5	1413.7	9764.5
3	8.19	0.116	201.18	507.9	640.6	3273.7
4	8.22	0.119	195.25	492.9	626.5	3156.4
5	8.39	0.071	331.10	835.8	1006.0	5577.4
6	8.18	0.075	329.06	830.6	909.9	6071.2
7	8.47	0.155	158.71	400.7	509.0	2595.3
8	8.16	0.128	267.39	675.1	796.7	4591.3
9	8.53	0.111	242.07	611.0	759.8	3922.7
10	8.34	0.074	323.50	816.5	974.2	5449.0
Average		**0.096**	**298.77**	**754.1**	**900.1**	**5317.4**
GPT						
1	20.95	0.221	265.12	669.1	669.1	2676.2
2	17.40	0.252	193.31	488.1	488.1	997.6
3	21.32	0.129	463.58	1170.2	1170.2	5232.1
4	17.82	0.104	478.79	1208.5	1208.5	5545.9
5	21.07	1.244	47.40	119.7	119.7	475.3
6	17.88	1.370	36.50	92.0	92.0	282.8
7	21.22	0.527	112.78	284.7	284.7	816.0
8	17.94	0.667	75.25	190.0	190.0	822.5
Average		**0.564**	**209.09**	**527.7**	**527.7**	**2106.2**
FWD/LWD		**5.6**	**0.7**	**0.7**	**0.7**	**0.7**
FWD/GPT		**1.3**	**1.6**	**1.6**	**1.6**	**2**
LWD/GPT		**0.2**	**2.3**	**2.3**	**2.3**	**2.9**

The AASHTO graph in Figure 71 suggests the maximum composite modulus of subgrade reaction is 2000 pci (543 MN/m^3). However, the composite modulus of subgrade reaction determined from FWD data in this study was as high as 3157 pci (857 MN/m^3). This can be

attributed to the increased stiffness provided by subgrade stabilization. This can also be confirmed by inspecting the backcalculated elastic moduli of supporting layer in Table 51 and Table 52.

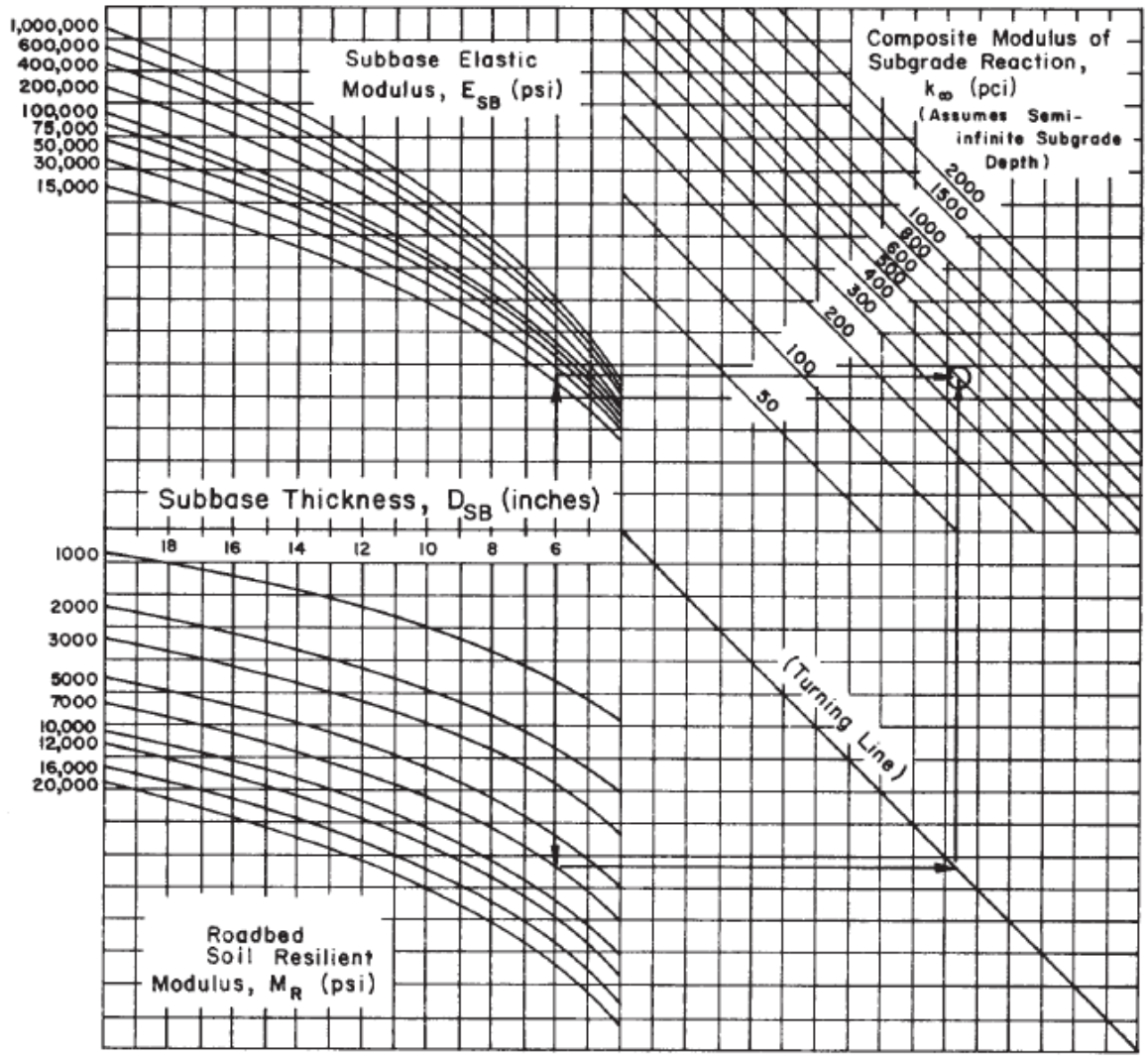

Figure 71. Chart for estimating composite modulus of subgrade reaction assuming a semi-infinite subgrade depth [AASHTO, 1993].

The modulus of subgrade reaction and the composite modulus of subgrade reaction determined from different tests vary because of the difference in load levels each device applies. The difference is smaller between FWD and LWD than between FWD and GPT and between LWD and GTP. GPT device almost always produces lower k-values than the other two, as can be seen in Figure 72 through Figure 75. The moduli of subgrade reaction for the different layers obtained from FWD measurements are presented in Figure 76. Each additional layer tends to increase the composite modulus of subgrade reaction, since the stiffness of the added layer is usually greater than those of the layers beneath. Although there is some variability in the composite modulus of subgrade reaction, the k-value is so high where there is a stabilized subgrade, with or without a base layer, it would not affect the level of stresses developed in the concrete slab.

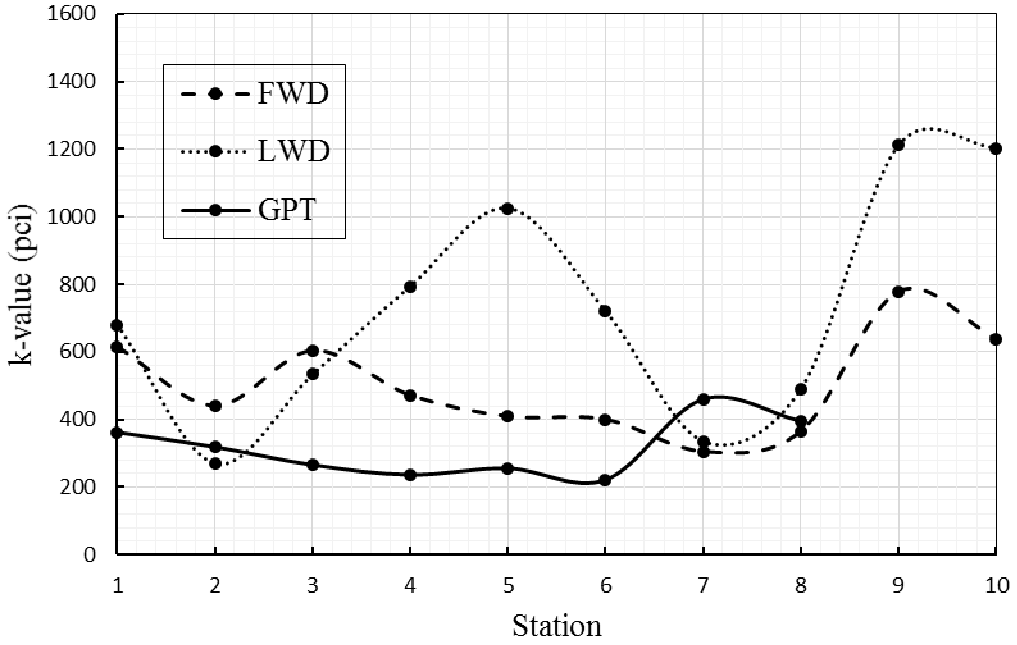

Figure 72. Modulus of subgrade reaction obtained from FWD, LWD, and GPT on subgrade at HAM-75-6.75. (1 Station = 100 ft = 30.5 m, 1 pci = 0.27 MN/m^3).

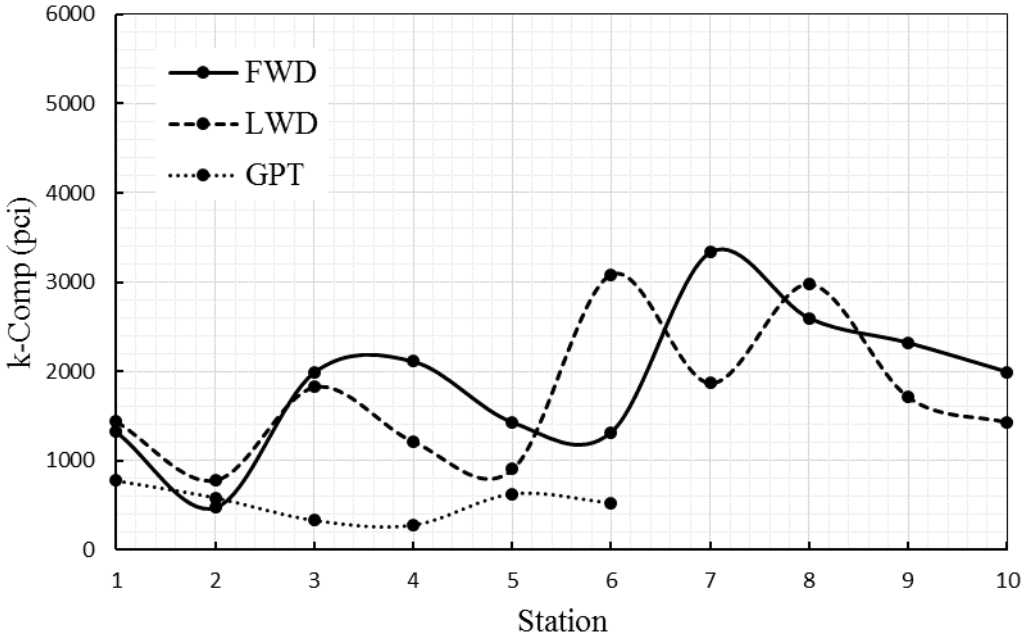

Figure 73. Composite modulus of subgrade reaction obtained from FWD, LWD, and GPT on stabilized subgrade at ALL-75-0.21-N. (1 Station = 100 ft = 30.5 m, 1 pci = 0.27 MN/m^3)

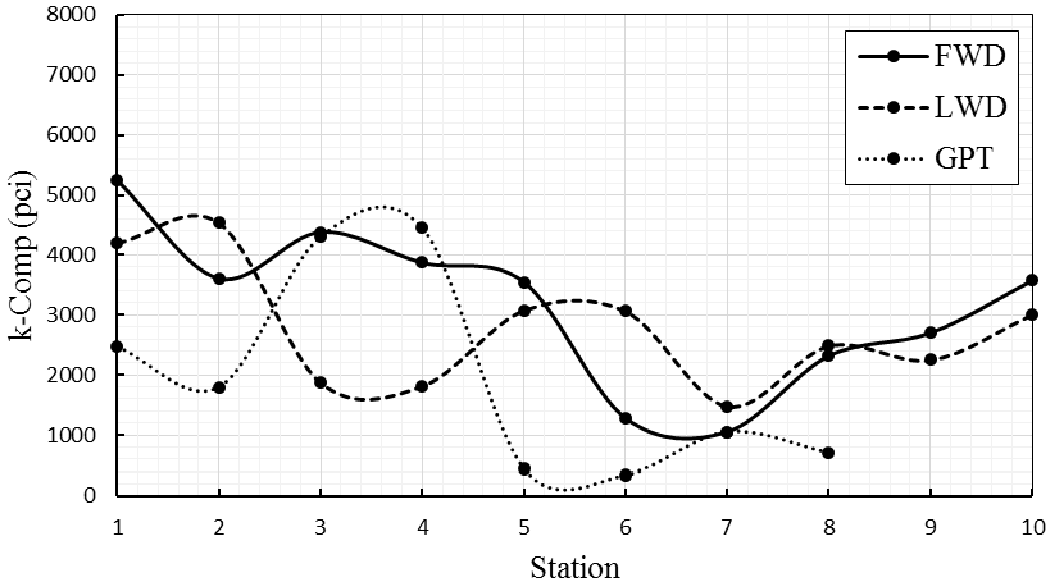

Figure 74. Composite modulus of subgrade reaction obtained from FWD, LWD, and GPT on base layer at HAM-75-2.30-N. (1 Station = 100 ft = 30.5 m, 1 pci = 0.27 MN/m^3)

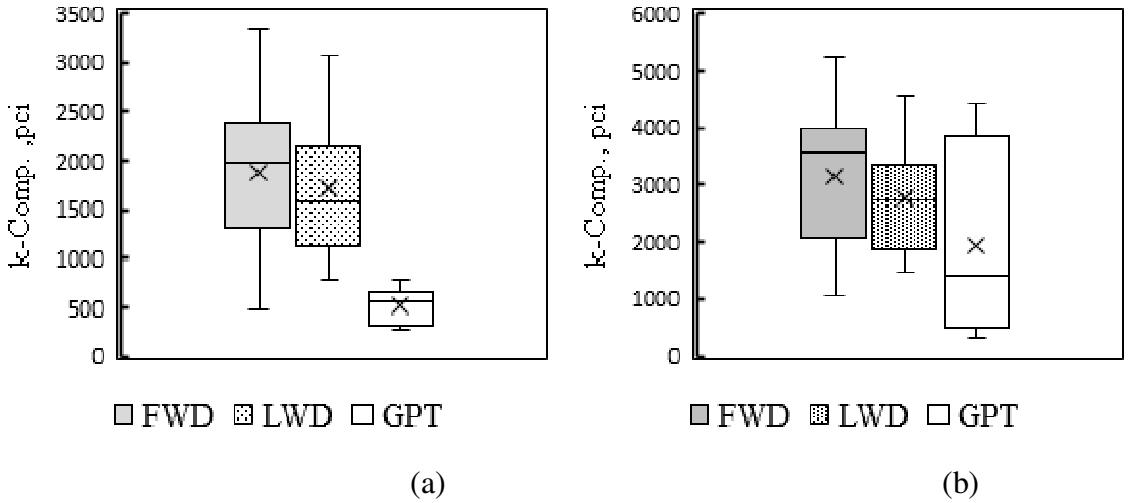

(a) (b)

Figure 75. Composite modulus of subgrade reaction versus test method: (a) on stabilized subgrade (b) on base. (1 pci = 0.27 MN/m^3)

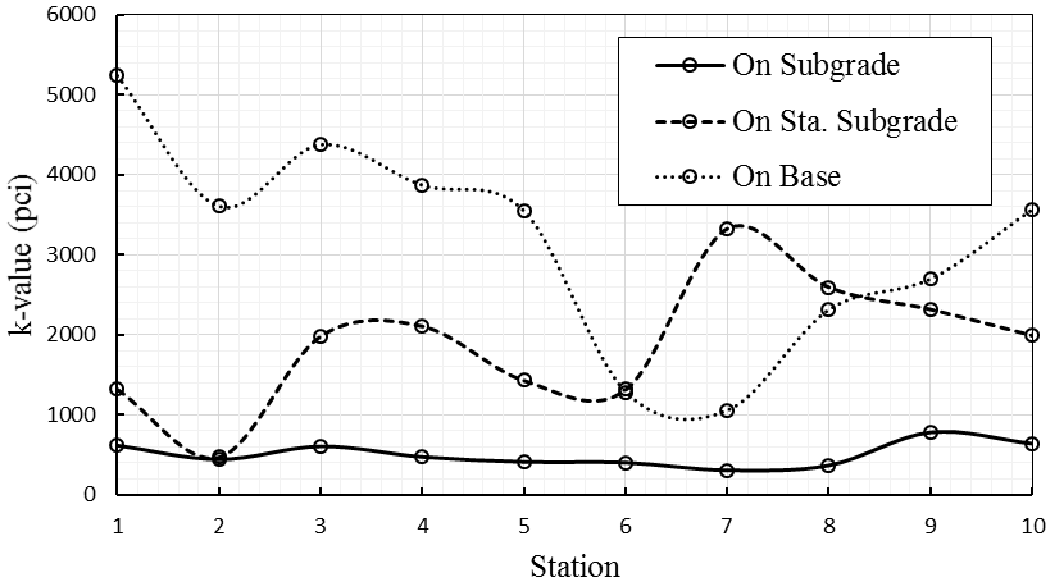

Figure 76. Modulus of subgrade reaction on each layer from FWD measurements at all three sites. (1 Station = 100 ft = 30.5 m, 1 pci = 0.27 MN/m^3)

17.3 Procedure for Estimating the k-value for chemically stabilized soils

AASHTO 1986 developed Equation 30 by considering the definition of modulus of subgrade reaction as the ratio between the applied load on circular non-rigid plate and the volume displaced directly beneath it. This assumption allows the constraint of "rigid" loading plate to be relaxed and, the elastic layer theory becomes applicable. AASHTO used an elastic layer computer program to predict the displaced volume and k-value under a 30 –in (0.76 m) diameter "flexible" plate for a range of roadbed soil resilient moduli, and developed the relationship shown in Figure 77. Also, the same concept was used to develop the composite modulus of subgrade reaction Equation 14 and the chart in Figure 71.

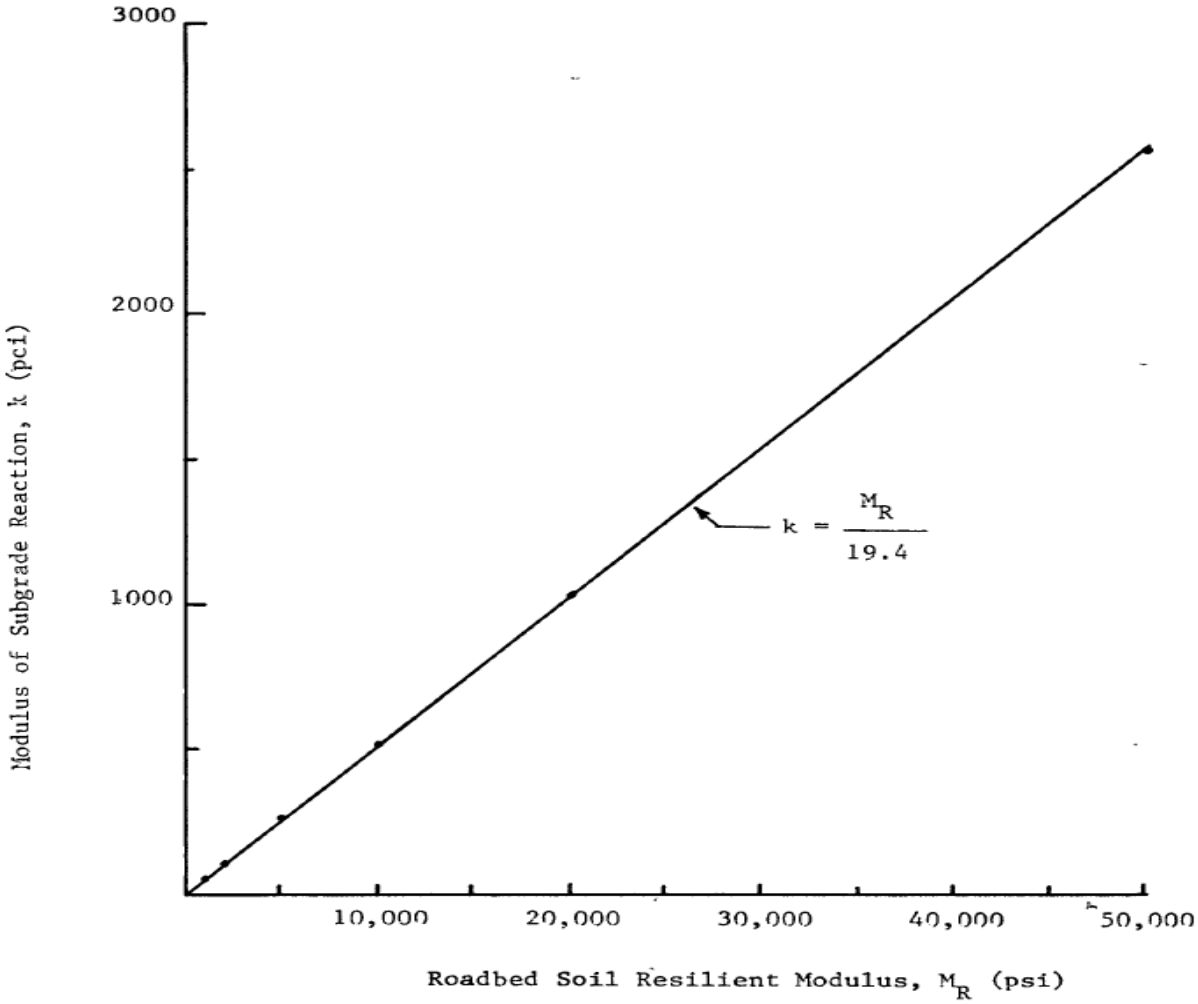

Figure 77. Theoretical relationship between the modulus of subgrade reaction and roadbed soil resilient modulus [AAHTO HH.2, 1986] (1 psi = 6.89 kPa, 1 pci = 0.27 MN/m^3).

The same concept can also be used to find possible similar relationships between the composite modulus of subgrade reaction and the resilient moduli of the stabilized subgrade and base using the data obtained from the FWD and LWD. The volume concept was already used in this study to determine the composite modulus of subgrade reaction from FWD and LWD based on Equation 27. This approach was also adopted by Netemeyer and Munsell [1995] as follows, using Figure 78 to indicate the variables D_0, D_6, D_{12}, and D_{eq} in Equations 34 and 35:

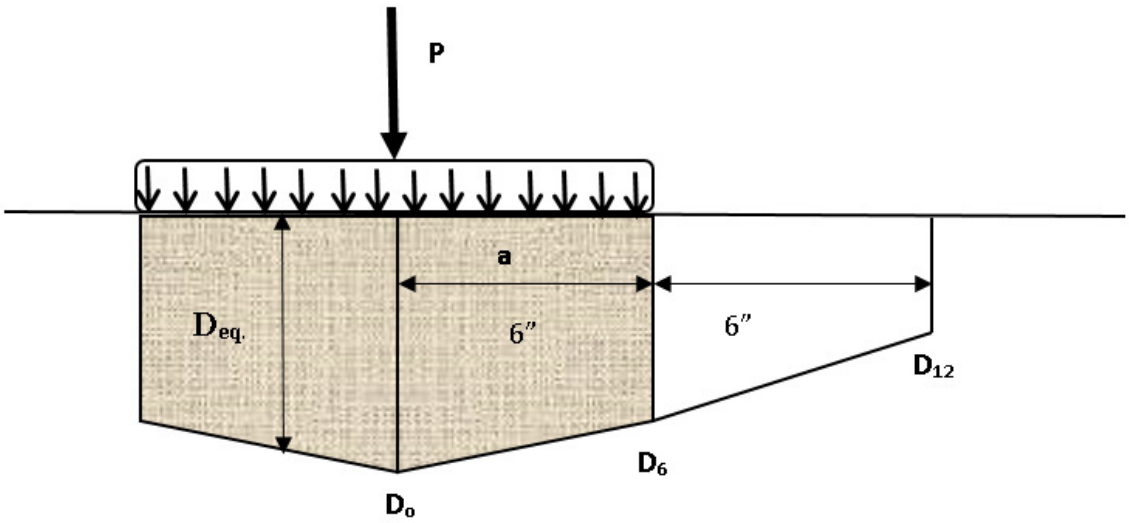

Figure 78. The displaced volume beneath the load plate (6" = 6 in = 152 mm)

$$\frac{D_o - D_{12}}{12} = \frac{D_6 - D_{12}}{6}$$
$$D_6 = \frac{D_o - D_{12}}{2} + D_{12} = \frac{1}{2}(D_o + D_{12})$$
$$D_{eq} = \frac{D_o + D_6}{2} = \frac{1}{2}\left(D_o + \frac{1}{2}(D_o + D_{12})\right) \quad (34)$$
$$D_{eq} = \frac{1}{4}(3D_o + D_{12})$$

$$Displaced\ Volume, V = \pi a^2 D_{eq}$$
$$k_{dynamic} = \frac{P}{V} \quad (35)$$
$$k_{static} = \frac{1}{2}k_{dynamic} = \frac{1}{2}\frac{P}{\pi a^2 D_{eq}}$$

The elastic moduli of stabilized subgrade and base layers were also determined using the concept of Odemark and Boussinesq described earlier. Figure 79 through Figure 90 present possible relationships between the composite modulus of subgrade reaction computed from Equation 27 and the elastic layer modulus based on back calculation from the FWD and LWD data. These are analogous to the relationship from AASHTO shown in Figure 77.

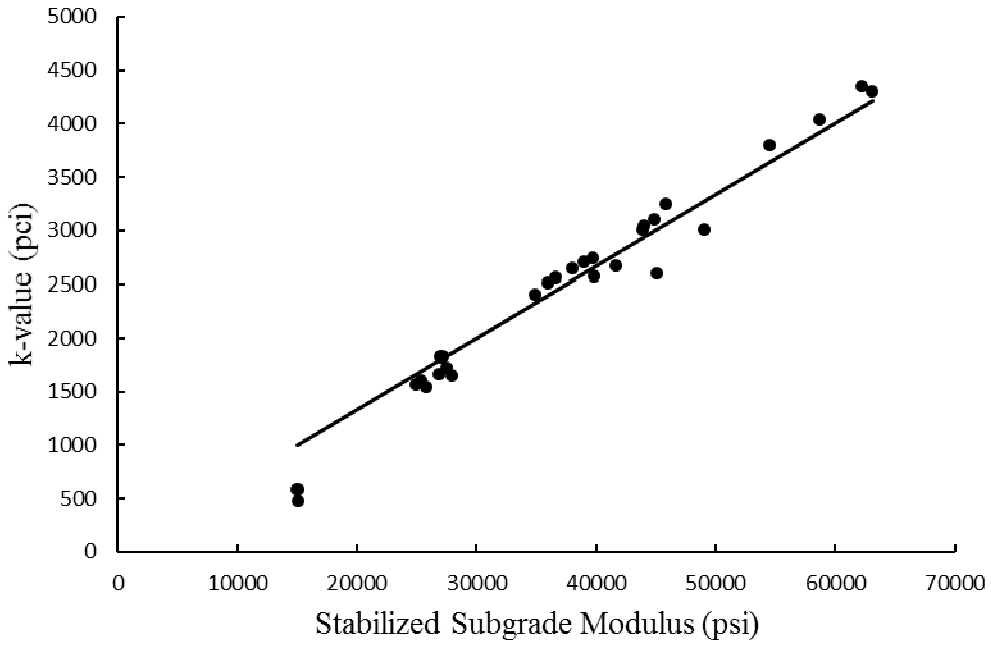

Figure 79. Composite modulus of subgrade reaction (k-value) versus stabilized subgrade modulus relationship based on FWD readings performed directly on stabilized subgrade. (1 psi = 6.89 kPa, 1 pci = 0.27 MN/m^3)

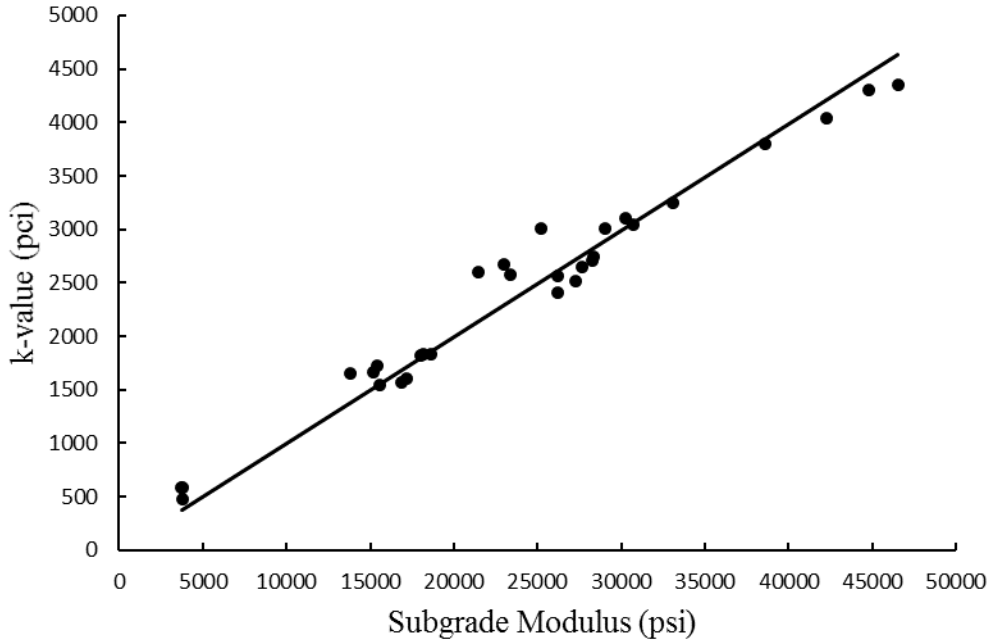

Figure 80. Composite modulus of subgrade reaction (k-value) versus subgrade modulus relationship based on FWD readings performed directly on stabilized subgrade. (1 psi = 6.89 kPa, 1 pci = 0.27 MN/m^3)

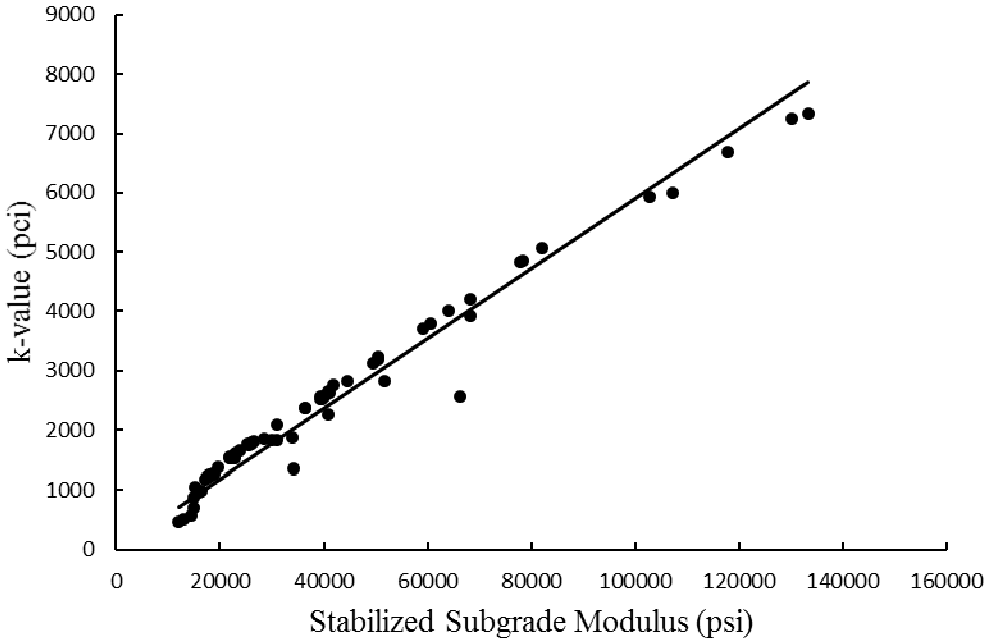

Figure 81. Composite modulus of subgrade reaction (k-value) versus stabilized subgrade modulus relationship based on LWD readings performed directly on stabilized subgrade. (1 psi = 6.89 kPa, 1 pci = 0.27 MN/m^3)

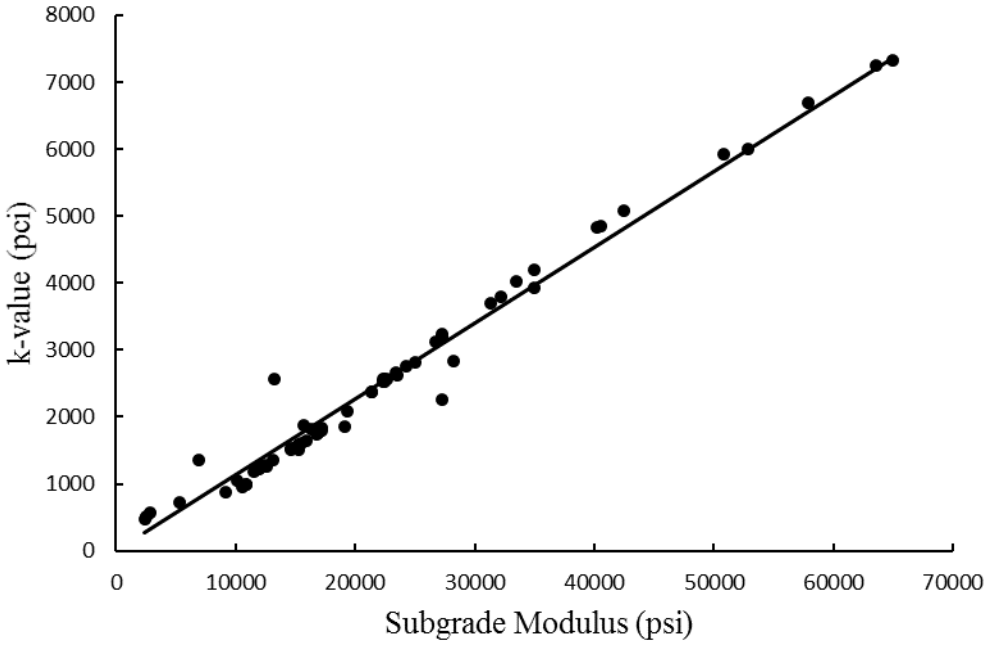

Figure 82. Composite modulus of subgrade reaction (k-value) versus subgrade modulus relationship based on LWD readings performed directly on stabilized subgrade. (1 psi = 6.89 kPa, 1 pci = 0.27 MN/m^3)

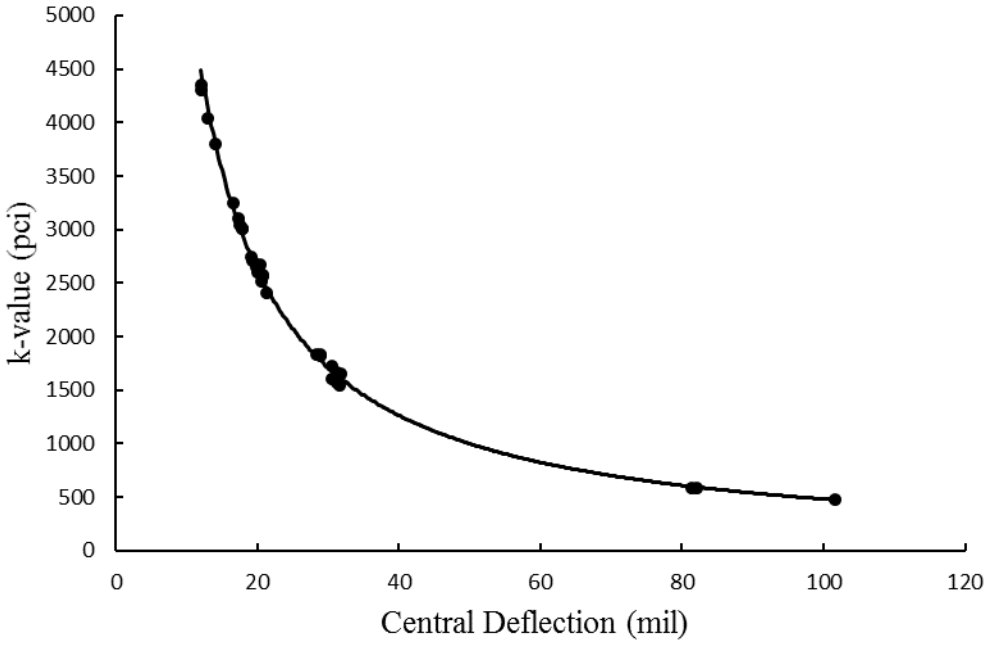

Figure 83. Composite modulus of subgrade reaction (k-value) versus surface deflection at center of load plate based on FWD readings performed directly on stabilized subgrade. (1 pci = 0.27 MN/m^3, 1 mil = 0.0254 mm)

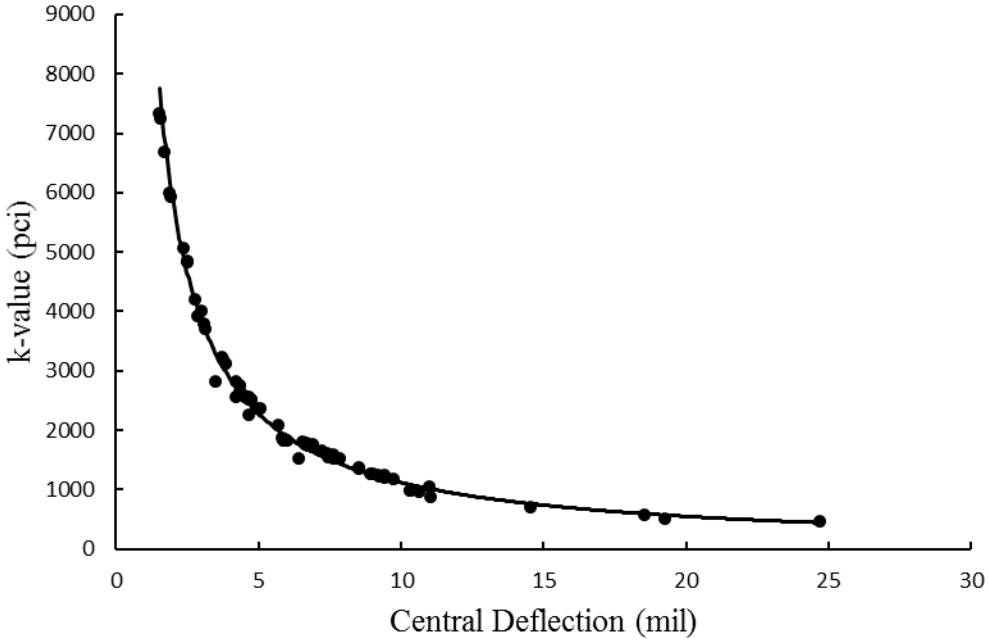

Figure 84. Composite modulus of subgrade reaction (k-value) versus surface deflection at center of load plate based on LWD readings performed directly on stabilized subgrade. (1 pci = 0.27 MN/m^3, 1 mil = 0.0254 mm)

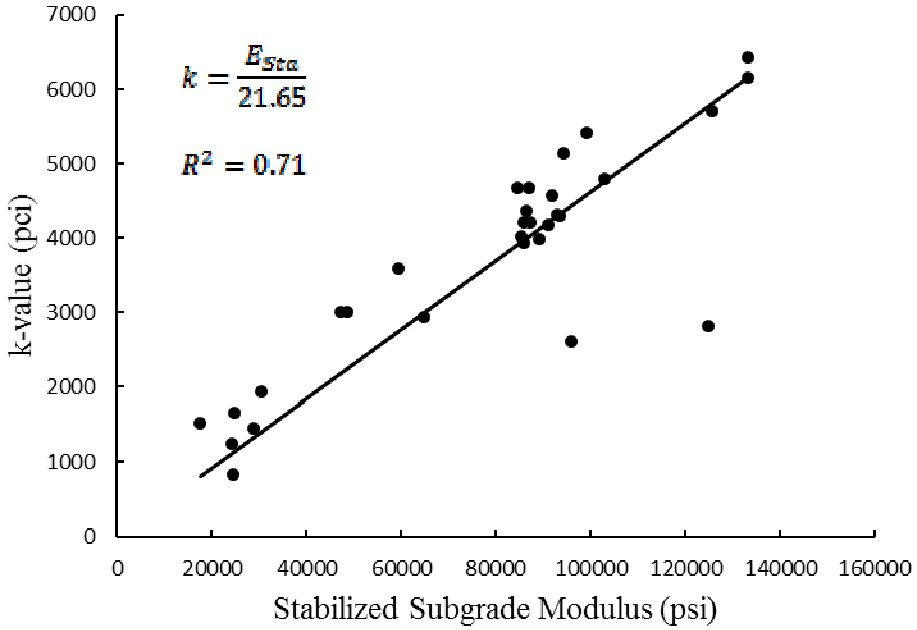

Figure 85. Composite modulus of subgrade reaction (k-value) versus stabilized subgrade modulus relationship based on FWD readings performed directly on base. (1 psi = 6.89 kPa, 1 pci = 0.27 MN/m^3)

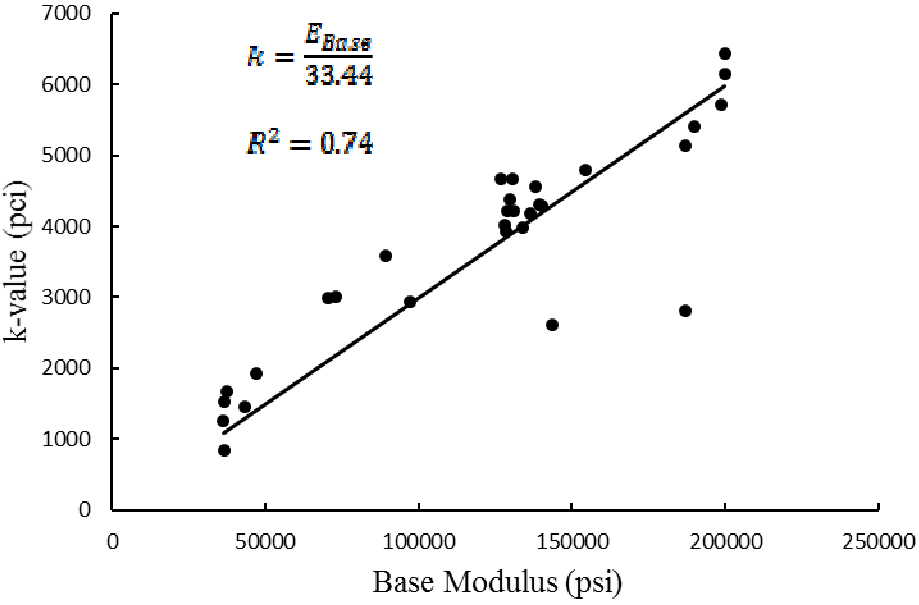

Figure 86. Composite modulus of subgrade reaction (k-value) versus base modulus relationship based on FWD readings performed directly on base. (1 psi = 6.89 kPa, 1 pci = 0.27 MN/m^3)

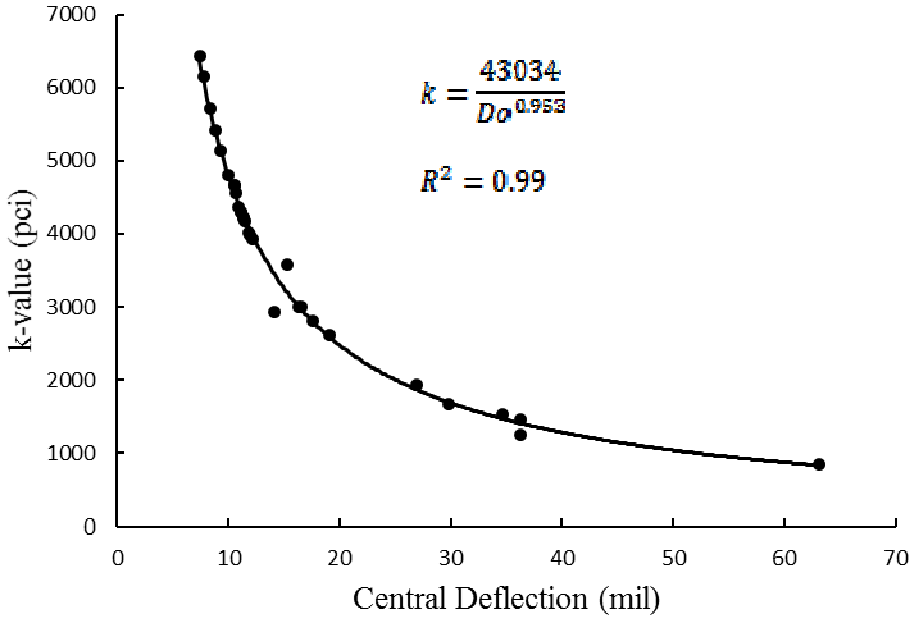

Figure 87. Composite modulus of subgrade reaction (k-value) versus surface deflection at center of load plate based on FWD readings performed directly on base. (1 pci = 0.27 MN/m^3, 1 mil = 0.0254 mm)

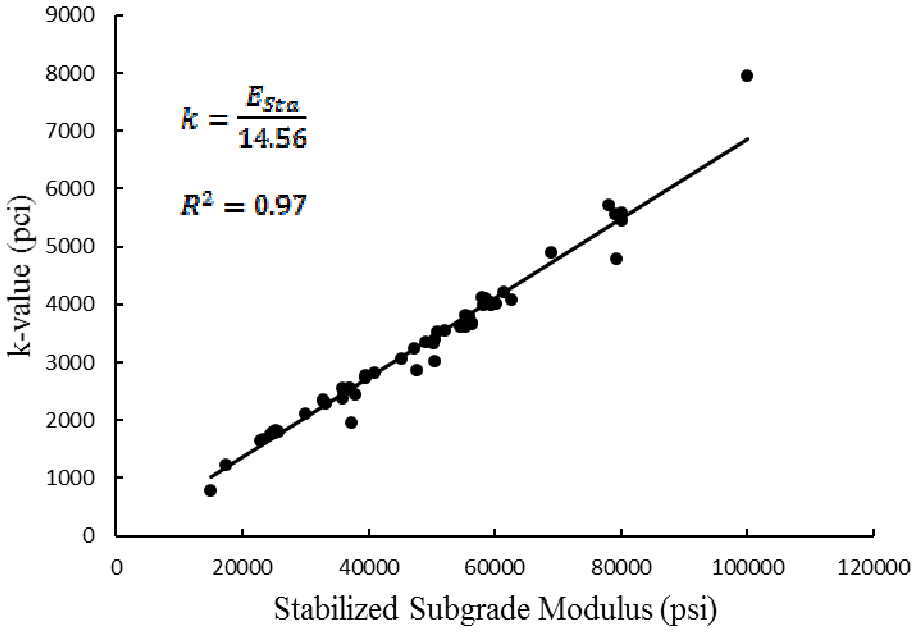

Figure 88. Composite modulus of subgrade reaction (k-value) versus stabilized subgrade modulus relationship based on LWD readings performed directly on base. (1 psi = 6.89 kPa, 1 pci = 0.27 MN/m^3)

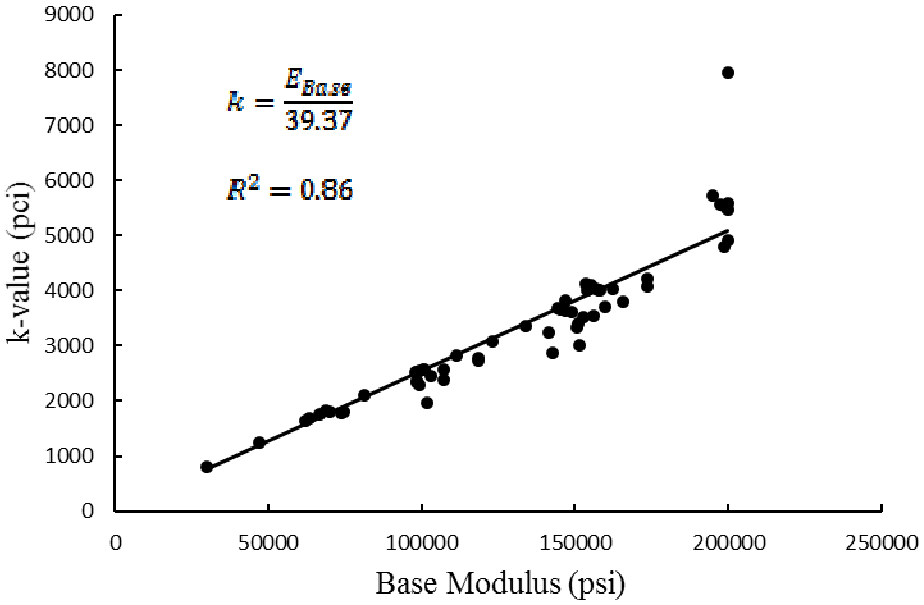

Figure 89. Composite modulus of subgrade reaction (k-value) versus base modulus relationship based on LWD readings performed directly on base. (1 psi = 6.89 kPa, 1 pci = 0.27 MN/m^3)

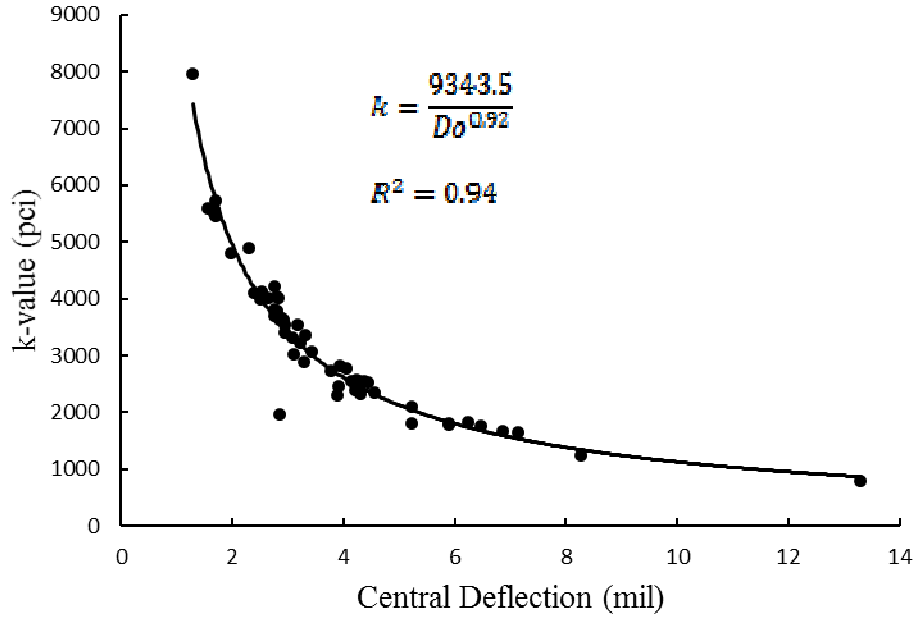

Figure 90. Composite modulus of subgrade reaction (k-value) versus surface deflection at center of load plate based on LWD readings performed directly on base. (1 pci = 0.27 MN/m^3, 1 mil = 0.0254 mm)

Figure 79 through Figure 90 show strong correlations ($R^2 \geq 0.71$, and usually $R^2 > 0.9$) between elastic layer moduli and the composite modulus of subgrade reaction. A summary of the relationships are presented in Table 53. Although these relationships have been developed using limited data, it shows it is possible to accurately predict the composite modulus of subgrade reaction by performing FWD or LWD measurements. The validity of these equations depends on the layer on which the testing was performed. However, these equations may also be valid

only for the sites on which testing was conducted in this study. More FWD and LWD data is required from soils of different types and various stabilization treatments to develop generalizable equations to estimate the modulus of subgrade reaction with chemically stabilized subgrade soils which can be applied across the state.

Another approach could be used to estimate the composite modulus of subgrade reaction is by using Equation 14 or the AASHTO chart in Figure 71 replacing the subgrade modulus with the stabilized subgrade modulus. Applying this approach resulted in composite k-values close to those calculated by Equation 27 and Equation 28, as shown in Figure 91.

Table 53. Relationships between the composite modulus of subgrade reaction *k* versus elastic layer moduli *E* and surface central deflection D_0.

Performed on	FWD	LWD
Stabilized Subgrade	$k = \frac{E_{Sta}}{15}$, $R^2 = 0.96$ $k = \frac{E_{SG}}{10.1}$, $R^2 = 0.96$ $k = \frac{61279}{Do^{1.053}}$, $R^2 = 0.99$	$k = \frac{E_{Sta}}{17}$, $R^2 = 0.97$ $k = \frac{E_{SG}}{8.82}$, $R^2 = 0.97$ $k = \frac{11894}{Do^{1.027}}$, $R^2 = 0.99$
Base layer	$k = \frac{E_{Sta}}{21.65}$, $R^2 = 0.71$ $k = \frac{E_{Base}}{33.44}$, $R^2 = 0.74$ $k = \frac{43034}{Do^{0.953}}$, $R^2 = 0.99$	$k = \frac{E_{Sta}}{14.56}$, $R^2 = 0.97$ $k = \frac{E_{Base}}{39.37}$, $R^2 = 0.86$ $k = \frac{9343.5}{Do^{0.92}}$, $R^2 = 0.94$

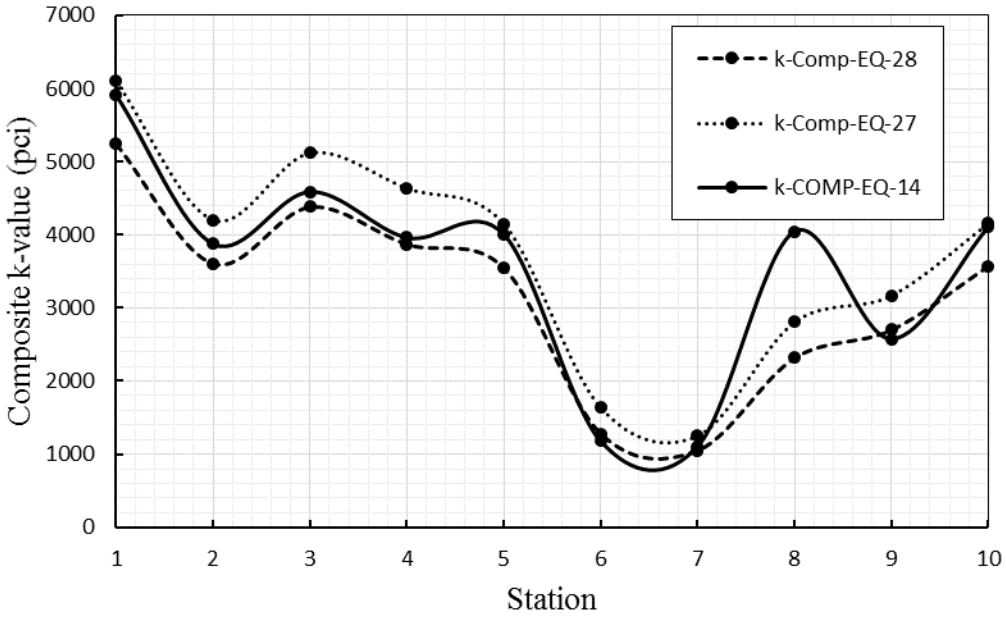

Figure 91. Composite k-value as determined from different approaches using Equation 14, Equation 27, and Equation 28, based on data from FWD readings performed on the base. (1 pci = 0.27 MN/m^3, 1 Station = 100 ft = 30.5 m)

The solid line in Figure 91 with the Equation 14 results lies between the lines marking the results for Equation 27 and Equation 28, with one notable exception at Station 8 and a smaller one at Station 9. This shows that Equation 14 can be used to estimate the results which would otherwise be obtained via FWD. The computation would use Equation 14, which is shown again for reference:

$$lnk_{\infty} = -2.807 + 0.1253(lnD_{SB})^2 + 1.062(lnM_R) + 0.1282(lnD_{SB})(lnE_{SB}) - 0.4114(lnD_{SB}) - 0.0581(lnE_{SB}) - 0.1317(lnD_{SB})(lnM_R)$$

where:

k_{∞} = composite modulus of subgrade reaction in pci with no bedrock
D_{SB} = subbase thickness in inches
M_R = resilient modulus of stabilized subgrade in psi
E_{SB} = elastic modulus of subbase layer in psi

It should also be noted that for M_R, use the value for the stabilized subgrade, rather than the untreated subgrade beneath. M_R, and E_{SB} may be backcalculated from FWD or LWD testing for the project. If deflection data are not available, E_{SB} can be estimated for a given reliability using Figure 92, and M_R can be estimated using the curves in Figure 93. Figure 94 can be used to directly estimate a k-value based on Equation 27 or Equation 28.

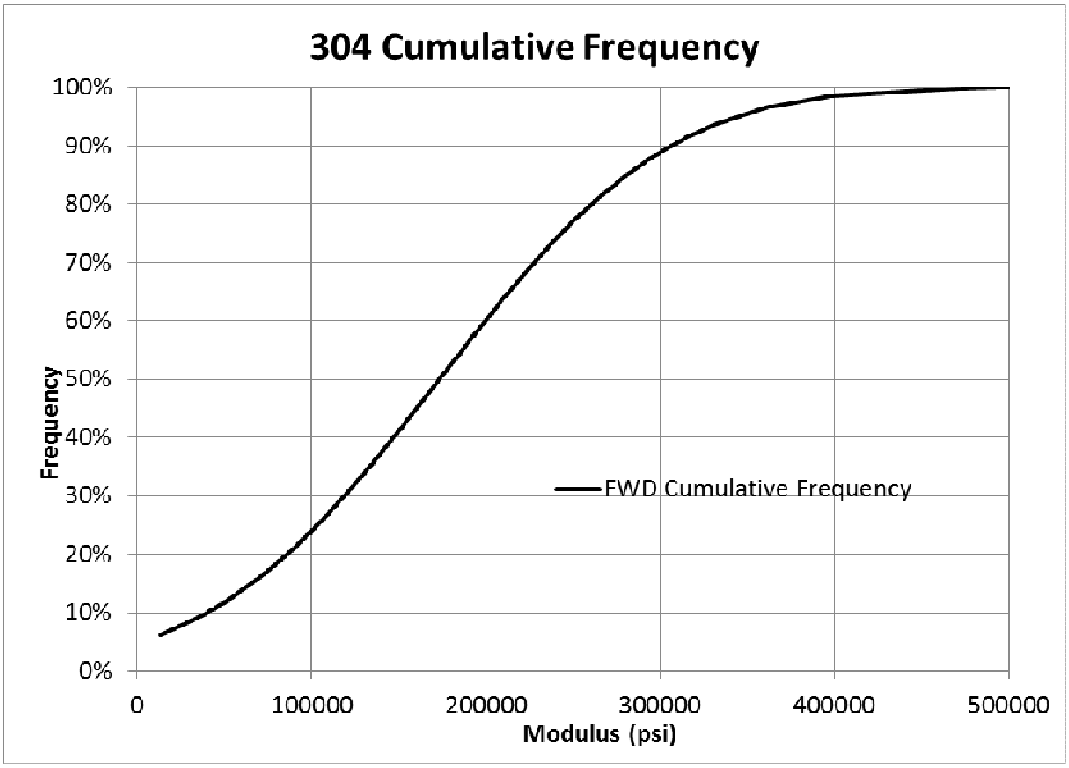

Figure 92. Graph for estimating E_{SB} based on reliability (frequency) for use with Equation 14. [Adapted from Sargand et al., 2014] (1 psi = 6.89 kPa)

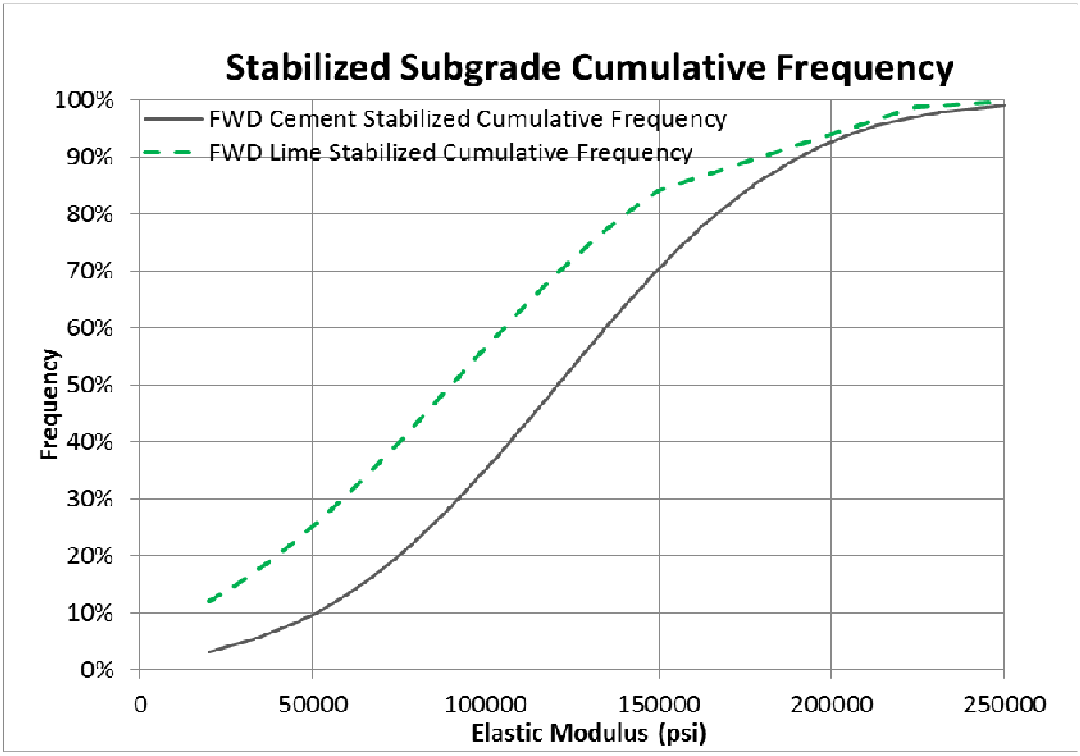

Figure 93. Graph for estimating M_R for stabilized subgrade based on reliability (frequency) for use with Equation 14. [Adapted from Sargand et al., 2014] (1 psi = 6.89 kPa)

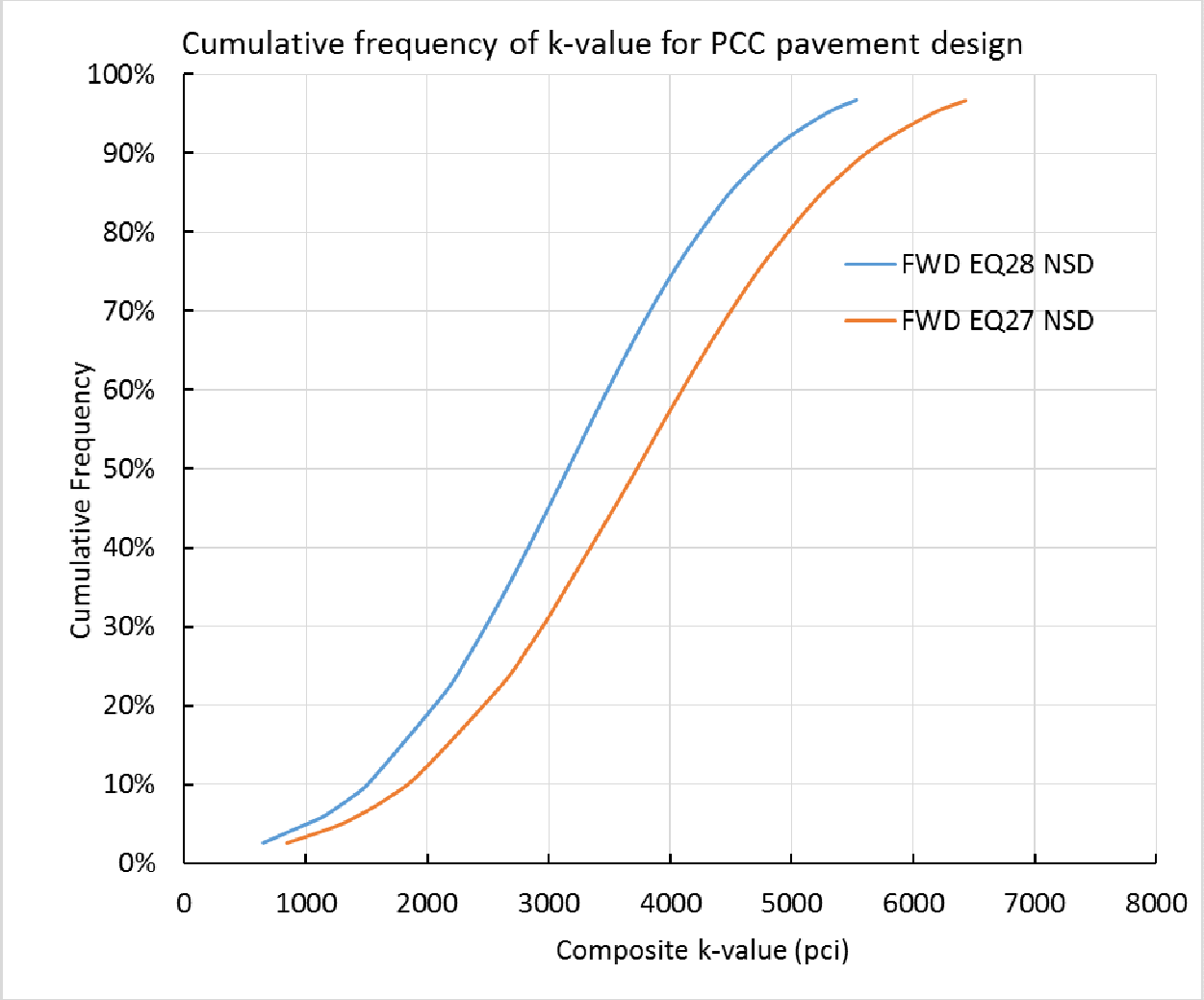

Figure 94. Graph for estimating composite k-value for concrete pavement design based on reliability (frequency) for use with Equation 27 and/or Equation 28. (1 psi = 6.89 kPa)

18 Conclusions and Recommendations

An extensive literature search was conducted to identify factors affecting rigid pavement response and performance. Temperature, traffic, and response data were collected and analyzed to better understand the rigid pavement behavior under representative traffic and weather conditions for Ohio. Three-dimensional finite element models were developed and validated with experimental data to estimate the critical stresses in concrete pavement and how they are affected by slab geometry and the presence of a shoulder for various slab thicknesses and lengths. Fatigue damage calculations and an economic analysis were carried out to determine the optimum slab thickness and length which would provide an acceptably long service life at the least cost. An evaluation of the same pavement geometries using AASHTOWare Pavement ME Design predicted end-of-life values for pavement smoothness and distress measures (IRI, faulting, and cracking), and confirmed the optimum geometry. The effect of weather across Ohio on PCC pavement performance as measured by AASHTOWare with the built-in Enhanced Integrated Climate Model (EICM) was determined by examining the output of selected pavement geometries as a function of weather station inputs. Procedures for determining k-values of chemically stabilized subgrade were proposed.

18.1 Conclusions

Based on this research, the following conclusions can be drawn:

- Slab cracking appears to be the dominant distress type in AASHTOWare for current designs. Predicted cracking decreased with increasing thickness.
- In the review of data from LTPP PCC test sections in Ohio and surrounding states, ranging in age from 5 to 36 years:
  - Sections with transverse cracks in at least 10% of slabs decreased from 60% for 8 in (203 mm) thickness to 29% for 11 in (279 mm) thickness. , validating the AASHTOWare analysis.
  - Faulting is not a major issue with current designs; 91% of the LTPP sections had faulting at or below the maximum acceptable criterion of 0.25 in (6.4 mm).
  - Fully 80% of the LTPP sections had an acceptable IRI (≤ 170 in/mi (2.70 m/km).
  - LTPP test sections on an unbound or combined base performed better than those on a bound base.
- The AADTT count analysis of the WIM data supplied by ODOT for I-70 found the most frequent large vehicles are FHWA Class 9. The most frequent axle spacing observed was 17 ft (5.2 m).
- The maximum negative temperature gradient was found in December, 2000 to be -0.51 C°/cm (-2.32 F°/in), and the maximum positive temperature gradient, in April, 2000, was +0.88 C°/cm (+4.0 F°/in).
- The 3D FEM created using ABAQUS showed the same general trends for concrete pavement responses as did the measured responses from the APLF test sections. The agreement was improved by using the actual amount of loss of support the pavement experienced during curing. The longitudinal loss of support is significantly influenced by slab length, while transverse loss of support is influenced by slab thickness.

- The critical stress analysis showed shorter and thicker slabs exhibited lower tensile stresses under combined effect of temperature gradient and truck load and under negative temperature gradient.
- Including the effective built-in temperature difference (EBITD) in the stress calculations increased the stress level significantly, by 56% under negative temperature gradient and by 46% for the temperature gradient with a truck load. Permanent built-in curl has a significant impact on determining the stress in the pavement.
- The maximum stresses occur when the axle spacing is similar to the slab length and axles are positioned at each end of the slab. The maximum stress is located at the top of the slab, near the center with a little shifting toward the end supporting the heavier axle. Increasing or decreasing the axle spacing slightly would not reduce the maximum tensile stress significantly.
- It is well understood that stresses on concrete pavements due to environmental factors are significantly greater than those due to traffic loads.
- Including PCC tied shoulders in the FEM reduced the stresses induced in the concrete slab by 9%, 13%, and 15% respectively for slab thicknesses of 9 in (229 mm), 12 in (305 mm), and 15 in (381 mm) under combined temperature and truck loads. With asphalt shoulders, the corresponding stresses were decreased by 4%, 6%, and 8%. No significant reduction was observed under temperature load only. Thus tied PCC shoulders provide more lateral support to the pavement than AC shoulders and provide more stress reduction under combined loading. Thicker concrete slabs exhibit more stress reduction from the presence of shoulders. Using a slab width of 14 ft (4.3 m) reduced the maximum tensile stress by less than 2%, which is not significant.
- The 50-year fatigue analysis showed shorter slab lengths resulted in lower stresses, and therefore longer fatigue life, for combined temperature and truck loads. The thickness needed for a 12 ft (3.7 m) slab length, the shortest evaluated, to obtain a 50 year life based on fatigue cracking was 9.5 in (241 mm), 7.6 in (193 mm), and 14.5 in (368 mm) for the PCA, Zero Maintenance, and MEPDG models respectively.
- The FEM analysis of PCC pavement studying the interaction of dowels and tie bars showed maximum stress under the dowel bars was unaffected by tie bar spacing (less than 1% change), while under the tie bars, a decrease in the maximum principal stress of 26% to 30% was noticed as tie bar spacing decreased to half its original value, from 30 in (760 mm) to 15 in (380 mm).
- The presence and spacing of tie bars has an impact on the maximum stresses experienced in the pavement slabs. Additional tie bars are associated with increased stress levels. The effects of the location of tie bars needs to be better understood.
- The results from the AASHTOWare Pavement ME simulation of long-term performance sections showed a slab thickness of less than 11 in (279 mm) will exceed cracking criteria before 50 years. A slab thickness of 12 in (305 mm) and length of 12 ft (3.7 m) exhibited superior performance in terms of IRI, faulting, and transverse cracking for the areas of the state with the most severe climatic conditions, as represented by the Cincinnati weather station. A slab thickness of 11 in (279 mm) would be adequate in the less severe climatic areas, such as Columbus.
- However, the economic analysis shows a slab length of 13.5 ft (4.1 m) and thickness of 12 in (305 mm) is an optimum concrete slab geometry for Ohio for the dowel bar and concrete costs considered, providing performance slightly less than a slab length of 12 ft (3.7 m) and

thickness of 12 in (305 mm) but still meeting performance criteria. Optimal thickness for other slab lengths have been presented for future consideration should the cost of the dowel bars or concrete change significantly. It should be noted this analysis relied on AASHTOWare software using national calibration factors. This analysis should be verified once ODOT completes local calibration of the models.

- Both the fatigue analysis using stresses determined from finite element analysis and the AASHTOWare PavementME show performance in terms of cracking will improve with decreasing slab length for the slab lengths considered; 12 ft (3.7 m) to 17 ft (5.2 m).
- Selecting different weather stations within Ohio for use in AASHTOWare Pavement ME Design showed little variation in the predicted IRI and faulting, less than 10%. However, greater variations were observed in the percent transverse cracking.
- The modulus of subgrade reaction (k-value) significantly increased when a layer of stabilized subgrade was included in the pavement design. Adding a dense graded aggregate base further increased the composite modulus of subgrade reaction. The modulus of subgrade reaction and the composite modulus of subgrade reaction determined from different test methods, FWD, LWD, and GPT, vary because of different loads applied by each device. A lower difference was found between values computed from FWD and LWD measurements than between either and GPT measurements. GPT device almost always produces the lowest k-value. Although there is some variability in the composite modulus of subgrade reaction, the k-value is so high it does not significantly affect the stresses in the concrete slab.
- Relationships between the composite modulus of subgrade reaction and the elastic layer modulus of base and/or stabilized subgrade could be established and used to predict k-value for a system with stabilized subgrade. The AASHTO method for determining the composite modulus of subgrade reaction could also be used on systems with stabilized subgrade by substituting the modulus of the stabilized subgrade for the modulus of untreated subgrade since it provides composite k-values comparable to those derived from FWD measurements. Two additional methods for determining composite k value are presented.

18.2 Recommendations

Based on the field data, the review of concrete pavement actual performance, and the comprehensive finite element model including live load, built-in curling, and temperature gradient, some recommendations can be made. It should be noted in the modeling the subgrade material, base material, and base thickness were all fixed and were not variables in this study. The recommendations are as follows:

- ODOT should adopt a slab length of 13.5 ft (4.1 m) for jointed plain concrete pavement. This slab length should be verified once ODOT completes local calibration of the AASHTOWare software. Even if the 13.5 ft (4.1 m) slab length proves to not be optimal, both FEM analysis and AASHTOWare analysis with national calibration factors indicate this length will perform better than the current 15 ft (4.6 m) length used by ODOT
- A slab thickness of 12 in (305 mm) with 13.5 ft (4.1 m) joint spacing is predicted to achieve a service life of at least 50 years, at the lowest initial cost, for typical Interstate traffic volume and truck configuration in Ohio based on this analysis.
- To ensure the pavement achieves long life, high performance material should be used including performance engineered concrete mixtures and alternative materials for tie and dowel bars.

- A procedure was created for determining the k value of chemically stabilized subgrade and should be incorporated in ODOT's current AASHTO 1993 rigid pavement design method.
- Construct a rigid test pavement in Ohio University's Accelerated Pavement Load Facility (APLF) with up to six sections built and instrumented to evaluate dowel bar and tie bar interactions, to help address questions on performance. This experiment could also provide data to develop or verify built-in curling models.

19 References

Abbas, Ala R., and Frankhouser, Andrew, *Improved Characterization of Truck Traffic Volumes and Axle Loads for Mechanistic-Empirical Pavement Design*, Report FHWA/OH-2012/21 for the Ohio Department of Transportation, December 2012.

Altoubat, S. A., and Lange, D. A. (2001). "Creep, shrinkage and cracking of restrained concrete at early age". *ACI Materials Journal*, *99*(3), 326-327.

American Association of State Highway and Transportation Officials (AASHTO). (1993). *AASHTO Guide for Design of Pavement Structures*, 1993 (Vol. 1). AASHTO, Washington, DC.

American Association of State Highway and Transportation Officials (AASHTO); 2008, *Mechanistic-Empirical Pavement Design Guide, A Manual of Practice*, July 2008 Interim Edition, Washington DC: ASSHTO, ISBN: 978-1-56051-423-7.

American Association of State Highway and Transportation Officials (AASHTO); 2010, *Guide for the Local Calibration of the Mechanistic-Empirical Pavement Design Guide*, First Edition, November 2010, ASSHTO, ISBN: 978-1-56051-449-7.

American Association of State Highway and Transportation Officials (AASHTO); 2015, *Mechanistic-Empirical Pavement Design Guide, A Manual of Practice*, Second Edition, August 2015, ASSHTO, ISBN: 978-1-56051-597-5.

American Association of State Highway and Transportation Officials (AASHTO), (2012). *LRFD Bridge design specifications*. AASHTO, Washington, DC.

ACI Committee 318 (2014) Building code requirements for structural concrete (ACI 318-14), with Commentary on Building code requirements for structural concrete (ACI 318R-14). American Concrete Institute, Farmington Hills, MI, September 2014.

Armaghani, J. M., Larsen, T. J., and Smith, L. L. (1987). "Temperature response of concrete pavements". *Transportation Research Record No. 1121*, pp. 23–33.

Awad, M.E. and Hilsdorf, H.K., (1974). "Strength and Deformation Characteristics of Plain Concrete Subjected to High Repeated and Sustained Loads," *Fatigue of Concrete: Abeles Symposium*, Detroit, MI, ACI Publication SP-41, ACI, Farmington Hills, MI, pp. 1-13.

Ballinger, C.A., (1972) "Cumulative Fatigue Damage Characteristics of Plain Concrete", *Transportation Research Record* 370 Highway Research Board, 1972.

Barker, W. R., and Alexander, D. R. (2012). *Determining the Effective Modulus of Subgrade Reaction for Design of Rigid Airfield Pavements Having Base Layers*. Geotechnical and Structures Laboratory, Engineer Research and Development Center, US Army Corps of Engineers, Vicksburg, MS.

Beckemeyer, C., Khazanovich, L., and Thomas Yu, H. (2002). Determining Amount of Built-in Curling in Jointed Plain Concrete Pavement: Case Study of Pennsylvania 1-80. *Transportation Research Record*, 1809, 85-92.

Beegle, D.J., and Sargand, S. M. (1995). *Three-Dimensional Modeling of Rigid Pavement*. Report ST/SS/95-002. Ohio Department of Transportation and FHWA, U.S. Department of Transportation, September 1995.

Bordelon, A. C., Roesler, J., and Hiller, J. E. (2009). *Mechanistic-empirical design concepts for jointed plain concrete pavements in Illinois*. Illinois Center for Transportation Series No. 09-052, Illinois Center for Transportation (ICT), University of Illinois, Urbana-Champaign, IL, July 2009.

Boussinesq, J. (1885). *Application des potentiels à l'étude de l'équilibre et du mouvement des solides élastiques*, Guthier-Villars, Paris, France.

Bureau of Transportation Statistics, (2018), "Road Condition" website. Available online at https://www.bts.gov/content/road-condition, accessed April 10, 2018.

Byrum, C. (2000). Analysis by high-speed profile of jointed concrete pavement slab curvatures. *Transportation Research Record*, 1730, 1-9.

Carlson, R. W. (1938). Drying shrinkage of concrete as affected by many factors. *Proceedings of the American Society for Testing and Materials*, ASTM, West Conshohocken, PA, Vol. 38, Pt. II, pp. 419–440.

Ceylan, H., Gopalakrishnan, K., Kim, S., Taylor, P., Alhasan, A. A., and Yang, S. (2016). *Impact of Curling and Warping on Concrete Pavement*. Report No. IHRB Project TR-668, Institute for Transportation, Iowa State University, Ames, IA, July 2016.

Channakeshava, C., F. Barzegar, and G. Z. Voyiadjis. (1993). "Nonlinear FE analysis of plain concrete pavements with doweled joints". ASCE *Journal of Transportation Engineering*, 119(5): 763–781.

Chatti, K., Buch, N., Haider, S. W., Pulipaka, A. S., Lyles, R. W., Gilliland, D., and Desaraju, P. (2005). "LTPP data analysis: Influence of design and construction features on the response and performance of new flexible and rigid pavements", NCHRP Web-only document 74, Transportation Research Board, National Academies, Washington, DC.

Chen, H., Dere, Y., Sotelino, E., & Archer, G. (2002). *Mid-panel cracking of Portland cement concrete pavements in Indiana.* JTRP Technical Report FHWA/IN/JTRP-2001/14. Joint Transportation Research Program, Indiana Department of Transportation and Purdue University, West Lafayette, Indiana, 146. DOI 10.5703/1288284313269.

Chou, E., Fournier, L., Luo, Z., and Wielinski, J. (2004). *Structural Support of Lime or Cement Stabilized Subgrade Used with Flexible Pavements*. Report No. FHWA/OH-2004/017 for the Ohio Department of Transportation, University of Toledo, Toledo, OH, November 2004.

Chou, Y. T. (1984). "Stress Analysis of Small Concrete Slabs on Grade". *Journal of Transportation Engineering*, ASCE, Vol. 110, No. 5, pp. 481-492.

Choubane, B., and Tia, M. (1995). "Analysis and Verification of Thermal-Gradient Effects on Concrete Pavement". *Journal of Transportation Engineering*, Vol. 121, No. 1, pp. 75-81.

Darter, M. I., and Barenberg, E.J. (1977). *Design of a Zero-maintenance Plain Jointed Concrete Pavement, Volume One-Development of Design Procedures*, Report No. FHWA-RD-77-111, Report for the Federal Highway Administration, University of Illinois, Urbana, IL, June 1977.

Darter, M. I. (1992). *Report on the 1992 U.S. Tour of European Concrete Highways*. US Tech, Publication No. FHWA-SA-93-012, Federal Highway Administration, Washington DC, 124.

Darter, M. I., Hall, K. T., and Kuo, C-M. (1995). *Support Under Portland Cement Concrete Pavements*. NCHRP Report 372, Transportation Research Board, Washington, DC, 56 p.

Darter, M. I., Von Quintus, H., Jiang, Y. J., Owusu-Antwi, E. B., and Killingsworth, B. M. (1997). *Systems for Design of Highway Pavements: Final Report, Catalog of Recommended Pavement Design Features*, Report No. NCHRP Project 1-32 For the Transportation Research Board, Washington, DC, May 1997.

Darter, M., Khazanovich, L., Snyder, M., Rao, S., and Hallin, J. (2001). "Development and calibration of a mechanistic design procedure for jointed plain concrete pavements". *Proceedings of 7th International Conference on Concrete Pavements: The Use of Concrete in Developing Long-Lasting Pavement Solutions for the 21st Century (Vol. 1)*. Orlando, FL, September 9-13, 2001.

Davids, W. G. (2000). "Effect of dowel looseness on response of jointed concrete pavements." *Journal of Transportation Engineering*, 126(1), 50–57.

Davids, W. G., Wang, Z., Turkiyyah, G., Mahoney, J. P., and Bush, D. (2003). "Three-dimensional finite element analysis of jointed plain concrete pavement with EverFE2.2." *Transportation Research Record* 1853, 92–117.

Dempsey, B. J. (1982). "Laboratory and field studies of channeling and pumping". *Transportation Research Record* 849.

Dere, Y., Asgari, A., Sotelino, E. D., and Archer, G. C. (2006). "Failure prediction of skewed jointed plain concrete pavements using 3D FE analysis." *Engineering Failure Analysis*, 13, 898–913.

Domenichini, L., and Marchionna A. (1981). "Influence of Stress Range on Plain Concrete Pavement Fatigue Design". *Proceedings of the Second International Conference on Concrete Pavement Design*, Purdue University, Lafayette, IN, April 14-16, 1981.

Duncan, J. M., and Lysmer, J. (Eds.). (1969). *Stresses and Deflections in Foundations and Pavements*. Institute of Transportation and Traffic Engineering, Department of Civil Engineering, University of California, Berkeley, CA.

Dynatest International A/S, (2010),".Elmod 6 Quick Start Manual 6.0. Available online at https://www.scribd.com/document/186906813/Elmod-6-Quick-Start, accessed August 15, 2017.

Eisenmann, J., and Leykauf, G. (1990). "Effect of paving temperatures on pavement performance". Paper presented at the 2nd International Workshop on Theoretical Design of Concrete Pavements, Madrid, Spain.

ERES (2002) NCHRP 1-37A Draft Document. *2002 Guide for the Design of New and Rehabilitated Pavement Structures*. ERES Consultants Division of ARA Inc., Champaign Illinois, May 2002.

ERES (2004) *Guide for Mechanistic-Empirical Design of New and Rehabilitated Pavement Structures*, Final Report prepared for Project 1-37A of the National Cooperative Highway Research Program, Transportation Resaearch Board, National Research Council, Washington DC by ARA, Inc. ERES Consultants Division, Chicago, IL, March 2004.

Fang, Y. F. (2001). "Environmental Influences on Warping and Curling of PCC Pavement". *Proceedings of 7th International Conference on Concrete Pavements: The Use of Concrete in Developing Long-Lasting Pavement Solutions for the 21st Century (Vol. 1)*. Orlando, FL, September 9-13, 2001.

Federal Highway Administration (FHWA), (2013), *2013 Status of the Nation's Highways, Bridges, and Transit: Conditions and Performance Report*, Exhibit 3-1, Report to Congress, Washington DC, United States Department of Transportation, Federal Highway Administration, p. 3-2.available at www.fhwa.dot.gov/policy/2013cpr as of June 2015, accessed April 10, 2018.

Grasley, Z. (2003). Internal relative humidity, drying stress gradients, and hygrothermal dilation of concrete. Portland Cement Association PCA R&D Serial No. 2625, University of Illinois, Urbana, IL.

Guo, H., Sherwood, J. A., and Snyder, M. B. (1995). "Component dowel bar model for load transfer systems in PCC pavements." *Journal of Transportation Engineering*, 121(3), 289–298.

Hall, K. T., Darter, M. I., and Chen-Ming, K. U. O. (1995). "Improved methods for selection of k-value for concrete pavement design". *Transportation Research Record* 1505, 128-136.

Hall, K. T., Darter, M. I., Hoerner, T. E., and Khazanovich, L. (1997). *LTPP Data Analysis. Phase I: Validation of Guidelines for k-Value Selection and Concrete Pavement Performance Prediction*, Report No. FHWA-RD-96-198.

Hall, K. T. (2000). "State of the Art and Practice in Rigid Pavement Design". A2B02: Committee on Rigid Pavement Design, Transportation Research Board, Washington, DC. Available online at http://onlinepubs.trb.org/onlinepubs/millennium/00105.pdf, accessed August 12, 2017.

Hammons, M. I. (1998). "Validation of Three-Dimensional Finite Element Modeling Technique for Joints in Concrete Airport Pavements". *Transportation Research Record* 1629, pp. 67-75.

Hatt, W. K. (1925). "The effect of moisture on concrete". *Transactions of the American Society of Civil Engineers*, 89(1), 270-307.

Hilsdorf, H.K., and Kesler, C.E., (1976) "Fatigue Strength Of Concrete Under Varying Flexural Stresses", *Proceedings of the American Concrete Institute*, vol. 63, 1966, pp. 1059-1976.

Huang, Y. H., and Wang, S. T. (1973). "Finite-Element Analysis of Concrete Slabs and its Implications for Rigid Pavement Design". *Highway Research Record* 466, pp. 55-79.

Huang, Y. H. (1993). Pavement Analysis and Design, Prentice Hall, Upper Saddle River, New Jersey.

Huang, Y.H. (2003). *Pavement Analysis and Design*, 2nd Edition, Prentice-Hall, New Jersey, USA.

Hveem. F. N. (1949). *A Report of an Investigation to Determine Causes for Displacement and Faulting at the Joints in Portland Cement Concrete Pavements on California Highways*. California Division of Highways, Materials and Research Department.

Ioannides, A. M., and Donnelly, J. P. (1984). "Three-Dimensional Analysis of Slab on Stress-Dependent Foundation". *Transportation Research Record* 1196, pp. 72-84.

Ioannides, A. M., and Donnelly, J. P. (1988). "Three-Dimensional Analysis of Slab on Stress-Dependent Foundation". *Transportation Research Record* 1196, pp. 72-84.

Janssen, D. J. (1986). "Moisture in Portland Cement Concrete", *Transportation Research Record* 1121, pp. 40–44.

Jenq, Y., C. Liaw and S. Kim (1993), "Effects of Temperature on Early Crack Formation in Portland Cement Concrete Pavement", *Transportation Research Record 1388*, National Research Council, Washington, D.C., pp. 35-41.

Jeong, J. H., and D. G. Zollinger, (2005). Environmental effects on the behavior of jointed plain concrete. ASCE *Journal of Transportation Engineering*, 131(2): 140–148.

Khazanovich, L., and Ioannides, A. M. (1993). "Finite Element Analysis of Slabs-On-Grade Using Higher Order Subgrade Soil Models". *Airport Pavement Innovations: Theory to Practice*, ASCE, New York, New York, 10017, pp. 16-30.

Khazanovich, L., Buch, N., and Gotlif, A. (2001). *Evaluation of alignment tolerances for dowel bars and their effects on joint performance*, Report No. RC-1395. Pavement Research Center of Excellence, Michigan State University, East Lansing, MI.

Kim, J., and Hjelmstad, K. D. (2003). "Three-dimensional finite element analysis of doweled joints for airport pavements." *Transportation Research Record* 1853, 100–109.

Kovler, K. (1999). A new look at the problem of drying creep of concrete under tension. *Journal of Materials In Civil Engineering*, 11(1), 84-87.

Kuo, C. (1994), *Three-Dimensional Finite Element Analysis of Concrete Pavement*, Ph.D. Thesis, University of Illinois at Urbana-Champaign.

Larson, R.M., and Smith, K.D. (2011). *Evaluation of Alternative Dowel Bar Materials and Coatings*, Pooled Fund Study TPF-5(188). Final Report FHWA/OH-2011/19 for Ohio Department of Transportation, Columbus, Ohio, November 2011. Available online at https://ntl.bts.gov/lib/43000/43200/43289/134411_FR.pdf, accessed December 12, 2017.

Lederle, R. E., R. W. Lothschutz, and J. E. Hiller. (2011). *Field Evaluation of Built-In Curling Levels in Rigid Pavements*. Report No. MN/RC 2011-16. Minnesota Department of Transportation, St. Paul, MN.

Lee, Y. H., and M. I. Darter. (1994a). "Loading and curling stress models for concrete pavement design". *Transportation Research Record* 1449: 101–113.

Lee, Y. H., and M. I. Darter. (1994b). "New predictive modeling techniques for pavements". *Transportation Research Record* 1449: 234–245.

Lim, S., Jeong, J. H., and Zollinger, D. G. (2009). "Moisture profiles and shrinkage in early-age concrete pavements". *International Journal of Pavement Engineering*. Vol. 10, Issue 1, p. 29-38.

Little, D. N. (1995) *Stabilization of Pavement Subgrades and Base Courses With Lime*, for the National Lime Association. Kendall Hunt Publishing Company, Dubuque, IA.

Little, D. N., Scullion, T., Kota, P. B. V. S., and Bhuiyan, J. (1995) *Identification of the structural benefits of base and subgrade stabilization*. Report No. FHWA/TX-94/1287-2 For the Texas Department of Transportation by the Texas Transportation Institute, College Station, TX, October 1995.

Littleton, P. C. (2003). *Effect of Stress State on Concrete Slab Fatigue Resistance*. Master's Thesis, University of Illinois, Urbana, IL.

Lu, Q., Zhang, Y., and Harvey, J.T. (2007) "Analysis of Truck Traffic Growth for the Mechanistic-Empirical Pavement Design Guide", *TRB 2007 Annual Meeting CD-ROM*, Paper No. 07-1592 presented at the 86th Annual Transportation Research Board Meeting, Washington DC, January 21-25, 2007.

Luoke, L., Yiqiu, T., Xiangbing, G., and Yunliang, L. I. (2009). "Characterization of contact stresses between dowels and surrounding concrete in jointed concrete pavement". *International Journal of Civil and Environmental Engineering*, 12(5), 23-27.

Mackiewicz, P. (2015). "Finite-element analysis of stress concentration around dowel bars in jointed plain concrete pavement". *Journal of Transportation Engineering*, 141(6), 06015001.

Mahboub, K. C., Liu, Y., and Allen, D. L. (2004). "Evaluation of temperature responses in concrete pavement." *Journal of Transportation Engineering*, 130(3), 395–401.

Maitra, S. R., Reddy, K. S., and Ramachandra, L. S. (2009). "Load transfer characteristics of dowel bar system in jointed concrete pavement". *Journal of Transportation Engineering*, 135(11), 813-821.

Mallela, J., and George, K. P. (1994). "Three-Dimensional Dynamic Response Model for Rigid Pavements". *Transportation Research Record* 1448, pp. 92-99.

Mallela, J.; Glover, L.T.; Darter, M.I.; Von Quintus, H.; Gotlif, A.; Stanley, M., Sadasivam, S. (2009). *Guidelines for Implementing NCHRP 1-37A M-E Design Procedures in Ohio*, Report No. FHWA/OH-2009/9 for the Ohio Department of Transportation, Applied Research Associates, Champaign IL, November 2009.

Masad, E., Taha, R., and Muhunthan, B. (1996). "Finite-Element Analysis of Temperature Effects on plain-Jointed Concrete Pavements". *Journal of Transportation Engineering*, ASCE, Vol. 122, No. 5, pp. 388-398.

Masada, T. and Sargand, S.M. (2002) *Laboratory Characterization of Materials and Data Management for Ohio-SHRP Projects (U.S. 23)*, Report No. FHWA/OHG-2001/07 for Ohio Department of Transportation (includes CD-ROM), January 2002.

Masada, T., Sargand, S. M., Abdalla, B., and Figueroa, J. L. (2004). *Material Properties for Implementation of Mechanistic-Empirical (ME) Pavement Design Procedures*, Report No. FHWA/OH-2003/021 for the Ohio Department of Transportation, February 2004.

Mather, B. (1963). Reports of the Committee on Durability of Concrete–Physical Aspects–Drying Shrinkage. Highway Research News, 26-29.

Miner, M. A. (1945). "Cumulative Damage in Fatigue". *Transactions of the American Society of Mechanical Engineers*, Vol. 67, pp. A159–A164.

Murdock, J.W. and C.E. Kesler, (1958). "Effect of Range of Stress on Fatigue Strength of Plain Concrete Beams," *Journal of the American Concrete Institute*, Vol. 30, No. 2, pp. 221-231.

Nantung, T. E. (2011). *High Performance Concrete Pavement in Indiana*. Report No. FHWA/IN/JTRP-2011/20. Indiana Department of Transportation, Division of Research and Development, West Lafayette, IN.

Nasim, M. A., Karamihas, S. M., Gillespie, W. H., and David S. (1991). "Behavior of a Rigid Pavement under Moving Dynamic Loads". *Transportation Research Record* 1307, pp. 129-135.

Nassiri, S. (2011). *Establishing permanent curl/warp temperature gradient in jointed plain concrete pavements*. PhD dissertation, University of Pittsburgh, Pittsburgh, PA.

Netemeyer, R., and Munsell, S. (1995). *Layer by layer evaluation of a PCC pavement as it was constructed: comparison of backcalculated material values to lab material values*, Report RDT 99-002 for Missouri Department of Transportation, Jefferson City, MO, May 1995.

Neville, A. M., and Meyers, B. L. (1964). *Creep of concrete: Influencing factors and prediction*. ACI Special Publication SP-9, American Concrete Institute, Detroit, MI, pp. 1–33.

Ohio Department of Highways (ODH), (1951), *A Survey of Pumping in Ohio*, A Cooperative study by Ohio State Highway Department and Portland Cement Association, Research Report No. 2, Columbus, OH, March 1, 1951.

Ohio Department of Transportation (ODOT), (2017), *Construction Administration Manual of Procedures*, Ohio Department of Transportation, Columbus, OH. Available online at https://www.dot.state.oh.us/Divisions/ConstructionMgt/Pages/2017-MOP.aspx, accessed December 7, 2017.

Ohio Department of Transportation (ODOT), (2014), *Pavement Design Manual*, Office of Pavement Engineering, Ohio Department of Transportation, Columbus, OH.

Owusu-Antwi, E. B., Titus-Glover, L., and Darter, M. I. (1998). *Design and Construction of PCC Pavements, Volume I: Summary of Design Features and Construction Practices That Influence Performance of Pavements*, Report No. FHWA-RD-98-052 for the Federal Highway Administration, Washington, DC, April 1998.

Packard, R. G. (1973). *Design of Concrete Airport Pavement*. Engineering Bulletin EB050.03P. Portland Cement Association, Skokie, IL.

Packard, R. G., and Tayabji, S. D. (1983). Mechanistic design of concrete pavements to control joint faulting and subbase erosion. Portland Cement Association.

Packard, Robert G., (1984). *Thickness Design for Concrete Highway and Street Pavements*. Engineering Bulletin from Portland Cement Association, Skokie, IL.

Park, J. Y., W. S. Yeom, S. H. Kim, and J. H. Jeong. (2015). "Environmental load for design of airport concrete pavements". *Proceedings of the Institution of Civil Engineers-Transport* 168(2): 139–149.

Parsons, T. A., and Hall Jr., J. W. (2003). "The Effects of Slab Size on PCC Pavement Performance". A Paper Presented at *Airfield Pavements, Challenges and New Technologies*, ASCE Transportation and Development Institute, Las Vegas, Nevada, September 21-24, 2003.

Poblete, M., Salsilli, R., Valenzuela, R., Bull, A., and Spratz, P. (1988). "Field evaluation of thermal deformations in undoweled PCC pavement slabs". *Transportation Research Record* 1207, 217-228.

Rao, C., Barenberg, E. J., Snyder, M. B., and Schmidt, S. (2001). "Effects of temperature and moisture on the response of jointed concrete pavements". *Proceedings of 7th International Conference on Concrete Pavements: The Use of Concrete in Developing Long-Lasting Pavement Solutions for the 21st Century (Vol. 1)*. Orlando, FL, September 9-13, 2001.

Rao, S., and J.R. Roesler (2004). "Cumulative Fatigue Damage Analysis of Concrete Pavement using Accelerated Pavement Testing Results," *Proceedings of the 2nd International Conference on Accelerated Pavement Testing*, Minneapolis, MN.

Rao, S. (2005). *Characterizing Effective Built-In Curling and Its Effect on Concrete Pavement Cracking*. PhD dissertation. University of Illinois at Urbana-Champaign, Urbana, IL, June 2005. Available online at https://www.ideals.illinois.edu/bitstream/handle/2142/29960/Rao_Shreenath.pdf, accessed August 14, 2017.

Rao, S., and J. R. Roesler. (2005a). *Characterization of Effective Built-in Curling and Concrete Pavement Cracking on the Palmdale Test Sections*. University of Illinois at Urbana-Champaign, Urbana, IL. Pavement Research Center, University of California Berkeley, Berkeley CA, May 2005. Available online at http://www.ucprc.ucdavis.edu/PDF/Eff%20Built-In%20Curling%20DRAFT.pdf, accessed August 12, 2017.

Rao, S., and J. R. Roesler. (2005b). "Characterizing effective built in curling from concrete pavement field measurements". ASCE *Journal of Transportation Engineering*, 131 (4): 320–327.

Roesler, J. R. (1998) *Fatigue of Concrete Beams and Slabs*. Ph. D. Dissertation, University of Illinois, Urbana, IL.

Roesler, J. R., Lange, D., and Ulreich, G. (2003). *Fracture behavior of full-scale, fiber-reinforced concrete slabs*. Report prepared for WR Grace, Inc., University of Illinois, Urbana, IL.

Rufino, D. M. (2003). *Mechanistic analysis of in-service airfield concrete pavement responses*. Doctoral dissertation, University of Illinois at Urbana-Champaign.

Sargand, S. M., Edwards, W., and Khoury, I. (2003). *Evaluation of Forces in Dowel Bars under Controlled Conditions*. Report for U.S. Department of Transportation and Federal Highway Administration, ORITE, Department of Civil Engineering, Ohio University, Athens, Ohio, 43 pp.

Sargand, S., and Abdalla, B. (2006). *Truck/Pavement/Economic Modeling and In-Situ Field Test Data Analysis Applications – Volume 2: Verification And Validation Of Finite Element Models For Rigid Pavement Using In Situ Data – Selection Of Joint Spacing*. Report No. FHWA/OH-2006/3B for Ohio Department of Transportation Office of Research and

Development and the U.S. Department of Transportation, Federal Highway Administration, June 2006.

Sargand, S., Khoury, I., Gray, J., and Al-Jhayyish, A. (2014). *Incorporating Subgrade Stabilization in Pavement Design and Construction*, Report FHWA/OH-2014/12 for Ohio Department of Transportation, October 2014.

Sargand, S. M., Green, R., Zhu, J., and Khoury, I. (2017). *Forensic Study of Early Failures with Unbonded Concrete Overlays*, Report FHWA/OH-2017/38 for Ohio Dept. of Transportation, November, 2017.

Saxena, P., Hoegh, K., Khazanovich, L., and Gotlif, A. (2009). "Laboratory and finite element evaluation of joint lockup." *Transportation Research Record* 2095, 34–42.

Schmidt, S. (2000). *Built-in curling and warping in PCC pavements*. M. S. Thesis, University of Minnesota, Minneapolis.

Sehn, A. L. (2002). *Evaluation of Portland Cement Concretes Containing Ground Granulated Blast Furnace Slag*. Report No. FHWA/OH-2002/022, for Ohio Department of Transportation, Department of Civil Engineering, University of Akron, Akron, Ohio, 164 pp.

Setiadji, B. H. (2009). *Closed-form backcalculation algorithms for pavement analysis*, Doctoral dissertation, National University of Singapore, Singapore.

Smith, K.D.; Peshkin, D.G.; Darter, M.I.; and Mueller, A.L.; (1990). Performance of Jointed Concrete Pavements, Volume III – Summary of Research Findings, Report FHWA-RD-89-138 for the Federal Highway Administration, ERES Consultants, Savoy, IL, November 1990.

Stark, David C. (1991). *The Significance of Pavement Design and Materials in D-Cracking*. Report No. FHWA/OH/91/009 for the Ohio Department of Transportation, Columbus, OH, June 1991.

Suprenant, B. A. (2002). "Why Slabs Curl". *Concrete International*, Vol. 24, No. 3, pp.56-61.

Tabatabaie, A. M., and Barenberg, E. J. (1978). "Finite Element Analysis of Jointed or Cracked Concrete Pavements". *Transportation Research Record* 671, pp. 11-19.

Tabatabaie, A. M., and Barenberg, E. J. (1980). "Structural analysis of concrete pavement systems." *Journal of Transportation Engineering*, 106(5), 493–506.

Tayabji, S. D., and Colley, B. E. (1986). *Analysis of Jointed Concrete Pavements*. Report No. FHWA/RD-86/041, Construction Technology Laboratories, Portland Cement Association, Skokie, IL, 68 p.

Tepfers, R. (1979). "Tensile Fatigue Strength of Plain Concrete," *Journal of the American Concrete Institute*, Vol. 76, pp. 919-933.

Tepfers, R. and Kutti, T (1979). "Fatigue Strength of Plain, Ordinary, and Lightweight Concrete," *Journal of the American Concrete Institute*, Vol. 76, ACI, Farmington Hills, MI, pp. 635-652.

Texas Department of Transportation (TXDOT). (2012). Traffic Recorder Instruction Manual. http://onlinemanuals.txdot.gov/txdotmanuals/tri/vehicle_classification_using_fhwa_13category_scheme.htm

Tia, M., Armaghani, J. M., Wu, C. L., Lei, S., and Toye, K. L. (1987). "FEACONS III computer program for analysis of jointed concrete pavements." *Transportation Research Record* 1136, 12–22.

Timm, D. H., and Barrett III, W. (2005). *Analysis of the 2002 Design Guide for Rigid Pavement*. Final Report ALDOT Project 930-554 (Rigid Pavement Design Portion), Highway Research Center, Harbert Engineering Center, Auburn, AL, October 10, 2005.

Tremper, B., and Spellman, D. L. (1963). Shrinkage of concrete-comparison of laboratory and field performance. Highway Research Record No. 3, TRB, National Research Council, Washington, D.C., pp. 30-61.

Uddin, W., Zhang, D., and Fernandez, F. (1994). "Finite Element Simulation of Pavement Discontinuities and Dynamic Load Response". *Transportation Research Record* 1448, pp. 100-106.

Uddin, W., R.M. Hackett, A. Joseph, Z. Pan, and A.B. Crawley (1995), "Three-Dimensional Finite-Element Analysis of Jointed Concrete Pavement with Discontinuities", *Transportation Research Record 1482,* TRB, National Research Council, Washington DC, p. 26-32.

Ullidtz, P. (1987). Pavement Analysis. Developments in Civil Engineering, 19 Elsevier, Amsterdam.

Unified Facilities Criteria (UFC) (2001). *Pavement design for airfields*. Report No. UFC 3-260-02, US Army Corp of Engineers, Naval Facilities Engineering Command, and Air Force Civil Engineer Support Agency, Washington, DC, June 30, 2001.

Vandenbossche, J. M. (2003). *Interpreting falling weight deflectometer results for curled and warped Portland cement concrete pavements*. Doctoral dissertation, University of Minnesota.

Vesić, A. S., and Saxena, S. K. (1969). "Analysis of structural behavior of road test rigid pavements". *Highway Research Record* 291.

Westergaard, H.M. (1925), "Theory of Stresses in Road Slabs", *Proceedings of the Fourth Annual Meeting of the Highway Research Board*.

William, G. W., and Shoukry, S. N. (2001). "3D finite-element analysis of temperature-induced stresses in dowel jointed concrete pavements." *International Journal of Geomechanics*, 1(3), 291–307.

Yoder, E. J., and Witczak, M. W. (1975). Principles of Pavement Design. Second Edition, Wiley-Interscience Publications, New York.

Ytterberg, R. F. (1987). "Shrinkage and Curling of Slabs on Grade--Part 1". *Concrete International*, 9(4), 22-30.

Ytterberg, R. F. (1987). "Shrinkage and Curling of Slabs on Grade-Part 2". *Concrete International*, 9(5), 54-61.

Ytterberg, R. F. (1987). "Shrinkage and Curling of Slabs on Grade-Part 3". *Concrete International*, 9(6), 72-81.

Yu, H. T., Smith, K. D., Darter, M. I., Jiang, J., and Khazanovich, L. (1995). *Performance of Concrete Pavements. Volume III: Improving Concrete Pavement Performance*, Report No. FHWA-RD-95-111 for the Federal Highway Administration, Washington, DC.

Yu, H., Khazanovich, L., Darter, M., and Ardani, A. (1998). "Analysis of concrete pavement responses to temperature and wheel loads measured from instrumented slabs". *Transportation Research Record* 1639, pp. 94-101.

Yu, H. T., and Khazanovich, L. (2001). "Effects of construction curling on concrete pavement behavior". *Proceedings of 7th International Conference on Concrete Pavements: The Use of Concrete in Developing Long-Lasting Pavement Solutions for the 21st Century (Vol. 1)*. Orlando, FL, September 9-13, 2001.

Yu, H. T., Khazanovich, L., and Darter, M. I. (2004). "Consideration of JPCP curling and warping in the 2002 design guide". In CD-ROM *Proceedings of the 83rd Annual Meeting of the Transportation Research Board*. Washington DC, January 2004.

Zaman, M., and Alvappillai, A. (1995). "Contact-element model for dynamic analysis of jointed concrete pavements." *Journal of Transportation Engineering*, 121(5), 425–433.

Zapata, C. E., and Houston, W. N. (2008). *Calibration and validation of the enhanced integrated climatic model for pavement design*, NCHRP Report 602. National Cooperative Highway Research Program, Transportation Research Board, Washington DC.

Zienkiewicz, O. C., and Cheung, Y. K. (1967). *The Finite Element Method in Structural and Continuum Mechanics*. McGraw-Hill Publishing Company Limited.

Zollinger, D. G., and Barenberg, E. J. (1989). *Proposed Mechanistic Based Design Procedure For Jointed Concrete Pavements*. Interim Report No. FHWA/IL/UI-225 for Illinois Department of Transportation.

ORITE • 233 Stocker Center • Athens, Ohio 45701-2979 • 740-593-0430
Fax: 740-593-0625 • orite@ohio.edu • http://www.ohio.edu/orite/